MODELING THE RADIATION FROM CAVITY-BACKED ANTENNAS ON PROLATE SPHEROIDS USING A HYBRID FINITE ELEMENT-BOUNDARY INTEGRAL METHOD

By

Charles Alphonso Macon

A DISSERTATION

Submitted to
Michigan State University
in partial fulfillment of the requirements
for the degree of

DOCTOR OF PHILOSOPHY

Department of Electrical and Computer Engineering

2001

ABSTRACT

MODELING THE RADIATION FROM CAVITY-BACKED ANTENNAS ON PROLATE SPHEROIDS USING A HYBRID FINITE ELEMENT-BOUNDARY INTEGRAL METHOD

By

Charles Alphonso Macon

Conformal antennas are increasingly being deployed on the surfaces of air and land vehicles. Quite often, the mounting surfaces are doubly curved. A characteristic property of these antennas is the curvature dependence of their input impedance, resonant frequency, and radiation pattern. In light of this, it is vital that conformal antenna models include surface curvature so that the effects of local surface geometry on their resonant behavior and radiation pattern can be predicted more precisely. This is especially important for a highly resonant antenna, such as the micostrip patch, due to its narrow bandwidth. In addition, advanced material antenna loadings are increasingly being used in practice. These factors motivate the development of a new approach to modeling the radiation from conformal antennas on convex, doubly curved platforms utilizing the hybrid finite element-boundary integral (FE-BI) method. The hybrid FE-BI method, which combines the finite element method with the method of moments, is extended to model convex, doubly curved platforms by means of a specially formulated asymptotic dyadic Green's function. This asymptotic Green's function, formulated within the context of the uniform theory of diffraction (UTD), incorporates the physics of interactions on the surface of an electrically large, perfect electrically conducting prolate spheroid and is highly amenable to numerical applications. The prolate spheroid is a canonical shape that

is sufficiently general to model the curvature of a convex, doubly curved mounting platform. The FE-BI method is used to investigate the effect of curvature variation on the resonant input impedance of a cavity-backed slot and a cavity-backed patch antenna recessed in the surfaces of prolate spheroids of varying dimensions. The effect of curvature variation on the far field radiation pattern of a cavity-backed patch antenna recessed in the surfaces of prolate spheroids of varying dimensions is also investigated using this method. Measured input impedance data for a patch antenna mounted on a planar and a doubly curved surface also is presented.

In memory of my father

Charles A. Macon Sr.

deg

enc

mer

thar

asp

insi

pers

Lab

also

Oh

Wil

year

and

am

chal

love

Etta

not

enco

ACKNOWLEDGMENTS

Many people have assisted my on this long journey towards the completion of this degree. I am especially grateful to my advisor Dr. Leo Kempel for his constant encouragement, support, and guidance throughout the years. He has been an outstanding mentor and friend. I would also like to thank my committee members. I would like to thank Dr. Edward Rothwell for providing me with useful advice on the experimental aspects of this research and Dr. Dennis Nyquist for offering his valuable theoretical insight. I would also like to thank Dr. Byron Drachman for providing his mathematical perspective. I am very grateful to Dr. Stephen Schneider of the Air Force Research Laboratory (AFRL/SNRP) for his sponsorship and enthusiastic support of this research. I also offer thanks to my office colleagues and friends: Chi-Wei Wu, Jeong Lee, and Jong Oh and to my lab colleagues and friends: Christopher Coleman, Jeff Meese, Ben Wilmhoff, and Dr. Mike Havrilla for all of their friendship and assistance through these years. I would also like to thank Dr. Tim Hogan and Dr. Sangeeta Lal for their generosity and assistance during the construction phase of my research.

The support of my family has been equally important throughout this journey. I am forever grateful to my father for teaching me how to persevere in the midst of life's challenges and to always put my trust in God. I am forever grateful to my mother for her love and support. I also would like to thank Samuel Parks and his family and Willy and Etta Tate for all of their strong support through very difficult times. Finally, but certainly not last, I am especially grateful to my loving wife Donyale for all of her love, support, encouragement, and patience with me during my years of school.

LIS

LIS

CH
Int

CH
Un

C
F

TABLE OF CONTENTS

Tal

Ta

Ta

Ta

Ta

LIST OF TABLES

Fig

Fi

Fi

Fi

Fi

F

F

F

LIST OF FIGURES

Figu

Figu

Figu

Figur

Figur

Figur

Figur

Figur

Figure

Figure

Figure

Figure

Figure

Figure

Figu

Figu

Figu

Co

veh

ante

ofte

need

affec

acco

mode

metho

the el

FE-BI

shaped

been u

comple

cylinde

curved

howeve

advanta

a prolat

detail la

canonica

CHAPTER 1

INTRODUCTION

Conformal antennas have become popular for mounting on the surfaces of air and land vehicles due to their low cost, aesthetic appeal, and light weight. In addition, conformal antennas improve the aerodynamic efficiency of vehicles by minimizing drag. Quite often, the surfaces of these vehicles are curved. In view of these applications, there is a need for an understanding of how the radiating characteristics of these antennas are affected by the local geometry of the mounting platform. A cost-effective means of accomplishing this is through the use of computational electromagnetics software to model the behavior of these antennas. The finite element-boundary integral (FE-BI) method has proven to be a versatile and accurate computational technique for modeling the electromagnetic radiation by conformal aperture antennas on curved platforms. The FE-BI method is versatile in that it is capable of modeling the radiation by arbitrarily shaped apertures composed of anisotropic materials. In the past, the FE-BI method has been used successfully to model the radiation by cavity-backed apertures possessing complex shapes recessed in planar and singly curved structures such as the circular cylinder [1]-[3]. A canonical shape, such as a circular cylinder, is used to model a singly curved surface in the cylindrical FE-BI formulation. From a practical standpoint, however, mounting platforms quite often are doubly curved; therefore, it would be advantageous to model a doubly curved platform using a suitable canonical shape such as a prolate spheroid. Due to its unique geometrical properties, to be discussed in greater detail later in this dissertation, the prolate spheroid serves as a mathematically convenient canonical shape for modeling convex doubly curved structures. Hence, an FE-BI form

since

in or

objec

confo

appro

elect

syste

corre

to so

whe

spher

paran

distan

spher

relati

expre

task a

radial

variou

formulation compatible with a prolate spheroidal geometry would be useful to a designer since an additional degree of freedom over a cylindrical formulation would be provided in order to more generally model the effects of platform curvature. In light of this, the objective of this research is to extend the FE-BI approach to model aperture antennas conformal to doubly curved platforms. To accomplish this, a new FE-BI formulation appropriate for modeling the radiation by a cavity-backed aperture recessed in a perfect electrically conducting (PEC) prolate spheroid is presented in this dissertation.

The vector Helmholtz equation is inseparable in the prolate spheroid coordinate system [4]. Therefore, a solution to this equation must be determined from the corresponding scalar Helmholtz equation. Applying the method of separation of variables to solve the scalar Helmholtz equation yields a solution of the form

$$\psi^{(h)}_{\binom{e}{o}mn} = S_{mn}(c,\eta)\,R^{(h)}_{mn}(c,\xi)\begin{Bmatrix}\cos m\varphi\\ \sin m\varphi\end{Bmatrix} \tag{1.1}$$

where $S_{mn}(c,\eta)$ is the angular spheroidal wave function, $R^{(h)}_{mn}(c,\xi)$ is the radial spheroidal wave function of the h kind, and e or o denotes even or odd symmetry. The parameter c is given by $c = kd$ where k is the wave number and d is the interfocal distance. The parameters η and ξ are prolate spheroidal coordinate variables; prolate spheroid geometry will be discussed in detail in Chapter 3. The lack of simple recurrence relationships among the spheroidal wave functions [4] leads to analytically complicated expressions which makes the numerical implementation of such functions a formidable task and not very practical for high frequency applications. The poor convergence of the radial functions for finite values of $c\xi$ has been acknowledged in the literature [5,6] and various schemes for improving their convergence rate have been proposed [4,6].

func

func

[7]

whe

repr

sphe

the p

the r

prol

the p

N fu

chos

[4].

vanis

for th

impli

expre

Tai [

shape

Once the scalar solution has been obtained, the **M** and **N** vector spheroidal wave functions are constructed by applying vector differential operators to the scalar wave function in conjunction with an appropriately chosen pilot vector in the following manner [7]

$$\begin{aligned} \mathbf{M} &= \nabla \psi \times \mathbf{p} \\ \mathbf{N} &= \frac{1}{k} \nabla \times \mathbf{M} \end{aligned} \tag{1.2}$$

where ψ is the scalar wave function, defined previously, and the pilot vector, representing either a constant or a position vector, is denoted by $\mathbf{p}$. In the cylindrical and spherical coordinate systems, the unit vectors $\hat{\mathbf{z}}$ and $\hat{\mathbf{R}}$, respectively, are chosen to be the pilot vector. By analogy with the spherical coordinate system, one may surmise that the radially directed unit vector $\hat{\boldsymbol{\xi}}$ could be used as pilot vector. However, a nuance of the prolate spheroidal coordinate system is that the **M** and **N** functions formulated using $\hat{\boldsymbol{\xi}}$ as the pilot vector do not satisfy the vector Helmholtz equation [8]. Furthermore, the **M** and **N** functions formulated with the position vector, expressed in spheroidal coordinates, chosen as the pilot vector are neither orthogonal among themselves or with each other [4]. Moreover, the boundary conditions requiring the tangential field components to vanish on a PEC prolate spheroid surface can only be satisfied by the **M** and **N** functions for the case of azimuthally symmetric fields or for the limiting case of $\xi = 0$ [9]. The implications of this are far-reaching in that the formulation of an exact closed-form expression for a dyadic Green's function, constructed from **M** and **N** using the method of Tai [10], applicable to the problem of radiation from azimuthally asymmetric arbitrarily shaped apertures may not be possible.

spher
condu
moda
scatte
terms
that a
obtai
functi
soluti
prola
direct
in a
arbitr
be av
polar
Howe
a furt
moda
exact
angle
geom
This a

Published literature treating the case of radiation by sources on a prolate spheroid is scarce. Most work has dealt with the reciprocal problem of scattering by a conducting prolate spheroid. Exact solutions to this problem have been found using the modal expansion technique. Schultz obtained an exact eigenfunction solution for the scattering of an axially incident plane electromagnetic wave by a prolate spheroid in terms of a series of spheroidal wave functions [8]. A major drawback to this solution is that a pair of infinite matrix equations must be truncated and solved simultaneously to obtain the unknown expansion coefficients. Due to the complexity of the spheroidal wave functions, such an approach would consume a significant portion of computer memory. A solution for the fields radiated by an electric dipole located on the tip of a conducting prolate spheroid was found by Hatcher and Leitner [11]. This solution was obtained by directly solving Maxwell's equations for the azimuthal component of the magnetic field in a prolate spheroidal coordinate system. Such an approach is not feasible for an arbitrarily shaped radiating aperture since the current distribution in the aperture may not be available in a closed form. Taylor obtained an exact solution for the scattering of a TM polarized electromagnetic wave by a prolate spheroid for broadside incidence [12]. However, the radiated field patterns were not included in his publication. Sinha presented a further refinement to the modal expansion technique [6]. Sinha augmented the exact modal expansion technique by introducing a special matrix transformation to obtain an exact solution for the scattering of an electromagnetic wave of arbitrary polarization and angle of incidence by a prolate spheroid. The transformation matrix is a function of the geometry of the scatterer and is independent of the direction of the observation angle. This approach was shown to be quite accurate in the resonance region. However, beyond the res

conver

functio

found

functio

and ma

Althou

approa

conver

expens

Specif

numer

involv

propor

electri

accura

does n

by an

in an e

diffrac

curvat

for the

the resonance region, the utility of this approach would be constrained by the poor convergence rate of the spheroidal wave functions at high frequencies. A dyadic Green's function for a spheroidal layered medium was developed by Giarola [13]; however, it was found to be in error due to an incorrectly assumed orthogonality between the **M** and **N** functions, as pointed out by Li *et al* [14]. Li formulated expressions for the exact electric and magnetic dyadic Green's functions of sources in a layered spheroidal medium [14]. Although rigorous, this formulation would not be feasible for application in the FE-BI approach developed in this work due to the aforementioned complexity and poor convergence of the **M** and **N** functions at high frequencies and to the computational expense involved in numerically computing the unknown expansion coefficients. Specifically, the unknown expansion coefficients in the exact Green's functions must be numerically determined by simultaneously solving a system of coupled equations involving infinite series that must be truncated. However, the truncation number is proportional to the largest electrical dimension of a prolate spheroid [6,14]. Hence, for an electrically large prolate spheroid, a large number of series terms would be needed to accurately determine the expansion coefficients. In summary, an exact vector solution does not appear to be practical for problems that involve the computation of the radiation by an arbitrarily shaped cavity-backed inhomogeneously filled aperture antenna recessed in an electrically large prolate spheroid.

In Chapter 2 of this work, an overview of the uniform geometrical theory of diffraction (UTD) is presented. The UTD solution for a singly curved surface of arbitrary curvature is developed from the canonical problem of determining the Green's function for the field excited by a magnetic dipole radiating on the surface of a canonical PEC infinit

dipole

soluti

conve

soluti

sphere

utilize

backe

topics

Green

the de

confo

validi

simul

patch

preser

and a

circul

corrob

recom

infinite circular cylinder. Next, the UTD solution for the canonical problem of a magnetic dipole radiating on the surface of a PEC sphere is presented. The development of a solution to the problem of a magnetic dipole radiating on the surface of an arbitrary convex, doubly curved PEC surface within the context of UTD is presented next. This solution is developed by means of a generalization of the canonical circular cylinder and sphere solutions.

In Chapter 3, the generalized dyadic Green's function, developed in Chapter 2, is utilized in the development of an FE-BI formulation appropriate for modeling cavity-backed aperture antennas conformal to doubly curved surfaces. Moreover, the following topics are discussed at length in Chapter 3: the specialization of the generalized dyadic Green's function by means of differential geometry to treat prolate spheroid surfaces and the development of an FE-BI formulation for modeling cavity-backed aperture antennas conformal to prolate spheroid surfaces. Analytical and numerical results to support the validity of the Green's function also are presented. In Chapter 4, the FE-BI numerical simulation results for the input impedance and radiation patterns exhibited by slot and patch antennas on prolate spheroids of varying curvature are presented. Chapter 5 presents the experimental results for the measurement of the input impedance of a square and a rectangular patch antenna for various orientations on a prolate spheroid model, circular cylinder, and ground plane. It will be shown that the experimental results corroborate the numerical results presented in Chapter 4. Conclusions and recommendations for future work are given in Chapter 6.

2.1 In

The a

field r

restric

the co

utility

series

a is

reasor

physic

mecha

mathe

conve

compl

to a p

modes

conve

field o

the po

requiri

approa

CHAPTER 2

UNIFORM THEORY OF DIFFRACTION

2.1 Introduction

The applicability of exact techniques for calculating the high-frequency electromagnetic field radiated or scattered by objects, such as the eigenfunction expansion method, is restricted to certain canonical shapes. These shapes have surfaces that are tangential to the constant surfaces of orthogonal curvilinear coordinate systems. Once derived, the utility of an exact eigenfunction series solution is restricted in that these eigenfunction series are poorly convergent at high frequencies and require on the order of $2ka$ (where a is the largest dimension of the source body and k is the wavenumber) terms for reasonable accuracy [15]. Moreover, eigenfunction series representations often mask the physics of the high-frequency behavior, thereby making it difficult to isolate the mechanisms of reflection and diffraction. In order to gain additional insight, special mathematical techniques, such as the Watson transformation, must be employed to convert the poorly convergent infinite eigenfunction series into a contour integral in the complex plane. Cauchy's residue theorem is then invoked to equate the contour integral to a pole residue series. Physically, the pole residues are associated with creeping wave modes that exponentially attenuate as they propagate into the shadow region of the convex body. This is the mechanism by which the diffracted field is generated. Since the field of a creeping wave attenuates with the distance traversed along the curved surface, the pole residue series is asymptotic to the electrical radius of curvature of the body, requiring only the first few terms to achieve suitable accuracy for large ka. Although this approach is rigorous, it is rather laborious and impractical for arbitrarily shaped bodies, being r

exist th

such as

T

analyz

strictes

results

extens

within

from s

geome

to be

diffrac

analog

of lea

betwe

refrac

infini

[18,1

being restricted once again to orthogonal coordinate systems for which eigenfunctions exist that are resolvable in terms of the known special functions of mathematical physics such as Bessel, Hankel, or Legendre functions.

The geometrical theory of diffraction (GTD) is an asymptotic technique for analyzing the diffraction from electrically large radiating objects. Although GTD is in the strictest sense a high-frequency technique, it has been found to yield reasonably accurate results at lower frequencies [15,16]. GTD was conceived by Keller [17] as a heuristic extension of geometrical optics to accommodate the phenomenon of diffraction. Hence, within a formalism that is analogous to geometrical optics, the high-frequency diffraction from surfaces is treated as a localized phenomenon that is dependent only on the local geometry and material properties at the point of diffraction. The diffraction mechanism, to be discussed in greater detail in the next section, is ascribed to the propagation of diffracted rays whose trajectories obey Fermat's principle of least propagation time analogous to the reflected and transmitted rays of geometrical optics. Fermat's principle of least propagation time asserts that out of all possible paths, a ray follows the path between two points for which the optical length, defined as the product of the index of refraction in the medium and the distance along a ray, is stationary with respect to infinitesimal variations in the path. The formulation of GTD is based on four postulates [18,19]:

(1) The trajectory of a diffracted ray is determined by a form of Fermat's least time principle that has been generalized to include points on the diffracting surface in the ray trajectory.

(2) Energy in a diffracted ray tube or strip is conserved.

C

illustra

and ar

define

in the

subter

and

GTD

exac

that

shad

attril

emp

deve

trad

Ess

(3) The variation in phase along a diffracted ray equals the product of the wavenumber of the medium and the distance traversed.

(4) The phenomenon of diffraction is local in nature.

Consider a magnetic dipole situated at a point Q' on a convex curved surface. As illustrated in Figure 2.1, the field region exterior to the dipole is divided into a shadow and an illuminated region by a tangent plane to the surface at Q'. The tangent plane defines the shadow boundary. Referring to Figure 2.1, the portion of the shaded regions in the vicinity of the shadow boundary is known as the transition region. The angle subtended by the shadow transition region is of the order of $1/m$ radians, where

$$m = \left[\frac{k\rho_g(Q')}{2} \right]^{1/3} \tag{2.1}$$

and $\rho_g(Q')$ is the radius of curvature of the surface at Q' [20]. A primary advantage of GTD over exact techniques is that it can be applied to generally shaped objects for which exact solutions do not exist. However, a well-known limitation of the GTD solution is that it fails at the caustics of diffracted rays, where it predicts infinite fields, and in the shadow transition region [21]. The failure of GTD in the shadow transition region is attributable to the poor convergence of the creeping wave modal series representation employed in the formulation of expressions for diffracted rays [22].

In order to overcome this limitation, the uniform theory of diffraction (UTD) was developed by Kouyoumjian and Pathak [20,22] to extend the range of validity for the traditional GTD to include the shadow transition region of general convex surfaces. Essentially, the UTD formulation is a generalization of uniform asymptotic solutions to

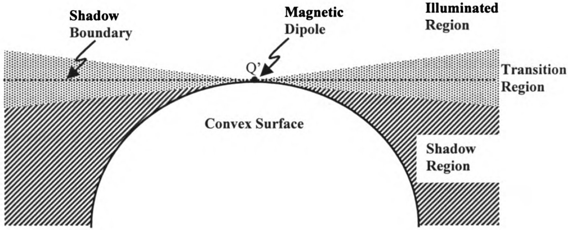

Figure 2.1 The field regions adjacent to a magnetic dipole situated on a perfectly conducting, convex surface.

canonica

sources (

structure

only the

ansatz o

fields at

problem

of the sh

current c

the body

transition

where r_c

current i

special

contour

Appendi

paramete

of the in

provides

interpreta

canonical problems, such as the diffracted field excited by electric and magnetic dipole sources on cylinders or spheres, to treat the problem of diffraction from arbitrarily shaped structures. Since the radiation by conformal apertures is the focus of this dissertation, only the canonical problems involving magnetic dipole sources will be considered. The ansatz of the UTD formulation is Fock's principle of the locality of electromagnetic fields at high frequencies. Fock's theory is based on his now classic solution to the problem of the current induced on the surface of a paraboloid of revolution in the vicinity of the shadow boundary by an impinging magnetic field. According to Fock's theory, the current distribution in the shadow transition region depends only on the local curvature of the body in the plane of incidence and on the impinging wave. The width of the transition region β is given by

$$\beta = \left(\frac{\lambda r_c^2}{\pi} \right)^{1/3} \tag{2.2}$$

where r_c is the radius of curvature of the body at the shadow boundary [23]. The induced current in the vicinity of the shadow boundary was expressed by Fock in terms of new special functions, now known as Fock functions, which are resolvable as canonical contour integrals involving the Airy function $w_1(\tau)$ or its derivative $w_1'(\tau)$ (see Appendix D) [23]. However, Fock's classic result suffered a flaw in that the distance parameter β, defined in (2.2), measures the distance along the direction of propagation of the incident field rather than along the curved surface of the body [24]. Goodrich [25], provides an exposition that brings Fock's theory in alignment with the creeping wave interpretation of the surface diffracted field that is intrinsic to GTD by redefining the distance

defined d

where ρ

along th

the posit

transitio

incidenc

represen

with the

as the p

basis of

excited

In

source

evaluati

asympt

transitic

asympt

given.

UTD, to

convex

distance parameter β as the distance measured along a surface geodesic. The newly defined distance parameter is given by [52]

$$\beta = \int_{Q'}^{Q} \left[\frac{k\rho_g}{2} \right]^{1/3} \frac{1}{\rho_g} ds \tag{2.3}$$

where ρ_g is the radius of curvature along a geodesic, ds is the incremental distance along the geodesic, Q is the position of an observation point on the surface, and Q' is the position of the source point. Fock surmised that since the current distribution in the transition region depends only on the local geometry of the surface at the point of incidence and the magnitude of the incident field at this point, Fock functions could represent the current distribution in the shadow transition region of any convex surface with the same principle radii of curvature at the point of incidence. This assertion, known as the principle of locality of the diffracted field in the penumbra region [23], forms the basis of UTD. By means of reciprocity, the same principle also can be applied to the field excited by an aperture on a convex surface.

In the next section, expressions for the diffracted field excited by a magnetic dipole source on a perfectly conducting circular cylinder are derived via an asymptotic evaluation of the exact dyadic Green's function for the circular cylinder. The canonical asymptotic solutions are expressed in terms of Fock functions that are convergent in the transition region and uniform across the illuminated and deep shadow regions. Next, the asymptotic solution for a magnetic dipole source on a perfectly conducting sphere is given. The procedure for generalizing these canonical solutions, within the context of UTD, to treat the problem of a magnetic dipole source on a perfectly conducting general convex surface will then be discussed. The expression for the dyadic Green's function of the surfa

generaliz

2.2 Cur

An expl

directly

path. th

geodesi

points o

infinites

surface

given b

where

The sy

system

conve

rays t

regior

trajec

incre

wher

the surface field excited by a magnetic dipole on a general convex surface based on the generalization procedure is given at the end of this chapter.

2.2 Curved Surface Diffraction

An explanation of the phenomenon of diffraction by convex curved surfaces follows directly from postulate one of the previous section. In propagating along the least-time path, the portion of the diffracted ray path lying along the convex surface must follow a geodesic path. A geodesic is by definition the path of minimal arc length joining two points on a surface or more precisely, the curve whose length is stationary with respect to infinitesimal pertubations in the path. Consider an aperture M situated in a convex curved surface S. The source in the aperture is represented by an equivalent magnetic dipole given by

$$d\mathbf{M}(\mathbf{r}') = \mathbf{E}(\mathbf{r}') \times \hat{\mathbf{n}} dA \tag{2.4}$$

where $\mathbf{E}$ is the electric field in the aperture and dA is an element of area in the aperture. The symbols $\mathbf{r}'$ and $\mathbf{r}$ are position vectors directed from the origin of the coordinate system to source and observation points on S, respectively. A magnetic dipole on a convex curved surface excites creeping waves that propagate along as surface diffracted rays that are directed away from the source in all directions to points in the shadow region. The surface diffracted rays shed energy along forward tangents to their trajectories. This phenomenon is depicted in Figure 2.2. The general form of the incremental surface field $d\mathbf{F}(\mathbf{r}|\mathbf{r}')$ excited by a magnetic dipole is given by [26]

$$d\mathbf{F}(\mathbf{r}|\mathbf{r}') = \frac{-jk}{4\pi} d\mathbf{M}(\mathbf{r}') \cdot \overline{\overline{\mathbf{T}}}(\mathbf{r}|\mathbf{r}') D \frac{e^{-jks}}{s} \tag{2.5}$$

where s is the geodesic distance between source and observation points on the surface and

surf

In (

ang

poi

of a

2.3

ma

Gre

$\bar{\bar{T}}($

ray

par

wh

bin

to

sol

fix

and D is the surface ray divergence factor which quantifies the change in width of a surface diffracted ray tube due to energy conservation and is given by

$$D = \sqrt{\frac{s d\psi_0}{\rho_c d\psi}} \tag{2.6}$$

In (2.6) $d\psi_0$ is the angle between adjacent surface rays at the source point, $d\psi$ is the angle between the backward tangents to a pair of adjacent surface rays at the observation point, and ρ_c is the radius of curvature of the geodesic circle centered at $\mathbf{r}$. The spread of a surface diffracted ray as it propagates along a curved surface is depicted in Figure 2.3. The parameter $\overline{\overline{\mathbf{T}}}(\mathbf{r}|\mathbf{r}')$ is a dyadic transfer function for the surface field excited by a magnetic dipole on a convex surface. It is proportional to the second-kind electric dyadic Green's function through the relationship $\overline{\overline{\mathbf{T}}}(\mathbf{r}|\mathbf{r}') = -jkY\overline{\overline{\mathbf{G}}}_{e2}(\mathbf{r}|\mathbf{r}')$. The parameter $\overline{\overline{\mathbf{T}}}(\mathbf{r}|\mathbf{r}')$ describes the launching of the surface ray field at $\mathbf{r}'$, the variation of the surface ray field between $\mathbf{r}$ and $\mathbf{r}'$, and the attachment of the ray field at $\mathbf{r}$. This dyadic parameter is given by

$$\overline{\overline{\mathbf{T}}}(\mathbf{r}|\mathbf{r}') = T_1\hat{\mathbf{t}}\hat{\mathbf{t}}' + T_2\hat{\mathbf{t}}\hat{\mathbf{b}}' + T_3\hat{\mathbf{b}}\hat{\mathbf{t}}' + T_4\hat{\mathbf{b}}\hat{\mathbf{b}}' \tag{2.7}$$

where $\hat{\mathbf{t}}$ is a ray-fixed unit vector tangent to the direction of propagation, $\hat{\mathbf{b}}$ is the binormal unit vector defined as $\hat{\mathbf{b}} = \hat{\mathbf{t}} \times \hat{\mathbf{n}}$, with $\hat{\mathbf{n}}$ being the outward unit normal vector to the surface, and T_i are coefficients that are deduced from the uniform asymptotic solutions to canonical problems to be described in the next section. An illustration of the fixed ray-based coordinate system is provided in Figure 2.4. In order to satisfy the

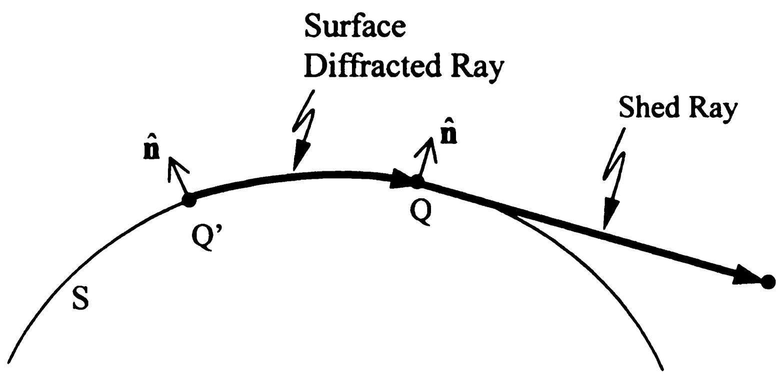

Figure 2.2 The mechanism of diffraction from a convex curved surface.

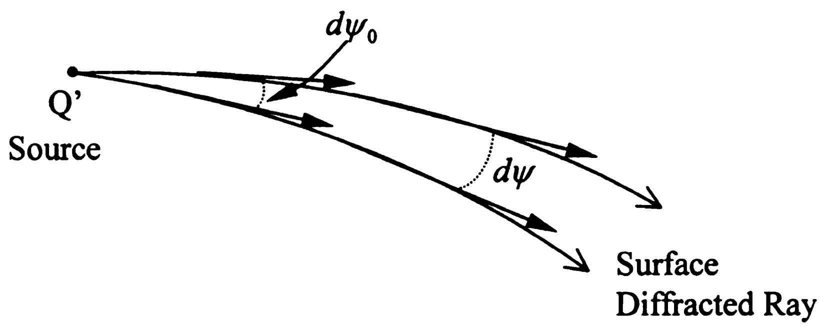

Figure 2.3 Spread of a surface diffracted ray strip due to energy conservation.

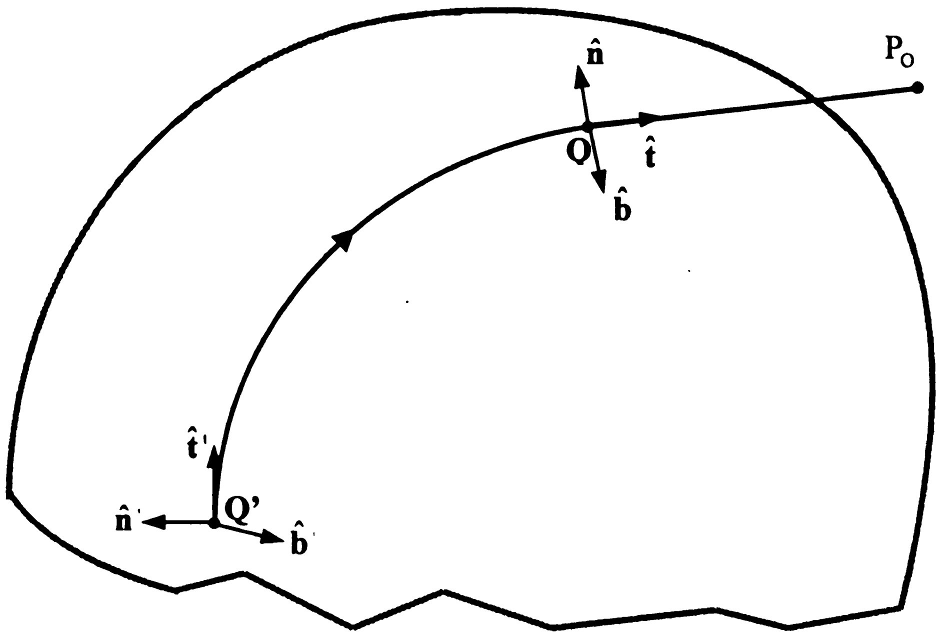

Figure 2.4 Fixed ray-based vector coordinate system.

requiren

region. t

paramet

shadow

series b

asympt

the dec

functio

the geo

converg

shadow

deviati

surface

Thus, t

2.2.1

Electr

2.2.1.1

The ex

the sec

$\rho = a$

tangen

requirement for rapidly convergent solutions that are continuous across the transition region, the elements are expressed uniformly in terms of Fock functions with the distance parameter β as their argument. In the deep shadow region where $\beta >> 0$, with the shadow boundary $\beta = 0$ taken as reference, the Fock functions revert to creeping wave series by means of Cauchy's residue theorem [22]. Appendix D presents details on the asymptotic behavior of Fock functions. The creeping wave series is rapidly convergent in the deep shadow region. Moreover, in the deep lit region where $\beta << 0$ the Fock functions may be approximated asymptotically with respect to β and are equivalent to the geometrical optics current distribution [22]. Therefore, UTD provides a rapidly convergent representation for the diffracted field that also is continuous across the shadow transition region. Furthermore, β can be viewed as a measurement of the deviation of a geodesic from a straight line. As the surface curvature decreases (e.g. surface becomes planar), $\beta \to 0$ and the magnitudes of the Fock functions approach one. Thus, the curved solution approximates the planar solution.

2.2.1 Uniform Asymptotic Evaluation of the Dyadic Green's Function for an Electrically Large Infinite Circular Cylinder

2.2.1.1 On-Surface

The exact eigenfunction series representation for the electric dyadic Green's function of the second kind for an axially infinite, PEC circular cylinder evaluated on the surface $\rho = a$ is given by (see Appendix C for the complete derivation and note that only sources tangential to the surface are considered)

$\overline{\overline{G}}_{e}(\rho,\phi$

$\left[\frac{nk_z k_\rho H}{k_\rho^2 \gamma^2 H_n}\right.$

where $\bar{\phi}$

$k_\rho = \sqrt{k^2}$

argumen

function

a rapidly

that is ar

explaine

converg

also kn

asympto

increase

geometr

shadow

accurate

Watson

and fro

dipole i

$$\overline{\overline{\mathbf{G}}}_{e2}\left(\rho,\phi,z\middle|a,\phi',z'\right)=\frac{1}{(2\pi)^2}\sum_{n=-\infty}^{\infty}e^{jn\bar{\phi}}\int_{-\infty}^{\infty}dk_z e^{-jk_z\bar{z}}\left\{\frac{1}{\gamma}\left[\frac{H_n^{(2)}{}'(\gamma)}{H_n^{(2)}(\gamma)}-\left(\frac{nk_z}{k_0\gamma}\right)^2\frac{H_n^{(2)}(\gamma)}{H_n^{(2)}{}'(\gamma)}\right]\hat{\boldsymbol{\varphi}}\hat{\boldsymbol{\varphi}}'+\right.$$

$$\left.\left[\frac{nk_zk_\rho H_n^{(2)}(\gamma)}{k_0^2\gamma^2H_n^{(2)}{}'(\gamma)}\right]\hat{\boldsymbol{\varphi}}\hat{\mathbf{z}}'+\left[\frac{nk_zk_\rho H_n^{(2)}(\gamma)}{k_0^2\gamma^2H_n^{(2)}{}'(\gamma)}\right]\hat{\mathbf{z}}\hat{\boldsymbol{\varphi}}'-\frac{1}{\gamma}\left[\left(\frac{k_\rho}{k_0}\right)^2\frac{H_n^{(2)}(\gamma)}{H_n^{(2)}{}'(\gamma)}\right]\hat{\mathbf{z}}\hat{\mathbf{z}}'\right\} \tag{2.8}$$

where $\bar{\phi}=\phi-\phi'$, $\bar{z}=z-z'$, $\gamma=k_\rho a$, k_0 is the free-space wave number, and $k_\rho=\sqrt{k_0^2-k_z^2}$. The cylinder radius is denoted by a. As the cylinder radius increases, the argument of the Hankel function grows. However, the numerical evaluation of the Hankel function becomes increasingly difficult for large arguments $(k_\rho a >> 1)$. In order to obtain a rapidly convergent expression for the dyadic Green's function of a large radius cylinder that is amenable to numerical evaluation, the Watson transformation [18] is employed. As explained previously, the Watson transformation effectively transforms a poorly convergent infinite eigenfunction series into a rapidly convergent series of pole residues, also known as the creeping wave series. The value of the pole residue series asymptotically approaches that of the original eigenfunction series as the argument $k_\rho a$ increases. The poles residues are physically interpreted as creeping waves launched at the geometrical optics shadow boundary and propagating along the cylinder surface into the shadow zone. Hence, the number of terms in the series that are needed for a reasonably accurate representation of the diffracted field decreases with increasing radius. The Watson transform is given by [27]

$$\sum_{n=-\infty}^{\infty}e^{jn\bar{\phi}}f(n)=\frac{-j}{2}\oint_C\frac{e^{-j\nu(\pi-\bar{\phi})}f(\nu)}{\sin\nu\pi}d\nu \tag{2.9}$$

and from (2.8) the $\hat{\mathbf{z}}$ component of the surface field attributed to a $\hat{\mathbf{z}}$ directed magnetic dipole is given by

In light of

where v

integrand

may be sp

$G_{\epsilon 2}^{\mp} =$

with sepe

2.6. Note

The subs

contour i

Therefor

The new

in Figure

$$G_{e2}^{zz} = \frac{-1}{(2\pi)^2} \sum_{n=-\infty}^{\infty} e^{jn\bar{\phi}} \int_{-\infty}^{\infty} e^{-jk_z \bar{z}} \frac{k_\rho H_n^{(2)}(\gamma)}{a k_0^2 H_n^{(2)}{}'(\gamma)} dk_z \tag{2.10}$$

In light of (2.9), (2.10) may be rewritten as

$$G_{e2}^{zz} = \frac{1}{(2\pi)^2} \frac{(k_\rho)}{k_0^2 a} \frac{j}{2} \int_{-\infty}^{\infty} e^{-jk_z \bar{z}} dk_z \oint_C \frac{e^{-jv(\pi-\bar{\phi})} H_v^{(2)}(\gamma)}{\sin v\pi H_v^{(2)}{}'(\gamma)} dv \tag{2.11}$$

where v is the complex order and C is the closed contour enclosing the poles of the integrand in (2.11), as depicted in Figure 2.5. The integral around the closed contour C may be split into two integrals

$$G_{e2}^{zz} = \frac{1}{(2\pi)^2} \frac{(k_\rho)}{k_0^2 a} \frac{j}{2} \int_{-\infty}^{\infty} e^{-jk_z \bar{z}} dk_z \left[\int_{C_1} \frac{e^{-jv(\pi-\bar{\phi})} H_v^{(2)}(\gamma)}{\sin v\pi H_v^{(2)}{}'(\gamma)} dv + \int_{C_2} \frac{e^{jv(\pi-\bar{\phi})} H_{-v}^{(2)}(\gamma)}{\sin v\pi H_{-v}^{(2)}{}'(\gamma)} dv \right] \tag{2.12}$$

with seperate integration paths denoted by C_1 and C_2, respectively, as shown in Figure 2.6. Note that the integration path is perturbed from the real axis by a tiny amount σ. The substitution $v \Rightarrow -v$ is made to reverse the direction of integration path C_2. The two contour integrals are subsequently merged via analytic continuation [27]

$$\begin{aligned} H_{-v}^{(2)}(\gamma) &= e^{-jv\pi} H_v^{(2)}(\gamma) \\ H_{-v}^{(2)}{}'(\gamma) &= e^{-jv\pi} H_v^{(2)}{}'(\gamma) \end{aligned} \tag{2.13}$$

Therefore, (2.12) becomes

$$G_{e2}^{zz} = \frac{1}{(2\pi)^2} \frac{k_\rho}{k_0^2 a} \frac{j}{2} \int_{-\infty}^{\infty} e^{-jk_z \bar{z}} dk_z \int_{C_1} \frac{\left(e^{-jv(\pi-\bar{\phi})} + e^{jv(\pi-\bar{\phi})}\right) H_v^{(2)}(\gamma)}{\sin v\pi H_v^{(2)}{}'(\gamma)} dv \tag{2.14}$$

The new integration path enclosing the complex zeros of the Hankel function is depicted in Figure 2.7. Factoring out $e^{j\pi v}$

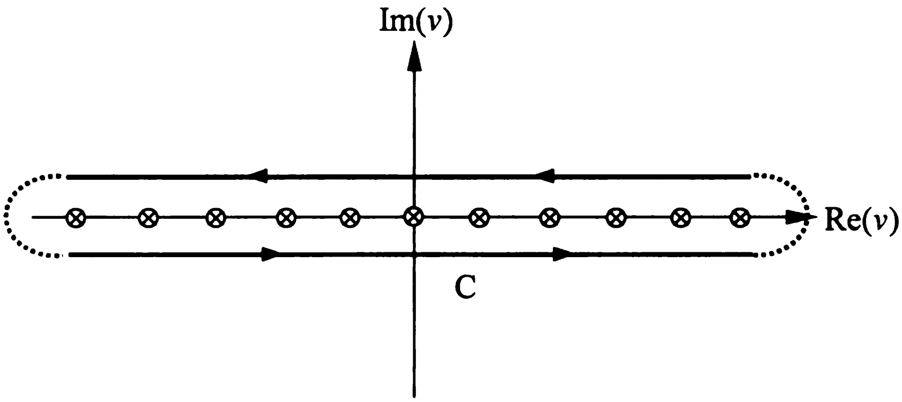

Figure 2.5 The Watson transform integration contour.

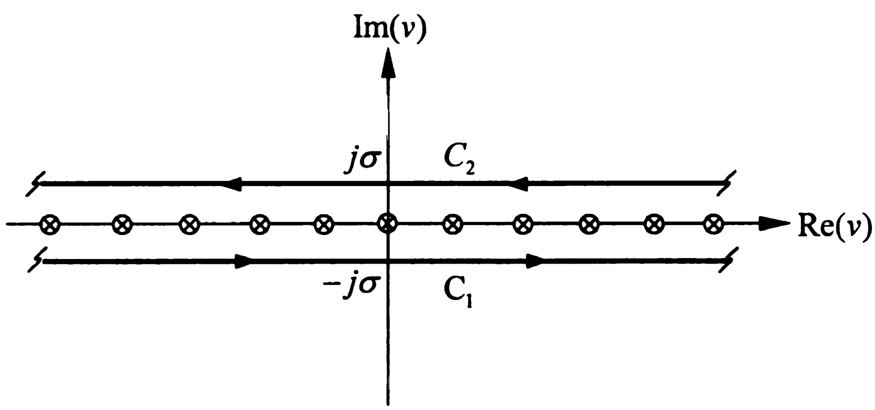

Figure 2.6 The integration contour for the Watson transform split into two segments.

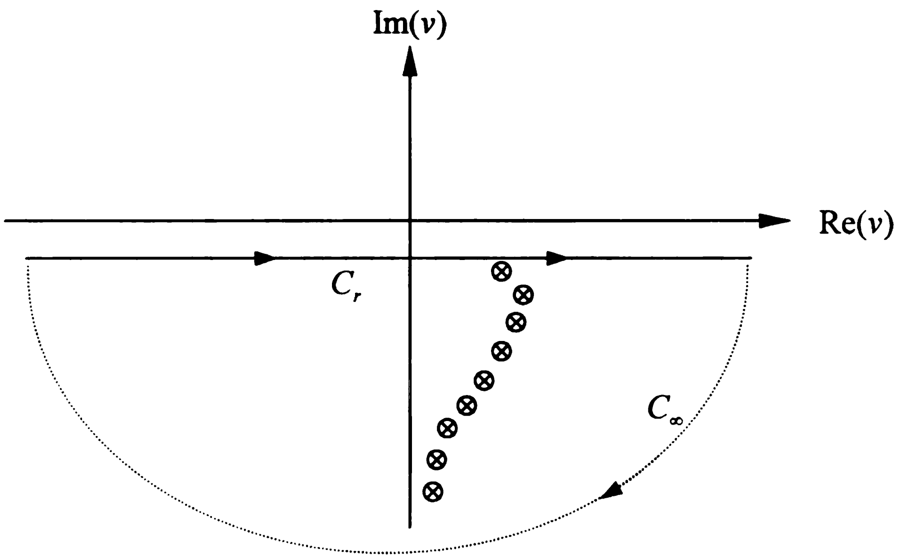

Figure 2.7 Deformation of the integration contour around the complex poles of the integrand arising from the zeros of the Hankel function.

an

is

rep

clo

exp

ord

into

2.8)

The

deri

wher

and

$$G_{e2}^{zz} = \frac{1}{(2\pi)^2} \frac{k_\rho}{k_0^2 a} \frac{j}{2} \int_{-\infty}^{\infty} e^{-jk_z \bar{z}} dk_z \int_{C_1} \frac{e^{j\pi v}\left(e^{-jv(2\pi-\bar{\phi})} + e^{jv\bar{\phi}}\right) H_v^{(2)}(\gamma)}{\sin v\pi H_v^{(2)}{}'(\gamma)} dv \tag{2.15}$$

and noting that $\mathrm{Im}\, v < 0$ from Figure 2.7, the expansion

$$\frac{e^{jv\pi}}{\sin v\pi} = 2j \sum_{l=0}^{\infty} e^{-jv2\pi l} \tag{2.16}$$

is utilized through a technique known as the Poisson sum formulation [18] where l represents the number of complete encirclements made by a creeping wave in either clockwise or counterclockwise directions. Since the magnitude of a creeping wave exponentially decays as it propagates along the surface, the contribution from the higher order (e.g. multiple encirclements for which $l > 0$) terms is negligible. Substituting (2.16) into (2.15) and retaining only the lowest order short and long path terms (refer to Figure 2.8) results in

$$G_{e2}^{zz} = \frac{-1}{(2\pi)^2} \frac{k_\rho}{k_0^2 a} \int_{-\infty}^{\infty} e^{-jk_z \bar{z}} dk_z \int_{C_1} \frac{\left(e^{-jv(2\pi-\bar{\phi})} + e^{jv\bar{\phi}}\right) H_v^{(2)}(\gamma)}{H_v^{(2)}{}'(\gamma)} dv \tag{2.17}$$

The leading terms in the uniform asymptotic expansion of the Hankel function and its derivative, for large γ, in terms of Fock-type Airy functions are given by [28]

$$\begin{aligned} H_v^{(2)}(\gamma) &\sim \frac{jw_2(\tau)}{m\sqrt{\pi}} \\ H_v^{(2)}{}'(\gamma) &\sim \frac{-jw_2{}'(\tau)}{m^2\sqrt{\pi}} \end{aligned} \tag{2.18}$$

where $w_2(\tau)$ is the Fock-type Airy function (see Appendix D), m is as defined in (2.1), and τ is defined in [27]

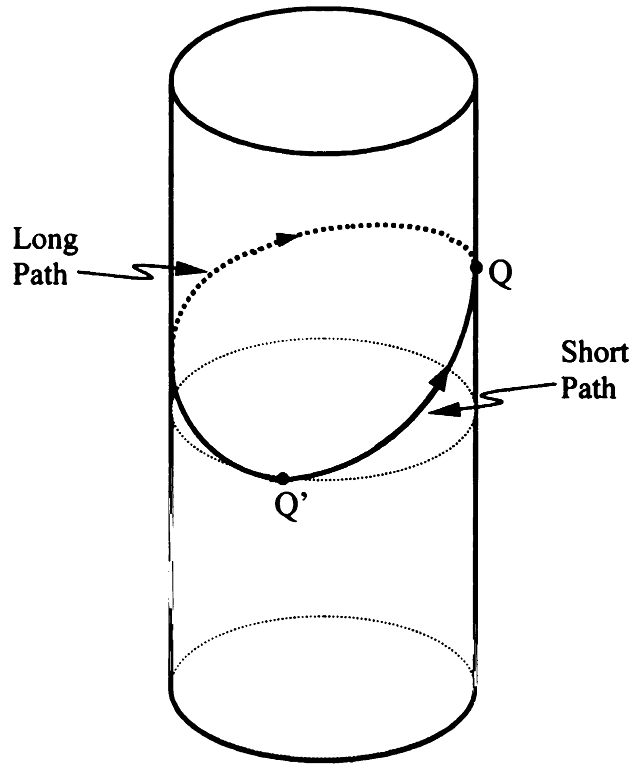

Figure 2.8 Lowest order short and long creeping wave paths on a circular cylinder.

Wit

onw

resu

wh

r-

wh

in

T

in

n

$$\tau = \frac{1}{m}(v - \gamma) \tag{2.19}$$

Without a loss of generality, only the short path term $e^{jv\bar{\phi}}$ is considering from this point onward. Substituting (2.18) into (2.17) and employing the change of variable $dv = md\tau$ results in

$$G_{e2}^{=} \sim \frac{1}{(2\pi)^2} \int_{-\infty}^{\infty} \left[e^{-jk_z \bar{z}} \frac{m^2 k_\rho}{k_0^2 a} \int_{\Gamma_1} \frac{w_2(\tau)}{w_2'(\tau)} e^{-jv\bar{\phi}} d\tau \right] dk_z \tag{2.20}$$

where the complex v-plane integration contour has been deformed into the complex τ-plane integration contour denoted by Γ_1 in Figure 2.9 [29]. Substituting complex v, which from (2.19) is given by

$$v = m\tau + k_\rho a \tag{2.21}$$

into (2.20), yields

$$G_{e2}^{=} \sim \frac{1}{(2\pi)^2} \int_{-\infty}^{\infty} \left[e^{-jk_z \bar{z}} \frac{m^2 k_\rho}{k_0^2 a} \int_{-\infty}^{\infty} \frac{w_2(\tau)}{w_2'(\tau)} e^{-jm\bar{\phi}\tau} e^{-jk_\rho a\bar{\phi}} d\tau \right] dk_z \tag{2.22}$$

This integral may be asymptotically approximated for $k_\rho a >> 1$ via saddle-point integration. To employ this method, (2.22) is recast into an appropriate standard form by means of the following polar coordinate transformation [29]

$$\begin{aligned} k_z &= k_0 \sin\alpha \\ k_\rho &= k_0 \cos\alpha \\ a\bar{\phi} &= s\cos\delta \\ \bar{z} &= s\sin\delta \\ \beta &= m\bar{\phi} \end{aligned} \tag{2.23}$$

where s is the geodesic distance between the source and observation points on the cylinder surface and δ is the angle subtended by the geodesic curve from the azimuthal

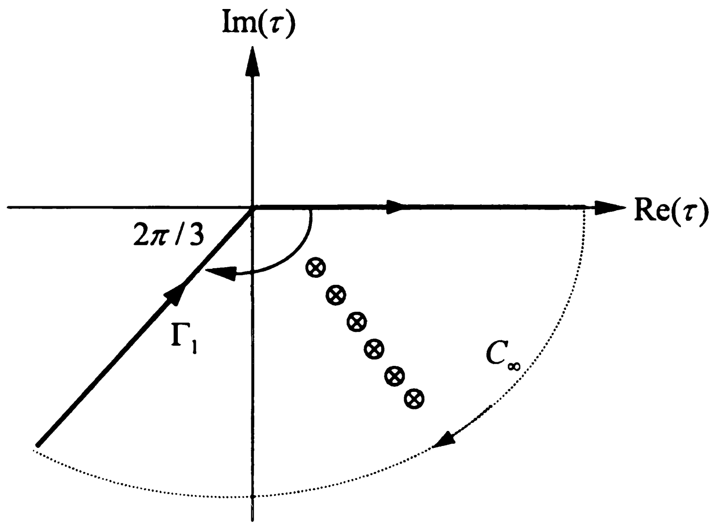

Figure 2.9 The integration path around the zeros of the Fock-type Airy function $w_2(\tau)$ and its derivative $w_2'(\tau)$ in the complex τ-plane.

plane of the cylinder. The mapping of the steepest descent path (SDP) from the complex k_z-plane onto the complex α-plane is accomplished by substituting (2.23) into (2.22). Hence (2.22) becomes

$$G_{e2}^{zz} = \frac{1}{(2\pi)^2} \int_{C_\alpha} \left[e^{-jk_0 s \cos(\alpha-\delta)} \frac{m^2 \cos^2 \alpha}{2\pi a} \int_{\Gamma_1} \frac{w_2(\tau)}{w_2'(\tau)} e^{-j\beta\tau} d\tau \right] d\alpha \tag{2.24}$$

In order to determine the SDP contour, complex α is decomposed into real and imaginary parts ($\alpha = \alpha' + j\alpha''$) and the phase term $e^{-j\cos(\alpha-\delta)}$ is re-evaluated for complex α resulting in

$$e^{-j\cos(\alpha'-\delta)\cosh\alpha'' + \sin(\alpha'-\delta)\sinh\alpha''} \tag{2.25}$$

In order for (2.24) to converge, the constraint $\sin(\alpha'-\delta)\sinh\alpha'' < 0$ must be satisfied. Furthermore, in order to eliminate the oscillations of the integrand along the SDP contour, the imaginary part of (2.25) must remain constant and equal to its value at the saddle point. Thus, the constraint $\cos(\alpha'-\delta)\cosh\alpha'' = 1$ determines the shape of the SDP contour in the complex α-plane. Expressing (2.24) in terms of the hard surface Fock function given by (see Appendix C for details on the Fock functions)

$$v(\beta) = \sqrt{\frac{j\beta}{4\pi}} \int_{\Gamma_1} \frac{w_2(\tau)}{w_2'(\tau)} e^{-j\beta\tau} d\tau \tag{2.26}$$

yields

$$G_{e2}^{zz} = \frac{1}{(2\pi)^2} \int_{C_\alpha} \left[\frac{m^2 \cos^2 \alpha}{2\pi a} \sqrt{\frac{4\pi}{j\beta}} v(\beta) e^{-jk_0 s \cos(\alpha-\delta)} \right] d\alpha \tag{2.27}$$

where β, defined in (2.3) specializes to $\beta = \frac{ms}{\rho_g}$ for a circular cylinder, and ρ_g is the radius of curvature along a geodesic given by

Deforming

Figure 2.1

point inte

dyadic Gr

Note that

in the pr

surface

curvatur

radiatin

express

invarian

result d

the ex

dyadic

expres

vector

expres

Emplo

$$\rho_g = \frac{a}{\cos^2 \delta} \tag{2.28}$$

Deforming the C_α integration contour in (2.27) into the SDP contour, as depicted in Figure 2.10, and asymptotically evaluating (2.27) for large $k_0 s$ via the method of saddle-point integration, yields the asymptotic expression for the $\hat{\mathbf{z}}\hat{\mathbf{z}}$ component of the electric dyadic Green's function for a magnetic dipole radiating on a circular cylinder

$$G_{e2}^{\overline{\overline{z}}} \sim v(\beta) \frac{e^{-jk_0 s}}{2\pi s} \tag{2.29}$$

Note that (2.29) is identical to the dyadic Green's function of a magnetic dipole radiating in the presence of a PEC ground plane, derived via image theory, modulated by the hard surface Fock function $v(\beta)$. The physical interpretation of this result is that as the curvature vanishes, (2.29) reverts to the dyadic Green's function for a magnetic dipole radiating in the presence of a PEC infinite ground-plane. This result, however, is not expressed within the framework of UTD. In order to recast this result in terms of the invariant ray-based unit vectors ($\hat{\mathbf{t}}, \hat{\mathbf{b}}$) of UTD, which can readily be compared with the result derived by Pathak [29], further manipulation is required. From physical reasoning, the expression for the cylindrical dyadic Green's function should recover the planar dyadic Green's function in the limit of zero curvature. Based on this assumption, an expression for the cylindrical dyadic Green's function in terms of the ray-based unit vectors may be heuristically developed by substituting (2.29) into the following expression for the planar dyadic Green's function

$$\overline{\overline{G}}_{e2} = \left(\overline{\overline{\mathbf{I}}} + \frac{1}{k_0^2} \nabla\nabla \right) \frac{e^{-jks}}{2\pi s} v(\beta) \tag{2.30}$$

Employing the identity from [30] which is given below

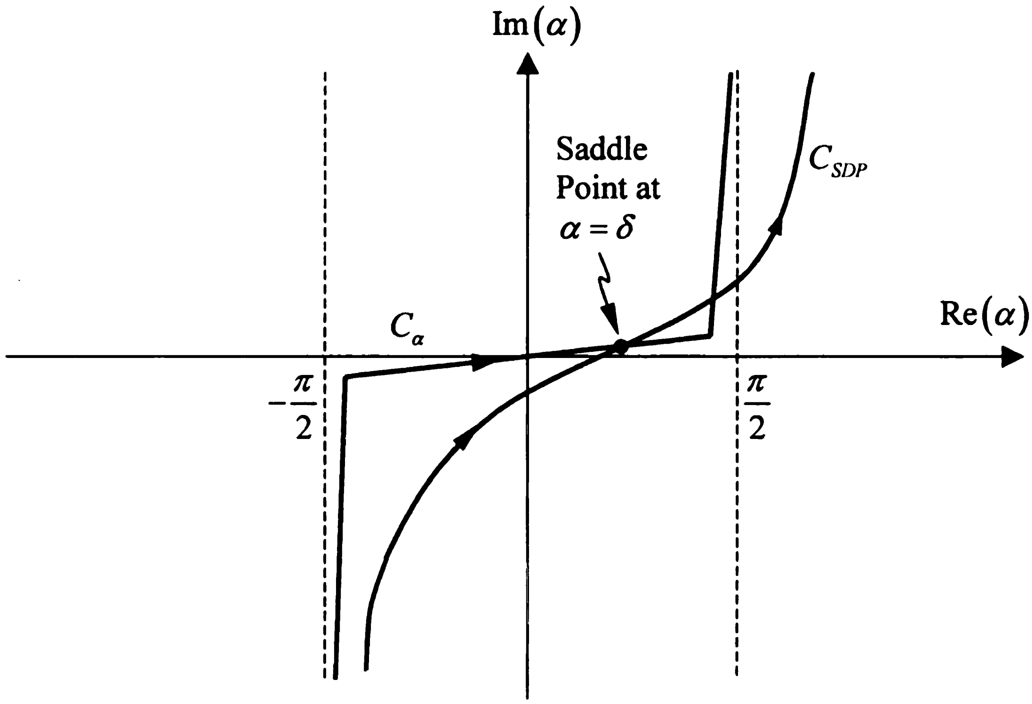

Figure 2.10 Deformation of the C_α contour into the steepest descent contour C_{SDP}.

$$\nabla\nabla\left[v(\beta)\frac{e^{-jk_0 s}}{2\pi s}\right]=\left\{\hat{\mathbf{R}}\hat{\mathbf{R}}\left[\frac{1}{R^2}+\left(jk_0+\frac{1}{R}\right)^2\right]-\left(\bar{\bar{\mathbf{I}}}-\hat{\mathbf{R}}\hat{\mathbf{R}}\right)\left(jk_0+\frac{1}{R}\right)\frac{1}{R}\right\}v(\beta)\frac{e^{-jk_0 s}}{2\pi s} \tag{2.31}$$

to evaluate (2.30) yields

$$\begin{aligned}\bar{\bar{G}}_{e2}&=\left\{\bar{\bar{\mathbf{I}}}\left[1-\frac{j}{k_0 s}\left(1-\frac{j}{k_0 s}\right)\right]+\hat{\mathbf{R}}\hat{\mathbf{R}}\left[\frac{2}{(k_0 s)^2}+\frac{2j}{k_0 s}-1\right]+\hat{\mathbf{R}}\hat{\mathbf{R}}\frac{j}{k_0 s}\left(1-\frac{j}{k_0 s}\right)\right\}v(\beta)\frac{e^{-jk_0 s}}{2\pi s}\\&=\left\{\left(\bar{\bar{\mathbf{I}}}-\hat{\mathbf{R}}\hat{\mathbf{R}}\right)-\left(\bar{\bar{\mathbf{I}}}-\hat{\mathbf{R}}\hat{\mathbf{R}}\right)q(1-q)+\hat{\mathbf{R}}\hat{\mathbf{R}}\left(2q-2q^2\right)\right\}v(\beta)\frac{e^{-jk_0 s}}{2\pi s}\\&=\left\{\bar{\bar{\mathbf{I}}}_s\left[1-q(1-q)\right]+\hat{\mathbf{R}}\hat{\mathbf{R}}\left(2q-2q^2\right)\right\}v(\beta)\frac{e^{-jk_0 s}}{2\pi s}\end{aligned} \tag{2.32}$$

where $q=\frac{j}{k_0 s}$, $\hat{\mathbf{R}}=(\mathbf{r}-\mathbf{r}')/|\mathbf{r}-\mathbf{r}'|$, and $\bar{\bar{\mathbf{I}}}_s=\bar{\bar{\mathbf{I}}}-\hat{\mathbf{R}}\hat{\mathbf{R}}$. Referring to Figure 2.11, it is apparent that $\hat{\mathbf{R}}$ is tangential to the direction of propagation for a creeping wave between a source and observation point on the cylinder surface. Therefore, setting $\hat{\mathbf{R}}=\hat{\mathbf{t}}$ and $\bar{\bar{\mathbf{I}}}_s=\hat{\mathbf{b}}\hat{\mathbf{b}}'$ allows (2.32) to be expressed in terms of the ray-based unit vectors of UTD. Therefore, (2.32) can be rewritten as

$$\bar{\bar{G}}_{e2}=\left\{\hat{\mathbf{b}}\hat{\mathbf{b}}'[1-q(1-q)]+\hat{\mathbf{t}}\hat{\mathbf{t}}'(2q-2q^2)\right\}v(\beta)\frac{e^{-jk_0 s}}{2\pi s} \tag{2.33}$$

To facilitate the numerical computation of $\bar{\bar{G}}_{e2}$, the explicit expressions for the ray-based unit vectors in terms of the geodesic angle δ that are given below

$$\begin{aligned}\hat{\mathbf{t}}&=\hat{\mathbf{z}}\sin\delta+\hat{\boldsymbol{\varphi}}\cos\delta\\\hat{\mathbf{b}}&=\hat{\boldsymbol{\varphi}}\cos\delta-\hat{\mathbf{z}}\sin\delta\end{aligned} \tag{2.34}$$

are substituted into (2.33). The subsequent evaluation of (2.33) yields the following expressions for all four of the components of the asymptotic dyadic Green's function for a circular cylinder:

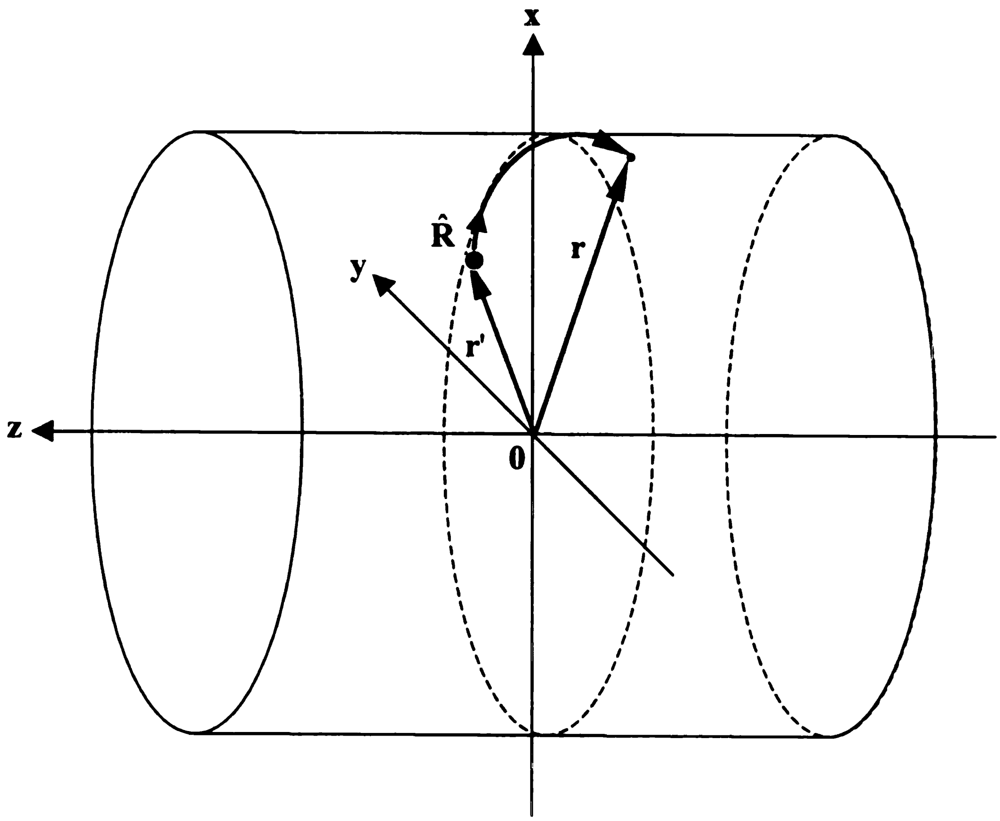

Figure 2.11 Position of source and observation points on the surface of a cylinder with respect to the origin.

$$G_{e2}^{zz}(a,\bar{\phi},\bar{z}) \sim \left[\sin^2\delta + q(1-q)(2-3\sin^2\delta)\right]v(\beta)\frac{e^{-jk_0 s}}{2\pi s} \tag{2.35}$$

$$G_{e2}^{z\phi} = G_{e2}^{\phi z}(a,\bar{\phi},\bar{z}) \sim -\sin\delta\cos\delta\left[1-3q(1-q)\right]v(\beta)\frac{e^{-jk_0 s}}{2\pi s} \tag{2.36}$$

$$G_{e2}^{\phi\phi}(a,\bar{\phi},\bar{z}) \sim \left[\cos^2\delta + q(1-q)(2-3\cos^2\delta)\right]v(\beta)\frac{e^{-jk_0 s}}{2\pi s} \tag{2.37}$$

Note that the $\hat{\boldsymbol{\varphi}}\hat{\boldsymbol{\varphi}}$-component in [29] contains a mixed term comprising both the hard, $v(\beta)$, and soft, $u(\beta)$, surface Fock functions. The soft Fock function $u(\beta)$ arises from the asymptotic evaluation of the first term enclosed within the brackets of the $\hat{\boldsymbol{\varphi}}\hat{\boldsymbol{\varphi}}$-component of the exact dyadic Green's function (2.8) by the procedure outlined above. With the inclusion of the mixed term (2.37) may be rewritten as [29]

$$\begin{aligned} G_{e2}^{\phi\phi}(a,\bar{\phi},\bar{z}) &\sim \left[\cos^2\delta + q(1-q)(2-3\cos^2\delta)\right]v(\beta)\frac{e^{-jk_0 s}}{2\pi s} \\ &+q\left[\sec^2\beta\big(u(\beta)-v(\beta)\big)\right] \end{aligned} \tag{2.38}$$

2.2.1.2 Far Zone

In this case, we begin with the expression for the exact electric dyadic Green's function of the second kind for an infinite, PEC circular cylinder given by

$$\begin{aligned} \bar{\bar{G}}_{e2}\left(\rho,\phi,z\middle|a,\phi',z'\right) = \frac{1}{(2\pi)^2}\sum_{n=-\infty}^{\infty} e^{jn\bar{\phi}}\int_{-\infty}^{\infty} dk_z e^{-jk_z\bar{z}} \Bigg\{ &\left[\frac{-jnH_n^{(2)}(x)}{\gamma x H_n^{(2)}(x)} + \frac{jn}{\gamma^2}\left(\frac{k_z}{k_0}\right)^2 \frac{H_n^{(2)}{}'(x)}{H_n^{(2)}{}'(\gamma)}\right]\hat{\boldsymbol{\rho}}\hat{\boldsymbol{\varphi}}' \\ -j\left[\frac{k_z k_\rho H_n^{(2)}{}'(x)}{\gamma k_0^2 H_n^{(2)}{}'(\gamma)}\right]\hat{\boldsymbol{\rho}}\hat{\mathbf{z}}' + \left[\frac{H_n^{(2)}{}'(x)}{\gamma H_n^{(2)}{}'(\gamma)} - \left(\frac{nk_z}{k_0\gamma}\right)^2 \frac{H_n^{(2)}(x)}{xH_n^{(2)}{}'(\gamma)}\right]&\hat{\boldsymbol{\varphi}}\hat{\boldsymbol{\varphi}}' + \left[\frac{nk_z k_\rho H_n^{(2)}(x)}{\gamma x k_0^2 H_n^{(2)}{}'(\gamma)}\right]\hat{\boldsymbol{\varphi}}\hat{\mathbf{z}}' \\ +\left[\frac{nk_z k_\rho H_n^{(2)}(x)}{\gamma^2 k_0^2 H_n^{(2)}{}'(\gamma)}\right]\hat{\mathbf{z}}\hat{\boldsymbol{\varphi}}' - \frac{1}{\gamma}&\left[\left(\frac{k_\rho}{k_0}\right)^2 \frac{H_n^{(2)}(x)}{H_n^{(2)}{}'(\gamma)}\right]\hat{\mathbf{z}}\hat{\mathbf{z}}'\Bigg\} \end{aligned} \tag{2.39}$$

where $x = k_\rho \rho$. This time, however, we asymptotically evaluate the exact Green's function for the case of a source point lying on the cylinder surface $\rho = a$, while an off-surface observation point is allowed to recede to infinity. Since the Hankel function requires $n >> k_\rho \rho$ for convergence, the exact Green's function becomes poorly convergent for large $k_\rho \rho$. In order to alleviate this problem, the method of steepest descent must be applied to derive an asymptotic approximation of the exact Green's function that is valid in the far zone. Substituting the following approximations, valid in the far field, into (2.39)

$$\lim_{\rho\to\infty} H_n^{(2)}{}'(x) \sim -jH_n^{(2)}(x) \tag{2.40}$$

$$\lim_{\rho\to\infty} \frac{H_n^{(2)}(x)}{x} \sim \lim_{\rho\to\infty} \frac{1}{e^{j\rho}\rho\sqrt{\rho}} = 0 \tag{2.41}$$

and evaluating, results in

$$\begin{aligned}\overline{\overline{G}}_{e2}\left(\rho,\phi,z\middle|a,\phi',z'\right) = \frac{1}{(2\pi)^2}\sum_{n=-\infty}^{\infty} e^{jn\bar{\phi}} \int_{-\infty}^{\infty} dk_z e^{-jk_z\bar{z}} &\left\{\left[\frac{n}{\gamma^2}\left(\frac{k_z}{k_0}\right)^2 \frac{H_n^{(2)}(x)}{H_n^{(2)}{}'(\gamma)}\right]\hat{\boldsymbol{\rho}}\hat{\boldsymbol{\varphi}}'\right. \\ -\left[\frac{k_z k_\rho H_n^{(2)}{}'(x)}{\gamma k_0^2 H_n^{(2)}{}'(\gamma)}\right]\hat{\boldsymbol{\rho}}\hat{\mathbf{z}}' - \left[\frac{jH_n^{(2)}{}'(x)}{\gamma H_n^{(2)}(\gamma)}\right]\hat{\boldsymbol{\varphi}}\hat{\boldsymbol{\varphi}}' + \left[\frac{nk_z k_\rho H_n^{(2)}(x)}{\gamma^2 k_0^2 H_n^{(2)}{}'(\gamma)}\right]\hat{\mathbf{z}}\hat{\boldsymbol{\varphi}}'& \\ \left. -\frac{1}{\gamma}\left[\left(\frac{k_\rho}{k_0}\right)^2 \frac{H_n^{(2)}(x)}{H_n^{(2)}{}'(\gamma)}\right]\hat{\mathbf{z}}\hat{\mathbf{z}}'\right\}&\end{aligned} \tag{2.42}$$

Before proceeding with the application of the method of steepest descent to (2.42), it is clearly evident that k_ρ goes through 0 along the interval of integration of k_z. As a result, special consideration must be given to the asymptotic evaluation of this integral because the arguments x and γ also pass through 0, thereby, challenging any asymptotic approximations that may be used. Since it is evident that (2.42) can be written in the form of a steepest descent integral via the substitution of an asymptotic expression for $H_n^{(2)}(x)$ into (2.42), it is known *a priori* that the major contribution to this integral comes from the region near the saddle-point where $k_\rho \neq 0$. Therefore, the use of the asymptotic form of the Hankel function for a large argument $x = k_\rho \rho >> 1$ is justified provided that the observation point is not in the vicinity of the axis of the cylinder where $\theta = 0$ or π radians. (Note: The near axis behavior will be discussed in the next section.)

In light of this, the second-kind Hankel function is factored out of the numerator and replacing by its large argument form for $x >> 1$

$$H_n^{(2)}(x) \sim \sqrt{\frac{2}{\pi x}} e^{-jx} e^{jn\pi/2} e^{j\pi/4} \tag{2.43}$$

under the constraint that $\theta \neq 0$ or π radians. Grouping all $\hat{\boldsymbol{\rho}}$ and $\hat{\mathbf{z}}$ terms together with the same unit source vectors, (2.42) becomes

$$\begin{aligned}\overline{\overline{G}}_{e2} \sim \frac{2}{(2\pi)^2} \sum_{n=-\infty}^{\infty} e^{jn\left(\bar{\phi}+\frac{\pi}{2}\right)} \int_{-\infty}^{\infty} e^{jk_z z'} \Bigg\{ & \frac{nk_z}{\gamma^2 k_0 H_n^{(2)}{}'(\gamma)} \left[\frac{k_z}{k_0} \hat{\boldsymbol{\rho}} - \frac{k_\rho}{k_0} \hat{\mathbf{z}} \right] \hat{\boldsymbol{\varphi}}' \\ & + \frac{1}{k_0 a H_n^{(2)}{}'(\gamma)} \left[\frac{k_z}{k_0} \hat{\boldsymbol{\rho}} - \frac{k_\rho}{k_0} \hat{\mathbf{z}} \right] \hat{\mathbf{z}}' - \frac{j}{\gamma H_n^{(2)}(\gamma)} \hat{\boldsymbol{\varphi}} \hat{\boldsymbol{\varphi}}' \Bigg\} \frac{e^{j\pi/4} e^{-j(k_\rho \rho + k_z z)}}{\sqrt{2\pi k_\rho \rho}} dk_z\end{aligned} \tag{2.44}$$

Making the substitution $\left[\frac{k_z}{k_0} \hat{\boldsymbol{\rho}} - \frac{k_\rho}{k_0} \hat{\mathbf{z}} \right] = \hat{\boldsymbol{\theta}}$ and decomposing (2.42) into dyadic components yields

$$\overline{\overline{G}}_{e2} \sim \frac{2}{(2\pi)^2} \sum_{n=-\infty}^{\infty} e^{jn\left(\bar{\phi}+\frac{\pi}{2}\right)} \left[G_{\theta\phi} \hat{\boldsymbol{\theta}} \hat{\boldsymbol{\varphi}}' + G_{\theta z} \hat{\boldsymbol{\theta}} \hat{\mathbf{z}}' + G_{\phi\phi} \hat{\boldsymbol{\varphi}} \hat{\boldsymbol{\varphi}}' \right] \tag{2.45}$$

where

$$G_{e2}^{\theta\phi} = \int_{-\infty}^{\infty} \frac{e^{jk_z z'} e^{j\pi/4} n k_z}{(k_\rho a)^2 k H_n^{(2)}{}'(k_\rho a)} \frac{e^{-j(k_\rho \rho + k_z z)}}{\sqrt{2\pi k_\rho \rho}} dk_z \tag{2.46}$$

$$G_{e2}^{\theta z} = \int_{-\infty}^{\infty} \frac{e^{jk_z z'} e^{j\pi/4}}{k_0 a H_n^{(2)}{}'(k_\rho a)} \frac{e^{-j(k_\rho \rho + k_z z)}}{\sqrt{2\pi k_\rho \rho}} dk_z \tag{2.47}$$

$$G_{e2}^{\phi\phi} = \int_{-\infty}^{\infty} \frac{e^{jk_z z'} e^{j\pi/4} (-j) e^{-j(k_\rho \rho + k_z z)}}{k_\rho a H_n^{(2)}(k_\rho a)\sqrt{2\pi k_\rho \rho}} dk_z \tag{2.48}$$

Each of the integrals in (2.46)-(2.48) is amenable to evaluation by the method of steepest descent under the constraint that $\theta \neq 0$ or π radians. The canonical steepest descent integral given by

$$G = \int_{SDP} F(k_z) e^{\kappa g(k_z)} dk_z \tag{2.49}$$

has first order solutions of the form

$$G(k_z) \sim \frac{\sqrt{2\pi} F\left(k_z^s\right) e^{\kappa g\left(k_z^s\right)} e^{j\psi}}{\left|\kappa g''\left(k_z^s\right)\right|^{1/2}} \tag{2.50}$$

where, κ denotes the large parameter, ψ is the angle at which the SDP contour intersects the saddle-point, and k_z^s denotes the saddle-point. Comparing (2.49) and (2.46)

$$g(k_z) = -j\left(\sqrt{k_0^2 - k_z^2} \sin\theta + k_z \cos\theta\right) \tag{2.51}$$

is obtained and the saddle-point can be found from $\left.\frac{d}{dk_z} g(k_z)\right|_{k_z = k_z^s} = 0$. Consequently, the saddle-point is given by $k_z^s = k\cos\theta$, where θ is the angle subtended from the z axis to an observation point in the far-zone. It follows that

$$g(k_z^s) = -jk_0 \text{ and } g''(k_z^s) = \frac{j}{k_0 \sin^2\theta} \tag{2.52}$$

where the double prime denotes second-order differentiation with respect to the argument k_z. Making the following substitutions, to express the parameters in (2.46) in terms of spherical coordinates in the far-zone:

$$k_\rho = k\sin\theta,\ \rho = R\sin\theta, \text{ and } z = R\cos\theta \tag{2.53}$$

and evaluating (2.46) at the saddle-point, the expression for $F_{\theta\phi}\left(k_z^s\right)$ becomes

$$F_{\theta\phi}\left(k_z^s\right)=\frac{ne^{jk\cos\theta z'}k\cos\theta}{\left(ka\sin\theta\right)^2 kH_n^{(2)}{}'(ka\sin\theta)\sin\theta\sqrt{2\pi kR}} \tag{2.54}$$

Setting the parameters $\kappa = R$ and $\psi = \dfrac{\pi}{4}$ and substituting (2.52) and (2.54) into (2.50) to obtain the asymptotic form of $G_{e2}^{\theta\phi}$ which is valid in the far-zone of the cylinder

$$G_{e2}^{\theta\phi} \sim \frac{e^{-jk_0R}}{k_0R}\frac{j2k_0\cos\theta e^{jk\cos\theta z'}}{(2\pi)^2(ka\sin\theta)^2}\sum_{n=-\infty}^{\infty}\frac{ne^{jn\left(\bar{\phi}+\frac{\pi}{2}\right)}}{H_n^{(2)}{}'(ka\sin\theta)} \tag{2.55}$$

The other components of the asymptotic dyadic Green's function are obtained through the same procedure and are given by the following:

$$G_{e2}^{\theta z} \sim \frac{e^{-jk_0R}}{k_0R}\frac{j2e^{jk\cos\theta z'}}{(2\pi)^2 a}\sum_{n=-\infty}^{\infty}\frac{e^{jn\left(\bar{\phi}+\frac{\pi}{2}\right)}}{H_n^{(2)}{}'(ka\sin\theta)} \tag{2.56}$$

$$G_{e2}^{\phi\phi} \sim \frac{e^{-jkR}}{k_0R}\frac{2k_0e^{-jk\cos\theta z'}}{(2\pi)^2 ka\sin\theta}\sum_{n=-\infty}^{\infty}\frac{e^{jn\left(\bar{\phi}+\frac{\pi}{2}\right)}}{H_n^{(2)}{}'(ka\sin\theta)} \tag{2.57}$$

To facilitate numerical computation, the eigenfunction representations in (2.55)-(2.57) can be further simplified. Decomposing the infinite summation into two separate sums, (2.55) can be rewritten as

$$G_{e2}^{\theta\phi} \sim \frac{e^{-jk_0R}}{k_0R}\frac{j2k_0\cos\theta e^{jk\cos\theta z'}}{(2\pi)^2\left(ka\sin\theta\right)^2}\left[\sum_{n=-\infty}^{0}\frac{nj^n e^{jn\bar{\phi}}}{H_n^{(2)}{}'\left(ka\sin\theta\right)}+\sum_{n=0}^{\infty}\frac{nj^n e^{jn\bar{\phi}}}{H_n^{(2)}{}'\left(ka\sin\theta\right)}\right] \tag{2.58}$$

Changing the interval of the first summation via the substitution $n \Rightarrow -n$ yields

$$G_{e2}^{\theta\phi} \sim \frac{e^{-jk_0R}}{k_0R}\frac{j2k_0\cos\theta e^{jk\cos\theta z'}}{(2\pi)^2\left(ka\sin\theta\right)^2}\left[\sum_{n=0}^{\infty}\frac{-nj^{-n}e^{-jn\bar{\phi}}}{H_{-n}^{(2)}{}'\left(ka\sin\theta\right)}+\sum_{n=0}^{\infty}\frac{nj^n e^{jn\bar{\phi}}}{H_n^{(2)}{}'\left(ka\sin\theta\right)}\right] \tag{2.59}$$

Analytic

applied t

Euler's

Apply

which

wher

proc

In s

axia

Analytic continuation of the Hankel functions, $H_{-n}^{(2)}{}'(\gamma) = e^{-j\pi n} H_n^{(2)}{}'(\gamma)$, is subsequently applied to merge the two summations

$$G_{e2}^{\theta\phi} \sim \frac{e^{-jk_0R}}{k_0R} \frac{j2k_0 \cos\theta e^{jk\cos\theta z'}}{(2\pi)^2 (ka\sin\theta)^2} \sum_{n=0}^{\infty} \frac{nj^n \left(e^{jn\bar{\phi}} - e^{-jn\bar{\phi}}\right)}{H_n^{(2)}{}'(ka\sin\theta)} \frac{2j}{2j} \tag{2.60}$$

Euler's identity is invoked to simplify (2.60) which leads to the final form

$$G_{e2}^{\theta\phi} \sim \frac{-e^{-jk_0R}}{k_0R} \frac{4k_0 \cos\theta e^{jk\cos\theta z'}}{(2\pi)^2 (ka\sin\theta)^2} \sum_{n=0}^{\infty} \frac{nj^n \sin\left(n\bar{\phi}\right)}{H_n^{(2)}{}'(ka\sin\theta)} \tag{2.61}$$

Applying the same procedure to (2.56) leads to

$$G_{e2}^{\theta z} \sim \frac{e^{-jk_0R}}{k_0R} \frac{j2e^{jk\cos\theta z'}}{(2\pi)^2 a} \sum_{n=-\infty}^{\infty} \frac{j^n \left(e^{jn\bar{\phi}} + e^{-jn\bar{\phi}}\right)}{H_n^{(2)}{}'(ka\sin\theta)} \frac{2}{2} \tag{2.62}$$

which upon simplification, results in

$$G_{e2}^{\theta z} \sim \frac{e^{-jk_0R}}{k_0R} \frac{j2e^{jk\cos\theta z'}}{(2\pi)^2 a} \sum_{n=-\infty}^{\infty} \frac{\varepsilon_n j^n \cos\left(n\bar{\phi}\right)}{H_n^{(2)}{}'(ka\sin\theta)} \tag{2.63}$$

where ε_n is Neumann's constant ($\varepsilon_n = 1,\ n = 0$ and $\varepsilon_n = 2,\ n \neq 0$). Following the same procedure, (2.57) becomes

$$G_{e2}^{\phi\phi} \sim \frac{e^{-jk_0R}}{k_0R} \frac{e^{jk\cos\theta z'}}{(2\pi)^2 ka\sin\theta} \sum_{n=0}^{\infty} \frac{\varepsilon_n j^n \cos\left(n\bar{\phi}\right)}{H_n^{(2)}\left(ka\sin\theta\right)} \tag{2.64}$$

In summary, the asymptotic expressions for the far-zone dyadic Green's function for an axially infinite, PEC circular cylinder in the shadow region are given by

$$G_{e2}^{\theta\phi} \sim \frac{-e^{-jk_0R}}{k_0R} \frac{4k_0 \cos\theta e^{jk\cos\theta z'}}{(2\pi)^2 (ka\sin\theta)^2} \sum_{n=1}^{\infty} \frac{nj^n \sin\left(n\bar{\phi}\right)}{H_n^{(2)}{}'(ka\sin\theta)} \tag{2.65}$$

$$G_{e2}^{\theta z} \sim \frac{e^{-jk_0R}}{k_0R} \frac{j2e^{jk\cos\theta z'}}{(2\pi)^2 a} \sum_{n=-\infty}^{\infty} \frac{\varepsilon_n j^n \cos\left(n\bar{\phi}\right)}{H_n^{(2)}{}'(ka\sin\theta)} \tag{2.66}$$

The asym

useful or

diameter

wavelen

consequ

argumen

approxin

the far-

these as

field rac

By

rewritte

Follow

contour

where

Figure

the sub

$$G_{e2}^{\phi\phi} \sim \frac{e^{-jk_0R}}{k_0R} \frac{e^{jk\cos\theta z'}}{(2\pi)^2 ka\sin\theta} \sum_{n=0}^{\infty} \frac{\varepsilon_n j^n \cos\left(n\bar{\phi}\right)}{H_n^{(2)}(ka\sin\theta)} \tag{2.67}$$

The asymptotic approximations to the dyadic Green's function given in (2.65)-(2.67) are useful only for an electrically small cylinder on the order of a few wavelengths in diameter. For a cylinder with a large radius of curvature with respect to the operating wavelength, these expressions are slowly convergent. As discussed previously, this is a consequence of the poor convergence property of the Hankel function with a large argument. Consequently, the Watson transformation will be used to develop asymptotic approximations to the expressions in (2.65)-(2.67) that are valid in the shadow region of the far-zone for an electrically large circular cylinder. Just as in the previous section, these asymptotic expressions are physically intepretated as components of the diffracted field radiated by creeping waves propagating along the cylinder surface.

By means of the Watson transformation, the axial component (2.56) can be rewritten as

$$G_{e2}^{\theta z} \sim \frac{-k\sin\theta e^{jk\cos\theta z'}}{4\pi^2\gamma} \oint_C \frac{e^{j\nu\left(\bar{\phi}-\frac{\pi}{2}\right)}}{\sin\nu\pi H_\nu^{(2)}{}'(\gamma)} d\nu \tag{2.68}$$

Following the same procedure as in the previous section, (2.68) is decomposed into two contour integrals

$$G_{e2}^{\theta z} \sim \frac{-k\sin\theta e^{jk\cos\theta z'}}{4\pi^2\gamma} \left[\int_{C_1} \frac{e^{j\nu\left(\bar{\phi}-\frac{\pi}{2}\right)}}{\sin\nu\pi H_\nu^{(2)}{}'(\gamma)} d\nu + \int_{C_2} \frac{e^{j\nu\left(\bar{\phi}-\frac{\pi}{2}\right)}}{\sin\nu\pi H_\nu^{(2)}{}'(\gamma)} d\nu \right] \tag{2.69}$$

where the integration paths of the two integrals in the complex ν-plane are depicted in Figure 2.6. Factoring out $e^{j\nu\pi}$ as before, merging the two integration paths, and making the substitution given by (2.18), (2.69) can be rewritten as where, f

asympto

closed a

arising

radius,

derivati

utilized

compu

and de

rewritte

where

as

Makin

compl

$$G_{e2}^{\theta z} \sim \frac{-jk\sin\theta e^{jk\cos\theta z'}}{2\pi^2\gamma}\sum_{l=0}^{\infty}\int_{C_1}\frac{\left[e^{-j\nu(\phi-\pi/2+2\pi l)}+e^{-j\nu\left[(3\pi/2-\bar{\phi})+2\pi l\right]}\right]}{H_\nu^{(2)}{}'(\gamma)}d\nu \tag{2.70}$$

where, for a large radius cylinder, $l=0$ is sufficient. In order to develop a uniform asymptotic representation for (2.70) in terms of a Fock function, the contour C_1 must be closed at infinity in the lower half-plane to enclose the complex poles of the integrand arising from the zeros of the Hankel function. Since γ is large for a cylinder of large radius, then in light of (2.21) $\nu \sim \gamma$. Hence, the uniform asymptotic expansion of the derivative of the Hankel function in terms of the Fock-type Airy function in (2.18) will be utilized. These functions are tabulated (see Appendix D) and are amenable for computation. Making the necessary substitutions, as was done for the on-surface case, and deforming the integration contour into Γ_1 according to Figure 2.9, (2.70) may be rewritten as

$$G_{e2}^{\theta z} \sim \frac{k\sin\theta e^{jk\cos\theta z'}}{4\pi}\left[\frac{1}{\sqrt{\pi}}\int_{\Gamma_1}\frac{\left[e^{-j\nu\Phi_1}+e^{-j\nu\Phi_2}\right]}{w_1{}'(\tau)}d\tau\right] \tag{2.71}$$

where $\Phi_1 = \frac{3\pi}{2}-\bar{\phi}$ and $\Phi_2 = \bar{\phi}-\frac{\pi}{2}$. Upon the substitution of (2.21), (2.71) is rewritten as

$$G_{e2}^{\theta z} \sim \frac{k\sin\theta e^{jk\cos\theta z'}}{4\pi}\left[e^{-j\gamma\Phi_1}\frac{1}{\sqrt{\pi}}\int_{\Gamma_1}\frac{e^{-jm\Phi_1\tau}}{w_2{}'(\tau)}d\tau + e^{-j\gamma\Phi_2}\frac{1}{\sqrt{\pi}}\int_{\Gamma_1}\frac{e^{-jm\Phi_2\tau}}{w_2{}'(\tau)}d\tau\right] \tag{2.72}$$

Making the substitution $m\Phi_{1,2} = \beta$ from (2.23), (2.72) is expressed in terms of the complex conjugate of the far-zone hard Fock function $g^{(u)}(\beta)^*$ which is given by [28]

$$g^{(u)}(\beta) = \frac{j^u}{\sqrt{\pi}}\int_{\Gamma_1}\frac{\tau^u e^{j\beta\tau}}{w_1{}'(\tau)}d\tau \tag{2.73}$$

where u c

terms of (

Followin

compone

In this ca

soft Foc

Noting

the far-z

The asy

function

cases an

At this

to the pr

into (2.7

where u denotes the order. Noting that $w_1'(\tau) = w_2'(\tau)^*$ allows (2.72) to be expressed in terms of (2.73) as

$$G_{e2}^{\theta z} \sim \frac{k \sin\theta e^{jk\cos\theta z'}}{4\pi} \sum_{p=1}^{2} e^{-j\gamma\Phi_p} g^{(0)}(m\Phi_p)^* \tag{2.74}$$

Following the same procedure, the Watson transformation is applied to the azimuthal component (2.57), which yields

$$G_{e2}^{\phi\phi} \sim \frac{jkm^2 e^{jk\cos\theta z'}}{2\pi\gamma} \left[e^{-j\gamma\Phi_1} \frac{1}{\sqrt{\pi}} \int_{\Gamma_1} \frac{e^{-jm\Phi_1\tau}}{w_2(\tau)} d\tau + e^{-j\gamma\Phi_2} \frac{1}{\sqrt{\pi}} \int_{\Gamma_1} \frac{e^{-jm\Phi_2\tau}}{w_2(\tau)} d\tau \right] \tag{2.75}$$

In this case, (2.75) can be expressed in terms of the complex conjugate of the far-zone soft Fock function $f^{(u)}(\beta)$ which is given by [28]

$$f^{(u)}(\beta) = \frac{j^u}{\sqrt{\pi}} \int_{\Gamma_1} \frac{\tau^u e^{j\beta\tau}}{w_1(\tau)} d\tau \tag{2.76}$$

Noting that $w_1(\tau) = w_2(\tau)^*$, the asymptotic approximation of the azimuthal component of the far-zone dyadic Green's function is given by

$$G_{e2}^{\phi\phi} \sim \frac{jkm^2 e^{jk\cos\theta z'}}{2\pi\gamma} \sum_{p=1}^{2} e^{-jk\gamma\Phi_p} f^{(0)}(m\Phi_p)^* \tag{2.77}$$

The asymptotic evaluation of the cross-polarized dyadic component of the Green's function in (2.55) via the Watson transformation is analogous to the axial and azimuthal cases and leads to the following expression

$$G_{e2}^{\theta\phi} \sim \frac{-jk\cos\theta e^{jk\cos\theta z'}}{2\pi^2\gamma^2} \int_{\Gamma_1} \frac{\left[e^{-j\nu\Phi_2} - e^{-j\nu\Phi_1}\right]\nu}{w_2'(\tau)} d\nu \tag{2.78}$$

At this juncture, the remaining evaluation procedure differs from the previous cases due to the presence of the parameter ν in the numerator of the integrand. Substituting (2.21) into (2.78) and applying the requisite change of variable $d\nu = m d\tau$, (2.78) becomes

G

+ j

Emp

(2.79

Sim

In

of

fo

in

bo

ar

n

2

T

in

pr

$$G_{e2}^{\theta\phi} \sim \frac{-jm\cos\theta e^{jk\cos\theta z'}}{4\pi\gamma} e^{-j\gamma\Phi_2} \frac{j}{\sqrt{\pi}} \int_{\Gamma_1} \frac{\tau e^{-jm\Phi_2\tau}}{w_2'(\tau)} d\tau + \frac{k\cos\theta e^{jk\cos\theta z'}}{4\pi} e^{-j\gamma\Phi_2} \frac{1}{\sqrt{\pi}} \int_{\Gamma_1} \frac{e^{-jm\Phi_2\tau}}{w_2'(\tau)} d\tau$$

$$+\frac{jkm\cos\theta e^{jk\cos\theta z'}}{4\pi\gamma} e^{-j\gamma\Phi_1} \frac{j}{\sqrt{\pi}} \int_{\Gamma_1} \frac{\tau e^{-jm\Phi_1\tau}}{w_2'(\tau)} d\tau - \frac{k\cos\theta e^{jk\cos\theta z'}}{4\pi} e^{-j\gamma\Phi_1} \frac{1}{\sqrt{\pi}} \int_{\Gamma_1} \frac{e^{-jm\Phi_1\tau}}{w_2'(\tau)} d\tau \quad (2.79)$$

Employing the complex conjugate of the far-zone hard Fock function defined in (2.73), (2.79) is rewritten as

$$G_{e2}^{\theta\phi} \sim \frac{jkm\cos\theta e^{jk\cos\theta z'}}{4\pi\gamma} e^{-j\gamma\Phi_1} g^{(1)}(m\Phi_1)^* - \frac{k\cos\theta e^{jk\cos\theta z'}}{4\pi} e^{-\gamma\Phi_1} g^{(0)}(m\Phi_1)^*$$

$$\frac{-jkm\cos\theta e^{jk\cos\theta z'}}{4\pi\gamma} e^{-j\gamma\Phi_2} g^{(1)}(m\Phi_2)^* + \frac{k\cos\theta e^{jk\cos\theta z'}}{4\pi} e^{-\gamma\Phi_2} g^{(0)}(m\Phi_2) \quad (2.80)$$

Simplifying (2.80) in the same manner as before leads to

$$G_{e2}^{\theta\phi} \sim \frac{k\cos\theta e^{jk\cos\theta z'}}{4\pi} \sum_{p=1}^{2} e^{-j\gamma\Phi_p} (-1)^p \left[g^{(0)}(m\Phi_p) - \frac{jm}{\gamma} g^{(1)}(m\Phi_p) \right]^* \quad (2.81)$$

In Summary, (2.74), (2.77), and (2.81) are rapidly convergent asymptotic representations of the electric dyadic Green's function that are valid in the far-zone of the shadow region for a canonical PEC circular cylinder. As discussed earlier, the analytical representation in terms of Fock functions ensures the convergence of these expressions in the shadow boundary transition region consistent with a UTD formulation. Moreover, since the hard and soft far-zone Fock functions are tabulated, these expressions are amenable to numerical computation.

2.2.1.3 Axial Singularities

The far-zone asymptotic dyadic Green's function for a PEC circular cylinder becomes infinite when evaluated at the vertical axis. This anomalous behavior is due to the presence of a singularity in the dyadic Green's function that is manifested only when the observation angle θ, subtended by an observation point in the far-zone from the z axis, approaches 0 or π radians. In this section, the component of the dyadic Green's function that exhibits this singularity is isolated by means of a small argument approximation. The argument γ of the Hankel function, as defined previously, is $\gamma = ka\sin\theta$. As the observation angle θ approaches the vertical cylinder axis at $\theta = 0$ radians, $\gamma \to 0^+$. In light of this, the following small argument approximations of the second-kind Hankel function given by [31]

$$\lim_{\gamma\to 0^+} H_0^{(2)}(\gamma) \sim -j\frac{2}{\pi}\ln\gamma \tag{2.82}$$

and

$$\lim_{\gamma\to 0^+} H_\nu^{(2)}(\gamma) \sim j\frac{1}{\pi}\Gamma(\nu)\left(\frac{2}{\gamma}\right)^\nu, \ \mathrm{Re}(\nu) > 0 \tag{2.83}$$

where $\Gamma(\nu)$ is the gamma function, in conjunction with the recurrence relationship [31]

$$2H_\nu^{(2)\prime}(\gamma) = H_{\nu-1}^{(2)}(\gamma) - H_{\nu+1}^{(2)}(\gamma) \tag{2.84}$$

are applied to evaluate the small argument approximations of the dyadic Green's function components given by (2.65)-(2.67). Invoking the recurrence formula (2.84) to expand the derivative of the Hankel function in (2.65)-(2.67), in the following manner

$$H_1^{(2)\prime}(\gamma) = \frac{1}{2}\left[H_0^{(2)}(\gamma) - H_2^{(2)}(\gamma)\right]$$

$$H_2^{(2)\prime}(\gamma) = \frac{1}{2}\left[H_1^{(2)}(\gamma) - H_3^{(2)}(\gamma)\right]$$

$$H_3^{(2)\prime}(\gamma) = \frac{1}{2}\left[H_2^{(2)}(\gamma) - H_4^{(2)}(\gamma)\right] \tag{2.85}$$

and evaluating each term of (2.85) via the small argument approximations in (2.82) and (2.83), the small argument approximations of the Green's dyadic components are obtained. Hence, (2.65)-(2.67) now are given by

$$\lim_{\gamma\to 0^+} G_{e2}^{\theta\phi} \sim \frac{-e^{-jk_0R}}{k_0R}\frac{4nke^{jkz'}\cos\theta\, j^n}{(2\pi)^2}\left[\frac{-2\pi\sin(\bar{\phi})}{4j+\gamma^2(2\ln\gamma-\pi)}+\frac{\pi\gamma\sin(2\bar{\phi})}{j(\gamma^2-8)}+\frac{\pi\gamma^2\sin(3\bar{\phi})}{2j(\gamma^2-24)}\right.$$

$$\left.+\frac{\pi\gamma^3\sin(4\bar{\phi})}{8j(\gamma^2-48)}+\ldots\right]<\infty \;\Rightarrow \text{bounded} \tag{2.86}$$

$$\lim_{\gamma\to 0^+} G_{e2}^{\theta z} \sim \frac{e^{-jk_0R}}{k_0R}\frac{2j^{n+1}e^{jk_0z'}e^{jn\left(\bar{\phi}-\frac{\pi}{2}\right)}}{(2\pi)^2 a}\left[\frac{j\pi\gamma}{2}+\frac{\cos(\bar{\phi})}{\left(\frac{1}{2}-\frac{j}{\pi}\left\{\frac{2}{\gamma^2}+\ln\gamma\right\}\right)}+\frac{\cos(2\bar{\phi})}{\left(\frac{j}{\pi\gamma}\left\{1-\frac{8}{\gamma^2}\right\}\right)}\right.$$

$$\left.+\frac{\cos(3\bar{\phi})}{\left(\frac{2j}{\pi\gamma^2}\left\{1-\frac{24}{\gamma^2}\right\}\right)}+\frac{\cos(4\bar{\phi})}{\left(\frac{8j}{\pi\gamma^2}\left\{1-\frac{48}{\gamma^2}\right\}\right)}+\ldots\right]<\infty \;\Rightarrow \text{bounded} \tag{2.87}$$

$$\lim_{\gamma\to 0^+} G_{e2}^{\phi\phi} \sim \frac{e^{-jk_0R}}{k_0R}\frac{ke^{-jk_0z'}j^n}{2\pi^2}\left[\frac{\pi}{\gamma(\pi-j2\ln\gamma)}+\frac{\pi\cos(\bar{\phi})}{2j}+\frac{\pi\gamma\cos(2\bar{\phi})}{4j}+\frac{\pi\gamma^2\cos(3\bar{\phi})}{16j}\right.$$

$$\left.+\frac{\pi\gamma^3\cos(4\bar{\phi})}{96j}+\ldots\right]=\infty \;\Rightarrow \text{unbounded} \tag{2.88}$$

The $G_{e2}^{\phi\phi}$ component of the dyadic Green's function becomes infinite as the observation point approaches the vertical axis giving rise to an infinite field at the vertical axis. The existence of singularities at the vertical axis is intrinsic to this type of problem and cannot be eliminated analytically.

2.2.3 (

The as

conve

frequ

rever

speci

expr

then

ray-

2.2.3 Generalization to Doubly Curved Surfaces

The asymptotic form of canonical solutions are generalized to treat the case of the general convex curved surface by means of the principle of locality for the propagation of high frequency radiation discussed in the previous section. The generalized solution should revert to the canonical solutions for the circular cylinder, sphere, and plane when specialized to those cases. Once the circular cylinder and sphere canonical solutions are expressed in terms of the ray-based unit vectors $\hat{\mathbf{t}}$, $\hat{\mathbf{b}}$, and $\hat{\mathbf{n}}$, the differences between them become apparent. Expressing the canonical circular cylinder solution in terms of the ray-based unit vectors following the methodology of [29] results in

$$\begin{aligned}
d\mathbf{H}_{\tan} \sim \mathbf{M}\cdot\Bigg(&\hat{\mathbf{b}}'\hat{\mathbf{b}}\left[\left(1-\frac{j}{ks}\right)v(\beta)+D^2\left(\frac{j}{ks}\right)^2 v(\beta)+\tau_0^2\frac{j}{ks}\{u(\beta)-v(\beta)\}\right] \\
&+\hat{\mathbf{t}}'\hat{\mathbf{t}}\left[D^2\frac{j}{ks}v(\beta)+\frac{j}{ks}u(\beta)-2\left(\frac{j}{ks}\right)^2 v(\beta)\right] \\
&+\left[\hat{\mathbf{t}}'\hat{\mathbf{b}}+\hat{\mathbf{b}}'\hat{\mathbf{t}}\right]\tau_0\frac{j}{ks}\{u(\beta)-v(\beta)\}\Bigg)DG(ks)
\end{aligned} \tag{2.89}$$

where the parameter τ_0 which uniquely specifies a helical geodesic path has been introduced. This parameter is defined as [29]

$$\tau_0 = \frac{T}{\kappa} \tag{2.90}$$

where T is the torsion of a surface diffracted ray and κ is the surface curvature along a geodesic. The surface curvature is defined as $\kappa = 1/\rho_g$. The expression for the surface field excited by a magnetic dipole on a perfectly conducting sphere may be found in a manner analogous to that of the circular cylinder. The ray-based expression for the surfa

give

wh

cas

rea

Thu

tors

by

q'i

two

pre

em

ge

in

q

te

surface magnetic field excited by a magnetic dipole on the surface of a PEC sphere is given by [29]

$$d\mathbf{H}_{\tan} \sim \mathbf{M} \cdot \left(\hat{\mathbf{b}}'\hat{\mathbf{b}} \left[\left(1 - \frac{j}{ks}\right) v(\beta) + D^2 \left(\frac{j}{ks}\right)^2 u(\beta) \right] + \hat{\mathbf{t}}'\hat{\mathbf{t}} \left[D^2 \frac{j}{ks} v(\beta) \right.\right.$$

$$\left.\left. + \frac{j}{ks}\left(1 - \frac{2j}{ks}\right) u(\beta) \right] \right) DG(ks) \tag{2.91}$$

where β specializes to $\beta = \dfrac{ms}{a}$ for a sphere, $s = a\theta$, and $D = \sqrt{\dfrac{\theta}{\sin\theta}}$. For the spherical case, the geodesic path of a creeping wave is a great circle. From the definition of D, it is readily apparent that the points $\theta = 0$ or π, are caustics of the surface diffracted rays. Thus, all surface diffracted rays converge at the two poles of the sphere. By setting the torsion factor $\tau_0 = 0$, the circular cylinder solution reverts to the spherical solution given by (2.91) except for the presence of the terms $q^2 v(\beta) G(ks)$ for the cylinder and $q^2 u(\beta) G(ks)$ for the sphere. Therefore, it is apparent that the differences between these two solutions are due to the effects of torsion on the surface diffracted rays and the presence of either a hard $v(\beta)$ or a soft $u(\beta)$ Fock function in the limiting expressions.

In view of this, the canonical cylinder and sphere solutions may be generalized by employing differential geometry to develop an expression for T_0 that is appropriate for a general convex surface and by introducing the dimensionless factors γ_s and γ_c to interpolate between the canonical cylinder and sphere solutions. Specifically, the terms $q^2 v(\beta) G(ks)$ and $q^2 u(\beta) G(ks)$ are properly weighted via γ_s and γ_c such that the correct term is present once the generalized solution has been specialized to either the circular cylinder c

differentia

with κ =

the princ

dimensio

weightin

where (

propert

In add

the arg

from

surfac

Note

gener

$\gamma_c = 1$

cylinder or sphere case. The generalized torsion factor is given by (2.90) where differential geometry is employed to generalize T as

$$T = \frac{\sin 2\delta}{2}(\kappa_2 - \kappa_1) \tag{2.92}$$

with $\kappa = \kappa_1 \cos^2 \delta + \kappa_2 \sin^2 \delta$. The parameters κ_1 and κ_2 are the surface curvatures along the principle surface directions (to be discussed in detail in Chapter 3). Furthermore, the dimensionless factors must satisfy the following constraint in order to provide the proper weighting

$$\gamma_c + \gamma_s = 1 \tag{2.93}$$

where ($\gamma_s = 1$, $\gamma_c = 0$) for a sphere, and ($\gamma_c = 1$, $\gamma_s = 0$) for a cylinder. In view of these properties, the dimensionless interpolating factors are given by [29]

$$\gamma_s = \frac{\kappa_1}{\kappa_2} \text{ and } \gamma_c = 1 - \gamma_s \tag{2.94}$$

In addition, the generalized form of the distance parameter given by (2.3) is employed in the arguments of the Fock functions to treat the general convex surface. Consequently, from (2.90), (2.92), (2.94) via (2.89), and (2.91), the dyadic Green's function for the surface field excited by a magnetic dipole on a general convex surface is given by [29]

$$\begin{aligned}\overline{\overline{\mathbf{G}}}_{e2}(\mathbf{r}|\mathbf{r}') \sim \Big(&\hat{\mathbf{b}}'\hat{\mathbf{b}}\{[1-q]v(\beta) + D^2q^2[\gamma_s u(\beta) + \gamma_c v(\beta)] + \tau_o^2 q[u(\beta) - v(\beta)]\} \\ &+\hat{\mathbf{t}}'\hat{\mathbf{t}}\{D^2 q v(\beta) + q u(\beta) - 2q^2[\gamma_s u(\beta) + \gamma_c v(\beta)]\} + (\hat{\mathbf{t}}'\hat{\mathbf{b}} + \hat{\mathbf{b}}'\hat{\mathbf{t}})\{\tau_o q[u(\beta) \\ &-v(\beta)]\}\Big) D G(k_0 s)\end{aligned} \tag{2.95}$$

Note that this solution satisfies the criteria for an appropriate asymptotic solution for a general convex surface in that it reduces to the canonical cylinder solution when ($\gamma_s = 0$, $\gamma_c = 1$) and to the canonical sphere solution when ($\gamma_s = 1$, $\gamma_c = 0$) and $\tau_0 = 0$. The generalized

geometry.

This deri

generalized Green's function in (2.95) may be specialized to a prolate spheroidal geometry. The prolate spheroidal dyadic Green's function components are given by

$$\begin{aligned}
&G_{e2}^{\varphi\varphi}(\xi_0:\theta,\varphi|\theta',\varphi')=\Big\{\Big(\cos^2\delta-q\big[(D^2+2)\cos^2\delta-(D^2+1)\big]\Big)v(\beta)\\
&+q^2\Big(\big[(D^2+2)\big]\cos^2\delta-2\Big)\big[\gamma_s u(\beta)+\gamma_c v(\beta)\big]\\
&+\big(\tau_o\cos\delta+\sin\delta\big)^2 q\big[u(\beta)-v(\beta)\big]\Big\}D\frac{k_o^2Y_o}{2\pi}qe^{-jk_os}
\end{aligned}\tag{2.96}$$

$$\begin{aligned}
&G_{e2}^{\eta\varphi}=G_{e2}^{\varphi\eta}(\xi_0:\theta,\varphi|\theta',\varphi')=\Big\{-\sin\delta\cos\delta\Big(v(\beta)-\big(D^2+2\big)qv(\beta)\\
&+\big(D^2+2\big)q^2\big[\gamma_s u(\beta)+\gamma_c v(\beta)\big]\Big)+\Big[\big(2\cos^2\delta-1\big)\tau_o-\\
&\big(\tau_o^2-1\big)\sin\delta\cos\delta\Big]q\big[u(\beta)-v(\beta)\big]\Big\}\frac{k_o^2Y_o}{2\pi}qe^{-jk_os}
\end{aligned}\tag{2.97}$$

$$\begin{aligned}
&G_{e2}^{\eta\eta}(\xi_0:\theta,\varphi|\theta',\varphi')=\Big\{\Big(\sin^2\delta-q\big[(D^2+2)\sin^2\delta-(D^2+1)\big]\Big)v(\beta)\\
&+q^2\Big(\big[(D^2+2)\big]\sin^2\delta-2\Big)\big[\gamma_s u(\beta)+\gamma_c v(\beta)\big]\\
&+\big(\tau_o\sin\delta-\cos\delta\big)^2 q\big[u(\beta)-v(\beta)\big]\Big\}D\frac{k_o^2Y_o}{2\pi}qe^{-jk_os}
\end{aligned}\tag{2.98}$$

This derivation of (2.96)-(2.98) will be discussed in detail in Chapter 3.

CHAPTER 3

FINITE ELEMENT-BOUNDARY INTEGRAL METHOD

3.1 Introduction

The finite element-boundary integral (FE-BI) method is a hybrid computational technique for solving general electromagnetic radiation and scattering problems. This technique has been used with much success in the past for modeling cavity-backed aperture antennas recessed in both flat and curved substrates. The FE-BI technique was first successfully used to model the radiation by a cavity-backed, rectangular aperture recessed in a planar ground plane by Jin and Volakis [1] at the University of Michigan. In this implementation, the cavity region was tessellated into rectangular brick elements. The use of rectangular brick elements results in a uniform mesh giving rise to a block Toeplitz boundary integral matrix. Consequently, iterative solutions of the matrix can be accelerated through the use of a Fast Fourier Transform (FFT) [1]. The utility of rectangular bricks, however, is strictly limited to rectangular geometries. Gong, et al. [32] at the University of Michigan further refined the technique by utilizing tetrahedral finite elements to model arbitrarily shaped apertures. Tetrahedral elements are advantageous in that they are the simplest shape capable of modeling arbitrarily shaped volumes and may be generated automatically by commercial meshers. Kempel at the University of Michigan first extended the FE-BI technique to accommodate cavity-backed apertures and microstrip patch antennas on curved substrates by utilizing specially formulated circular cylinder shell elements [2,3]. These shell elements are singly curved and capable of uniformly discretizing a volume bounded by a singly curved surface with a constant radius of curvature (e.g. the surface of an infinite circular cylinders). As the radius of curvature approaches infinity (the flat case), a shell element becomes functionally equivalent to a rectangular brick. Analogous to the rectangular case, the uniform discretization of singly curved regions with shell elements results in a boundary integral matrix that is block Toeplitz and, therefore, amenable to a fast iterative solution employing FFT. The motivation for the use of bricks and shells was the need to minimize the computational burden associated with the boundary integral due to limitations in computer memory and processing speed at the time. The FFT-based iterative solver efficiently utilizes memory ($O(N_s)$) while minimizing compute time ($O(N_s \log_2 N_s)$), where N_s is the number of surface unknowns. Traditional vector matrix multiply routines require $O\left(N_s^2\right)$ of memory and $O\left(N_s^3\right)$ of compute time. However, with the recent advent of high performance computers and the availability of large blocks of random access memory, the limitations on the complexity of conformal antennas that can be modeled has been relaxed. A major limitation of the brick and shell element approach is that they can only be used to accurately represent volumes delimited by canonical surfaces and, therefore, they are not applicable to arbitrary geometries.

Consequently, in order to extend the range of applicability of the FE-BI technique to the most generally shaped structures while preserving its computational efficiency, right triangular prism elements were developed by Ozdemir et. al. at the University of Michigan [33]. Prism elements are advantageous in that they are capable of modeling arbitrary geometries while yielding fewer unknowns than tetrahedral elements [33], and they are not as geometry constrained as bricks and shells. However, there is a drawback in that distorted prisms are not functionally capable of accurately representing electric fields because they lack tangential continuity across their faces. This defect is the result of their vertically oriented edges not being perpendicular to the planes of their triangular faces [30] resulting in a nonuniform cross-sectional surface area. In modeling cavity-backed apertures of arbitrary shape, the best features of prisms and tetrahedra are combined by the following procedure. The aperture is discretized into a mesh of triangular elements, which are then extruded by means of distorted prisms into the cavity. Each prism is subsequently decomposed into three tetrahedral elements. In this manner, extrusion can be used to form the volumetric mesh with elements that correctly represent the unknown electric field. This method was recently used by Macon *et al.* [34] for arbitrary apertures recessed in a circular cylinder.

In this chapter, the FE-BI method will be extended to model cavity-backed, arbitrarily shaped apertures recessed in electrically large, doubly curved surfaces. A domain decomposition approach is inherent in the FE-BI formulation for modeling cavity-backed apertures in that the computational domain is broken into an interior and an exterior region. The finite element method is used to model the volumetric fields in the interior region. A boundary integral is employed to enforce the requisite conditions (e.g. tangential magnetic field continuity across the aperture) for mesh truncation at the doubly curved aperture surface via a specially formulated asymptotic electric dyadic Green's function. The doubly curved surface is modeled as an electrically large, perfect electrically conducting (PEC) prolate spheroid. As illustrated in Figure 3.1, by allowing the axial and azimuthal radii of curvature, in turn, to approach infinity, the circular cylinder and plane may be recovered as limiting cases. The formulation of the asymptotic dyadic Green's function within the context of UTD and its analytical and numerical valida

regior

3.2 F

The

Begi

wh

fie

im

re

validation will be covered. Finally, the formulation of the far-zone fields in the exterior region by means of the surface equivalence principle will be covered.

3.2 FE-BI Formulation

The FE-BI equation is derived from the weak form of the vector wave equation. Beginning with the time-harmonic form of Maxwell's equations

$$\nabla \times \mathbf{E}^{\text{int}} = -jk_o Z_o \overline{\overline{\mu}}_r \cdot \mathbf{H}^{\text{int}} \tag{3.1}$$

$$\nabla \times \mathbf{H}^{\text{int}} = jk_o Y_o \overline{\overline{\varepsilon}}_r \cdot \mathbf{E}^{\text{int}} + \mathbf{J} \tag{3.2}$$

where $\mathbf{E}^{\text{int}}$ is the unknown interior electric field, $\mathbf{H}^{\text{int}}$ is the unknown interior magnetic field, $k_o = 2\pi / \lambda_0$ is the free-space wave number, $Z_o = \sqrt{\frac{\mu_0}{\varepsilon_0}}$ is the free-space wave impedance, $\overline{\overline{\varepsilon}}_r$, and $\overline{\overline{\mu}}_r$ are the relative anisotropic permittivity and permeability, respectively, given by

$$\overline{\overline{\varepsilon}}_r = \begin{bmatrix} \varepsilon_{xx} & \varepsilon_{xy} & \varepsilon_{xz} \\ \varepsilon_{yx} & \varepsilon_{yy} & \varepsilon_{yz} \\ \varepsilon_{zx} & \varepsilon_{zy} & \varepsilon_{zz} \end{bmatrix} \tag{3.3}$$

$$\overline{\overline{\mu}}_r = \begin{bmatrix} \mu_{xx} & \mu_{xy} & \mu_{xz} \\ \mu_{yx} & \mu_{yy} & \mu_{yz} \\ \mu_{zx} & \mu_{zy} & \mu_{zz} \end{bmatrix} \tag{3.4}$$

Note that the $e^{j\omega t}$ time convention is assumed and suppressed throughout this dissertation. Substituting (3.2) into the curl of (3.1) we get the vector wave equation

$$\nabla \times \left[\overline{\overline{\mu}}_r^{-1} \cdot \nabla \times \mathbf{E}^{\text{int}} \right] - k_o^2 \overline{\overline{\varepsilon}}_r \cdot \mathbf{E}^{\text{int}} = -jk_o Z_o \mathbf{J}^{imp} \tag{3.5}$$

where $\mathbf{J}^{imp}$ is the impressed current due to the excitation source. The method of weighted residuals is employed whereby the inner product of (3.5) and an edge-based, vector testin

the w

wher

The

wei

der

(CT

thr

the

fu

w

sy

m

T

to

testing function, $\mathbf{W}_i$, is taken over the computational volume V. This procedure yields the weak form of the vector wave equation which is given by

$$\int_{V_i} \left\{ \mathbf{W}_i \cdot \nabla \times \left[\overline{\overline{\mu}}_r^{-1} \cdot \nabla \times \mathbf{E}^{\text{int}} \right] - k_o^2 \mathbf{W}_i \cdot \overline{\overline{\varepsilon}}_r \cdot \mathbf{E}^{\text{int}} \right\} dV = f_i^{\text{int}} \tag{3.6}$$

where the interior excitation function used to model probe feeds is given by

$$f_i^{\text{int}} = -jk_o Z_o \int_{V_i} \mathbf{W}_i \cdot \mathbf{J}^{imp} dV \tag{3.7}$$

The weak form of the vector wave equation approximates the vector wave equation in a weighted sense over the computational domain V. Note that (3.6) contains second-order derivatives of the unknown electric field. Since constant tangential/linear normal (CT/LN) vector basis functions are used, it is necessary that the order of (3.6) be reduced through the application of the first vector Green's theorem. The application of the theorem transfers a curl operator from the unknown electric field and onto the testing function, after which (3.6) becomes

$$\int_{V_i} \left[\nabla \times \mathbf{W}_i \cdot \overline{\overline{\mu}}_r^{-1} \cdot \nabla \times \mathbf{E}^{int} + k_o^2 \mathbf{W}_i \cdot \overline{\overline{\varepsilon}}_r \cdot \mathbf{E}^{int} \right] dV - jk_o Z_o \int_{S_i} \mathbf{W}_i \cdot \hat{\xi} \times \mathbf{H}^{\text{int}} dS = f_i^{int} \tag{3.8}$$

where $\hat{\xi}$ is the outward-directed unit normal vector in the prolate spheroidal coordinate system. Equation (3.8) is underdetermined in that it contains unknown electric and magnetic fields; however, the testing function represents the unknown electric field only. The interior magnetic field $\mathbf{H}^{\text{int}}$ cannot be found easily; however, an expression for the total magnetic field, just exterior to the aperture, may be found from

$$\mathbf{H}^{ext} = \mathbf{H}^{inc} + \mathbf{H}^{ref} + \mathbf{H}^{ap} \tag{3.9}$$

where $\mathbf{H}^{inc}$ is the incident magnetic field, $\mathbf{H}^{ref}$ is the reflected magnetic field, and $\mathbf{H}^{ap}$, determined via the surface equivalence theorem, is the magnetic field attributed to the aperture fields which is given by

$$\mathbf{H}^{ap} = jk_0 Y_0 \int_{S_{ap}} \overline{\overline{G}}_{e2} \cdot \hat{\xi}' \times \mathbf{E}^{int} dS' \tag{3.10}$$

An electric dyadic Green's function of the second kind [10] is used to convert the tangential electric field in the aperture to an exterior magnetic field. The natural boundary condition, $\hat{\xi} \times \mathbf{H}^{int} = \hat{\xi} \times \mathbf{H}^{ext}$, is enforced across the aperture surface by substituting the expression for the total magnetic field just exterior to the aperture into (3.8). Upon evaluating (3.8), we obtain the coupled FE-BI equation given by

$$\begin{aligned}&\iiint_V \left[\nabla \times \mathbf{W}_i \cdot \overline{\overline{\mu}}_r^{-1} \cdot \nabla \times \mathbf{E}^{int} - k_0^2 \mathbf{W}_i \cdot \overline{\overline{\varepsilon}}_r \cdot \mathbf{E}^{int} \right] dV + k_o^2 \int_S \int_{S'} (\hat{\xi} \times \mathbf{W}_i) \cdot \overline{\overline{G}}_{e2} \cdot (\hat{\xi}' \times \mathbf{E}^{int}) dS' dS \\ &= f^{\text{int}} + f^{ext}\end{aligned} \tag{3.11}$$

where f^{ext} is the exterior source excitation function given by

$$f_i^{ext} = -jk_o Z_o \int_{S_i} \mathbf{W}_i \cdot \hat{\xi} \times (\mathbf{H}^{inc} + \mathbf{H}^r) dS \tag{3.12}$$

Note that the surface integral in (3.11) has support only over the nonmetallic portions of the aperture. The FE-BI equation in (3.11) is not yet in a form that is suitable for numerical implementation. The unknown interior electric field must be expanded throughout the computational volume in terms of subdomain, edge-based vector expansion (e.g. basis) functions $\mathbf{W}_j$

$$\mathbf{E} = \sum_{j=1}^{N} E_j \mathbf{W}_j \tag{3.13}$$

In this formulation, Galerkin's testing procedure is utilized whereby the vector basis functions, $\mathbf{W}_j$, are CT/LN functions and identical to the testing functions $\mathbf{W}_i$. Note that the expansion functions become identical to the testing functions on the aperture surface ($\xi = \xi_0$), thereby, enforcing the essential boundary condition $\hat{\xi} \times \mathbf{E}^{int} = \hat{\xi} \times \mathbf{E}^{ext}$ across the aperture surface. The unknown complex coefficient associated with each free edge of the volumetric finite element mesh is given by E_j. A free edge is any edge that is not tangential to a PEC surface since a total electric field formulation is being used in this work. Hence, any edge that is tangential to a PEC surface has an expansion coefficient equal to zero. Substituting (3.13) into (3.11) gives the final discretized FE-BI equation that is amenable to computation

$$\sum_{j=1}^{N} E_j \left[\begin{array}{l} \iiint_V \left\{ \nabla \times \mathbf{W}_i \cdot \overline{\overline{\mu}}_r^{-1} \cdot \nabla \times \mathbf{W}_j - k_o^2 \mathbf{W}_i \cdot \overline{\overline{\varepsilon}}_r \cdot \mathbf{W}_j \right\} dV \\ + k_o^2 \int_{S_i} \int_{S_j} (\hat{\xi} \times \mathbf{W}_i) \cdot \overline{\overline{G}}_{e2} \cdot (\hat{\xi}' \times \mathbf{W}_j) dS' dS \end{array} \right] = f_i^{\text{int}} + f_i^{ext} \tag{3.14}$$

3.3 Finite Element Matrix Elements

In this formulation, the volumetric unknown electric field is expanded within a tetrahedral element in terms of CT/LN vector basis functions. CT/LN basis functions provide a constant tangential component along one edge, while the tangential component along the other edges equals zero. In addition, these basis functions provide a linearly varying normal component along each edge. Tetrahedral elements are formed from prism elements by first generating a planar surface mesh of triangular elements, mapping the surface mesh onto the prolate spheroid surface, and extruding each surface element into

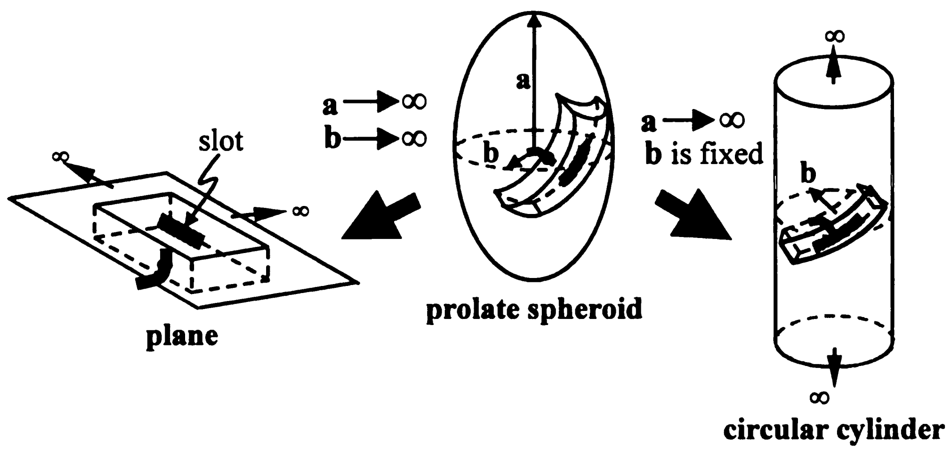

Figure 3.1 Topological transformation of a prolate spheroid into a plane and a circular cylinder in the limits of zero azimuthal and axial curvatures and zero axial and finite azimuthal curvatures, respectively.

the cavity volume by means of prism elements. The prisms are, subsequently, divided into tetrahedra. The process of extrusion essentially amounts to growing the mesh along a direction that has been defined as normal to the surface in a particular orthogonal coordinate system (in this case, the $\hat{\xi}$ direction). This process entails generating finite elements for each layer of the mesh by duplicating the aperture node distribution in all of the lower layers. Thus, in order to form the layer, the aperture nodes are generated at the interface of the first and second layer. Elements for the current layer are generated from those nodes and the bottom nodes of the previous layer. Edges are subsequently formed based on the chosen finite element. The scheme that is used in subdividing prism elements into tetrahedral elements is illustrated in Figure 3.2 [35]. Two types of prism elements are used in order to prevent the diagonal edges of adjacent prisms from crossing, thereby, ensuring tangential field continuity across each face. Once the tetrahedral elements have been generated, the unknown electric field is expanded in terms of the vector basis function given by

$$\mathbf{W}_j = (L_{j1}\nabla L_{j2} - L_{j2}\nabla L_{j1})l_j \tag{3.15}$$

In (3.15), the subscripts denote the two local node numbers defining the edge directed from $j1$ to $j2$, l_j is the length of the j^{th} edge, and the nodal basis functions are given by

$$L_j = \frac{1}{6V^e}(a_j^e + b_j^e x + c_j^e y + d_j^e z) \tag{3.16}$$

where the coefficients a_j^e, b_j^e, c_j^e and d_j^e are found from the coordinates of the four local nodes that define the tetrahedral element and V^e is the volume of the tetrahedral element given by

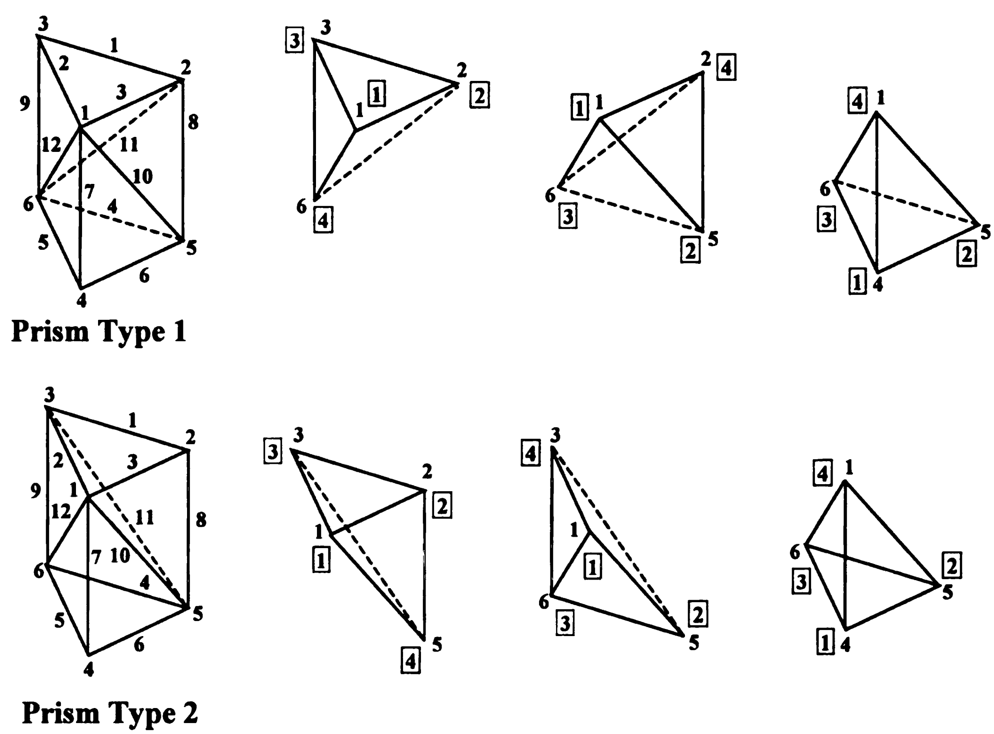

Figure 3.2 Subdivision of the two types of prisms into tetrahedra.

$$V^e = \frac{1}{6}\left\{\begin{matrix}(x_1-x_4)\left[(y_2-y_4)(z_3-z_4)-(y_3-y_4)(z_2-z_4)\right]+ \\ (y_1-y_4)\left[(z_2-z_4)(x_3-x_4)-(z_3-z_4)(x_2-x_4)\right]+ \\ (z_1-z_4)\left[(x_2-x_4)(y_3-y_4)-(x_3-x_4)(y_2-y_4)\right]\end{matrix}\right\} \tag{3.17}$$

The key benefit of using this type of element in the FE-BI formulation is that the vector basis function and its curl are easily expressed in terms of Cartesian unit vectors. In light of this, the curl of $\mathbf{W}_j$ is given by

$$\nabla \times \mathbf{W}_j = \frac{2l_j}{(6V^e)^2}\left[\hat{x}\left(c_{j1}d_{j2}-c_{j2}d_{j1}\right)+\hat{y}\left(d_{j1}b_{j2}-d_{j2}b_{j1}\right)+\hat{z}\left(b_{j1}c_{j2}-b_{j2}c_{j1}\right)\right] \tag{3.18}$$

3.4 Boundary Integral Matrix Elements

3.4.1 Selfcell Evaluation of the Boundary Surface Integral

The selfcell evaluation is the local planar approximation due to the small cell dimensions relative to a wavelength. This is in regards to the surface integral term in (3.14). As discussed previously, the FE-BI method is a hybrid method combining the finite element method with the method of moments. The boundary integral is formulated as an integrodifferential equation that can be solved by the method of moments. The tangential electric field in the aperture is expanded in terms of a set of divergence free, vector basis functions having support over two triangular patch regions sharing an edge. These basis functions were first introduced by Rao, Wilton, and Glisson [36] and will, henceforth, be referred to as RWG basis functions. The expansion of the tangential electric field in the aperture in terms of RWG basis functions begins with the formulation of the magnetic field just exterior to the aperture in terms of an electric vector potential and a magnetic scalar potential given by

$$\mathbf{H}^{ext} = -j\omega\mathbf{F} - \nabla\Phi_m \tag{3.19}$$

where the electric vector potential $\mathbf{F}$ is given by

$$\mathbf{F} = \frac{\varepsilon_o}{2\pi}\int_{S'}\mathbf{K}_s(\mathbf{r}')\frac{e^{-jkR}}{R}dS' \tag{3.20}$$

and the magnetic scalar potential Φ_{mag} is given by

$$\Phi_{mag} = \frac{1}{2\pi\mu_0}\int_{S'}\sigma_{mag}(\mathbf{r}')\frac{e^{-jkR}}{R}dS' \tag{3.21}$$

In (3.19) and (3.20), the magnetic surface current density is given by $\mathbf{K}_s(\mathbf{r}')$ and the magnetic surface charge density is given by $\sigma_{mag}(\mathbf{r}')$. The distance between source and observation points on the surface is given by

$$R = |\mathbf{r} - \mathbf{r}'| \tag{3.22}$$

where $\mathbf{r}$ and $\mathbf{r}'$ are position vectors directed from the origin of the coordinate system to observation and source points, respectively, on the prolate spheroid surface. Expressing the surface charge density in terms of the magnetic surface current density via a purely fictitious magnetic continuity equation

$$\nabla_s'\cdot\mathbf{K}_s(\mathbf{r}') = -j\omega\sigma_{mag}(\mathbf{r}') \tag{3.23}$$

the scalar potential equation may be rewritten as

$$\Phi_{mag} = -\frac{1}{j\omega 2\pi\mu_0}\int_{S'}\nabla_s'\cdot\mathbf{K}_s(\mathbf{r}')\frac{e^{-jkR}}{R}dS' \tag{3.24}$$

By enforcing tangential magnetic field continuity across the aperture, we obtain

$$\hat{\mathbf{n}}\times\left\{-j\omega\mathbf{F} - \nabla\Phi_{mag}\right\} = \hat{\mathbf{n}}\times\mathbf{H}^{int} \tag{3.25}$$

which, upon the substitution of the electric (3.20) and magnetic (3.24) potentials in terms of the magnetic surface current, (3.19) becomes an integrodifferential equation amenable to solution by the method of moments.

The RWG basis function $\mathbf{f}_n(\mathbf{r})$ used to expand the magnetic surface current $\mathbf{K}_s(\mathbf{r}')$ across the aperture is given by [36]

$$\mathbf{f}_n(\mathbf{r}) = \begin{cases} \dfrac{l_n}{2A_n^+}\boldsymbol{\rho}_n^+, & \mathbf{r} \in \mathrm{T}_n^+ \\ \dfrac{-l_n}{2A_n^-}\boldsymbol{\rho}_n^-, & \mathbf{r} \in \mathrm{T}_n^- \\ 0, & \text{otherwise} \end{cases} \tag{3.26}$$

where $\mathbf{r}$ is a global position vector from the origin of the coordinate system to a point on the surface, $\boldsymbol{\rho}_n^{\pm}$ is a local position vector, which is given by

$$\boldsymbol{\rho}_i^{\pm}(\mathbf{r}) = \pm(\mathbf{r} - \mathbf{r}_i) \tag{3.27}$$

in global coordinates, where $\mathbf{r}_i$ is the position vector to vertex opposite edge i, l_n is the length of the n$^{\text{th}}$ edge of a triangular patch, and $A_n^{\pm}$ is the area of triangle $T_n^{\pm}$. The RWG basis function is associated with a free aperture edge of the tessellated surface, vanishing everywhere on the surface except in the region bounded by two triangles bordering the edge. Figure 3.3 illustrates the n$^{\text{th}}$ edge shared by two triangular patches T_n^+ and T_n^-. The following properties of the RWG basis functions render them amenable to modeling surface current within triangular regions [36].

(1) The vector basis function only has a component that is normal to an edge shared by two triangles. There are no components that are normal to the remaining triangle boundary edges. Consequently, there are no line charges at the boundary edges.

(2) The normal component of the basis function to a common edge is equal to the height of a triangle $T_n^{\pm}$. The edge n is the base of the triangle and the height is given by $\frac{2A_n^{\pm}}{l_n}$. This normalizes the basis function to unity.

Furthermore, the surface divergence of the basis function within a triangular region is given by [36]

$$\nabla_s \cdot \mathbf{f}_n(\mathbf{r}) = \begin{cases} \dfrac{l_n}{A_n^+}, & \mathbf{r} \in \mathrm{T}_\mathrm{n}^+ \\ \dfrac{-l_n}{A_n^-}, & \mathbf{r} \in \mathrm{T}_\mathrm{n}^- \\ 0, & \text{otherwise} \end{cases} \tag{3.28}$$

Taking the inner product of (3.25) with the set of vector testing functions denoted by $\mathbf{f}_m$, we obtain

$$\sum_{m=1}^{N}\left[j\omega\langle \mathbf{F},\mathbf{f}_m\rangle - \langle \nabla_s \Phi_{mag},\mathbf{f}_m\rangle\right] = \langle \hat{n}\times\mathbf{H}^{int},\mathbf{f}_m\rangle$$

$$\Rightarrow j\omega\int_S \mathbf{F}\cdot\mathbf{f}_m dS - \int_S \nabla_s \Phi_{mag}\cdot\mathbf{f}_m dS = \int_S \hat{n}\times\mathbf{H}^{int}\cdot\mathbf{f}_m dS \tag{3.29}$$

where the inner product is denoted by $\langle \mathbf{A}\cdot\mathbf{B}\rangle = \int_S \mathbf{A}\cdot\mathbf{B}dS$. Applying the surface vector identity in [37] to the second term on the left-hand side of (3.29)

$$j\omega\int_S \mathbf{F}\cdot\mathbf{f}_m dS - \int_S \nabla_s\cdot\left(\Phi_{mag}\mathbf{f}_m\right)dS + \int_S \Phi_{mag}\nabla_s\cdot\mathbf{f}_m dS = \int_S \hat{n}\times\mathbf{H}^{int}\cdot\mathbf{f}_m dS \tag{3.30}$$

The second term on the left-hand side involves integration over the surface S of a closed three-dimensional body. This surface integral may be evaluated by splitting the closed surface S into two surfaces S_1 and S_2 bounded by the contours C_1 and C_2, respectively, directed in opposite directions and applying a two-dimensional version of the divergence theorem

$$j\omega\int_S \mathbf{F}\cdot\mathbf{f}_m dS-\left(\int_{S_1}\nabla_s\cdot\left(\Phi_{mag}\mathbf{f}_m\right)dS+\int_{S_2}\nabla_s\cdot\left(\Phi_{mag}\mathbf{f}_m\right)dS\right)+\int_S \Phi_{mag}\nabla_s\cdot\mathbf{f}_m dS=\int_S \hat{\mathbf{n}}\times\mathbf{H}^{int}\cdot\mathbf{f}_m dS$$

$$\Rightarrow j\omega\int_S \mathbf{F}\cdot\mathbf{f}_m dS-\left(\oint_{C_1}\hat{\mathbf{n}}\cdot\Phi_{mag}\mathbf{f}_m dl+\oint_{C_2}\hat{\mathbf{n}}\cdot\Phi_{mag}\mathbf{f}_m dl\right)$$
$$+\int_S \Phi_{mag}\nabla_s\cdot\mathbf{f}_m dS=\int_S \hat{\mathbf{n}}\times\mathbf{H}^{int}\cdot\mathbf{f}_m dS \tag{3.31}$$

Hence, (3.31) now becomes

$$j\omega\int_S \mathbf{F}\cdot\mathbf{f}_m dS+\int_S \Phi_{mag}\nabla_s\cdot\mathbf{f}_m dS=\int_S \hat{\mathbf{n}}\times\mathbf{H}^{int}\cdot\mathbf{f}_m dS \tag{3.32}$$

Employing the method of moments to solve this system, we expand the magnetic surface current in the aperture in the set of RWG basis functions

$$\mathbf{K}_s(\mathbf{r}')\cong\sum_{n=1}^{N} I_n\mathbf{f}_n(\mathbf{r}') \tag{3.33}$$

where I_n is the unknown weighting coefficient and N is the number of non-boundary edges. Note that $\mathbf{K}_s(\mathbf{r}')=\mathbf{E}^{ext}\times\hat{\mathbf{n}}$ and $\mathbf{W}_n=\hat{\mathbf{n}}\times\mathbf{f}_n(\mathbf{r}')$. Employing Galerkin's method whereby the set of vector testing functions, denoted by $\mathbf{f}_m(\mathbf{r})$, is set equal to the RWG basis functions $\mathbf{f}_n(\mathbf{r})$ we obtain

$$j\omega\int_S\left[\frac{\varepsilon_o}{2\pi}\int_{S'}\mathbf{f}_n\frac{e^{-jkR}}{R}dS'\right]\cdot\mathbf{f}_m dS-\int_S\left[\frac{1}{2\pi\mu_0}\int_{S'}\nabla_s\cdot\mathbf{f}_n\frac{e^{-jkR}}{R}dS'\right]\nabla_s\cdot\mathbf{f}_m dS$$
$$=\hat{\mathbf{n}}\times\mathbf{H}^{int} \tag{3.34}$$

Substituting (3.26) and (3.28) into (3.34), we obtain the boundary integral impedance matrix

$$Z_{nm} = \frac{jk_0 Y_0 l_n l_m}{8\pi} \left\{ \int_S \int_{S'} \frac{\varepsilon_n \varepsilon_m}{A_n^\pm A_m^\pm} \boldsymbol{\rho}_n^\pm(\mathbf{r}') \cdot \boldsymbol{\rho}_m^\pm(\mathbf{r}) \frac{e^{-jkR}}{R} dS' dS - \frac{4}{k_0^2} \int_S \int_{S'} \frac{\varepsilon_n \varepsilon_m}{A_n^\pm A_m^\pm} \frac{e^{-jkR}}{R} dS' dS \right\} \quad (3.35)$$

where

$$\varepsilon_n = \begin{cases} +1, & \mathbf{r}' \in T_n^+ \\ -1, & \mathbf{r}' \in T_n^- \end{cases} \quad (3.36)$$

and

$$\varepsilon_m = \begin{cases} +1, & \mathbf{r} \in T_m^+ \\ -1, & \mathbf{r} \in T_m^- \end{cases}. \quad (3.37)$$

In light of (3.35), the electric vector potential given by (3.20) may be rewritten as

$$\mathbf{F} = \frac{1}{A_m^\pm A_n^\pm} \int_{T_m^\pm} \int_{T_n^\pm} \boldsymbol{\rho}_m^\pm(\mathbf{r}) \cdot \boldsymbol{\rho}_n^\pm(\mathbf{r}') \frac{e^{-jkR}}{R} dS' dS \quad (3.38)$$

and the magnetic scalar potential given by (3.21) may be rewritten as

$$\Phi_m = \frac{1}{A_m^\pm A_n^\pm} \int_{T_m^\pm} \int_{T_n^\pm} \frac{e^{-jkR}}{R} dS' dS. \quad (3.39)$$

The potential integrals given by (3.38) and (3.39) may be evaluated over the source and observation triangle regions $T_m^\pm$ and $T_n^\pm$ most efficiently by expressing them in terms of normalized local area coordinates $(\varsigma_1, \varsigma_2, \varsigma_3)$ [38]. The local area coordinates are defined within a triangular region in the following manner

$$\varsigma_1 = \frac{A_1}{A^q}, \varsigma_2 = \frac{A_2}{A^q}, \varsigma_3 = \frac{A_3}{A^q} \quad (3.40)$$

where A_1, A_2 and A_3 are the areas of the sub-triangles and A^q is the area of the entire triangular patch. The local area coordinate system within a triangle is depicted in Figure 3.4. The normalized area coordinates satisfy the following constraint

$$\varsigma_1 + \varsigma_2 + \varsigma_3 = 1 \tag{3.41}$$

As a result, only two coordinates are independent. The local area coordinates may be converted to Cartesian coordinates via the following vector transformation

$$\mathbf{r} = \varsigma_1 \mathbf{r}_1 + \varsigma_2 \mathbf{r}_2 + \varsigma_3 \mathbf{r}_3 \tag{3.42}$$

where $\mathbf{r}_i$ is a position vector from the origin to the i[th] vertex of a triangle. Surface integration over a triangular region T^q effectively transforms the kernels of the integrals given in (3.38) and (3.39) from a function of position defined in Cartesian coordinates to a function of position defined in local area coordinates as given by

$$\int_{T^q} K(\mathbf{r}) dS = \int_0^1 \int_0^{1-\varsigma_2} K[\varsigma_1 \mathbf{r}_1 + \varsigma_2 \mathbf{r}_2 + (1 - \varsigma_1 - \varsigma_2)\mathbf{r}_3] d\varsigma_1 d\varsigma_2 \tag{3.43}$$

After the transformation, the potential integrals in (3.38) and (3.39) are re-expressed in terms of local area coordinates. Hence, (3.38) and (3.39) may be rewritten as

$$\mathbf{F} = \frac{1}{A^p} \int_{T^p} \boldsymbol{\rho}_m^{\pm}(\mathbf{r}) \cdot \left[\frac{1}{A^q} \int_{T^q} \boldsymbol{\rho}_n^{\pm}(\mathbf{r}') \frac{e^{-jkR}}{R} dS' \right] dS \tag{3.44}$$

and

$$\Phi_m = \frac{1}{A^p} \int_{T^p} \left[\frac{1}{A^q} \int_{T^q} \frac{e^{-jkR}}{R} dS' \right] dS . \tag{3.45}$$

Before the integrals in (3.44) and (3.45) can be numerically evaluated, the singularity in each of their kernels must first be isolated if the test and source points coalesce. This is done inside of the bracketed expressions by adding and substracting out the singularity. Evaluating (3.44) in this manner yields the expression

$$\frac{1}{A^q}\int_{T^q}\rho_n^{\pm}(\mathbf{r}')\frac{e^{-jkR}}{R}dS' = \frac{1}{A^q}\int_{T^q}\rho_n^{\pm}(\mathbf{r}')\frac{e^{-jkR}-1}{R}dS' + \frac{1}{A^q}\left\{\int_{T^q}\frac{\rho'-\rho}{R}dS' \right.$$
$$\left. +(\rho-\rho_n)\int_{T^q}\frac{1}{R}dS'\right\} \tag{3.46}$$

The first term on the right-hand side of (3.46) has a bounded kernel, while the bracketed term on the right-hand side contains the singularity. Having isolated the singularity, (3.46) may now be expressed in terms of the local area coordinates, resulting in the expression

$$\frac{1}{A^q}\int_{T^q}\rho_n^{\pm}(\mathbf{r}')\frac{e^{-jkR}}{R}dS' = 2\int_0^1\int_0^{1-\varsigma_1}\rho_n^{\pm}(\mathbf{r}')\frac{e^{-jkR}-1}{R}d\varsigma_1'd\varsigma_2' + \frac{1}{A^q}\left\{\int_{T^q}\frac{\rho'-\rho}{R}dS' \right.$$
$$\left. +(\rho-\rho_n)\int_{T^q}\frac{1}{R}dS'\right\} \tag{3.47}$$

The first term on the right-hand side of (3.47) is now bounded and expressed in terms of local area coordinates. Therefore, it may be evaluated by numerical integration over each triangular patch on the surface [39]. However, the second term on the right-hand side is singular and must be evaluated analytically. Appendix A provides details on the evaluation of surface integrals over triangular regions. Evaluating the bracketed expression in (3.45) in a similar manner yields the following expression

$$\frac{1}{A^q}\int_{T^q}\frac{e^{-jkR}}{R}dS' = 2\int_0^1\int_0^{1-\varsigma_1}\frac{e^{-jkR}-1}{R}d\varsigma_1 d\varsigma_2 + \frac{1}{A^q}\int_{T^q}\frac{1}{R}dS' \tag{3.48}$$

Analogous to (3.47), the first term is bounded and well-suited for evaluation by numerical integration over the triangular patch, while the second term containing the singularity must be evaluated analytically [39].

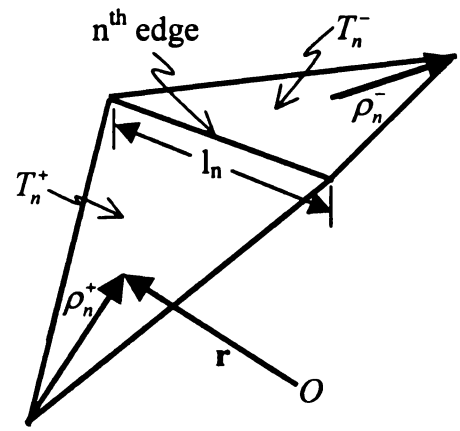

Figure 3.3 RWG basis functions supported within the triangular regions T_n^- and T_n^+ sharing a common edge n.

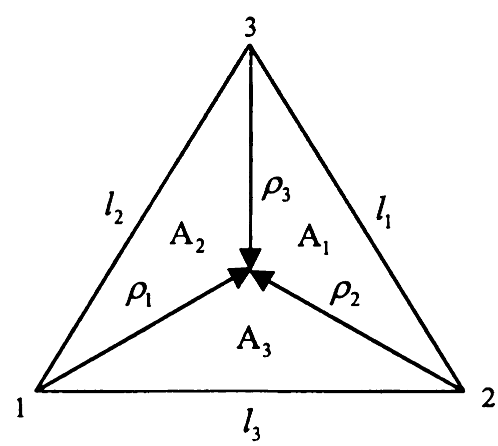

Figure 3.4 Local area coordinate system defined within a triangular region.

3.4.2 Asymptotic Dyadic Green's Function Formulation

The exact condition for finite element mesh truncation is provided by the boundary integral by means of a dyadic Green's function. The electric dyadic Green's function of the second kind [10] couples the tangential electric and magnetic fields in the aperture and enforces the boundary condition on the tangential electric field over the PEC prolate spheroid surface. This dyadic Green's function is used in the hybrid FE-BI formulation (3.14) and is denoted by $\overline{\overline{G}}_{e2}$. Due to the poor convergence and high computational expense of an exact form of the dyadic Green's function for electrically large bodies, an asymptotic form for an electrically large, PEC prolate spheroid will be derived. The asymptotic Green's function physically represents surface diffracted rays (e.g. creeping waves) that are excited by a magnetic dipole (e.g. aperture) on the PEC prolate spheroid surface. The formulation begins with the UTD expression for the surface magnetic field excited by a unit infinitesimal magnetic dipole on an arbitrary convex curved surface developed by Pathak [29] which is given by

$$\begin{aligned}\overline{\overline{\mathbf{G}}}_{e2}(\mathbf{r}\,|\,\mathbf{r}') \sim \Big(&\hat{\mathbf{b}}'\hat{\mathbf{b}}\big\{[1-q]v(\beta)+D^2q^2\left[\gamma_s u(\beta)+\gamma_c v(\beta)\right]+\tau_o^2 q\left[u(\beta)-v(\beta)\right]\big\}\\ &+\hat{\mathbf{t}}'\hat{\mathbf{t}}\big\{D^2qv(\beta)+qu(\beta)-2q^2\left[\gamma_s u(\beta)+\gamma_c v(\beta)\right]\big\}+(\hat{\mathbf{t}}'\hat{\mathbf{b}}+\hat{\mathbf{b}}'\hat{\mathbf{t}})\big\{\tau_o\, q\big[u(\beta)\\ &-v(\beta)\big]\big\}\Big)DG(k_0 s)\end{aligned} \tag{3.49}$$

where $\hat{\mathbf{t}}'$and $\hat{\mathbf{t}}$ are the unit tangent vectors to the geodesic path, $\hat{\mathbf{b}}'$and $\hat{\mathbf{b}}$ are the binormal vectors to the geodesic path, $v(\beta)$ and $u(\beta)$ are the hard and soft surface Fock functions, respectively, which physically represent the attenuation of a surface diffracted ray for various orientations of its geodesic trajectory along a convex curved surface. In this work, prime coordinates denote source points, while unprimed coordinates denote testing or observation points. The Fock functions critically depend on the Fock distance pa

at

G

γ

U

w

pa

w

de

st

ga

ga

cr

ar

3

A

ar

3

c

parameter β which provides the mathematical link between surface curvature and attenuation. For a flat surface, $\beta = 0$, resulting in $v(\beta) = 1$ and $u(\beta) = 1$. Hence, the Green's function for the curved surface reverts to the planar form. The parameters τ_o, γ_s, γ_c, q, and D are geodesic path and curvature dependent parameters intrinsic to the UTD formulation. In (3.49), $G(k_0 s)$ is given by

$$G(k_0 s) = -\frac{k_0 Y_0}{2\pi j} \frac{e^{-jk_0 s}}{k_0 s} \tag{3.50}$$

where k_0 and Y_0 are the free-space wavenumber and admittance, respectively. The parameter s is the length of the geodesic path on the spheroid surface. These parameters will be discussed in greater detail in the following sections as explicit formulas will be developed for each of them within the prolate spheroidal coordinate system. As an initial step, the prolate spheroid coordinate system is defined; next, an orthogonal surface geodesic coordinate system is defined via the formalism of differential geometry. The geodesic coordinate system provides the framework for the calculation of the surface curvatures, the derivation of explicit expressions for the geodesic path, UTD parameters, and the ray-fixed unit vectors.

3.4.2.1 Prolate Spheroid Coordinate System

A prolate spheroid is generated by rotating an ellipse about its major semi-axis. Consider an ellipse with major and minor semi-axes a and b, respectively, as depicted in Figure 3.5. In this figure, f and f' denote the two foci, d is the interfocal distance, while $c = d/2$. The eccentricity e of the spheroid is given by

$$e = \frac{c}{\sqrt{b^2 + c^2}} \tag{3.51}$$

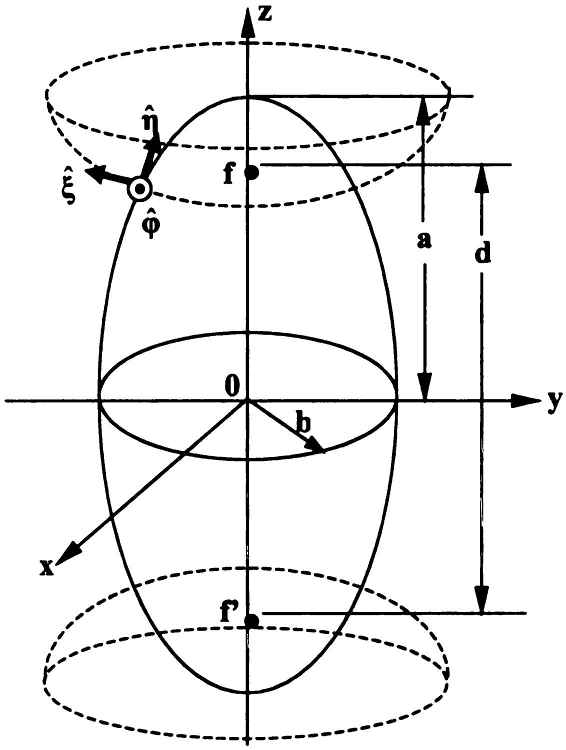

Figure 3.5 Prolate spheroidal geometry.

The

The

$(\eta.$

coo

wl

Le

da

el

(3

le

The following Pythagorean relationship exists among a, b and c

$$c^2 = a^2 - b^2 \tag{3.52}$$

The prolate spheroidal coordinates form a right-handed system when taken in the order (η, ξ, φ). The transformation between prolate spheroid coordinates and Cartesian coordinates (x, y, z) is given by

$$x = c\left[\left(\xi^2 - 1\right)\left(1 - \eta^2\right)\right]^{1/2} \cos\varphi \tag{3.53}$$

$$y = c\left[\left(\xi^2 - 1\right)\left(1 - \eta^2\right)\right]^{1/2} \sin\varphi \tag{3.54}$$

$$z = c\xi\eta \tag{3.55}$$

where

$$0 \le \varphi \le 2\pi, \quad -1 \le \eta \le 1, \text{ and } 1 \le \xi < \infty. \tag{3.56}$$

Let

$$\xi_0 = \cosh\psi \equiv \text{constant} \tag{3.57}$$

define the prolate spheroid surface. Substituting (3.57) and $\eta = \cos\theta$, where θ is the elevational angle subtended by a point on the spheroid surface from the z axis, into (3.53), (3.54) and (3.55), and applying the hyperbolic trigonometric identity

$$\cosh^2\psi - \sinh^2\psi = 1 \tag{3.58}$$

leads to

$$x = c\sinh\psi \sin\theta \cos\varphi \tag{3.59}$$

$$y = c\sinh\psi \sin\theta \sin\varphi \tag{3.60}$$

$$z = c\cosh\psi \cos\theta \tag{3.61}$$

Since

made

Sub

surf

Th

co

B

a

s

d

Since ψ is constant for a prolate spheroid of fixed size, the following substitutions can be made for convenience

$$a = c\cosh\psi, b = c\sinh\psi \tag{3.62}$$

Substituting (3.62) into (3.59), (3.60) and (3.61) yields the parametric equations for the surface of a prolate spheroid in terms of the spherical coordinates (θ,φ)

$$x = b\sin\theta\cos\varphi \tag{3.63}$$

$$y = b\sin\theta\sin\varphi \tag{3.64}$$

$$z = a\cos\theta \tag{3.65}$$

The parametric equation for a position vector $\mathbf{r}$ from the origin of the prolate spheriodal coordinate system to a point on the surface is now given by

$$\mathbf{r}(\theta,\varphi) = b\sin\theta\cos\varphi\hat{\mathbf{x}} + b\sin\theta\sin\varphi\hat{\mathbf{y}} + a\cos\theta\hat{\mathbf{z}} \tag{3.66}$$

By specifying the dimensions of a prolate spheroid in terms of it major and minor semi-axes (e.g. $a \mathrm{x} b$) and the angular location of a point on the surface in terms of the spherical coordinates (θ,φ), the position of point on a prolate spheroid surface may be defined with respect to the Cartesian axes (x,y,z). This parameterization facilitates the projection of points of the spheroid surface onto Cartesian coordinate axes for the evaluation of integrals in conjunction with the RWG basis functions. Differential geometry may now be applied to determine the mutually orthogonal principal directions on the surface and the surface curvature along those directions. Knowledge of the surface curvature is essential for calculating the UTD surface ray parameters, which will be discussed later in this chapter.

3.4.2

As

curv

surf

diff

and

a c

w

(3

T

3.4.2.2 Surface Geometry

As a preliminary step in deriving the asymptotic dyadic Green's function, the surface curvature must be determined. Expressions for the curvature along mutually orthogonal surface directions will be derived within the context of differential geometry. In differential geometry, a surface is uniquely defined by its first fundamental form (FFF) and its second fundamental form (SFF) [40]. The coefficients E, F and G of the FFF for a curved surface are given by

$$E = \frac{\partial \mathbf{r}(\theta,\varphi)}{\partial \theta} \cdot \frac{\partial \mathbf{r}(\theta,\varphi)}{\partial \theta} \tag{3.67}$$

$$F = \frac{\partial \mathbf{r}(\theta,\varphi)}{\partial \theta} \cdot \frac{\partial \mathbf{r}(\theta,\varphi)}{\partial \varphi} \tag{3.68}$$

$$G = \frac{\partial \mathbf{r}(\theta,\varphi)}{\partial \varphi} \cdot \frac{\partial \mathbf{r}(\theta,\varphi)}{\partial \varphi} \tag{3.69}$$

where $\mathbf{r}(\theta,\varphi)$ was defined previously in (3.66). Upon the substitution of (3.66) into (3.67)-(3.69), expressions for the FFF coefficients are obtained

$$E = b^2 \cos^2\theta + a^2 \sin^2\theta \tag{3.70}$$

$$F = 0 \tag{3.71}$$

$$G = b^2 \sin^2\theta \tag{3.72}$$

The SFF coefficients are determined from the following expressions

$$L = \frac{\partial^2 \mathbf{r}}{\partial u^2} \cdot \hat{\mathbf{n}} \tag{3.73}$$

$$M = \frac{\partial^2 \mathbf{r}}{\partial u \partial v} \cdot \hat{\mathbf{n}} \tag{3.74}$$

$$N = \frac{\partial^2 \mathbf{r}}{\partial v^2} \cdot \hat{\mathbf{n}} \tag{3.75}$$

wh

Si

ex

S

where $\hat{\mathbf{n}}$ is the unit normal vector to the surface given by

$$\begin{aligned}\hat{\mathbf{n}} &= -\frac{\dfrac{\partial \mathbf{r}}{\partial u}\times\dfrac{\partial \mathbf{r}}{\partial v}}{\left|\dfrac{\partial \mathbf{r}}{\partial u}\times\dfrac{\partial \mathbf{r}}{\partial v}\right|} \\ &= \frac{a\sin\theta\cos\varphi\hat{\mathbf{x}} + a\sin\theta\sin\varphi\hat{\mathbf{y}} + b\cos\theta\hat{\mathbf{z}}}{\left(b^2\cos^2\theta + a^2\sin^2\theta\right)^{1/2}}\end{aligned} \tag{3.76}$$

Similarly, the substitution of (3.66) and (3.76) into (3.73)-(3.75) yields the following expressions for the SFF coefficients

$$L = \frac{ab}{(b^2\cos^2\theta + a^2\sin^2\theta)^{1/2}} \tag{3.77}$$

$$M = 0 \tag{3.78}$$

$$N = \frac{ab\sin^2\theta}{(b^2\cos^2\theta + a^2\sin^2\theta)^{1/2}} \tag{3.79}$$

Since $F = M = 0$, it follows from differential geometry that curves lying along the curves $\theta = \text{constant}$ and $\varphi = \text{constant}$ are orthogonal and, therefore, define a surface geodesic coordinate system aligned with the principle surface directions [40]. The unit vectors $\hat{\boldsymbol{\eta}}$ and $\hat{\boldsymbol{\varphi}}$ are aligned with the principal surface directions θ and φ, respectively.

Now that the FFF and SFF coefficients have been determined, the surface curvature along each of the principle surface directions can be found. Expressions for the principle surface curvatures κ_1 and κ_2 along the principle surface directions $\hat{\boldsymbol{\eta}}$ and $\hat{\boldsymbol{\varphi}}$, respectively, are found from [30]

$$\kappa_1(\theta) = \frac{L}{E} = \frac{ab}{(b^2\cos^2\theta + a^2\sin^2\theta)^{3/2}} \tag{3.80}$$

$$\kappa_2(\theta) = \frac{N}{G} = \frac{a}{b(b^2\cos^2\theta + a^2\sin^2\theta)^{1/2}}\,. \tag{3.81}$$

Obs

(θ.

the

seer

3.4.

Ha

det

par

obs

par

ang

tar

me

an

in

ch

th

T

a

u

l

Observe that in the case of a prolate spheroid, the principle surface curvatures at a point (θ, φ) on the surface are functions of the elevational angle θ. This property determines the fundamental nature of geodesic paths on a prolate spheroid surface, which will be seen later.

3.4.2.3 Calculating the Geodesic Path

Having determined the principal surface curvatures, an important step in the determination of the GTD ray parameters has been completed. However, before these parameters can be computed an expression for the geodesic path between a source and an observation point must be determined. This is due to the fact that each of the GTD parameters depends not only on the surface curvature but also on the geodesic trajectory angle. In this formulation, the geodesic trajectory angle is the angle subtended by a tangent to the geodesic curve from the z axis; hence, the geodesic angle provides a measure of the torsion of a geodesic curve. For a space curve, torsion is defined as the amount by which the curve twists in the normal direction to the osculating plane, which in this case, is the azimuthal plane of the spheroid. Geodesics on a circular cylinder are characterized by constant torsion, whereas geodesics on a prolate spheroid, by virture of the angular dependence of their FFF coefficients, are characterized by a variable torsion. This implies that the torsion at a point on a geodesic is a function of angular position along the surface. Thus, in order to determine the geodesic angle, an explicit formula for tracing geodesic paths on the surface of a prolate spheroid is required.

The derivation of a geodesic path formula begins with the specification of the arc length between two arbitrary points P_1 and P_2 on a curved convex surface given by

$$s = \int_{P_1}^{P_2} \left(Edu^2 + 2Fdudv + Gdv^2 \right)^{1/2} \tag{3.82}$$

where E, F and G are the FFF coefficients derived in the previous section. Substituting (3.70), (3.71) and (3.72) into (3.82) and rearranging terms yields

$$s = \int_{P_1}^{P_2} \left[\left(b^2 \cos^2\theta + a^2 \sin^2\theta \right) + b^2 \sin^2\theta \left(\frac{d\varphi}{d\theta} \right)^2 \right]^{1/2} d\theta \tag{3.83}$$

Since a geodesic is defined as the arc joining two points on a surface such that the arc length is minimal, the equation for the geodesic may be found by determining the extremum of this integral. Inspection of the kernel of (3.83) reveals it to be in the form of a functional $f(0, \varphi'; \theta)$, where φ' denotes the derivative of φ with respect to θ. We would like to find the condition under which this functional is an extremum. From the calculus of variations, it is well known that a necessary (but not sufficient) condition for $f(0, \varphi'; \theta)$ to be an extremum is for it to satisfy the Euler-Lagrange equation [41] given by

$$\frac{\partial}{\partial\varphi} f(\varphi, \varphi'; \theta) - \frac{d}{d\theta} \frac{\partial}{\partial\varphi'} f(\varphi, \varphi'; \theta) = 0 \tag{3.84}$$

which, owing to the fact that $\varphi = 0$, reduces to

$$\frac{d}{d\theta} \frac{\partial}{\partial\varphi'} f(0, \varphi'; \theta) = 0 \tag{3.85}$$

The evaluation of (3.85) leads to the ordinary differential equation (ODE)

$$\frac{d}{d\theta} \left\{ \frac{\left(b^2 \sin^2\theta \right) \varphi'}{\left(b^2 \cos^2\theta + a^2 \sin^2\theta + b^2 \sin^2\theta [\varphi'] \right)^{1/2}} \right\} = 0 \tag{3.86}$$

The condition

$$\frac{\left(b^2 \sin^2\theta\right)\varphi'}{\left(b^2\cos^2\theta + a^2\sin^2\theta + b^2\sin^2\theta\left[\varphi'\right]\right)^{1/2}} = c_1 \tag{3.87}$$

where c_1 is a constant, must hold in order for the ODE in (3.86) to be satisfied. Solving for φ' in (3.87) leads to

$$\varphi' = \frac{d\varphi}{d\theta} = \frac{c_1\left(b^2\cos^2\theta + a^2\sin^2\theta\right)^{1/2}}{b\sin\theta\left(b^2\sin^2\theta - c_1^2\right)^{1/2}} \tag{3.88}$$

which upon integration yields the equation of a geodesic given by

$$\varphi(\theta) = \int \frac{c_1\left(a^2\sin^2\theta + b^2\cos^2\theta\right)^{1/2}}{b\sin\theta\left(b^2\sin^2\theta - c_1^2\right)^{1/2}} d\theta + c_2 \tag{3.89}$$

where c_1 and c_2 are integration constants that must be determined by specifying the starting and ending points of the geodesic.

The algorithm for determining the constants c_1 and c_2 involves first specifying the starting point (φ_s, θ_s) and end point (φ_f, θ_f) of a geodesic path on the prolate spheroid surface in spherical coordinates. The constant c_2 is equated with the initial azimuthal angle φ_s and c_1 is set to an initial geodesic angle in radians. A trial geodesic path is traced for each c_1 by numerically integrating (3.89) from φ_s to φ_f. The value of the azimuthal angle obtained by adding the result of the numerical integration to c_2 is denoted by φ_{trial}. Next, φ_{trial} is compared to φ_f via $\left|\varphi_{trial} - \varphi_f\right| < tol$, where tol is a prescribed tolerance value. If φ_{trial} falls within this tolerance, the routine terminates and the curved that has been traced is the geodesic path. Furthermore, the value of c_1 obtained from this routine is saved and utilized in the computation of the remaining UTD parameters that require this constant. However, if this condition is not met, then the algorithm repeats until this condition is met. Figure 3.6 shows a typical geodesic traced along a prolate spheroid surface by this algorithm.

Having developed an explicit formula for tracing the geodesic path, the geodesic path length s and geodesic angle δ may now be calculated. As mentioned previously, the geodesic angle is the angle subtended by a tangent to the geodesic curve from the z axis, as depicted in Figure 3.7. From differential geometry, the relationship between the geodesic angle and the FFF coefficients is given by [40]

$$\sin\delta = \sqrt{G}\frac{dv}{ds} \tag{3.90}$$

$$\frac{dv}{du} \equiv \frac{d\varphi}{d\theta} = c_1\sqrt{\frac{E}{G(G-c_1^2)}} \tag{3.91}$$

and

$$\frac{du}{ds} \equiv \frac{d\theta}{ds} = \sqrt{\frac{G-c_1^2}{EG}} \tag{3.92}$$

Taking the reciprocal of (3.92), the geodesic path length s is given by

$$s = \int_{\theta_s}^{\theta_f} \frac{b\sin\theta\left(a^2\sin^2\theta + b^2\cos^2\theta\right)^{1/2}}{\left(b^2\sin^2\theta - c_1^2\right)^{1/2}} d\theta \tag{3.93}$$

where the angular position of the source θ_s (or starting point) and diffraction θ_f (or ending point) of a surface diffracted ray are taken as integration limits. Note that for the range of locations of geodesic endpoints considered in this work, the value of c_1 never exceeds G. Furthermore, from (3.70) and (3.72) $E > 0$ and $G > 0$ for all elevation angles. Hence, the expressions inside the radicals of (3.91) and (3.92) are always positive in this work. Substituting (3.70), (3.72), (3.91) and (3.92) into (3.90) and solving for

δ y

con

The

ang

the

the

this

geo

for

wher

Subs

giver

we o

Note

surfac

δ yields the geodesic angle $\delta(\theta, c_1)$ in terms of the elevation angle θ and integration constant c_1

$$\delta(\theta, c_1) = \sin^{-1}\left(\frac{c_1}{b\sin\theta}\right) \tag{3.94}$$

The equation for the geodesic angle corroborates physical intuition in that the geodesic angle of a point on a geodesic curve would depend not only on the location of a point on the surface but also on the particular geodesic upon which it lies. Closely associated with the geodesic path length is the generalized Fock parameter β. As discussed in Chapter 2, this dimensionless parameter expresses the ratio of the distance of a point from the geometrical optics shadow boundary to the width of the transition region. The expression for β given in Chapter 2 is repeated here for convenience

$$\beta = \int_{P_s}^{P_d} \frac{m}{\rho_g} ds \tag{3.95}$$

where as before m is given by

$$m = \left(\frac{k\rho_g}{2}\right)^{1/3} \tag{3.96}$$

Substituting (3.80) and (3.81) into Euler's equation from differential geometry which is given by

$$\kappa(\theta) = \kappa_1 \cos^2\delta(\theta) + \kappa_2 \sin^2\delta(\theta) \tag{3.97}$$

we obtain the expression for the geodesic curvature, which is given by

$$\kappa(\theta) = \frac{ab^4 + (a^3 - ab^2)c_1^2}{b^3(a^2\sin^2\theta + b^2\cos^2\theta)^{3/2}} \tag{3.98}$$

Note that the geodesic curvature is angularly dependent as will be the case for most of the surface ray parameters. As mentioned previously, this is a consequence of the fact that th

th

S

th

ca

to

Fi

(1

(2

(3

Fo

be

the geodesic path exhibits variable torsion. The geodesic radius of curvature $\rho_g(\theta)$ is just the reciprocal of (3.98) and is given by

$$\rho_g(\theta) = \frac{b^3(a^2\sin^2\theta + b^2\cos^2\theta)^{3/2}}{ab^4 + (a^3 - ab^2)c_1^2} \tag{3.99}$$

Substituting (3.96), (3.99) and the reciprocal of (3.92) into (3.95) and evaluating leads to the expression for β given by

$$\beta(\theta) = \left(\frac{\pi}{\lambda_0}\right)^{1/3} \int_{\theta_s}^{\theta_d} \frac{a\sin\theta(b^4 + \left[a^2 - b^2\right]c_1^2)^{2/3}}{b\left[\left(a^2\sin^2\theta + b^2\cos^2\theta\right)\left(b^2\sin^2\theta - c_1^2\right)\right]^{1/2}} d\theta \tag{3.100}$$

The numerical integrations involved in tracing the geodesic path and in the calculation of the associated geodesic parameters can be quite time consuming. In order to expedite the calculation of these parameters, the following limiting cases depicted in Figure 3.8 may be handled seperately:

(1) The geodesic endpoints lie close together and are situated on a quasi-cylindrical midsection of the spheroid (Figure 3.8a).

(2) The geodesic endpoints share the same azimuthal angle, lying on a circular arc (Figure 3.8b).

(3) The geodesic endpoints share the same elevation angle and, thus, lie on an elliptical arc (Figure 3.8c).

For the first case, the following heuristic approximation to the geodesic path length has been found to be reasonably accurate:

$$s_{app} \approx \sqrt{\left(\rho_{avg}\overline{\varphi}\right)^2 + E\left(\theta, e\right)^2} \tag{3.101}$$

wh

$\bar{\varphi}$ =

wh

su

th

ap

re

T

a

F

f

v

where ρ_{avg} is the average of the azimuthal radii of curvature of the two endpoints, $\bar{\varphi} = \varphi - \varphi'$, and $E(\theta, e)$ is Legendre's elliptic integral of the second kind [42] given by

$$E(\theta, e) = a \int_{\theta_1}^{\theta_2} \sqrt{1 - e^2 \cos^2 \theta}\, d\theta \tag{3.102}$$

where e is the eccentricity, defined previously, θ_1, and θ_2 are the elevation angles subtended by the endpoints of the geodesic from the z-axis. From Table 3.1, it is apparent that the geodesic path length computed from (3.93) compares quite favorably with the approximation to the geodesic path length given by (3.98) over the quasi-cylindrical region.

The approximation to the Fock distance parameter for the first case is given by

$$\beta \approx k s_{app} \left(\frac{\cos^2 \theta}{\sqrt{2} k \rho_{avg}} \right)^{2/3} \tag{3.103}$$

and the geodesic angle is approximated by

$$\delta \approx \tan^{-1} \left[\frac{E(\theta, e)}{\rho_{avg} \bar{\varphi}} \right] \tag{3.104}$$

For cases (2) and (3), (3.96) reverts to the circular arc length and the elliptic arc length formulas, respectively. For the second case, β is given by

$$\beta = \int_{\theta_1}^{\theta_2} \frac{m}{\rho_g} \sqrt{1 - e^2 \cos^2 \theta}\, d\theta \tag{3.105}$$

While for the third case, β is given by

$$\beta = \frac{ms}{\rho_g} \tag{3.106}$$

Note that $\delta = 0$ and $\delta = \frac{\pi}{2}$ radians for the second and third cases, respectively.

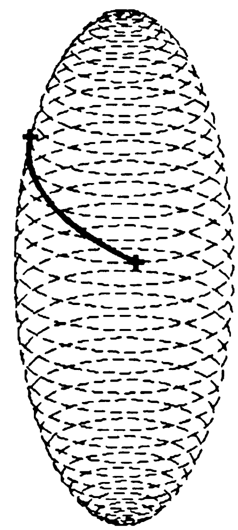

Figure 3.6 A geodesic on a prolate spheroid surface traced via numerical integration.

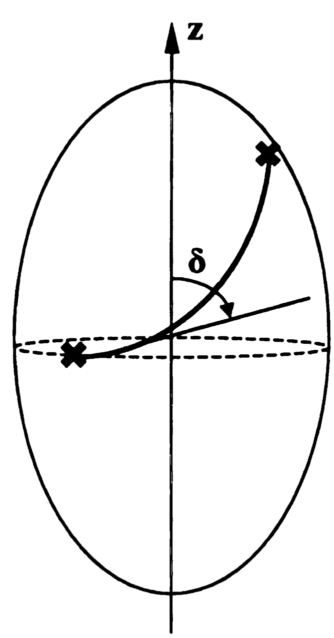

Figure 3.7 The geodesic angle.

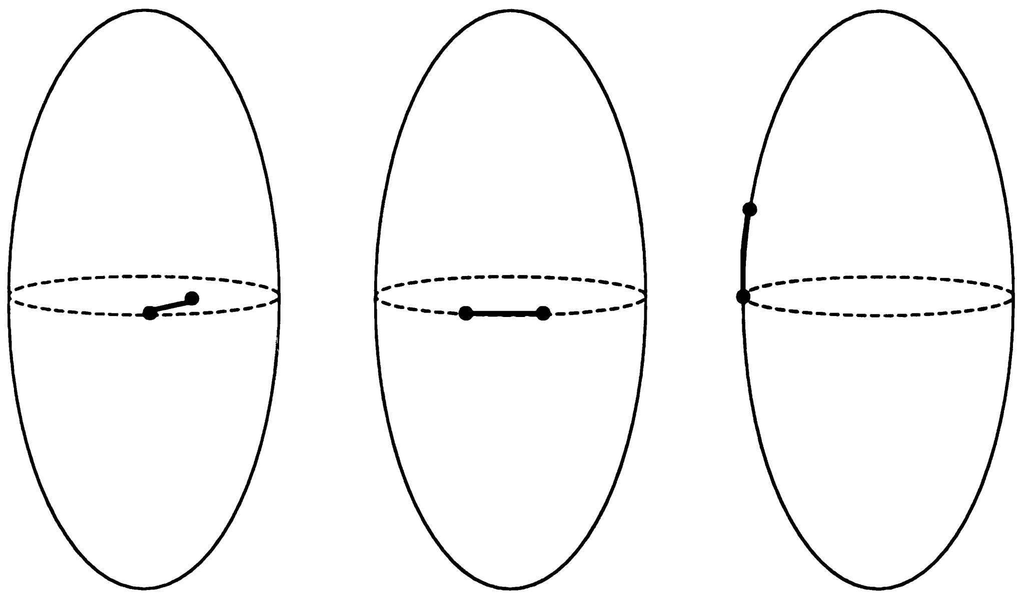

Figure 3.8 Limiting cases for the the geodesic path length: (a) quasi-cylindrical, (b) circular arc, and (c) elliptical arc.

Table 3.1 Comparison of approximate and exact geodesic path lengths between two points located on the midsections of two prolate spheroids. The approximate geodesic path length is denoted by s_{app} and the exact geodesic path length is denoted by s_{geo}.

Angular Position of Geodesic Endpoints $(\theta_s,\ \theta_f),\ (\varphi_s,\ \varphi_f)$	**Major and Minor Axes of Prolate Spheroid** a = 400 cm b = 40 cm	**Major and Minor Axes of Prolate Spheroid** a = 50 cm b = 40 cm
$(90^0, 88^0), (0^0, 10^0)$	s_{geo} = 15.6017 cm s_{app} = 15.6072 cm $\%error = 0.03535$	s_{geo} = 7.1870 cm s_{app} = 7.1941 cm $\%error = 0.09870$
$(90^0, 88^0), (0^0, 15^0)$	s_{geo} = 17.5099 cm s_{app} = 17.4491 cm $\%error = 0.3473$	s_{geo} = 10.7394 cm s_{app} = 10.6133 cm $\%error = 1.1744$
$(90^0, 88^0), (0^0, 20^0)$	s_{geo} = 19.9119 cm s_{app} = 19.7411 cm $\%error = 0.8574$	s_{geo} = 14.3168 cm s_{app} = 14.0671 cm $\%error = 1.7441$
$(90^0, 88^0), (0^0, 25^0)$	s_{geo} = 22.6185 cm s_{app} = 22.3452 cm $\%error = 1.2082$	s_{geo} = 17.8799 cm s_{app} = 17.5350 cm $\%error = 1.9289$
$(90^0, 88^0), (0^0, 30^0)$	s_{geo} = 25.5564 cm s_{app} = 25.1646 cm $\%error = 1.5331$	s_{geo} = 21.5222 cm s_{app} = 21.0102 cm $\%error = 2.3788$

3.4

No

ma

the

Th

Th

ra

ta

sa

ap

su

nu

bu

ob

of

3.4.2.4 UTD Surface Ray Parameters

Now that the geodesic parameters have been determined, the UTD surface ray parameters may now be calculated. The torsion $\tau(\theta)$ is obtained by substituting (3.80) and (3.81) into the following expression:

$$\begin{aligned}\tau(\theta) &= \frac{\sin 2\delta}{2}(\kappa_2 - \kappa_1) \\ &= \frac{c_1(b^2\sin^2\theta - c_1^2)^{1/2} a(b^2 - a^2)}{b^3(a^2\sin^2\theta + b^2\cos^2\theta)^{3/2}}\end{aligned} \tag{3.107}$$

The torsion factor τ_o may now be calculated via

$$\begin{aligned}\tau_o(\theta) &= \frac{\tau(\theta)}{\kappa(\theta)} \\ &= \frac{c_1 a(b^2 - a^2)\left[(b^2\sin^2\theta - c_1^2)(a^2\sin^2\theta + b^2\cos^2\theta)\right]^{1/2}}{ab^4 + a^3c_1^2 - ab^2c_1^2}\end{aligned} \tag{3.108}$$

The ray divergence factor D, which quantifies the amount by which a surface diffracted ray spreads within a tube, is analytically determined by evaluating the angle between tangent vectors to adjacent geodesic paths. The adjacent geodesic paths, traced from the same source point, are angularly seperated by approximately 1.0^0. However, for this application, the attenuation in the magnitude of the Green's function attributable to the surface divergence factor was found to be negligible. Hence, in order to expedite the numerical determination of this factor without imposing an unnecessary computational burden associated with the numerical computation of two geodesics for every source and observation point, a heuristic expression for D was derived based on the known values of D for a circular cylinder and a sphere

$$D = \left(1.0 - \frac{\kappa_1(\theta)}{\kappa_2(\theta)}\right) + \frac{\kappa_1(\theta)}{\kappa_2(\theta)}\sqrt{\frac{\theta}{\sin\theta}}$$

For

sph

resu

and

No

ex

di

de

Th

ar

$$= (1-\gamma_c) + \gamma_s \sqrt{\frac{\theta}{\sin\theta}} \tag{3.109}$$

For the case of a sphere where $\kappa_1 = \kappa_2$, $D = \sqrt{\dfrac{\theta}{\sin\theta}}$, which is the well-known result for a sphere; for the case of circular cylinder where $\kappa_1 = 0$, $D = 1$, which is the well-known result for a circular cylinder. The interpolating factors γ_s and γ_c are given by

$$\begin{aligned} \gamma_s(\theta) &= \frac{\kappa_1(\theta)}{\kappa_2(\theta)} \\ &= \frac{b^2}{a^2\sin^2\theta + b^2\cos^2\theta} \end{aligned} \tag{3.110}$$

and

$$\begin{aligned} \gamma_c(\theta) &= \frac{\kappa_2(\theta)-\kappa_1(\theta)}{\kappa_2(\theta)} \\ &= \frac{(a^2-b^2)\sin^2\theta}{a^2\sin^2\theta + b^2\cos^2\theta} \end{aligned} \tag{3.111}$$

Now that explicit formulas for the UTD surface ray parameters have been derived, expressions for the ray-fixed unit vectors $\hat{\mathbf{t}}$ and $\hat{\mathbf{b}}$ with respect to the principle surface directions $\hat{\boldsymbol{\eta}}$ and $\hat{\boldsymbol{\varphi}}$ must be derived. Note that $\hat{\boldsymbol{\eta}} = -\hat{\boldsymbol{\theta}}$. See Appendix B for the derivation of this result.

The unit tangent vector $\hat{\mathbf{t}}$ is given by

$$\hat{\mathbf{t}} = \hat{\boldsymbol{\eta}}\cos\delta + \hat{\boldsymbol{\varphi}}\sin\delta \tag{3.112}$$

and the unit binormal vector $\hat{\mathbf{b}}$ is given by

$$\begin{aligned} \hat{\mathbf{b}} &= \hat{\mathbf{t}} \times \hat{\mathbf{n}} \\ &= \hat{\boldsymbol{\varphi}}\cos\delta - \hat{\boldsymbol{\eta}}\sin\delta \end{aligned} \tag{3.113}$$

where δ is the geodesic angle, defined previously, and the unit normal vector to the surface is $\hat{\mathbf{n}} = \hat{\boldsymbol{\xi}}$. Substituting (3.112) and (3.113) along with the UTD parameters into (3.49) and after considerable algebraic manipulation, the components of the asymptotic dyadic Green's function for the PEC, electrically large prolate spheroid are obtained and are given by

$$
\begin{aligned}
G_{e2}^{\varphi\varphi}(\xi_0:\theta,\varphi|\theta',\varphi') = &\Big\{\Big(\cos^2\delta - q\big[(D^2+2)\cos^2\delta-(D^2+1)\big]\Big)v(\beta) \\
&+q^2\Big(\big[(D^2+2)\big]\cos^2\delta-2\Big)\big[\gamma_s u(\beta)+\gamma_c v(\beta)\big] \\
&+(\tau_o\cos\delta+\sin\delta)^2 q\big[u(\beta)-v(\beta)\big]\Big\} D\frac{k_o^2 Y_o}{2\pi} q e^{-jk_o s}
\end{aligned} \tag{3.114}
$$

$$
\begin{aligned}
G_{e2}^{\eta\varphi} = G_{e2}^{\varphi\eta}(\xi_0:\theta,\varphi|\theta',\varphi') = &\Big\{-\sin\delta\cos\delta\Big(v(\beta)-\big(D^2+2\big)qv(\beta) \\
&+\big(D^2+2\big)q^2\big[\gamma_s u(\beta)+\gamma_c v(\beta)\big]\Big)+\Big[\big(2\cos^2\delta-1\big)\tau_o - \\
&\big(\tau_o^2-1\big)\sin\delta\cos\delta\Big]q\big[u(\beta)-v(\beta)\big]\Big\}\frac{k_o^2 Y_o}{2\pi} q e^{-jk_o s}
\end{aligned} \tag{3.115}
$$

$$
\begin{aligned}
G_{e2}^{\eta\eta}(\xi_0:\theta,\varphi|\theta',\varphi') = &\Big\{\Big(\sin^2\delta - q\big[(D^2+2)\sin^2\delta-(D^2+1)\big]\Big)v(\beta) \\
&+q^2\Big(\big[(D^2+2)\big]\sin^2\delta-2\Big)\big[\gamma_s u(\beta)+\gamma_c v(\beta)\big] \\
&+(\tau_o\sin\delta-\cos\delta)^2 q\big[u(\xi)-v(\xi)\big]\Big\} D\frac{k_o^2 Y_o}{2\pi} q e^{-jk_o s}
\end{aligned} \tag{3.116}
$$

3.4.3 Validation of the Prolate Spheroid Dyadic Green's Function

In this section, the validity of the asymptotic dyadic Green's function for the prolate spheroid given in (3.114)-(3.116) is established analytically and numerically.

3.4.3.1 Analytical

Beginning with the expressions for the Green's function given in (3.114)-(3.116), we proceed by allowing the radius of curvature along the axial direction to approach infinity, while maintaining a fixed azimuthal radius of curvature. In this case, the prolate spheroid topologically approximates an infinite circular cylinder. Consequently, the magnitude of the asymptotic prolate spheroidal dyadic Green's function should approach the magnitude of the asymptotic dyadic Green's function for a PEC, infinite circular cylinder. The values of surface curvatures along the axial and azimuthal directions become

$$\kappa_1 = \lim_{a\to\infty}\left\{\frac{ab}{\left(a^2\sin^2\theta + b^2\cos^2\theta\right)^{3/2}}\right\} = 0 \tag{3.117}$$

and

$$\kappa_2 = \lim_{a\to\infty}\left\{\frac{a}{b\left(a^2\sin^2\theta + b^2\cos^2\theta\right)^{1/2}}\right\} = \frac{1}{b} \tag{3.118}$$

From (3.117) and (3.118), the geodesic curvature κ now becomes

$$\begin{aligned}\kappa &= \kappa_1\cos^2\delta + \kappa_2\sin^2\delta \\ &\cong \frac{\sin^2\delta}{b}\end{aligned} \tag{3.119}$$

The torsion factor τ_0 becomes

$$\begin{aligned}\tau_0 &= \frac{\sin\delta\cos\delta}{\kappa}\left(\kappa_2 - \kappa_1\right) \\ &\cong \frac{\cos\delta}{\sin\delta} = \cot\delta\end{aligned} \tag{3.120}$$

The interpolating factors now become $\gamma_s = \frac{\kappa_1}{\kappa_2} = 0$ and $\gamma_c = \frac{\kappa_2 - \kappa_1}{\kappa_2} = 1$

For a circular cylinder $D = 1$. Substituting (3.117), (3.118), (3.119), (3.120), and the interpolating factors into the dyadic components given in (3.114)-(3.116) we have for the $G_{e2}^{\varphi\varphi}$ component

$$\lim_{a\to\infty} G_{e2}^{\varphi\varphi}(\theta,\varphi|\theta',\varphi') = \Big\{\Big(\cos^2\delta - q\big[(D^2+2)\cos^2\delta - (D^2+1)\big]\Big)v(\xi)$$
$$+q^2\Big(\big[(D^2+2)\big]\cos^2\delta - 2\Big)\big[\gamma_s u(\xi) + \gamma_c v(\xi)\big]$$
$$+(\tau_o\cos\delta + \sin\delta)^2 q\big[u(\xi) - v(\xi)\big]\Big\} D\frac{k_o^2 Y_o}{2\pi} q e^{-jk_o s}$$
$$= \Big\{\Big(\cos^2\delta - q\big[3\cos^2\delta - 2\big]\Big)v(\xi)$$
$$+q^2\big(3\cos^2\delta - 2\big)v(\xi)$$
$$+\left(\frac{\cos\delta}{\sin\delta}\cdot\cos\delta + \sin\delta\right)^2 q\big[u(\xi) - v(\xi)\big]\Big\}\frac{k_o^2 Y_o}{2\pi} q e^{-jk_o s}$$
$$= \Big\{\cos^2\delta\, v(\xi) + q(1-q)(2 - 3\cos^2\delta)v(\xi)$$
$$+q\csc^2\delta\big[u(\xi) - v(\xi)\big]\Big\}\frac{k_o^2 Y_o}{2\pi} q e^{-jk_o s} \tag{3.121}$$

similarly, for the $G_{e2}^{\varphi\eta} = G_{e2}^{\eta\varphi}$ components

$$\lim_{a\to\infty} G_{e2}^{\varphi\eta}(\theta,\varphi|\theta',\varphi') = \Big\{-\sin\delta\cos\delta\Big(v(\xi) - \big(D^2+2\big)qv(\xi)$$
$$+\big(D^2+2\big)q^2\big[\gamma_s u(\xi) + \gamma_c v(\xi)\big]\Big) + \Big[\big(2\cos^2\delta - 1\big)\tau_o$$
$$-\big(\tau_0^2 - 1\big)\sin\delta\cos\delta\Big]q\big[u(\xi) - v(\xi)\big]\Big\}\frac{k_0^2 Y}{2\pi} q e^{-jk_0 s}$$
$$= \Big\{-\sin\delta\cos\delta\big(v(\xi) - 3qv(\xi)$$
$$+3q^2 v(\xi) + \left[\big(2\cos^2\delta - 1\big)\frac{\cos\delta}{\sin\delta} -\right.$$
$$\left.\left(\frac{\cos^2\delta}{\sin^2\delta} - 1\right)\sin\delta\cos\delta\right] q\big[u(\xi) - v(\xi)\big]\Big\}\frac{k_o^2 Y_o}{2\pi} q e^{-jk_o s}$$
$$= \Big\{\sin\delta\cos\delta\big[1 - 3q(1-q)\big]v(\xi)\Big\}\frac{k_o^2 Y_o}{2\pi} q e^{-jk_o s} \tag{3.122}$$

and finally for the $G_{e2}^{\eta\eta}$ component

$$\lim_{a\to\infty} G_{e2}^{\eta\eta}(\theta,\varphi\,|\,\theta',\varphi') = \Big\{\Big(\sin^2\delta - q\big[3\sin^2\delta - 2\big]\Big)v(\xi)$$
$$+q^2\big(3\sin^2\delta - 2\big)v(\xi)$$
$$+\left(\frac{\cos\delta}{\sin\delta}\cdot\sin\delta - \cos\delta\right)^2 q\big[u(\xi) - v(\xi)\big]\Big\}\frac{k_o^2 Y_o}{2\pi} q e^{-jk_o s}$$

r

a

s

up

asy

Gre

mac

that

with

the re

along

helical

the ma

Green's

away *fr*

indicati

$$= \left\{ \sin^2 \delta v(\xi) + q(1-q)(2 - 3\sin^2 \delta) v(\xi) \right\} \frac{k_o^2 Y_o}{2\pi} q e^{-jk_o s} \qquad (3.123)$$

As seen from the limits of the components in (3.121)-(3.123), the asymptotic prolate spheroid Green's function reverts to the asymptotic circular cylinder Green's function in the limit of an infinite radius of curvature along the axial direction η [2].

3.4.3.2 Numerical

To further validate the prolate spheroid asymptotic dyadic Green's function, the relative magnitudes of its components are compared with those of the circular cylinder asymptotic dyadic Green's function as a function of the electrical geodesic path length s/λ_0. The electrical geodesic path length is expressed in terms of wavelengths. Based upon the analysis of the previous section, it is expected that the prolate spheroid asymptotic dyadic Green's function will reduce to the circular cylinder asymptotic dyadic Green's function in the limit of an infinite axial radius of curvature. A comparison can be made by first tracing the geodesic path between a set of source and observation points that are confined to the quasi-cylindrical midsection of a $40.0\lambda \times 4.0\lambda$ prolate spheroid with an initial geodesic angle $\delta_s = 15.8^0$ as shown in Figure 3.9. A comparison between the relative magnitudes of the asymptotic prolate spheroid Green's function components along this geodesic with those of the asymptotic cylindrical Green's function along a helical geodesic for which $\delta = 15.8^0$ is given in Figure 3.10. There is a rapid increase in the magnitude of the Green's function near the origin due to the singularity of the Green's function at the source point. As the creeping wave propagates a few wavelengths away from the source, the magnitude exhibits a constant rate of attenuation which is indicative of the characteristic exponential decay of a creeping wave. Along the spheroid surface there is greater curvature along the φ direction than along the η direction, hence, the attenuation of the $G_{e2}^{\varphi\varphi}$ component is greatest, while the attenuation of the $G_{e2}^{\eta\eta}$ component is least. As expected, the relative magnitude and attenuation of the $G_{e2}^{\varphi\eta}$ component lies in between values of $G_{e2}^{\eta\eta}$ and $G_{e2}^{\varphi\varphi}$ over the extent of the geodesic. Figure 3.11 depicts a geodesic path between a set of source and observation points that are oriented such that the initial geodesic angle $\delta_s = 26.2^0$ is larger than in the previous case. From Figure 3.12, it is evident that the prolate spheroid asymptotic Green's function magnitudes along this geodesic are almost identical to the magnitudes of the cylindrical asymptotic Green's function along a helical geodesic for which $\delta = 26.2^0$. The attenuation of each component is less because the geodesic path spans the portion of the spheroid surface which exhibits less curvature than in the previous case. In Figure 3.13, a geodesic path on a $40.0\lambda \times 4.0\lambda$ prolate spheriod with an initial geodesic angle given by $\delta_s = 30.1^0$ is depicted. As seen in Figure 3.14, the relative magnitudes of the prolate spheroid Green's function begins to deviate from the cylindrical Green's function along the helical geodesic for which $\delta = 30.1^0$. This is due to the fact that the prolate spheroid surface exhibits curvature along both the axial and azimuthal directions along the geodesic trajectory depicted in Figure 3.13, while the circular cylinder exhibits curvature only in the azimuthal direction along the helical geodesic.

The effect of moving the source and observation points closer to the tip of a prolate spheroid is examined next. For the geodesic trajectory depicted in Figure 3.15 and its associated dyadic component magnitudes shown in Figure 3.16, the attenuation of $G_{e2}^{\eta\eta}$ is greatest within four wavelengths of the source, tapering off to a steady decay rate afterwards. This is most likely due to the fact that the geodesic does not follow a straight path along the η direction. Instead, it follows the variably curved surface contour. On the other hand, the $G_{e2}^{\varphi\varphi}$ and $G_{e2}^{\varphi\eta}$ components exhibit a constant rate of attenuation after approximately two wavelengths from the source. This is due to the constant rate of curvature along the φ direction. As expected, the magnitude of the $G_{e2}^{\varphi\eta}$ component lies in between the magnitudes of the other two components. Placing the source and observation points even closer to the tip, as shown in Figure 3.17, primarily effects the magnitude of $G_{e2}^{\eta\eta}$, as gleaned from an examination of Figure 3.18. In this figure, $G_{e2}^{\eta\eta}$ exhibits a rapid decay rate, followed by a slight plateau and culminating in a steady decay rate. This phenomenon is a consequence of the twisting of the geodesic curve, along the variably curved η direction. The behavior of the dyadic Green's function components for the geodesic trajectory orientations considered in the previous cases appears to be consistent with the physical behavior that one would expect for creeping wave propagation along a variably curved surface [43, 44]. With the derivation and validation of an appropriate electric dyadic Green's function for the electrically large, PEC prolate spheroid, the boundary integral is completely specified.

3.5 Solving the FE-BI System

The coupled finite element and boundary integral equation given in (3.14) generates a large sparse matrix and a fully populately matrix, respectively. This type of system is amenable to solution by an iterative technique. An iterative approach for large sparse matrices is preferable to a direct approach due to the phenomenon of fill-in associated with direct methods, that utilize matrix factorization schemes such as LU decomposition. Specifically, the upper or lower triangular matrices, into which a large sparse matrix would be factored, may not represent the sparsity pattern of the original sparse matrix. However, iterative solutions methods do not employ fill-in, which allows them to maintain the sparsity of the system.

In order to employ an iterative technique, the FE-BI equation in (3.14) may be rewritten in matrix form as [2]

$$\begin{bmatrix} A_{aa}+G & A_{ai} \\ A_{ia} & A_{ii} \end{bmatrix}\begin{bmatrix} E^{ap} \\ E^{int} \end{bmatrix}=\begin{bmatrix} A_{aa} & A_{ai} \\ A_{ia} & A_{ii} \end{bmatrix}\begin{bmatrix} E^{ap} \\ E^{int} \end{bmatrix}+\begin{bmatrix} G & 0 \\ 0 & 0 \end{bmatrix}\begin{bmatrix} E^{ap} \\ E^{int} \end{bmatrix}=\begin{bmatrix} 0 \\ f^{int} \end{bmatrix} \qquad (3.124)$$

where $[A]$ is the finite element matrix, $[G]$ is the boundary integral matrix, E^{int} is the unknown electric field in the cavity, E^{ap} is the unknown electric field in the aperture, f^{int} denotes the interior excitation due to a probe feed. Note that $f_i^{ext}=0$ in (3.14) for the case of interior excitation while $f_i^{int}=0$ for the case of exterior excitation. The decomposition of the FE-BI matrix in this manner allows the matrix-vector product, which is the most computationally expensive task in the iterative approach, in each partition to be optimized for solution by an iterative solver. As an example, since the finite element matrix is sparse, the matrix can be stored in an efficient compressed sparse row (CSR) fashion [45] and the matrix multiply scheme can be optimized for a sparse matrix. Furthermore, although the boundary integral matrix is fully populated, it is symmetric. Hence, only the upper (or lower) triangle needs to be stored. Thus, the boundary integral matrix-vector product can be optimized for a symmetric matrix.

For this problem, the biconjugate gradient (BiCG) iterative scheme is chosen rather than the conjugate gradient scheme (CG). The BiCG scheme is a variation of the CG method and is applicable to asymmetric as well as symmetric systems of linear equations. The main advantage of using BiCG is that for symmetric matrices, Jacob's algorithm employs only one matrix-vector product, as opposed to the CG scheme which employs two matrix-vector products [46]. Moreover, the BiCG scheme converges faster than the CG scheme. The trade-off, however, is that the convergence of BiCG is more erratic than that of CG [30] (See Appendix E for a listing of BiCG pseudocode).

3.6 Radiation

3.61 Input Impedance

Once the electric fields in the cavity $\mathbf{E}^{int}$ and aperture $\mathbf{E}^{ap}$ have been determined by solving (3.124) with a suitable iterative solver such as the BiCG scheme, the input impedance can be found. The input impedance is calculated from the ratio of the voltage at the input port to the current flowing into the port. The simplest type of feed is a Hertzian dipole feed where the source is a filament of current. For a normally directed probe feed (e.g. directed along the $\hat{\xi}$-direction) that is positioned at (η_s, φ_s) on the surface of a prolate spheroid, (3.7) is evaluated as

$$\begin{aligned} f_i^{int} &= -jk_0 Z_0 Il W_i(\eta_s, \varphi_s) \\ &= -jk_0 Z_0 Il \end{aligned} \tag{3.125}$$

For this case, the input impedance can be computed using Gauss' Law

$$Z_{in} = \frac{-1}{I_{in}} \sum_{n=1}^{6} E_{j(n)} \int \hat{\mathbf{l}} \cdot \mathbf{W}_{j(n)} dl' \tag{3.126}$$

where n is the number of edges, $\hat{\mathbf{l}}$ denotes the orientation of the probe-feed, $E_{j(n)}$ are the coefficients of the electric field determined by solving the FE-BI system, and as defined previously $\mathbf{W}_{j(n)}$ are the vector basis functions. The total electric field at the feed location is determined by summing over all the edges of the element, which would be the six edges of the tetrahedral containing the probe-feed in this case, and integrating over the length of the probe. Since this approach relies upon an accurate field calculation in the vicinity of the feed, it is important to finely sample the computational volume in the vicinity of the probe-feed.

3.6.2 Near-to-Far Field Transformation

Once the tangential electric field in the aperture has been determined, the field radiated by the aperture can be determined from the surface equivalence principle. In applying this principle, a suitable dyadic Green's function which effectively transforms the tangential surface electric field to an exterior radiated magnetic field in the geometric optics region must be derived. The surface topology in the immediate vicinity of an aperture situated on an electrically large prolate spheroid may be regarded as locally planar. Hence, a planar approximation may be used to determine the exterior magnetic field radiated by a magnetic current distribution over the aperture in the geometrical optics region of an electrically large prolate spheroid. The geometrical optics region is of primary interest since the antennas under investigation in this dissertation radiate primarily in the geometrical optics region. From image theory, the transformation of a magnetic surface current source on a PEC plane to an exterior magnetic field is given by twice the free-space dyadic Green's function

$$\overline{\overline{\mathbf{G}}}_{e2}^{far}(\mathbf{r}|\mathbf{r}') = 2\overline{\overline{\mathbf{G}}}_0 = \left(\overline{\overline{I}} + \frac{\nabla\nabla}{k_0^2}\right)\frac{e^{-jkR}}{2\pi R} \tag{3.127}$$

where $\mathbf{r}$ and $\mathbf{r}'$ are position vectors to the observation and source points, respectively, $\overline{\overline{I}}$ is the dyadic unit vector (or idem factor) given by

$$\overline{\overline{I}} = \hat{x}\hat{x}' + \hat{y}\hat{y}' + \hat{z}\hat{z}', \tag{3.128}$$

and the distance between the source and observation points is given by $R = |\mathbf{r} - \mathbf{r}'|$. In the far zone, (3.119) may be expressed as

$$\left(\hat{x}\hat{x}'+\hat{y}\hat{y}'+\hat{z}\hat{z}'\right)\frac{e^{-jk_0 r}}{2\pi r}e^{jk_0\hat{r}\cdot\mathbf{r}'} \tag{3.129}$$

Since the far field is evaluated in spherical coordinates, a near field to far field transformation for a magnetic surface current distribution over a quasiplanar patch may be found be expressing the source vector in (3.121) in prolate spheroidal coordinates, while expressing the observation vector in spherical coordinates. Hence, the dyadic Green's function which effectively transforms a surface magnetic current to an exterior geometrical optics far-zone magnetic field may be written as

$$\begin{aligned}\overline{\overline{G}}_{e2}^{far}(\theta,\varphi|\xi',\eta',\varphi') &= \hat{\theta}\hat{\xi}'G_{e2}^{\theta\xi'}+\hat{\theta}\hat{\eta}'G_{e2}^{\theta\eta'}+\hat{\theta}\hat{\varphi}'G_{e2}^{\theta\varphi'}+\hat{\varphi}\hat{\xi}'G_{e2}^{\varphi\xi'}+\hat{\varphi}\hat{\eta}'G_{e2}^{\varphi\eta'}\\&+\hat{\varphi}\hat{\varphi}'G_{e2}^{\varphi\varphi'}\end{aligned} \tag{3.130}$$

where each of the components are given by

$$G_{e2}^{\theta\xi'} = \frac{\left(a\cos\theta\sin\theta'\cos(\varphi-\varphi')-b\sin\theta'\cos\theta'\right)}{\sqrt{a\sin^2\theta'+b\cos^2\theta'}}\frac{e^{-jk_0 r}}{2\pi r}e^{jk_0\left[b\sin\theta'\sin\theta\cos(\varphi-\varphi')+a\cos\theta\cos\theta'\right]} \tag{3.131}$$

$$G_{e2}^{\theta\eta'} = -\frac{\left(b\cos\theta\cos\theta'\cos(\varphi-\varphi')+a\sin\theta'\sin\theta'\right)}{\sqrt{a\sin^2\theta'+b\cos^2\theta'}}\frac{e^{-jk_0 r}}{2\pi r}e^{jk_0\left[b\sin\theta'\sin\theta\cos(\varphi-\varphi')+a\cos\theta\cos\theta'\right]} \tag{3.132}$$

$$G_{e2}^{\theta\varphi'} = \cos\theta\sin\left(\varphi-\varphi'\right)\frac{e^{-jk_0 r}}{2\pi r}e^{jk_0\left[b\sin\theta'\sin\theta\cos(\varphi-\varphi')+a\cos\theta\cos\theta'\right]} \tag{3.133}$$

$$G_{e2}^{\varphi\xi'} = \frac{a\sin\theta'\sin(\varphi'-\varphi)}{\sqrt{a\sin^2\theta'+b\cos^2\theta'}}\frac{e^{-jk_0 r}}{2\pi r}e^{jk_0\left[b\sin\theta'\sin\theta\cos(\varphi-\varphi')+a\cos\theta\cos\theta'\right]} \tag{3.134}$$

$$G_{e2}^{\varphi\eta'} = \frac{b\cos\theta'\sin(\varphi-\varphi')}{\sqrt{a\sin^2\theta'+b\cos^2\theta'}}\frac{e^{-jk_0 r}}{2\pi r}e^{jk_0\left[b\sin\theta'\sin\theta\cos(\varphi-\varphi')+a\cos\theta\cos\theta'\right]} \tag{3.135}$$

$$G_{e2}^{\varphi\varphi'} = \cos(\varphi-\varphi')\frac{e^{-jk_0 r}}{2\pi r} e^{jk_0\left[b\sin\theta'\sin\theta\cos(\varphi-\varphi')+a\cos\theta\cos\theta'\right]} \tag{3.136}$$

Employing surface equivalence, the exterior magnetic field may be determined by evaluating the radiation integral over the aperture surface

$$\mathbf{H}^{far}(\theta,\varphi) = jk_0 Y_0 b \int_{S_{ap}} \overline{\overline{\mathbf{G}}}_{e2}^{far}(r,\theta,\varphi|\xi',\eta',\varphi')\cdot\left[\hat{\xi}\times\mathbf{E}(\xi_0,\eta',\varphi')\right]d\varphi' d\eta' \tag{3.137}$$

whose components are given by

$$\begin{aligned} H_\varphi^{far} &= -jk_0 Y_0 \int_{S_{ap}} \left\{\left[\frac{b\cos\theta'\sin\bar{\varphi}}{\sqrt{a^2\sin^2\theta'+b^2\cos^2\theta'}}\right]E_\varphi \right. \\ &\left. +\cos\bar{\varphi}E_\eta\right\} e^{jk_0\left[b\sin\theta'\sin\theta\cos\bar{\varphi}+a\cos\theta'\cos\theta\right]} d\varphi' d\eta' \end{aligned} \tag{3.138}$$

$$\begin{aligned} H_\theta^{far} &= -jk_0 Y_0 \int_{S_{ap}} \left\{\left[\frac{b\cos\theta\cos\theta'\cos\bar{\varphi}+a\sin\theta\sin\theta'}{\sqrt{a^2\sin^2\theta'+b^2\cos^2\theta'}}\right]E_\varphi \right. \\ &\left. +\cos\theta\sin\bar{\varphi}E_\eta\right\} e^{jk_0\left[b\sin\theta'\sin\theta\cos\bar{\varphi}+a\cos\theta'\cos\theta\right]} d\varphi' d\eta' \end{aligned} . \tag{3.139}$$

In the far-zone, the electric field components may be derived from the magnetic field components via the following relationships

$$\begin{aligned} E_\theta &= Z_0 H_\varphi \\ E_\varphi &= -Z_0 H_\theta \end{aligned} \tag{3.140}$$

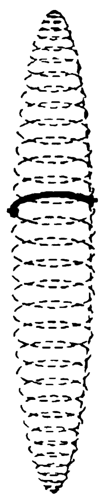

Figure 3.9 The geodesic trajectory between two points located at $(\theta_s = 79.0^0, \varphi_s = 0.0^0)$ and $(\theta_f = 80.0^0, \varphi_f = 160.0^0)$ on a $40.0\lambda \times 4.0\lambda$ prolate spheroid for which $\delta_s = 15.8^0$.

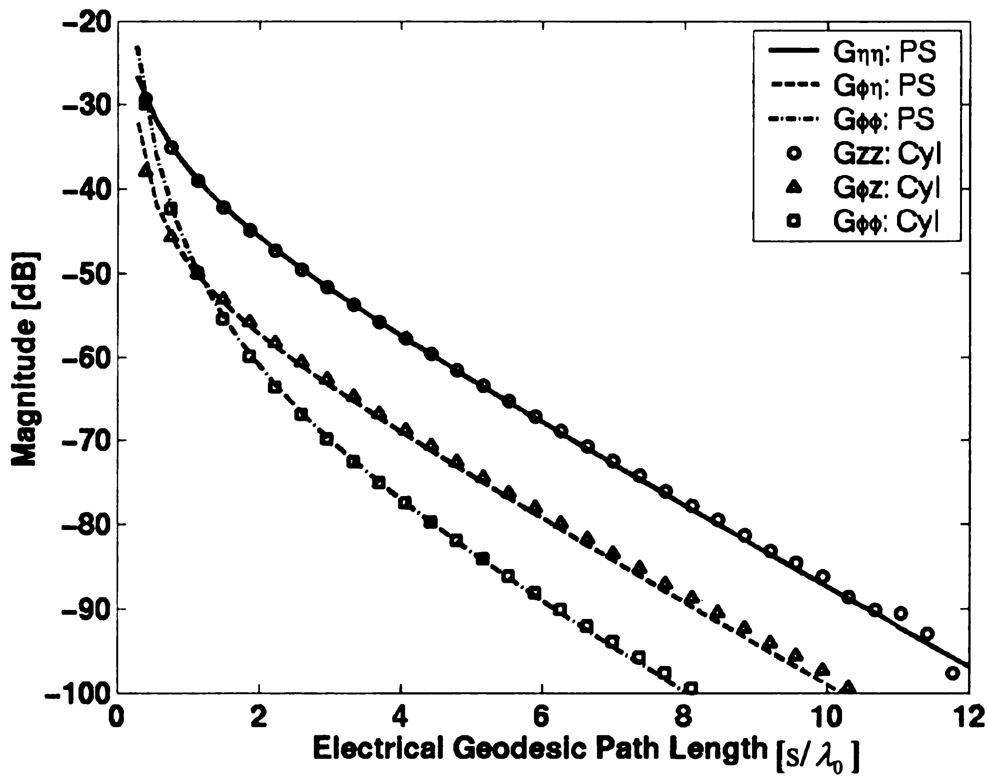

Figure 3.10 Comparison of the relative magnitudes of the prolate spheroidal asymptotic dyadic Green's function components along the geodesic trajectory depicted in Figure 3.9 and the components of the cylindrical asymptotic dyadic Green's function along the helical geodesic for which $\delta = 15.8^0$ on a circular cylinder with an equivalent azimuthal radius.

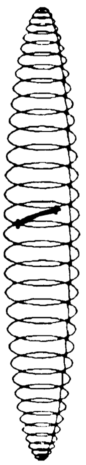

Figure 3.11 The geodesic trajectory between two points located at $\left(\theta_s = 90.0^0, \varphi_s = 30.0^0\right)$ and $\left(\theta_f = 87.0^0, \varphi_f = 92.0^0\right)$ on a $40.0\lambda \times 4.0\lambda$ prolate spheroid for which $\delta_s = 26.2^0$.

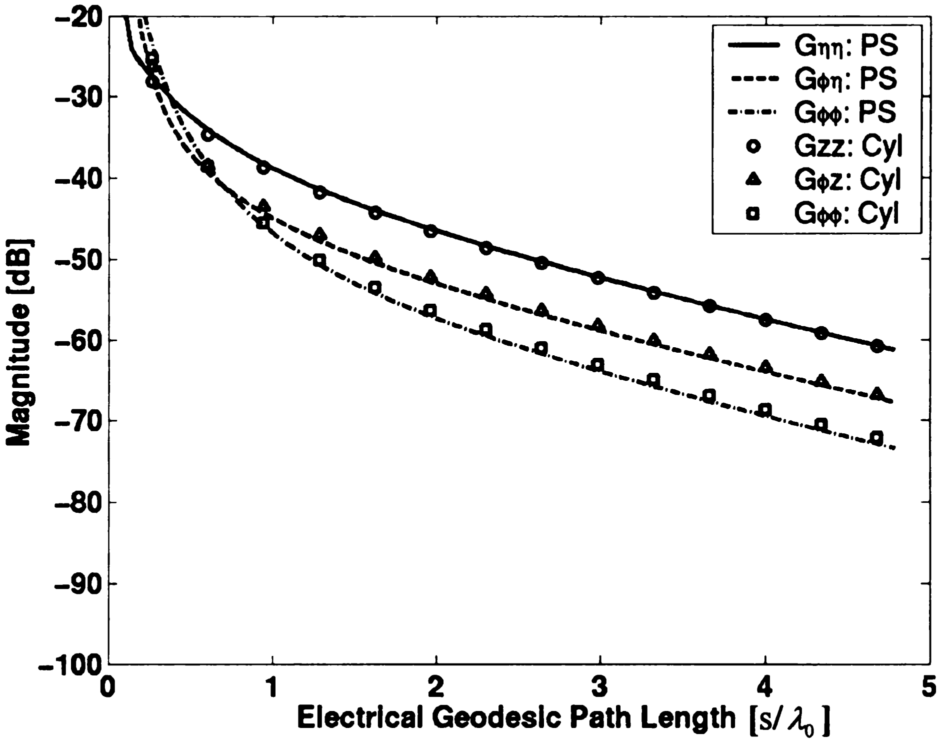

Figure 3.12 Comparison of the relative magnitudes of the prolate spheroidal asymptotic dyadic Green's function components along the geodesic trajectory depicted in Figure 3.11 and the components of the cylindrical asymptotic dyadic Green's function along the helical geodesic for which $\delta = 26.2^0$ on a circular cylinder with an equivalent azimuthal radius.

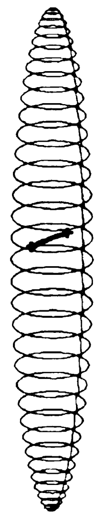

Figure 3.13 The geodesic trajectory between two points located at $(\theta_s = 90.0^0, \varphi_s = 30.0^0)$ and $(\theta_f = 87.0^0, \varphi_f = 82.5^0)$ on a $40.0\lambda \times 4.0\lambda$ prolate spheroid for which $\delta_s = 30.1^0$.

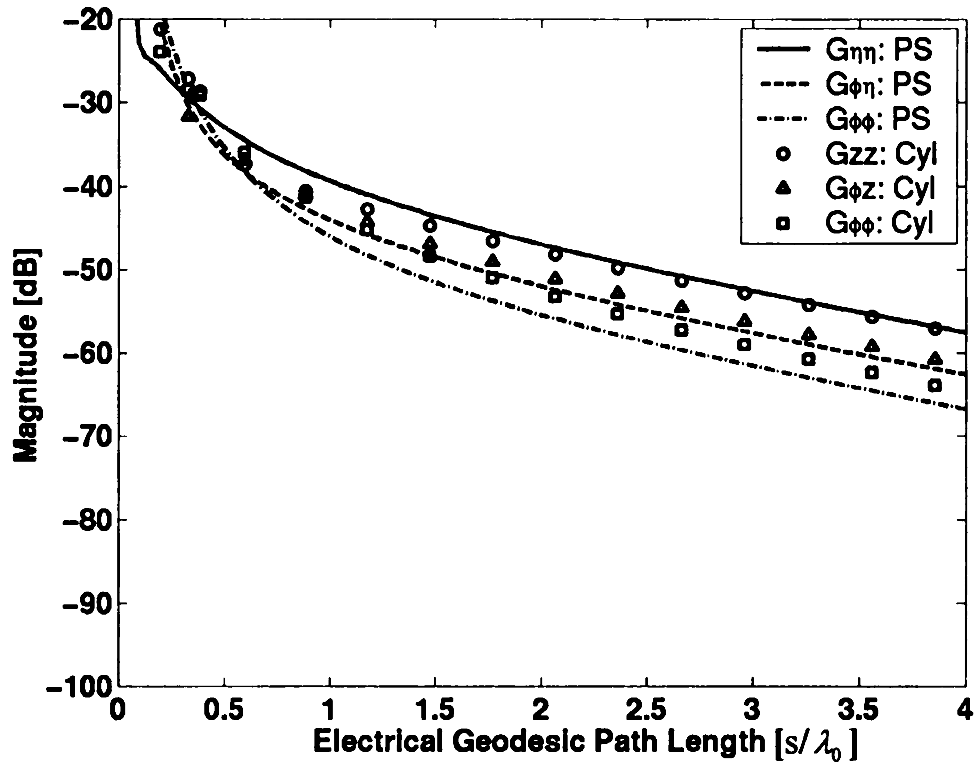

Figure 3.14 Comparison of the relative magnitudes of the prolate spheroidal asymptotic dyadic Green's function components along the geodesic trajectory depicted in Figure 3.13 and the components of the cylindrical asymptotic dyadic Green's function along the helical geodesic for which $\delta = 30.1^0$ on a circular cylinder with an equivalent azimuthal radius.

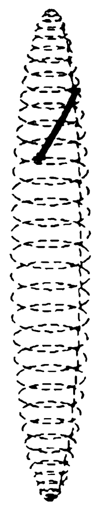

Figure 3.15 Geodesic trajectory between the points $(\theta_s = 50.0^0, \varphi_s = 0.0^0)$ and $(\theta_f = 70.0^0, \varphi_f = 70.0^0)$ on a $40.0\lambda \times 4.0\lambda$ prolate spheroid.

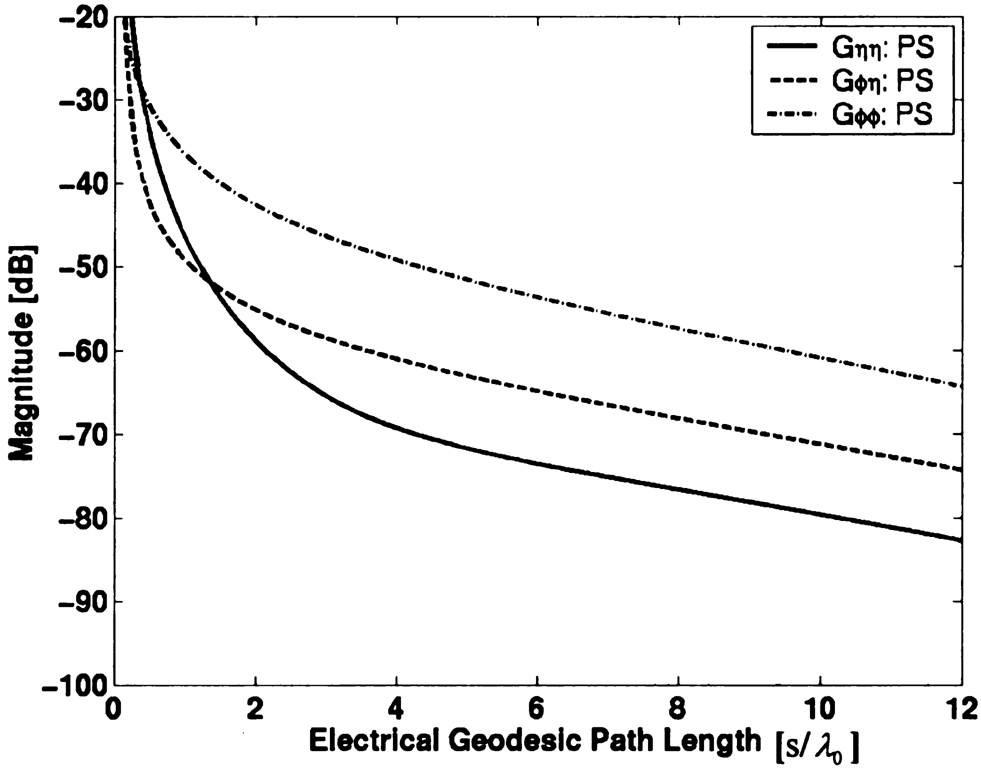

Figure 3.16 Relative magnitudes of the prolate spheroidal dyadic Green's function components along the geodesic trajectory depicted in Figure 3.15.

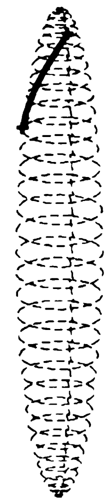

Figure 3.17 The geodesic trajectory between two points at $\left(\theta_s = 30.0^0, \varphi_s = 0.0^0\right)$ and $\left(\theta_f = 60.0^0, \varphi_f = 100.0^0\right)$ on a $40.0\lambda \times 4.0\lambda$ prolate spheroid.

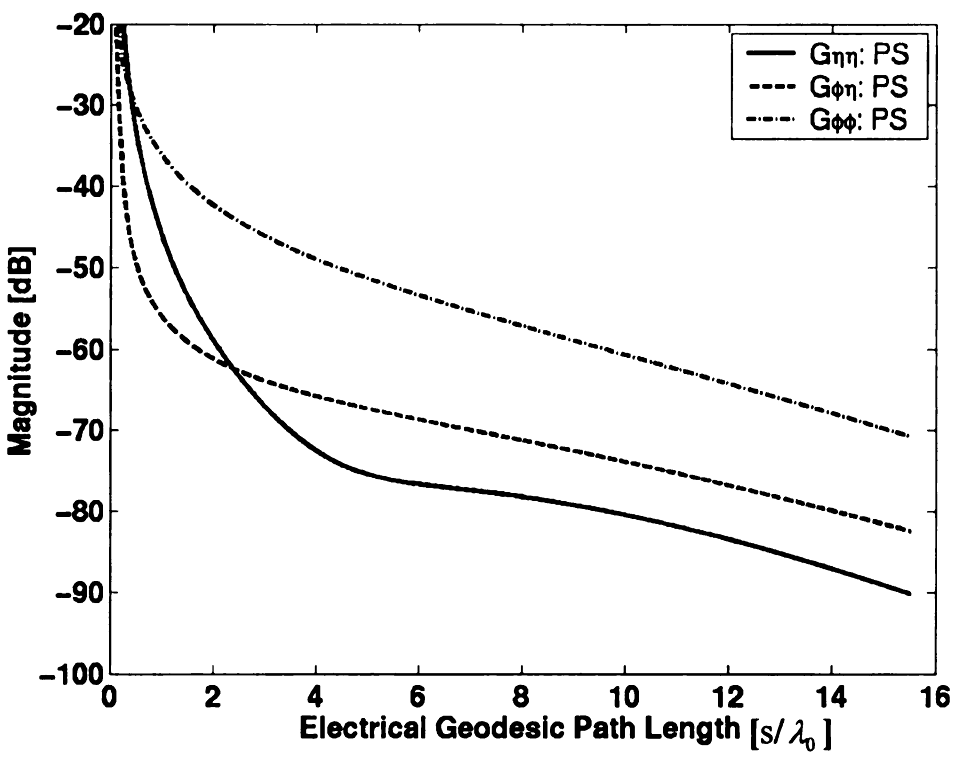

Figure 3.18 Relative magnitudes of the prolate spheroidal dyadic Green's function components along the geodesic trajectory depicted in Figure 3.17.

4.

In

ba

of

of

pr

cu

ca

lig

th

da

4.2

4.2

In

an

a p

slo

sph

pla

in

$\dot{\varphi}$ -

CHAPTER 4

NUMERICAL RESULTS

4.1 Introduction

In this chapter, FE-BI simulation results for the resonant input impedance of a cavity-backed slot antenna and a cavity-backed patch antenna that are conformal to the surface of a prolate spheroid are presented. In addition, numerical results for the radiation pattern of the conformal patch antenna in the geometrical optics region of a prolate spheroid are presented. Although published results for waveguide antennas flush-mounted on doubly curved surfaces is becoming available [47], published data on the input impedance of cavity-backed patch antennas conformal to prolate spheroid surfaces is nonexistent. In light of this, this work will be validated by comparing the doubly curved results with those of the limiting planar and cylindrical-rectangular geometries for which reference data exists.

4.2 Input Impedance Studies

4.2.1 Cavity-Backed Slot Antenna

In this section, FE-BI numerical results for the input impedance of a cavity-backed, slot antenna recessed in a PEC prolate spheroid are presented. Since the resonant frequency of a planar-rectangular cavity is well known, it is modeled first. The antenna consists of a slot that is cut into a cavity with doubly curved walls that conform to the prolate spheroidal geometry. In the limit of zero curvature, the cavity geometry reverts to a planar-rectangular geometry with the following dimensions: 6.0 cm in length, 3.875 cm in width, and 1.2 cm in thickness. The slot is 2.5 cm in length, parallel to the $\hat{\varphi}$-direction, and 0.125 cm in width, parallel to the $\hat{\eta}$-direction. The cavity is assumed to be air-filled with a permittivity $\varepsilon = 1.0 - j0.01$. Note that a small loss is introduced to speedup convergence. FE-BI simulation results for a normally directed (e.g. along the $\hat{\xi}$-direction) probe feed positioned along the bottom of the cavity so as to excite the fundamental TE_{011} mode of the limiting planar-rectangular cavity are presented. In order to assess the sensitivity of the cavity's resonant frequency to curvature variation along the elevational and azimuthal directions, the following orientations of the slot antenna with respect to the vertical axis of the prolate spheroid are modeled: horizontal, vertical, and tilted at 45^0 with respect to the vertical axis.

Following the procedure for generating the FE mesh outlined in Chapter 3, the antenna surface is first discretized into a triangular mesh, as shown in Figure 4.1. Next, the surface mesh is extruded into the cavity volume via triangular distorted prism elements, which subsequently are decomposed into tetrahedral elements. The position of the probe feed is depicted in Figure 4.2. The resulting six-layer FE mesh for the slot antenna is depicted in Figure 4.3. The electrical length of each side of a tetrahedral element is $\lambda_0 / 40$ at the resonant frequency of the cavity. This yields an FE mesh comprised of 53,568 elements, 56,742 total unknowns, and 47 aperture unknowns. The creation of the FE mesh required 16 minutes and the simulation over the frequency range 4.0 to 5.5 GHz at a frequency step of 0.025 required two hours to run on a XEON 450 MHz machine.

In Figures 4.4 and 4.5, the resonant input resistance and reactance of the horizontally oriented slot antenna on a prolate spheroid are plotted for varying curvatures and compared with the limiting planar and cylindrical values. From these plots, it is quite apparent that for large axial and azimuthal radii of curvatures, the resonant frequency of

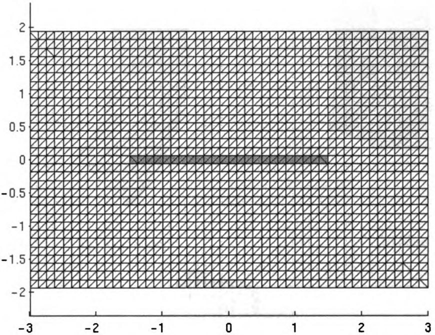

Figure 4.1 Surface mesh for the slot antenna.

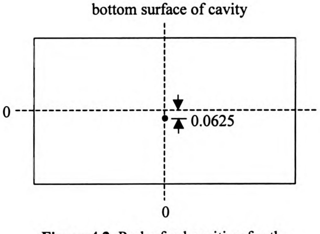

Figure 4.2 Probe feed position for the slot antenna.

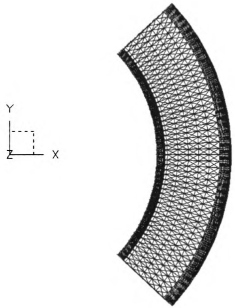

(a) Top View

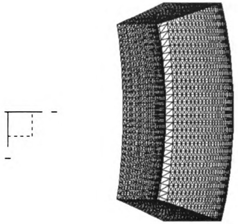

(b) Side View

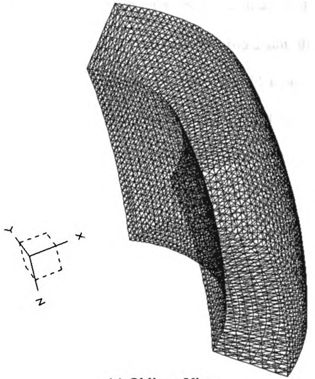

(c) Oblique View

Figure 4.3 Different views of the six-layer doubly curved finite element mesh for the slot antenna.

the doubly curved cavity approaches the theoretical resonant frequency of the fundamental TE_{011} mode for the limiting 6.0 x 3.875 x 1.2 cm planar-rectangular cavity which is 4.61GHz. This is to be expected because the surface appears planar in the vicinity of the slot antenna. As the curvature of the spheroid increases, the magnitude of the input resistance also increases for this slot orientation. A similar phenomenon occurs for the case of a vertically oriented slot whereby the magnitude of the input resistance increases with decreasing curvature. By allowing the axial radius of curvature a to become very large (e.g. a = 400 cm) and the azimuthal radius of curvature b to remain fixed at 8 cm, the prolate spheroid shape approaches that of the circular cylinder. Hence, one would expect the input impedance of the patch on the prolate spheroid to approach the value of input impedance for a patch on a circular cylinder with the same radius. This idea is supported by Figures 4.6 and 4.7. For the 45^0 tilted slot, there is good agreement between the planar input impedance and prolate spheroid input impedance with large axial and circumferential curvatures, as seen in Figures 4.8 and 4.9. Moreover, for a large axial radius of curvature and a relatively small fixed azimuthal radius of curvature, the prolate spheroid results agree with those of the circular cylinder with the same azimuthal radius. This result is consistent with those of the vertically and horizontally orientated slot. Note that the magnitude of the input resistance decreases slightly for the prolate spheroid surface curvature that is intermediate between the limiting planar and cylindrical values. These results support the assertion of the planar-rectangular cavity being the limiting case for the doubly curved cavity as the radii of curvature of the cavity walls approach infinity and the cylindrical-rectangular cavity being the limiting case for the doubly curved cavity as the axial radius of curvature approaches infinity.

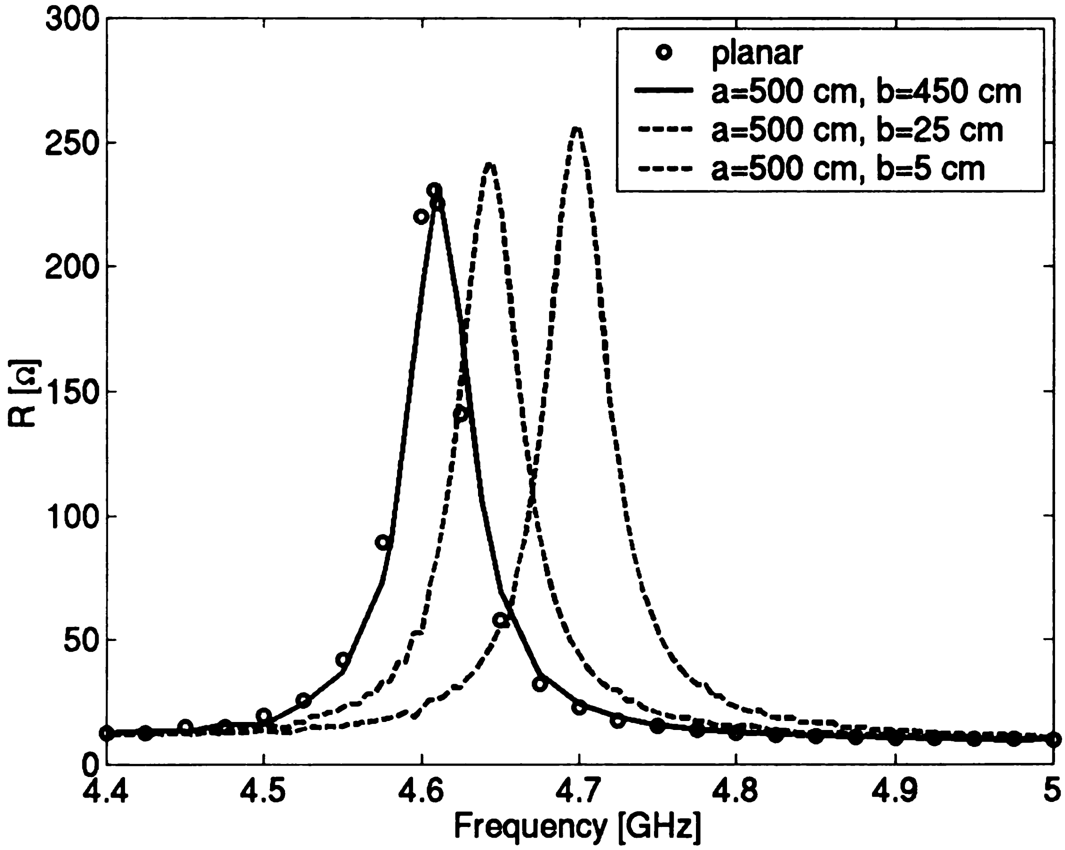

Figure 4.4 Input resistance of the horizontally oriented slot antenna.

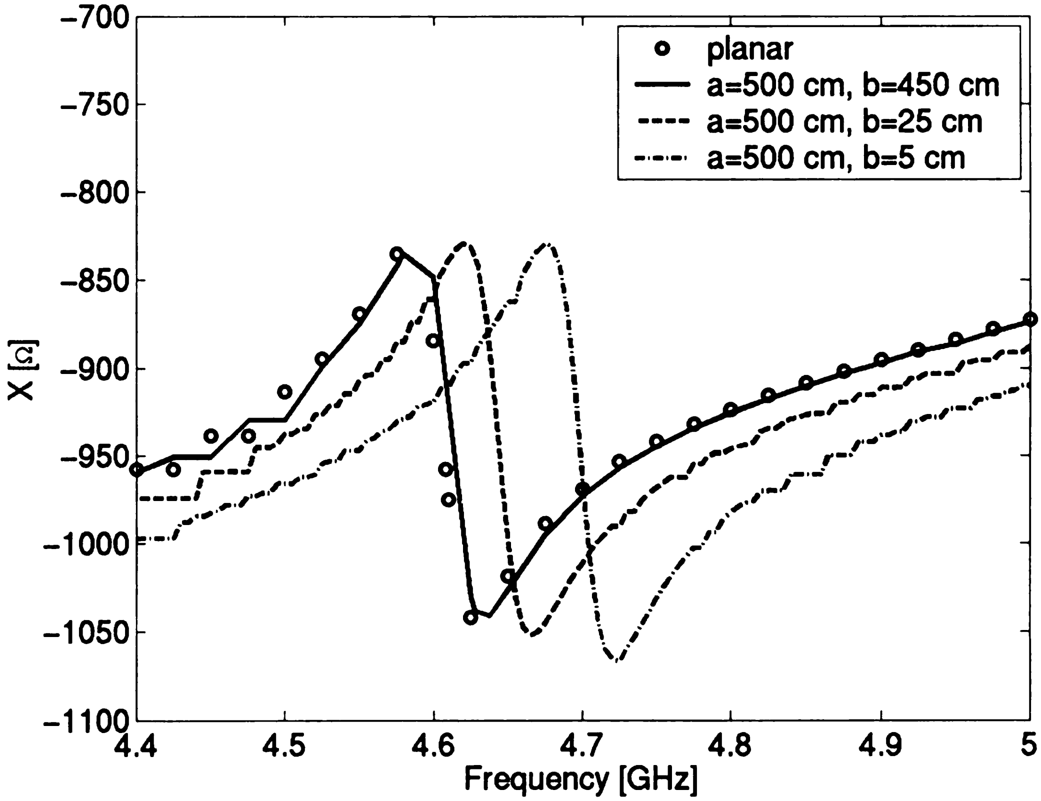

Figure 4.5 Input reactance of the horizontally oriented slot antenna.

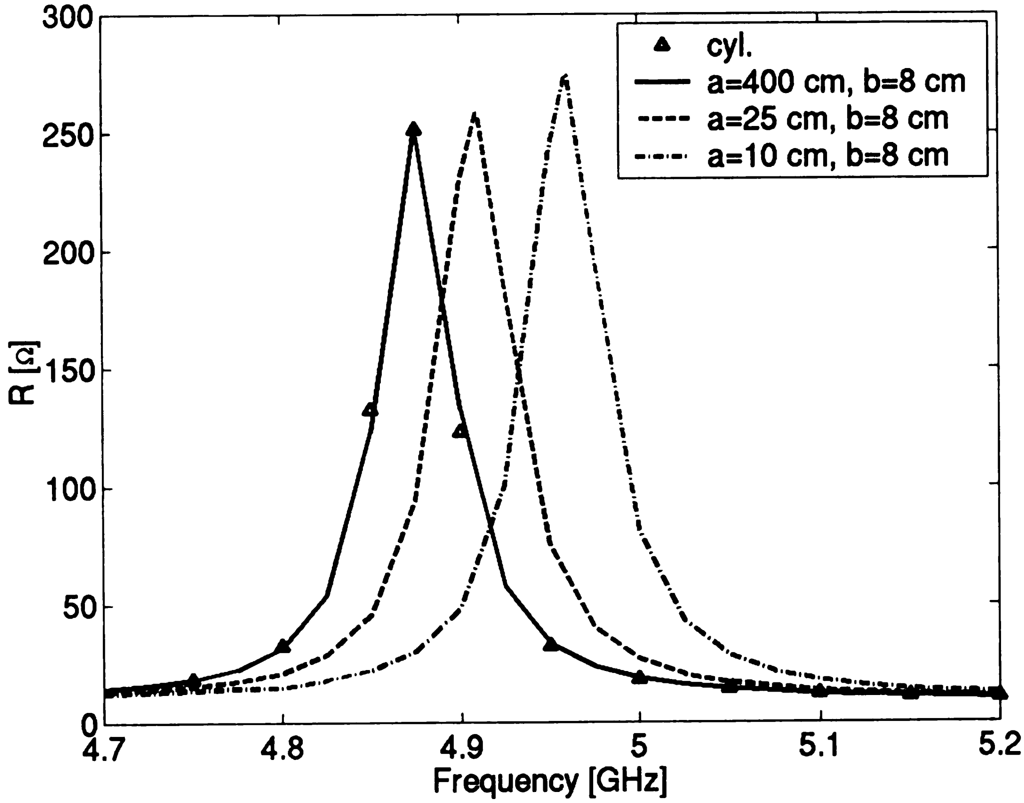

Figure 4.6 Input resistance of the vertically oriented slot antenna

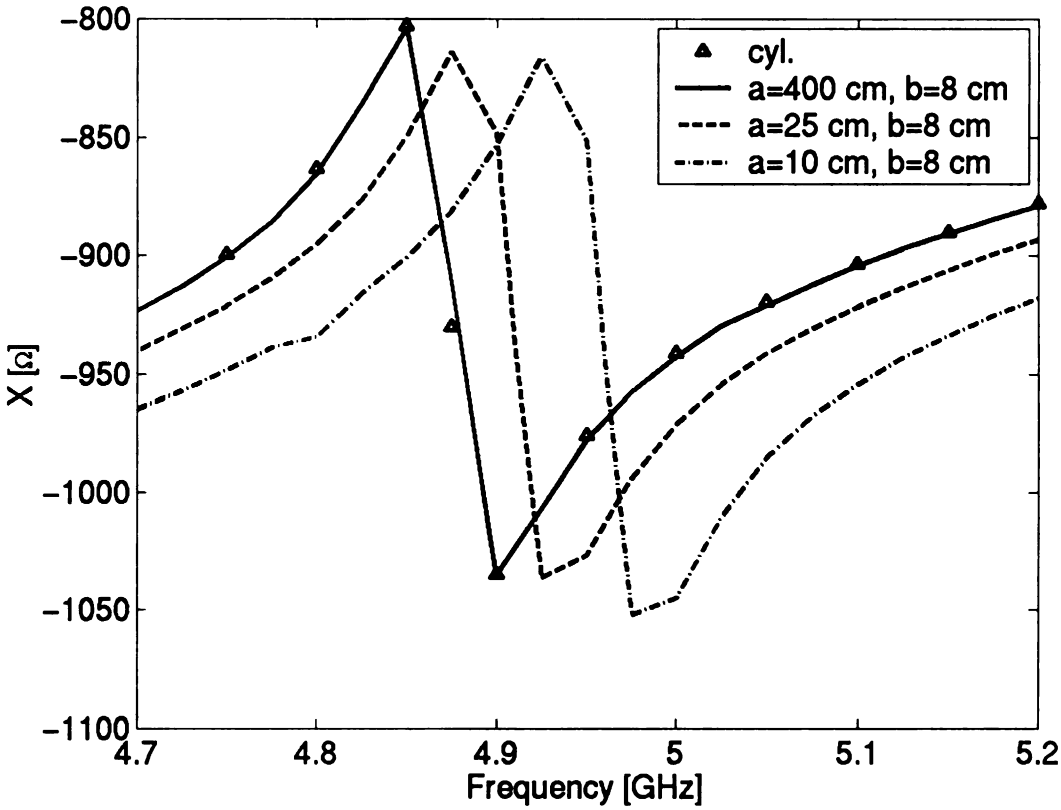

Figure 4.7 Input reactance of the vertically oriented slot antenna.

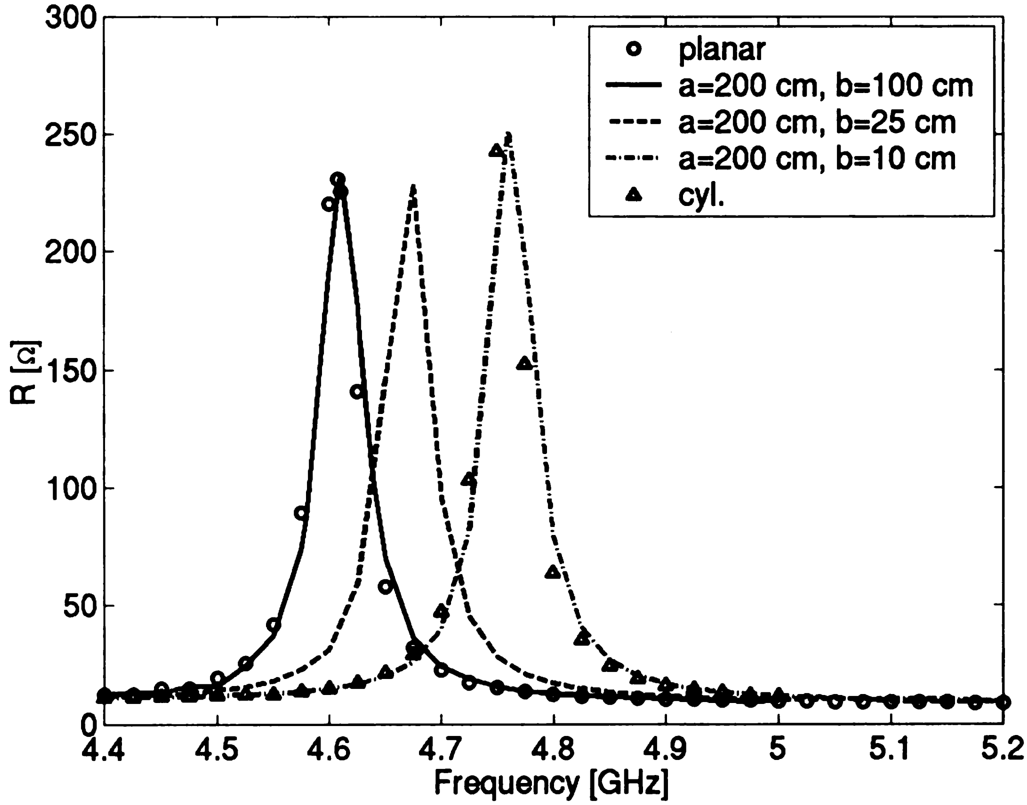

Figure 4.8 Input resistance of the slot antenna oriented 45^0 with respect to the vertical axis of the prolate spheroid

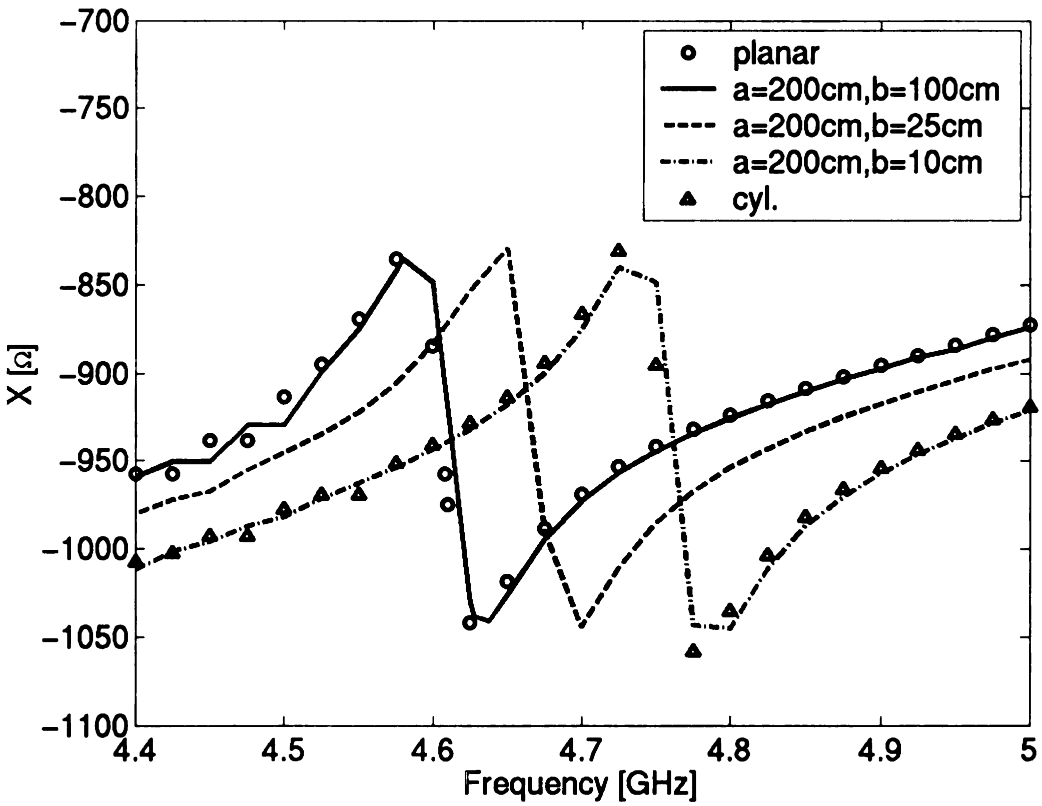

Figure 4.9 Input reactance of the 45^0 oriented slot antenna.

4.2.2 Cavity-Backed Conformal Patch Antenna

The resonant behavior of cylindrical-rectangular conformal patches has been investigated using the FE-BI method [2]. For this type of conformal patch antenna, the input impedance and resonant frequency exhibits a dependence on surface curvature. The degree of depends on the orientation of the antenna and the location of the probe feed. The purpose of this section is to simulate the behavior of the input impedance and resonant frequency of cavity-backed patch antennas that are recessed in doubly curved prolate spheroid surfaces as the surface curvature and antenna orientation are varied.

4.2.2.1 2.5 cm x 2.5 cm Patch

The first antenna to be modeled consists of a 2.5 x 2.5 cm metallic patch printed on a substrate of thickness 0.0762 cm residing in a 5.0 x 5.0 cm aperture. The substrate is composed of a dielectric material with permittivity $\varepsilon = 3.2 - j0.045$. The surface mesh for the antenna is shown in Figure 4.10. The behavior of the input impedance and resonant frequency for two different probe feed locations, as illustrated in Figure 4.11, are modeled in this study. The FE mesh for the patch antenna, generated by the procedure described in Chapter 3, is shown in Figure 4.12. Following the FE-BI procedure, the normal electric field beneath the patch is calculated and then used to calculate the input impedance. For the probe feed location in Figure 4.11a, a normal electric field beneath the patch exhibiting a polarization along the spheroid's axial direction is excited. From the input impedance spectrum of the axially polarized patch, shown in Figure 4.13, it is apparent that the resonant frequency is practically independent of surface curvature variation. A plot of the strength of the normal electric field under the patch for this polarization is shown in Figure 4.14. For the probe feed location in Figure 4.11b, a normal electric field exhibiting a polarization along the spheroid's azimuthal direction is excited. The input impedance spectrum for this polarization is shown in Figure 4.15. From this plot, it is evident that the resonant frequency exhibits a strong dependence on the surface curvature variation along the azimuthal direction. As the azimuthal curvature increases, the resonant frequency also increases. The magnitude of the normal electric field beneath the patch for this polarization is provided in Figure 4.16. Both of these results are quite reasonable since the degree of curvature along the azimuthal direction is large in comparison to the axial direction. Finally, we consider the case of a conformal patch that is rotated by 45^0 with respect to the azimuthal plane of the spheroid. Based on the previous results, it is expected that the input impedance for this case would display a curvature dependence that lies in between that of the axially and circumferentially polarized cases. The input impedance spectrum and normal electric field strength for this case are given in Figures 4.17 and Figure 4.18, respectively. From Figure 4.17, one can see that the resonant behavior for this case agrees with the expected result in that as the surface curvature increases, the resonant frequency also increases.

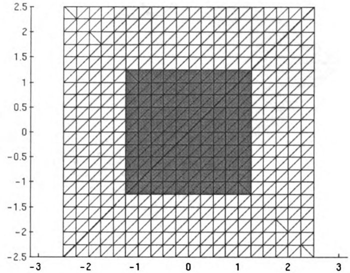

Figure 4.10 Surface mesh for a 2.5 x 2.5 cm conformal patch antenna.

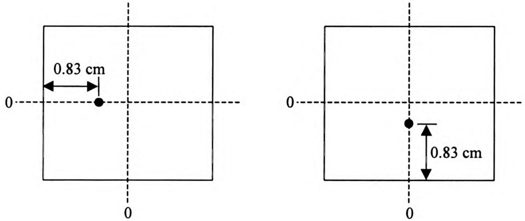

Figure 4.11 Position of the probe feed for the 2.5 x 2.5 cm patch antenna.

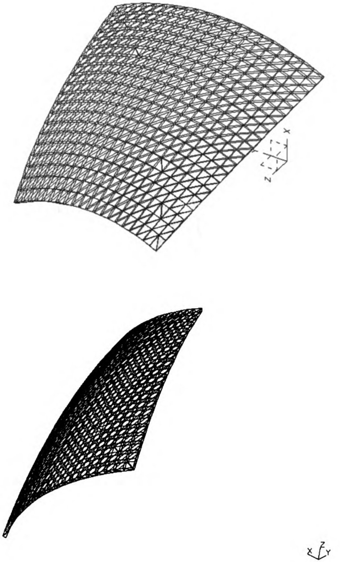

Figure 4.12 Different views of the finite element mesh for a 2.5 x 2.5 cm patch antenna conformal to a doubly curved prolate spheroid surface.

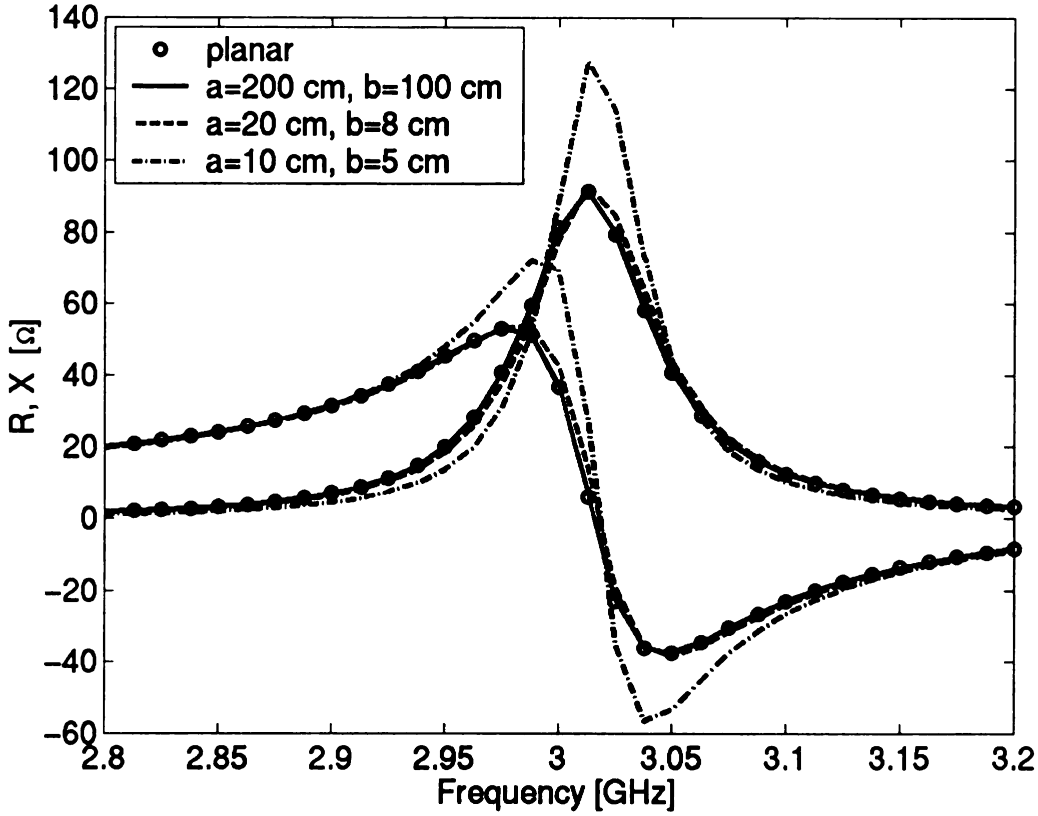

Figure 4.13 Input impedance of the axially polarized 2.5 x 2.5 cm patch antenna.

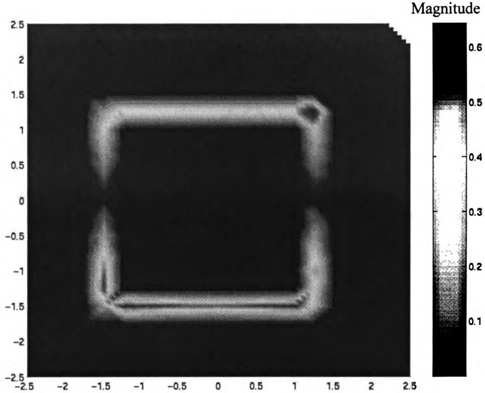

Figure 4.14 Magnitude of the axially polarized normal electric field beneath the 2.5 x 2.5 cm patch.

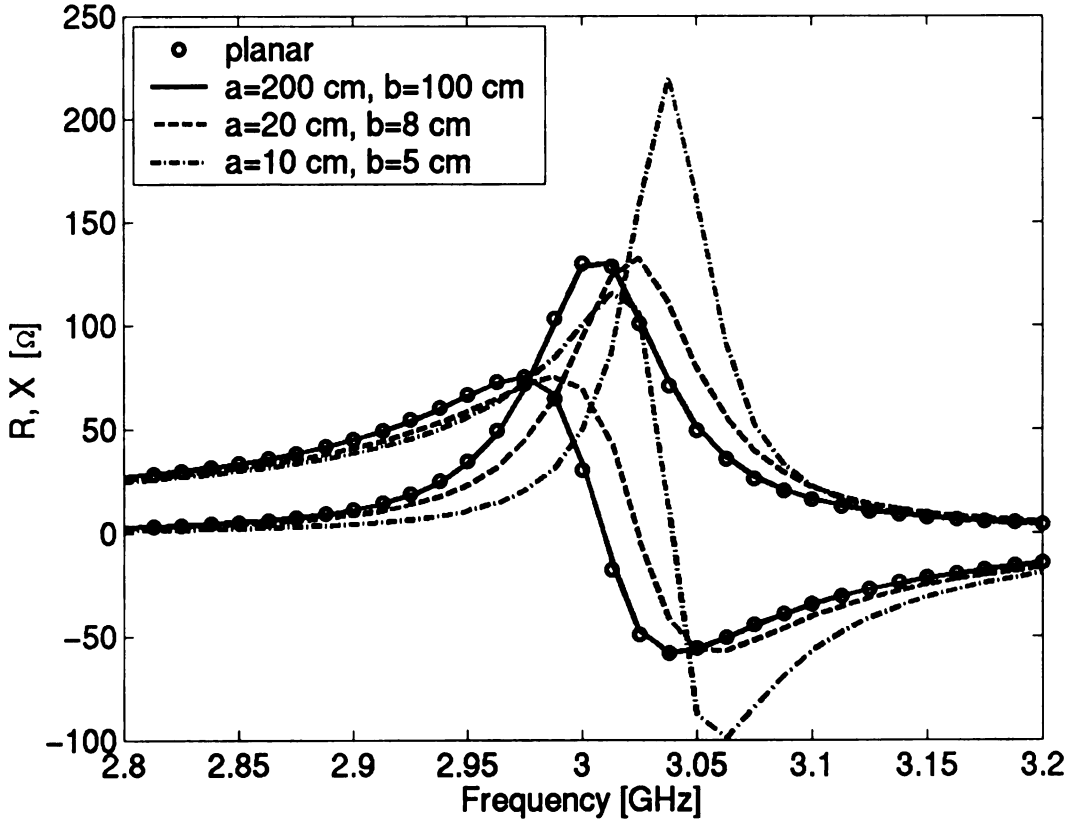

Figure 4.15 Input impedance of the azimuthally polarized 2.5 x 2.5 cm patch antenna.

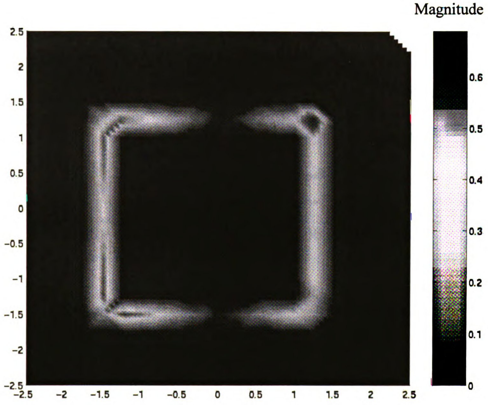

Figure 4.16 Magnitude of the azimuthally polarized normal electric field beneath the 2.5 x 2.5 cm patch.

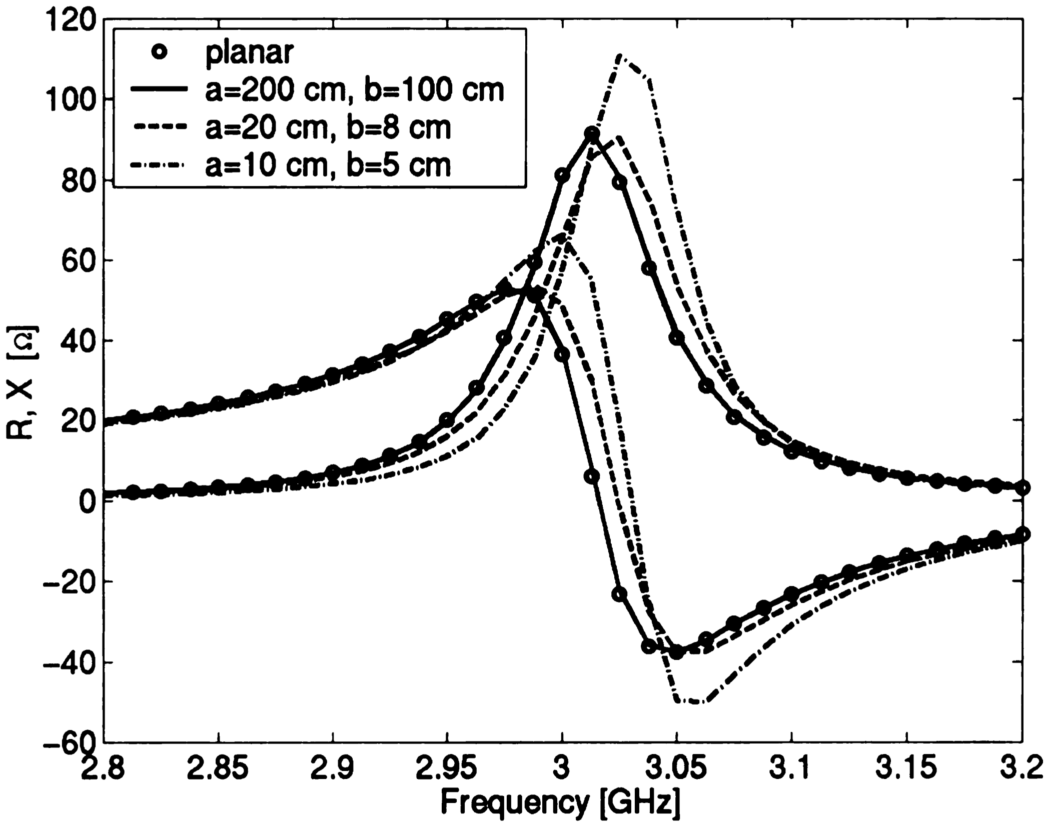

Figure 4.17 Input impedance of the 45^0 rotated 2.5 x 2.5 cm patch antenna.

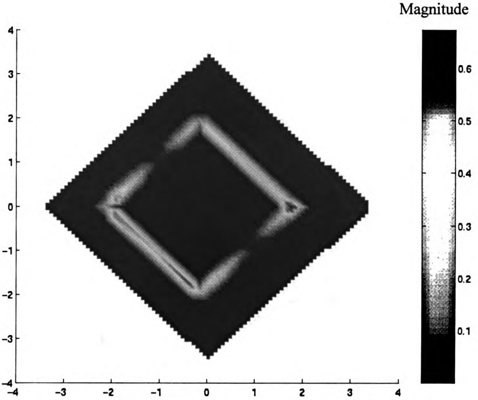

Figure 4.18 Magnitude of the normal electric field beneath the 45^0 rotated 2.5 x 2.5 cm patch.

4.2.2.2 3.0 cm x 3.0 cm Patch

In order to assess the effect of patch size on the curvature sensitivity of the input impedance, the input impedance of a larger patch antenna is investigated. For this case, a 3.0 x 3.0 cm metallic within a 6.0 x 6.0 cm aperture is modeled. The same permittivity and substrate thickness from the previous is used. Once again, the patch is excited by a normally directed probe-feed positioned so as to excite the same field polarizations as for the 2.5 x 2.5 cm patch. The probe feed is located 1.0 cm from the bottom of the patch along its centerline as depicted in Figure 4.19.

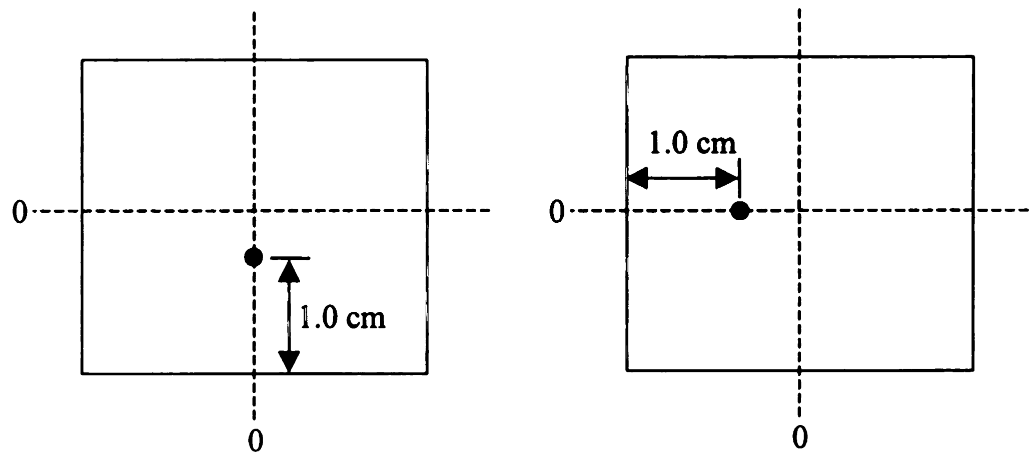

Figure 4.19 Probe feed positions on the 3.0 x 3.0 cm patch.

Analogous to the previous case, for a probe-feed positioned along the axial centerline, an axially polarized field is excited. For this polarization, the resonant frequency of the input impedance is practically independent of curvature, although there is a slight shift as the surface curvature increases (a = 10 cm and b = 5 cm). However, the main difference between this and the previous case is the decrease in the magnitude of the input impedance for large surface curvature, as seen in Figure 4.21. The circumferentially polarized case, shown in Figure 4.22, exhibits a high degree of curvature dependence which is consistent with the circumferential polarization of the previous case. The increase in patch size does not appear to effect the amount by which the resonant frequency shifts. Finally, for the 45^0 rotated patch, the curvature dependence of the resonant frequency appears to lie in between that of the axial and circumferential case, as seen in Figure 4.23. This is consistent with the result obtained in the previous section for the 45^0 rotated patch.

Finally, the input impedance of the 3.0 x 3.0 cm patch as a function of elevational position on 17.0 x 15.0 cm spheroid is considered in this study. The different elevational positions are depicted in Figure 4.20.

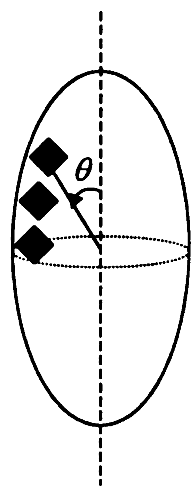

Figure 4.20 Elevational positions along the surface of a prolate spheroid.

Since the axial curvature of a prolate spheroid is relatively low at the midsection and progressively increases towards the pole, it is worthwhile to assess the effect that such curvature variation would have on the input impedance. Comparing Figure 4.24 with

Figure 4.25, it is apparent that the resonant frequency of the circumferentially polarized patch exhibits a greater sensitivity to curvature variation than that of the axially polarized patch as it is moved progressively closer to the pole of the spheroid. This result is consistent with the previous cases.

The effect of surface curvature variation on the placement of the 45^0 rotated patch is examined next in Figures 4.26 a, b, and c. For this case, an unexpected phenomenon occurs. For the patch located at an elevation angle $\theta = 80^0$, the single mode splits into two modes which resonate at 2.51 GHz and 2.56 GHz. Raising the patch to the position $\theta = 70^0$ the two modes resonate at 2.48 GHz and 2.60 GHz. At position $\theta = 60^0$, the two modes resonate at 2.41 GHz and 2.69 GHz are excited. Hence, as the patch is located closer to the pole of the spheroid, the difference in the resonant frequencies of the two modes increases. The normal electric field excited in this configuration, is shown Figure 4.27.

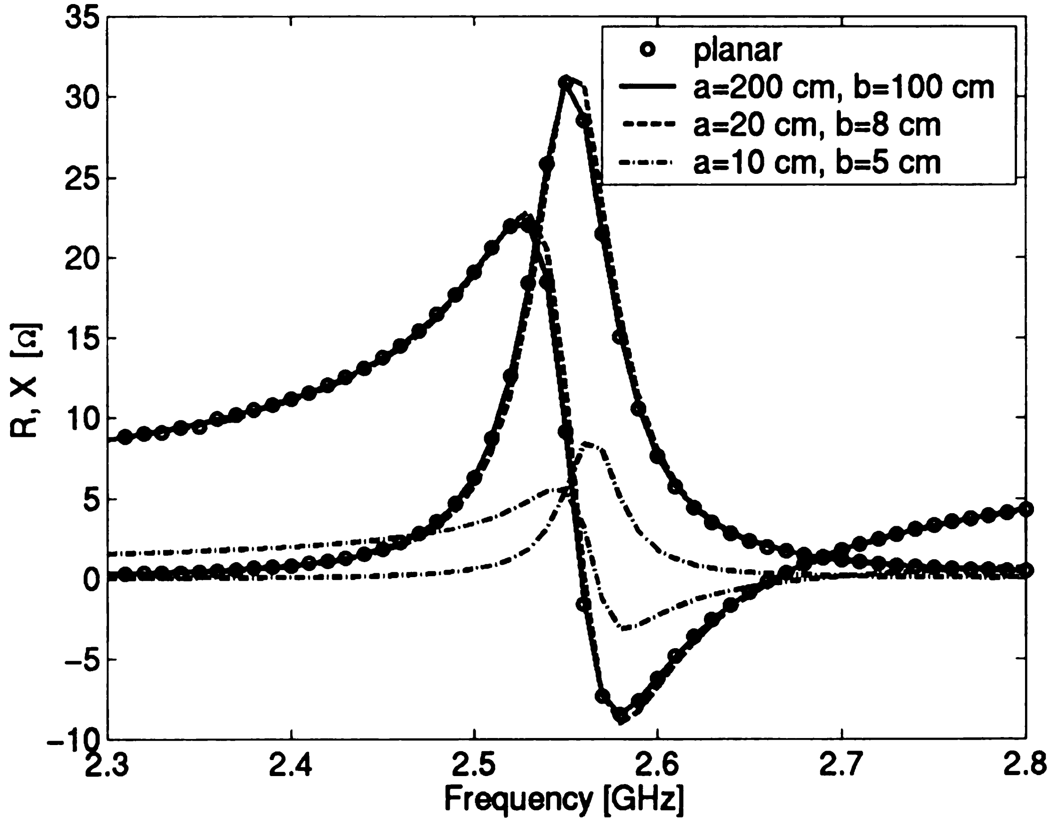

Figure 4.21 Input impedance of the axially polarized 3.0 x 3.0 cm patch antenna.

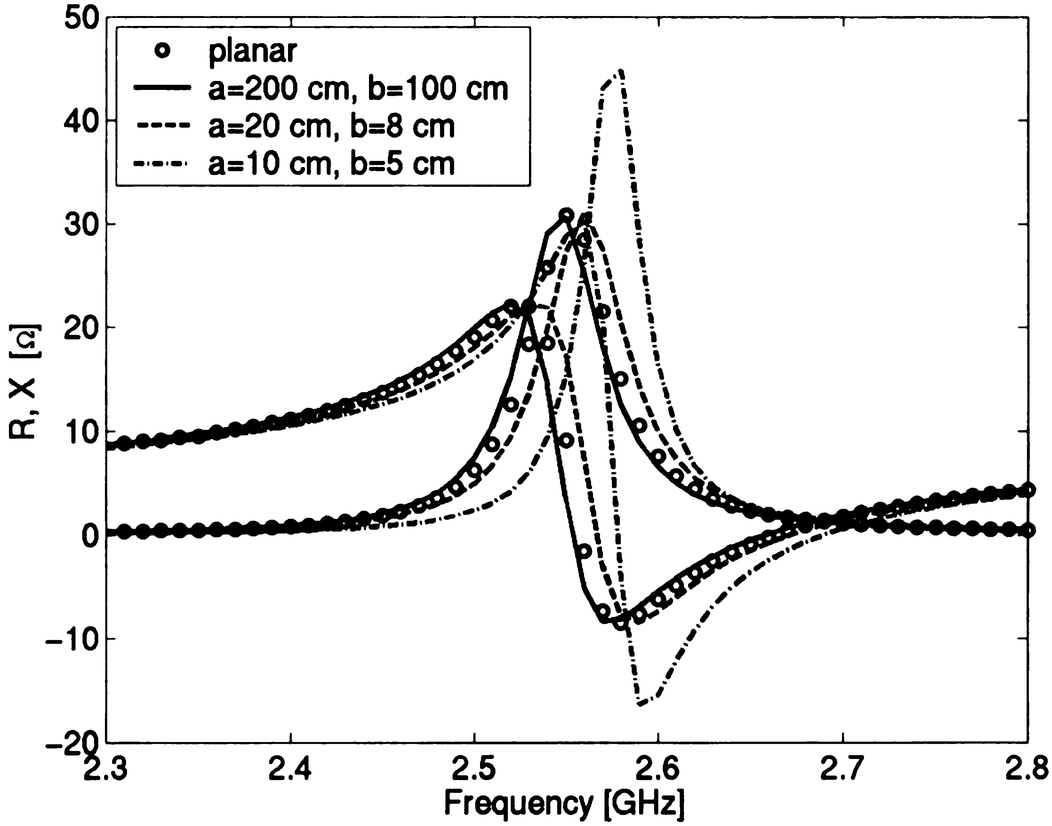

Figure 4.22 Input impedance of the azimuthally polarized 3.0 x 3.0 cm patch antenna.

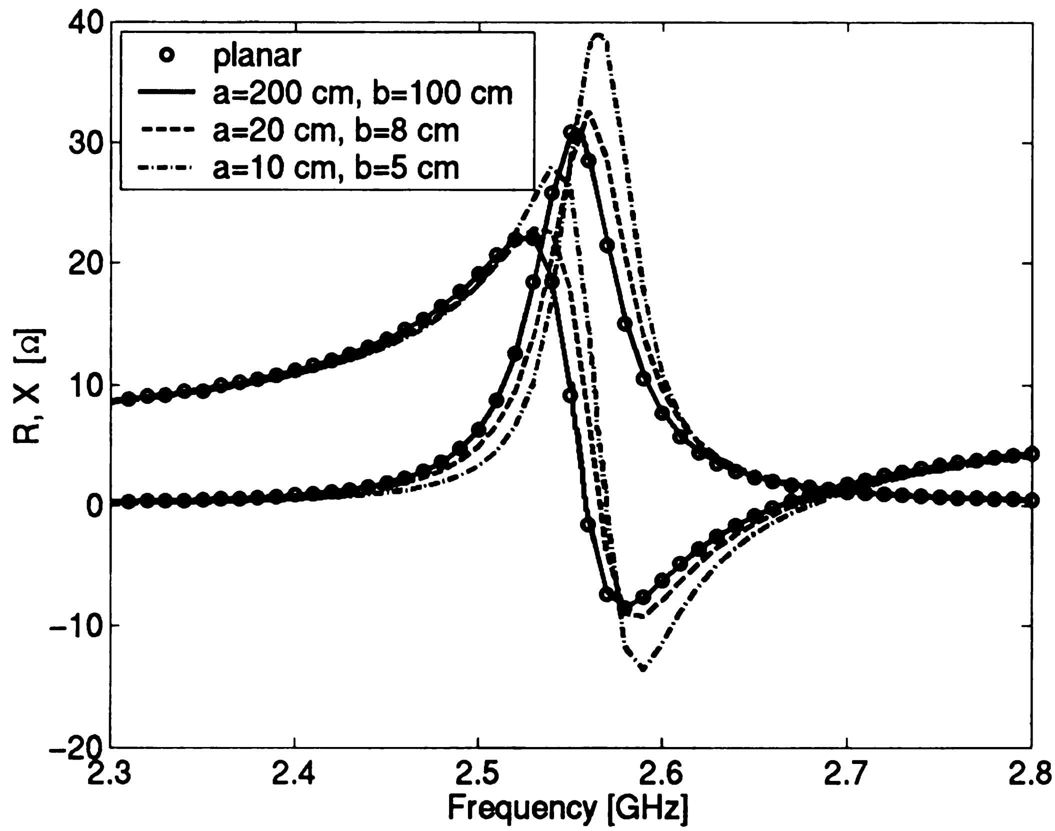

Figure 4.23 Input impedance of the 45^0 rotated 3.0 x 3.0 cm patch antenna.

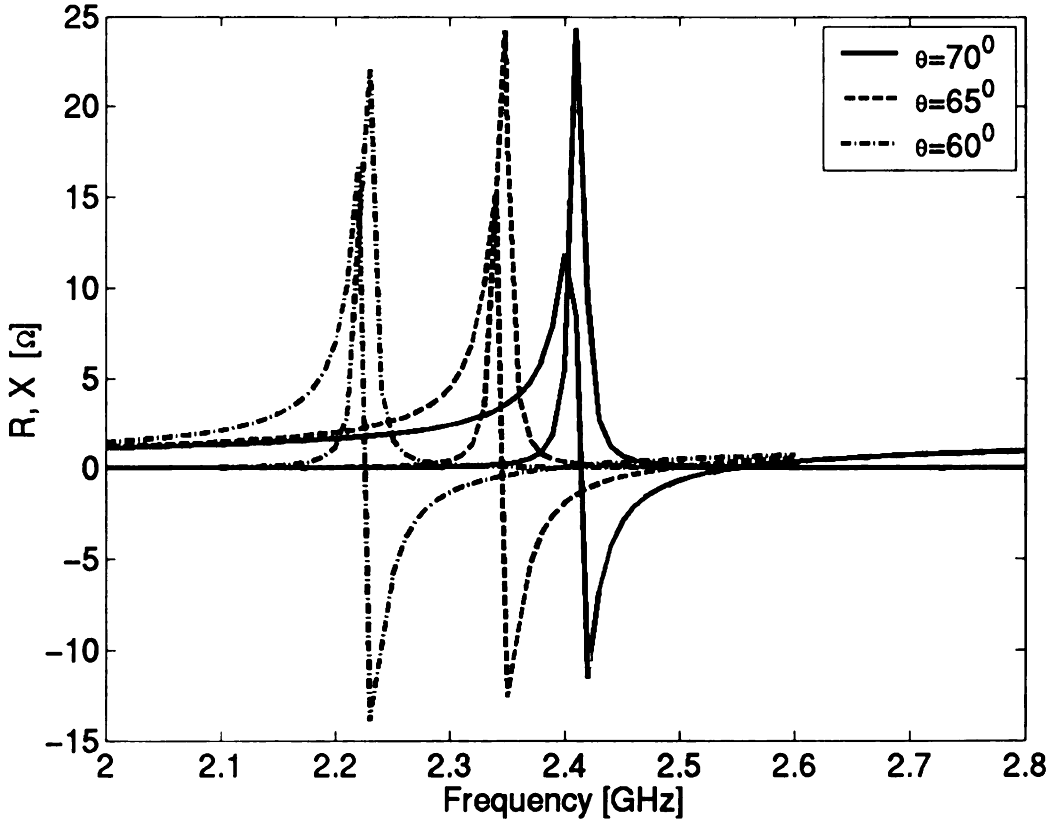

Figure 4.24 Input impedance of the axially polarized 3.0 x 3.0 cm patch antenna as a function of elevation angle.

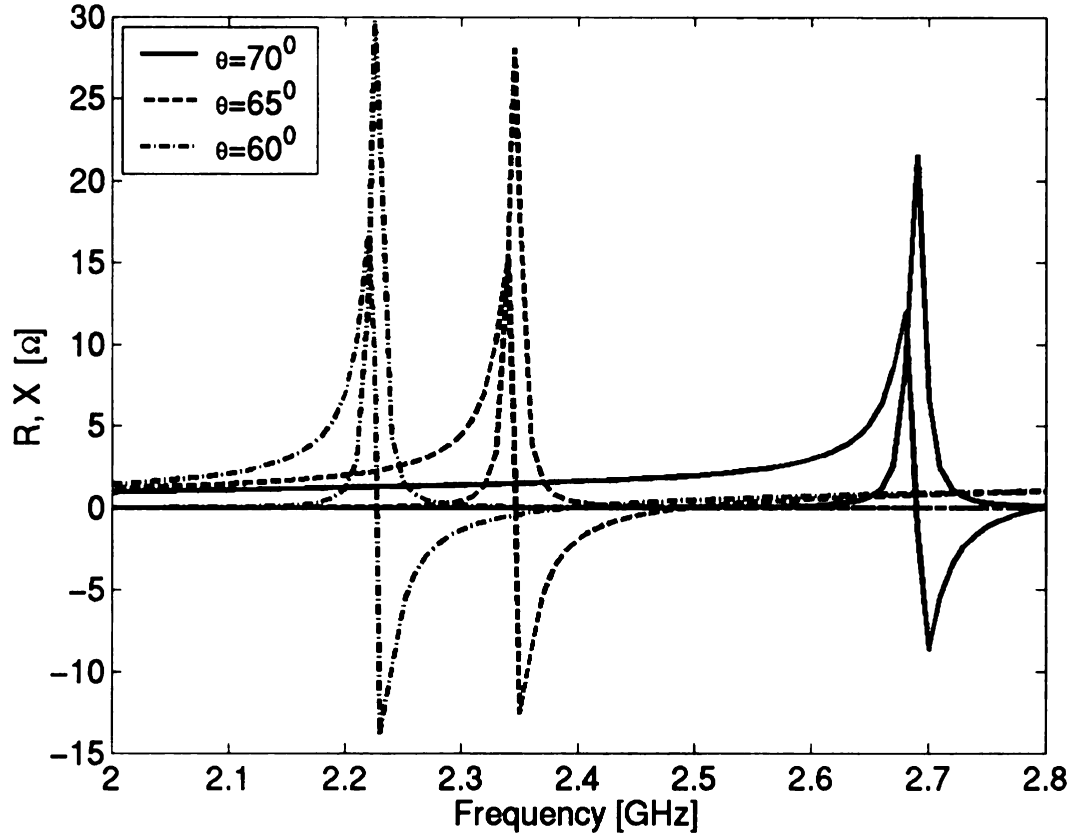

Figure 4.25 Input impedance of the azimuthally polarized 3.0 x 3.0 cm patch antenna as a function of elevation angle.

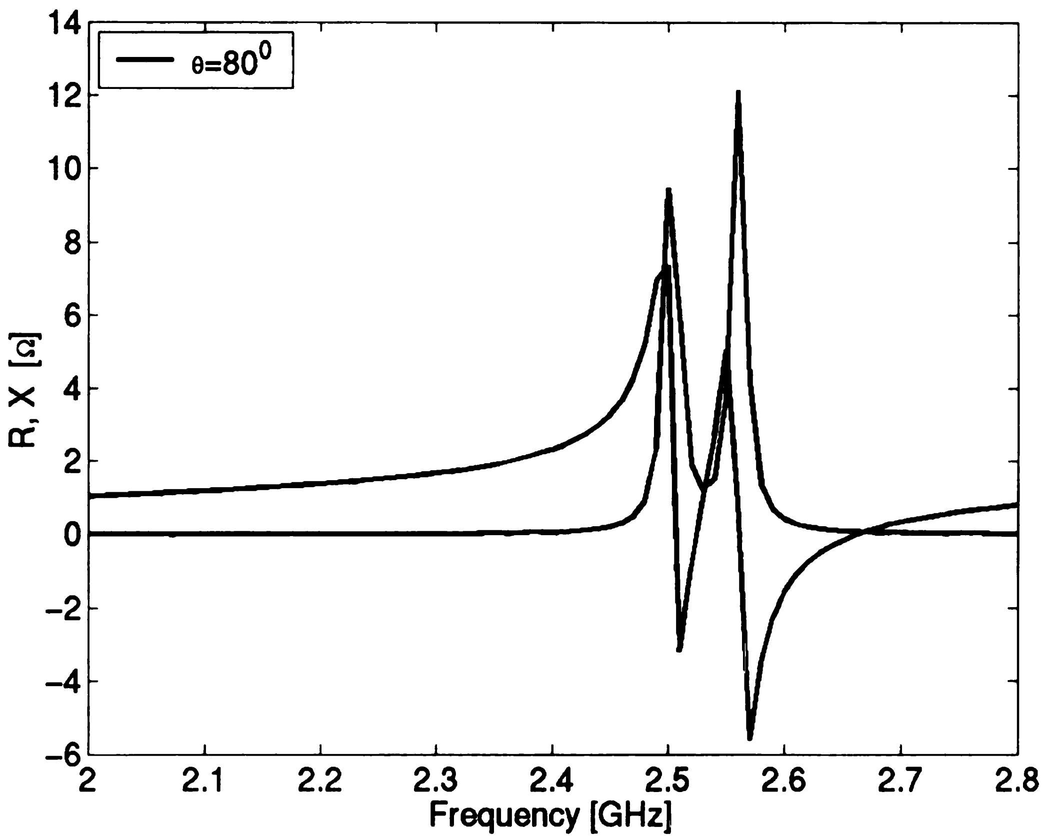

Figure 4.26(a) Input impedance of the 45^0 rotated 3.0 x 3.0 cm patch antenna mounted at the elevation angle $\theta = 80^0$.

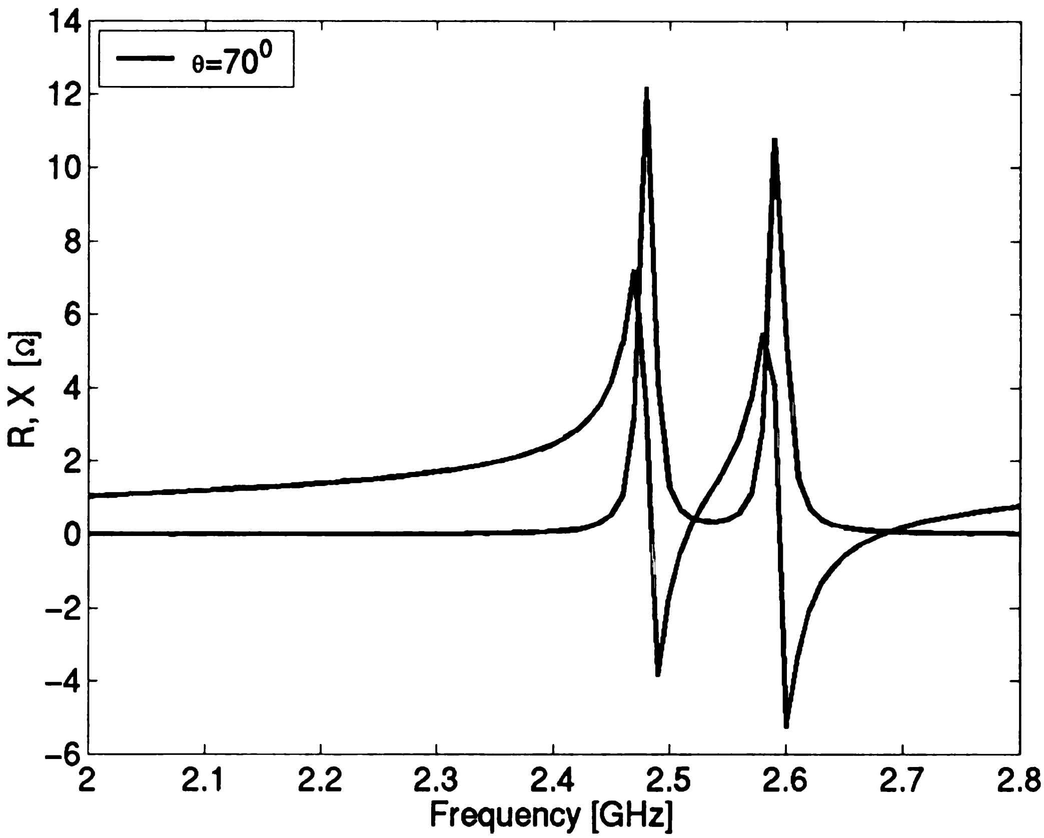

Figure 4.26(b) Input impedance of the 45^0 rotated 3.0 x 3.0 cm patch antenna mounted at the elevation angle $\theta = 70^0$.

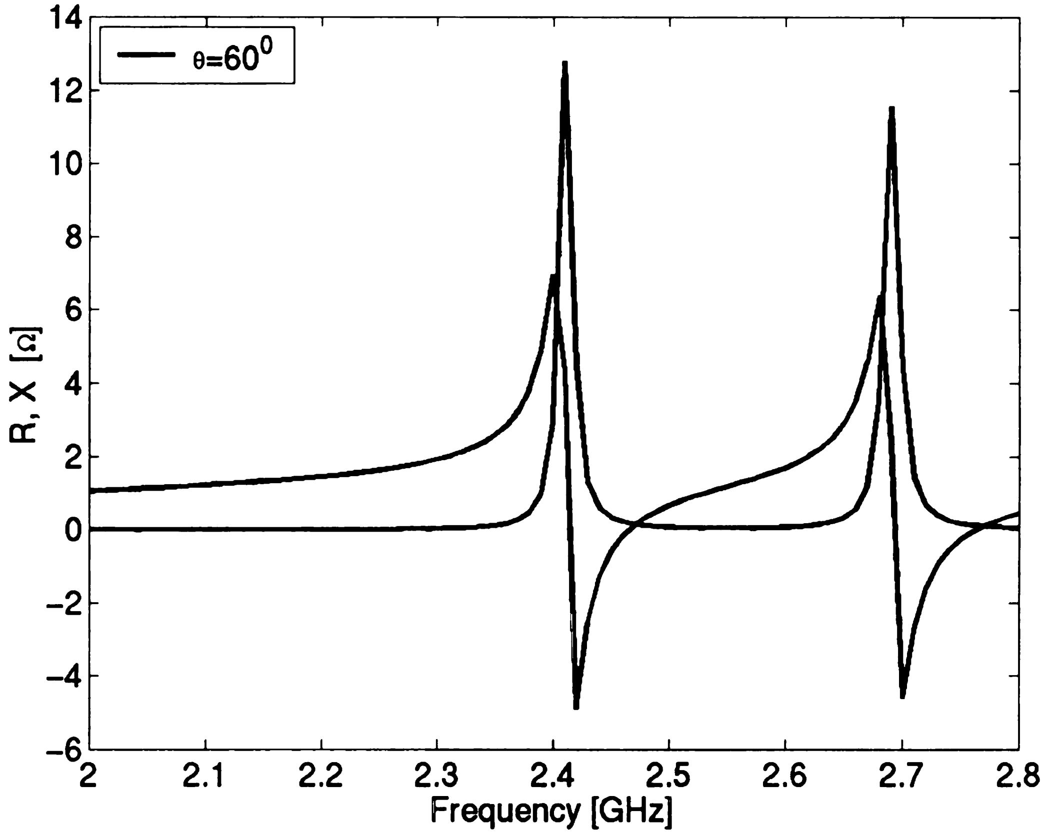

Figure 4.26(c) Input impedance of the 45^0 rotated 3.0 x 3.0 cm patch antenna mounted at the elevation angle $\theta = 60^0$.

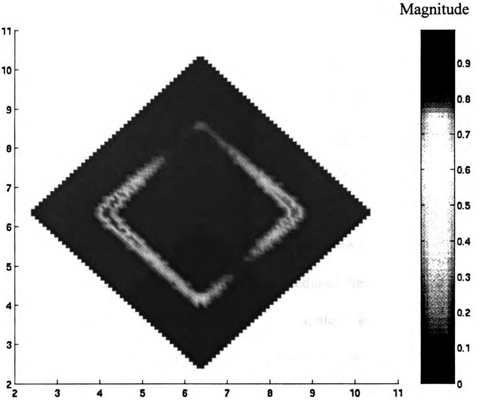

Figure 4.27 Magnitude of the normal electric field associated with Figure 4.26(c).

4.3 Far-field Radiation Pattern

The far-zone radiated field of a 3.0 x 3.0 cm patch in the geometrical optics region of a prolate spheroid is calculated in this section. Due to the scarcity of published data on this topic, the validity of the FE-BI simulation results is assessed by comparisons with the results of the planar and cylindrical tetrahedral element based FE-BI programs [2,3]. The planar tetrahedra based code has been experimentally verified [48], while the cylindrical tetrahedra based code has been shown to agree quite well with the experimentally verified cylindrical shell based FE-BI code [3]. In Figure 4.28, the azimuthal plane far-zone field radiated by a 2.5 x 2.5 cm patch in the geometrical optics region of a 200 x 100 cm prolate spheroid at 3.09 GHz is compared with the far-zone field radiated by a patch antenna on a planar surface. As seen in this plot, the radiated field pattern of a patch on an electrically large prolate spheroid matches the radiated field pattern of a patch radiating on a plane. This result agrees with expectations. Comparisons between the radiated field pattern in the azimuthal plane of a patch residing on an infinite circular cylinder of radius 8 cm and the field pattern of a patch located at different elevation angles on different sized prolate spheroids are given in Figures 4.29 through 4.31. As expected, there is good agreement between the field pattern of the patch on the cylinder and the field pattern of the patch positioned at the equator of a 200 x 8 cm prolate spheroid. As the elevational position of the patch along the prolate spheroid is raised, the E_φ component begins to deviate from the cylindrical result. The distortion is due to the deviation of the surface profile along the η (or θ) direction of the spheroid from the flat profile along the axial direction of a circular cylinder. There is practically no deviation in the E_θ component, however. This is due to the fact that the deviation in the azimuthal radius of curvature from the cylindrical limit as the patch is moved along the spheroid in the elevational direction is neglible. The same effect is seen as the patch is moved along the surfaces of a 20 x 8 cm spheroid and 10 x 8 cm spheroid. There is just a slight difference between the 20 x 8 cm and 200 x 8 cm cases in the vicinity of the null of the E_φ component. The E_θ component, however, exhibits negligible change. For the 10 x 8 cm prolate spheroid case, both field components deviate from the cylindrical results. For this case, the deviation exhibiting by the E_θ component arises from the change in azimuthal radius of curvature as the patch is moved towards the pole of the spheroid. From these cases, it is evident that the E_θ component of the far field radiated by a conformal patch located in a region near the equator ($\leq \pm 20^0$) of a quasi-cylindrical (e.g. highly elongated) prolate spheroid may be approximated with reasonable accuracy by the cylindrical E_θ value. However, the cylindrical approximation to the prolate spheroidal E_φ component is valid only at the equator of the prolate spheroid. For a patch located above or below the equator, the E_φ deviates significantly from the cylindrical value.

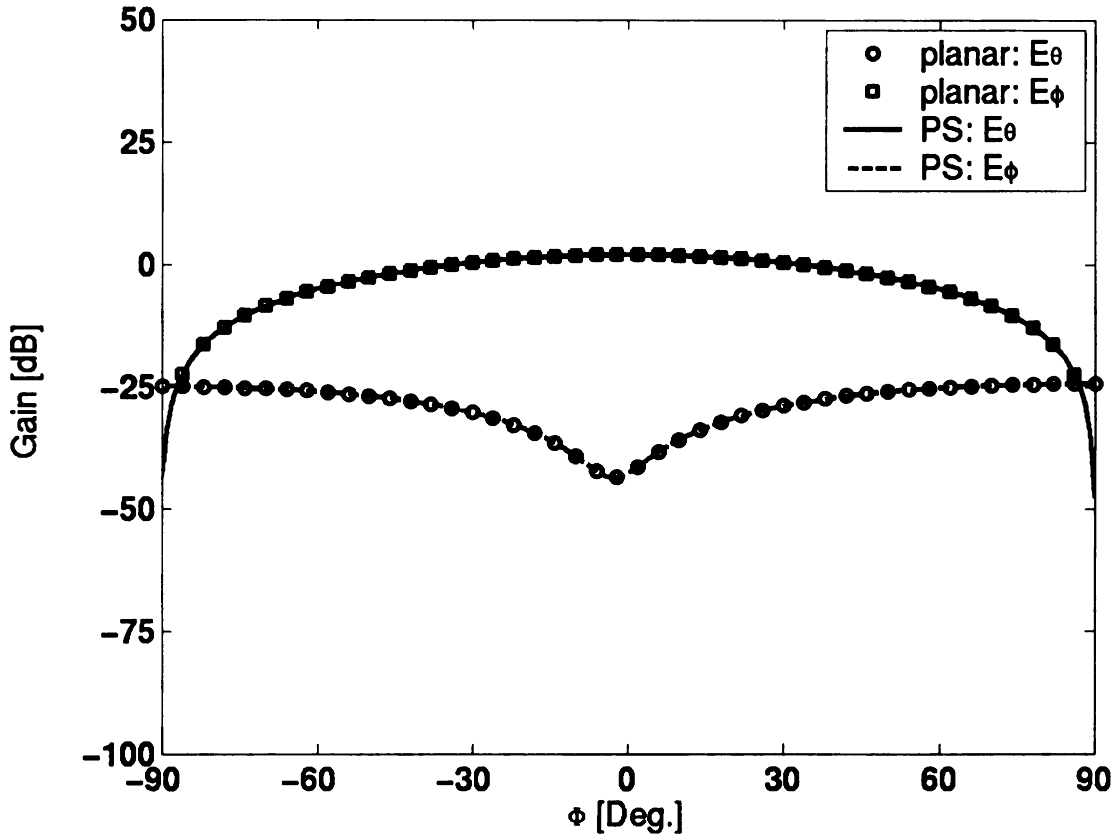

Figure 4.28 Comparison of the azimuthal plane radiated field of a 2.5 x 2.5 cm patch antenna in the geometrical optics region of a 200 x 100 cm prolate spheroid with the radiated field of a patch residing on a planar surface.

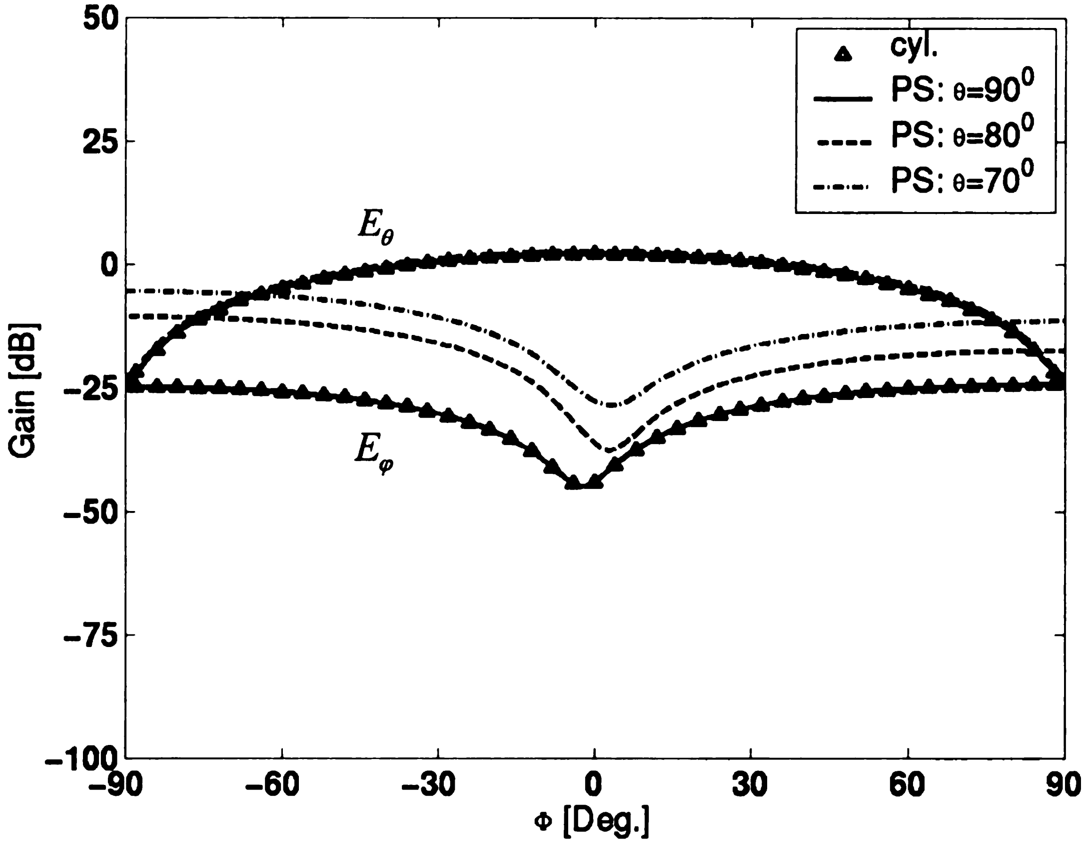

Figure 4.29 Comparison of the azimuthal radiated field of a 2.5 x 2.5 cm patch antenna mounted on a 200 x 8 cm prolate spheroid at specified elevational angles with the azimuthal field of an identical patch antenna mounted on a circular cylinder with an 8 cm radius.

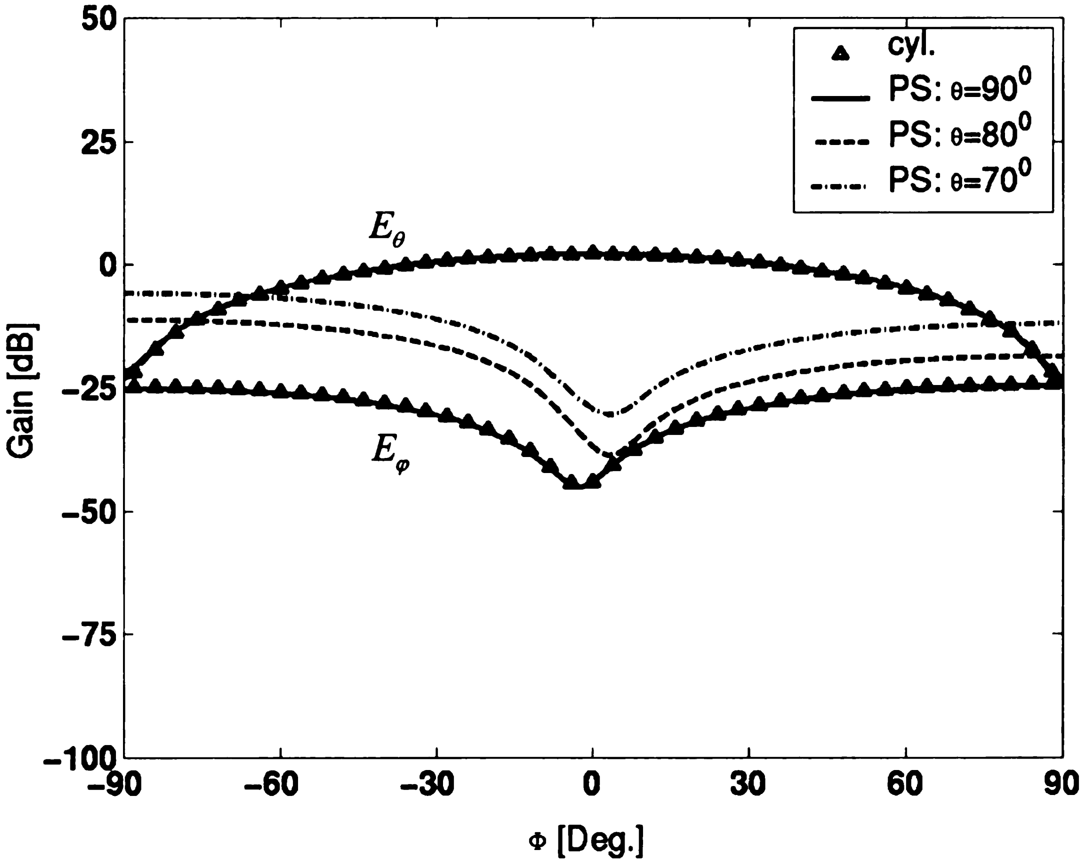

Figure 4.30 Comparison of the azimuthal radiated field of a 2.5 x 2.5 cm patch antenna mounted on a 20 x 8 cm prolate spheroid at specified elevational angles with the azimuthal field of an identical patch antenna mounted on a circular cylinder with an 8 cm radius.

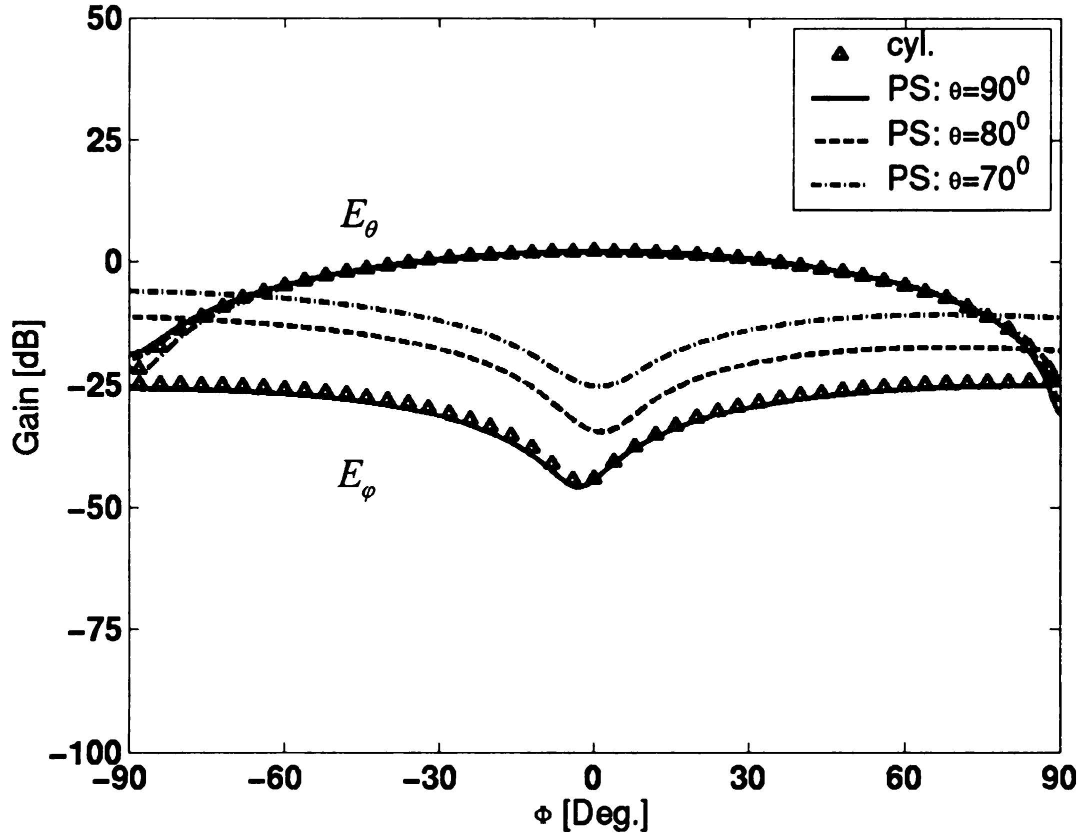

Figure 4.31 Comparison of the azimuthal radiated field of a 2.5 x 2.5 cm patch antenna mounted on a 10 x 8 cm prolate spheroid at specified elevational angles with the azimuthal field of an identical patch antenna mounted on a circular cylinder with an 8 cm radius.

CHAPTER 5

EXPERIMENTAL RESULTS

5.1 Introduction

In order to verify the FE-BI simulation results presented in the preceding chapter, the measured input impedance of a patch antenna mounted on a ground plane and on a prolate spheroid are presented in this chapter. For the case of a patch antenna radiating on a ground plane, the purpose of the experiment is to assess the accuracy of the resonant frequency and magnitude of the input impedance as predicted by the prolate spheroidal FE-BI routine in the planar limit (e.g. large axial and azimuthal radii of curvature). For the case of the patch antenna radiating on a prolate spheroid, the purpose of the experiment is to assess the effect of surface curvature variation on the input impedance of the patch at various elevational positions on the spheroid surface. The lack of published experimental data on the input impedance of patch antennas conformal to prolate spheroidal surfaces may be due to the considerable difficulty involved in constructing this type of configuration. The presentation of the experimental results is preceded by a discussion of the antenna fabrication and experimental setup.

5.2 Antenna Fabrication

The fabrication of the patch antennas to be used in these experiments is discussed in this section. The dimensions of the first antenna to be considered are as follows: 3.0 x 3.0 cm patch within a 6.0 x 6.0 cm aperture. The face of the antenna is milled from GML 1100 copper clad laminated board with a thickness of 0.0236 cm. The laminated board consists of a layer of dielectric material with a permittivity $\varepsilon = 3.29 - j0.0132$ at 2.5 GHz sandwiched between two copper layers. The feed configuration consists of a female SMA connector soldered to 3.2 cm of semi-rigid coaxial cable. The coax center conductor provides the probe feed for the antenna. As shown in Figure 5.1b, a 0.914 mm (0.0360 in) hole through which the center conductor of the coaxial cable connects to the patch is drilled 0.98 cm from the bottom edge and 1.48 cm from the left edge of the patch. To prevent a short circuit between the patch and back antenna surfaces, the center conductor is encased by a teflon tube to insulate it from the walls of the top and bottom copper layers of the laminated board before it is fed through the probe feed hole. The center conductor is soldered to the patch while the outer conductor is soldered to the metallic back surface of the antenna. The 4.0 x 3.0 cm patch is fabricated from the same material using the same procedure, except that the feed-through hole for the center conductor is located 0.52 cm from the bottom edge and 1.99 cm from the left edge of the patch as shown in Figure 5.1.

The fabrication of the patch antenna to be mounted on a metal foil covered bowl, which simulates a PEC prolate spheroid, is described next. The maximum radius of the bowl is 14.74 cm and its height is 17.0 cm. The dimensions of the conformal patch antenna are as follows: 3.0 x 3.0 cm patch within a 6.0 x 6.0 cm aperture. Since the antenna must conform to the doubly curved surface of the bowl, it is fabricated from GML 1100 copper clad laminated board with a thickness of 0.014 cm in order to minimize buckling along the surface of the bowl. The thinness of the board necessitates a different fabrication technique than was used for the thicker patch antenna. In view of the thinness of the metallic layer, the face of the antenna is chemically etched from the GML 1100 board using a full-strength ferric chloride solution. In Figure 5.2 cross-sectional and top views detailing the construction of the patch antenna are provided. The probe feed consists of an SMA connector soldered to 4.55 cm of semi-rigid coaxial cable. A 0.914 mm hole through which the center conductor is fed is drilled 1.01 cm from the bottom and 1.54 cm from the left edge of the patch. A caveat of constructing a patch antenna out of such thin board is that it is quite difficult to ensure electrical isolation across the dielectric when solder is applied near the probe feed hole to electrically bond the center and outer conductors to the patch and back surfaces, respectively, of the antenna. Hence, in order to ensure electrical isolation between the back and patch surfaces, the following technique is used. First, nonconductive epoxy (Stycast 2850FT) is used to structurally bond the coaxial outer and center conductors to the bottom and patch surfaces, respectively, and also to prevent metallic debris from entering the hole and shorting across the top and bottom surfaces. Next, to prevent a short circuit between the patch and back antenna surfaces, the center conductor is encased by a teflon tube to insulate it from the walls of the top and bottom copper layers of the laminated board before it is fed through the probe feed hole. Finally, instead of solder, a silver coating obtained from the evaporation of a colloidal silver solution is applied to furnish a low impedance electrical connection between the coax outer conductor and the bottom surface and between the center conductor and patch surface as shown in Figure 5.2.

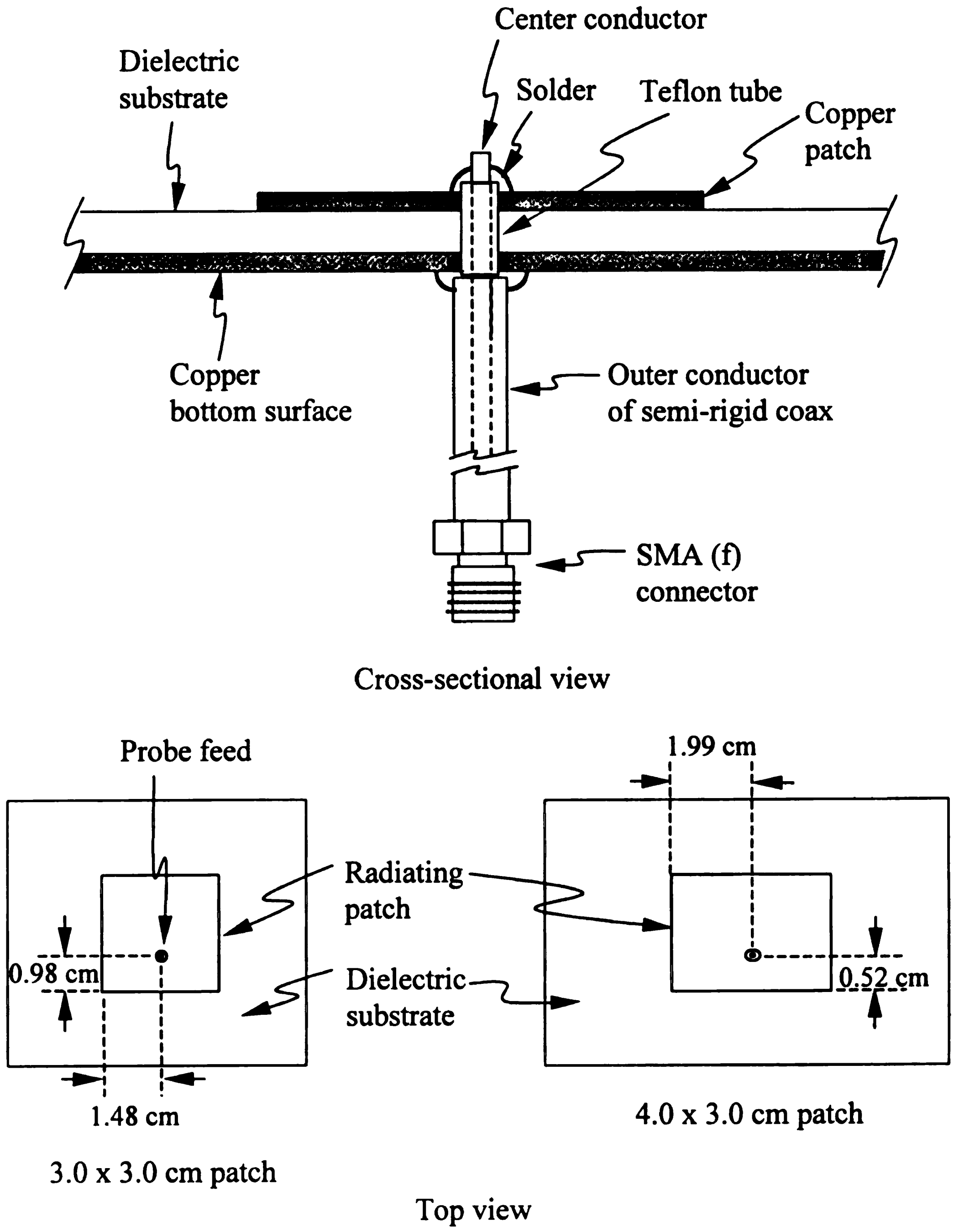

Figure 5.1 Construction of 3.0 x 3.0 cm and 4.0 x 3.0 cm patch antennas for mounting on a metallic ground plane.

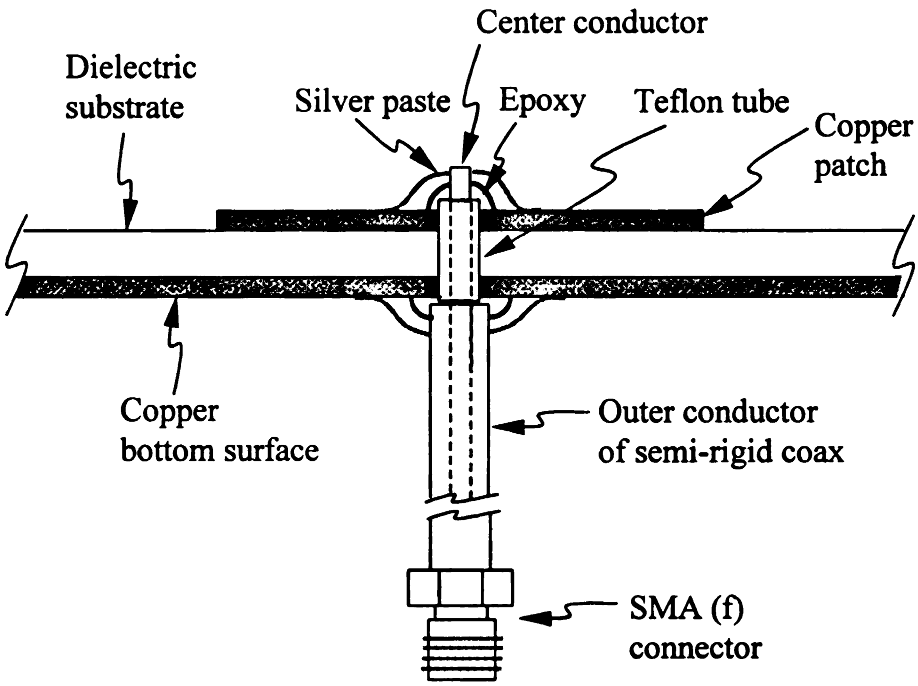

Cross-sectional view

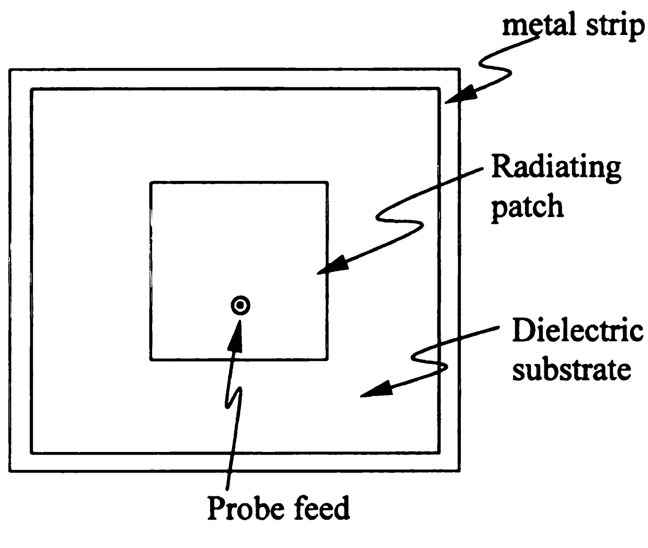

Top view

Figure 5.2 Construction of a 3.0 x 3.0 cm patch antenna for mounting on a doubly curved platform.

5.3 Experimental Setup and Measurements

5.3.1 Ground Plane

The S_{11} of a patch antenna mounted on a PEC ground plane was measured using the Hewlett-Packard 8753D network analyzer over the range 1.0-6.0 GHz. A PEC ground plane was simulated by a large flat aluminum covered sheet as depicted in Figure 5.3.

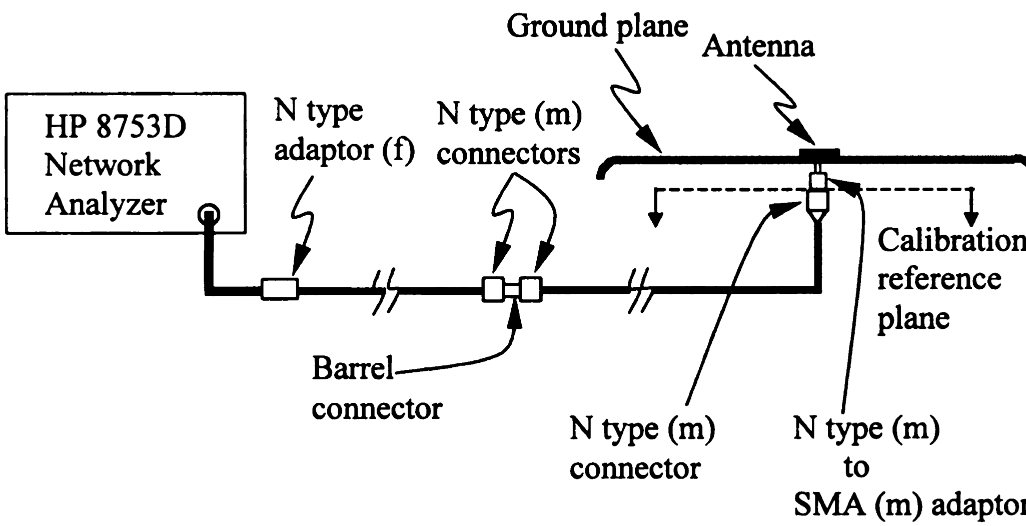

Figure 5.3 Experimental setup for the patch antenna on a ground plane.

The S_{11} of the antenna alone cannot be measured directly. In order to determine the antenna S_{11}, the electrical length of the feed from the tip of the SMA connector along the micro-coax cable to the point where the outer conductor is bonded to the back surface of the antenna must be calibrated out. In order to accomplish this, the coaxial cable feed first is cut to the length to be used in the antenna fabrication. Next, the cable is shorted at the end and the S_{11} of the shorted cable is measured over the frequency range 1.0-6.0 GHz and saved. The following calibration formula is used to remove the S_{11} of the probe feed:

$$S_{11}(ant) = -\left[\frac{S_{11}(sys)}{S_{11}(coax)}\right] \tag{5.1}$$

where $S_{11}(sys)$ is the measured S_{11} for the antenna which includes the probe feed, $S_{11}(coax)$ applies to the shorted probe feed, and $S_{11}(ant)$ is the desired S_{11} for the antenna alone. Now that the length of coaxial cable from the tip of the SMA connector to the point where it is bonded to the back surface of the antenna has been calibrated out, $S_{11}(ant)$ is converted to the input impedance Z_{11} of the antenna via the following formula:

$$Z_{11} = Z_0 \frac{(1+S_{11})}{(1-S_{11})} \tag{5.2}$$

where $Z_0 = 50\Omega$, the characteristic impedance of the coaxial feed.

In Figure 5.4, the input impedance of the 3.0 x 3.0 cm patch radiating on the ground plane measured over the frequency range 1.0 to 6.0 GHz is given. The FE-BI simulation results are provided for comparison. As seen in the plot, the FE-BI routine predicts the lowest order and two higher order resonant modes. Focusing on the frequency range in the vicinity of the dominant mode, the measured input impedance data is compared with the FE-BI simulation results for (a = 800 cm and b=700 cm) in Figure 5.5. For comparison against measured data over this narrow frequency range, fairly stringent criteria are used in the FE-BI simulation. The sampling factor used in the generation of the finite element mesh is $\lambda_0/92$ at the resonant frequency, resulting in 13,824 elements and 5,040 aperture unknowns. The FE-BI simulation required approximately eleven hours to run on a XEON 450 MHz machine. As seen in the plot, the measured resonant frequency is 2.71 GHz and the numerical result is 2.63 GHz. This represents an error of 2.95%. In Figure 5.6, the input impedance of a 4.0 x 3.0 cm patch radiating on a ground plane measured over the same frequency range as in the previous case is compared against the FE-BI simulation results. As seen in the plot, the FE-BI routine predicts the lowest order and two higher order resonant modes. As in the previous case, the measured input impedance data is compared with the FE-BI simulation results in the vicinity of the dominant mode resonant frequency, as shown in Figure 5.7. The same sampling factor is used over this frequency range as in the previous case, yielding a finite element mesh with 18,432 elements and 6,744 aperture unknowns. As seen in the plot, the measured resonant frequency is 2.70 GHz and the numerical result is 2.64 GHz. This represents an error of 2.22%.

One possible source of experimental error is the discrepancy between the modeled and actual location of the feed point on the patch. As the feed point is positioned closer to the center, the magnitude of the electric field at the feed point for the excited mode decreases, resulting in a reduction in the magnitude of the input impedance. The method of antenna construction could be another source of error. In applying solder to electrically bond the inner and outer conductors of the coaxial feed to the patch and back surfaces, respectively, the metallic surface in the vicinity of these points is heated to approximately 650^0 F, which is the temperature of the soldering iron. It is quite possible that the temperature of the dielectric layer in the vicinity of the feed which is in immediate contact with the heated metallic surface would exceed the range of stability of the dielectric constant. From the data sheet for the GML 1100 substrate (manufacured by GIL Technologies), the dielectric constant of the material is stable only in the temperature range $-131^0 F$ to $257^0 F$. Published data on the value of the dielectric constant outside of this temperature range is not available.

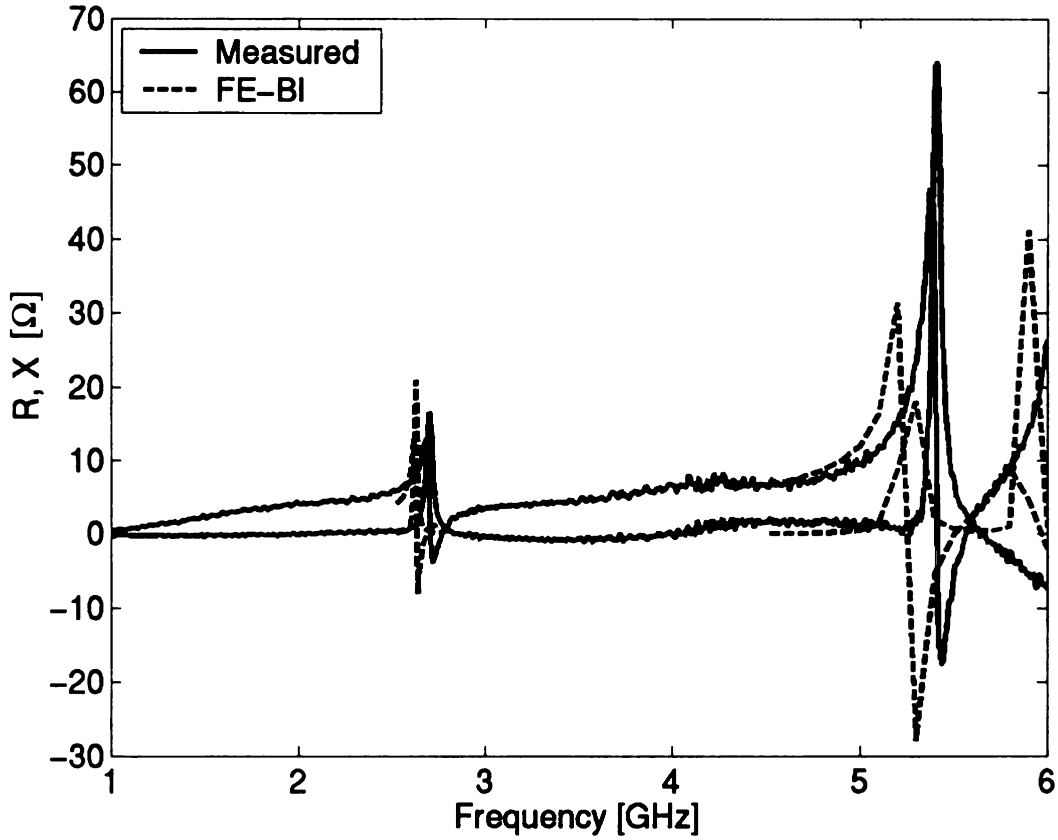

Figure 5.4 Comparison of the measured and FE-BI simulated input impedance of a 3.0 x 3.0 cm patch antenna radiating on a metallic ground plane.

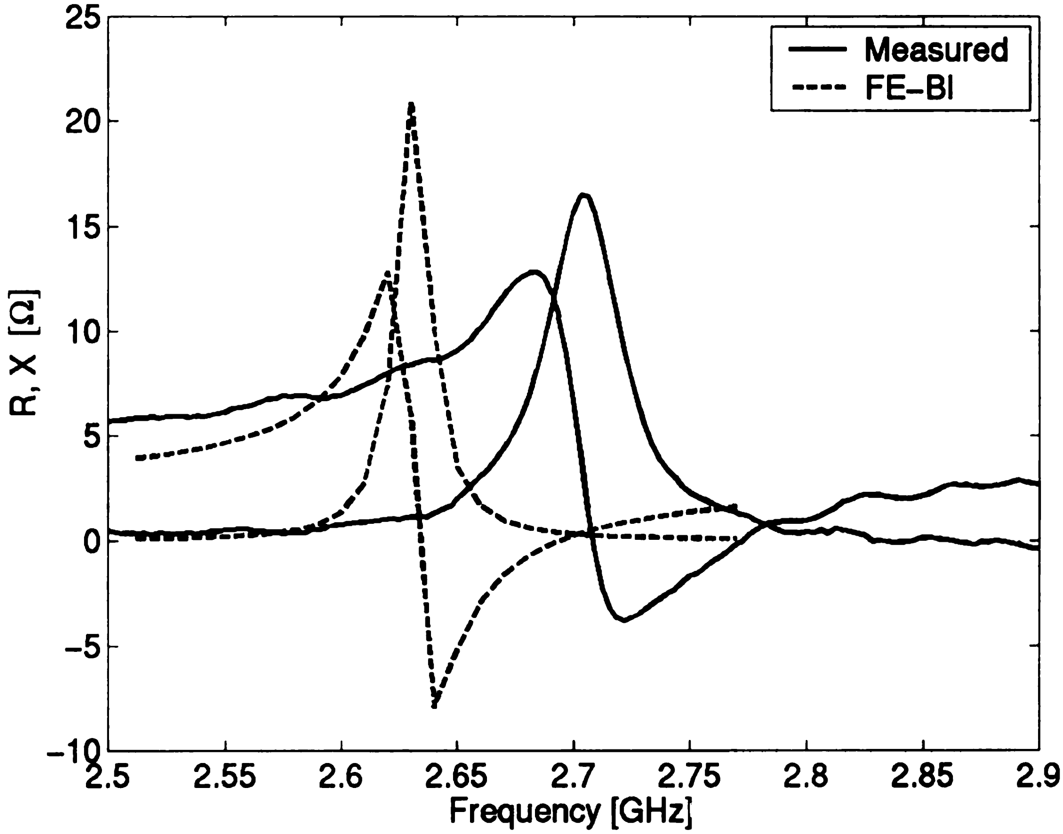

Figure 5.5 Comparison of measured and FE-BI simulation results near the resonant frequency of the dominant mode of the 3.0 x 3.0 cm patch antenna.

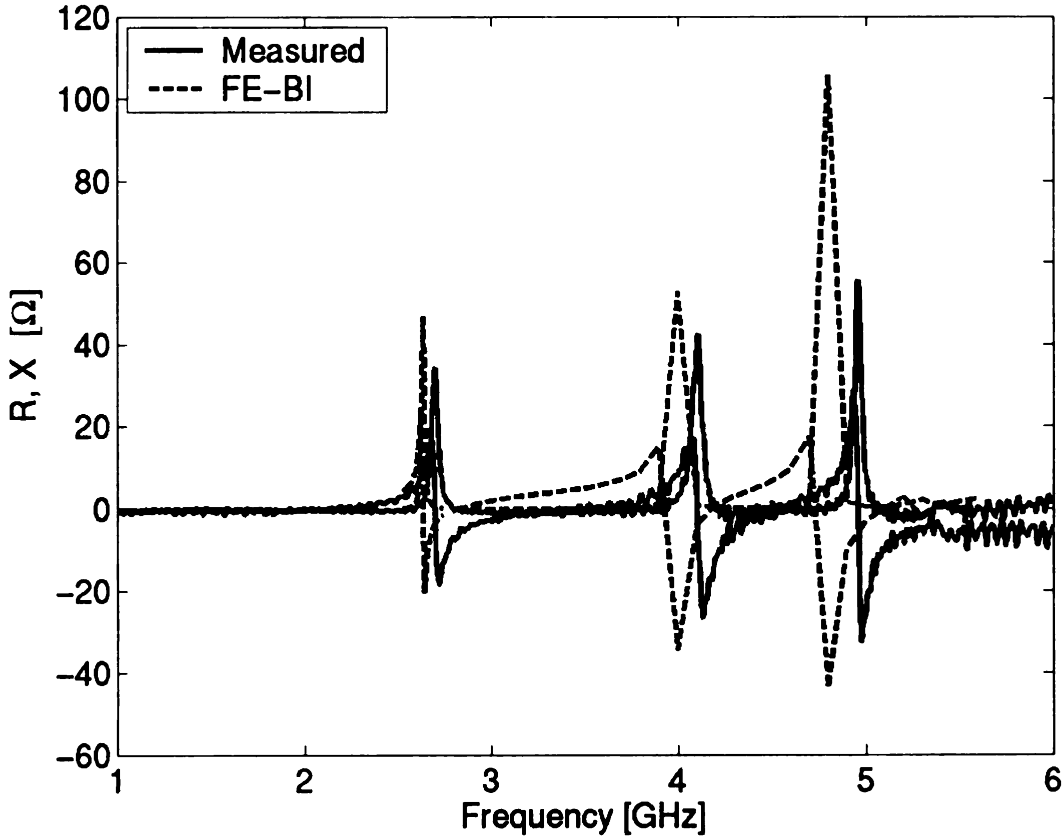

Figure 5.6 Comparison of the measured and FE-BI simulated input impedance of a 4.0 x 3.0 cm patch antenna radiating on a metallic ground plane.

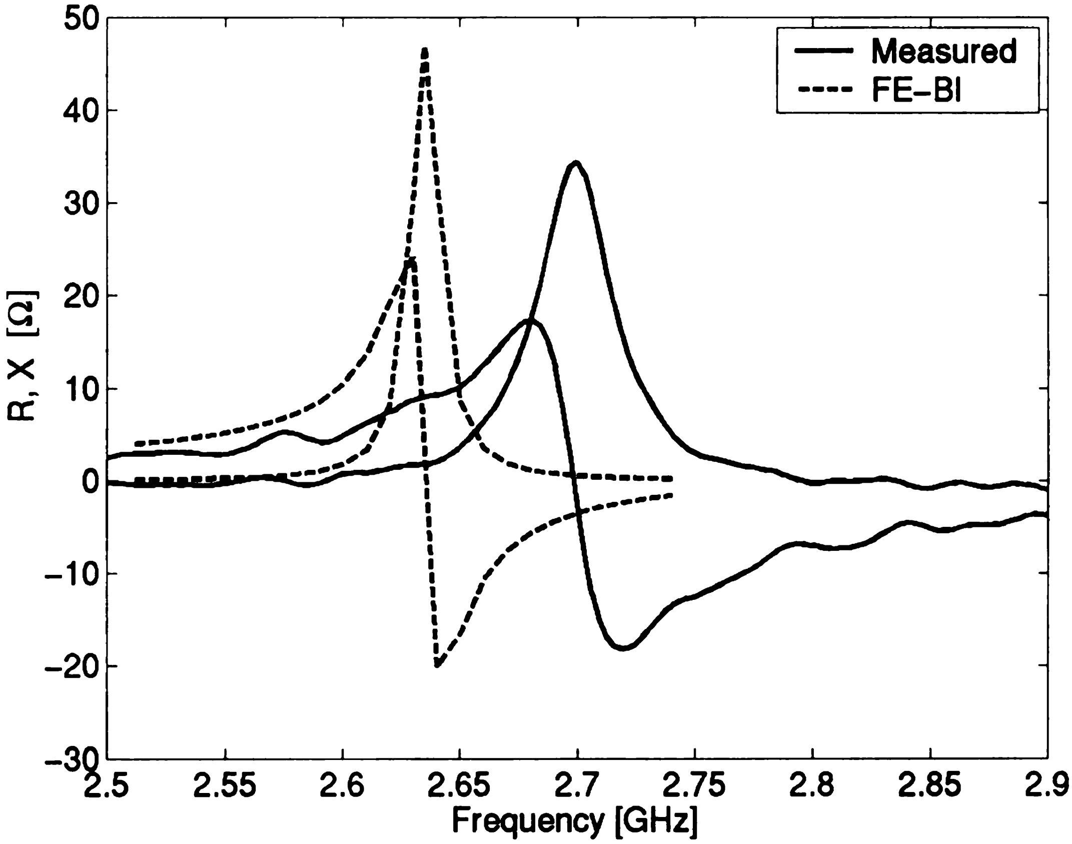

Figure 5.7 Comparison of measured and FE-BI simulation results near the resonant frequency of the dominant mode of the 4.0 x 3.0 cm patch antenna.

5.3.2 Prolate Spheroid

This experiment is designed to measure the effect of surface curvature variation on the input impedance of a patch antenna. In order to simulate an electrically large, perfectly conducting prolate spheroid, the outer surface of a plastic bowl is covered in several layers of aluminum foil. Holes with a diameter of 0.94 cm, large enough for the SMA connector on the antenna feed to pass through, are drilled at consecutive elevational positions along the bowl surface. In order to minimize the possibility of electromagnetic coupling with nearby metallic objects, the measurements are taken with the antenna configuration placed inside an anechoic chamber. The network analyzer is calibrated using an 85032B Type N calibration kit. However, the SMA type connector on the probe feed to the antenna necessitates the use of an Type N-to-SMA adaptor to transition from the male N type cable to the female SMA probe feed on the antenna. The weight of this configuration places considerable strain on the joint at the interface between the semi-rigid coax of the probe feed and the bottom surface of the antenna. As a result, considerable bracing is required at the attachment point of the Type N-to-SMA adaptor on the antenna probe feed. Note that there is considerable buckling of the antenna as it is mounted on the surface of the bowl, despite efforts to minimize its occurrence. The S_{11} of the antenna system, which includes the feed configuration, is measured over the frequency range 1.0 to 6.0 GHz, sampled at 1,600 points. The experimental setup is shown in Figure 5.8.

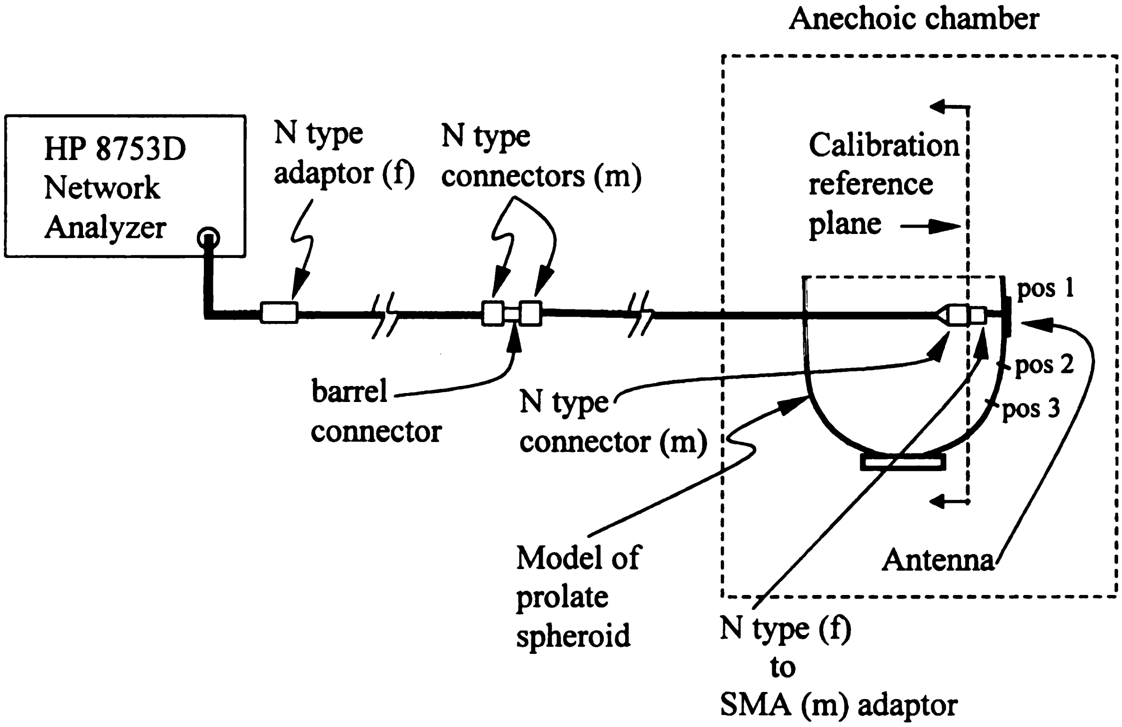

Figure 5.8 Experimental setup for modeling the 3.0 x 3.0 cm patch antenna mounted on a doubly curved platform.

In Figures 5.9, 5.10, and 5.11, the measured input impedance as a function of elevational position for various antenna orientations is presented. In Figure 5.9, the measured input impedance of a 3.0 x 3.0 cm patch excited for axial polarization is given for various elevation angles along a 17.0 x 14.75 cm prolate spheroid. From this plot, the resonant frequency exhibits negligible shifts between the 70^0 and 50^0 positions. Between the 50^0 and 40^0 positions, however, there is a significant shift in the resonant frequency.

In addition, it is observed that the magnitude of the input impedance decreases between the 70^0 and 50^0 positions. However, it increases between the 50^0 and 40^0 positions. In Figure 5.10, the measured input impedance of a 3.0 x 3.0 cm patch excited for azimuthal polarization is given. In this figure, the resonant frequency appears to shift as the surface curvature decreases. Moreover, the magnitude appears to decreases as the surface curvature increases. The measured results for a 45^0 rotated patch at different elevational positions along the bowl are given in Figure 10.11. Between 70^0 and 50^0 the resonant frequency appears to decrease, but between 50^0 and 40^0 it appears to increase, although not by a large amount.

Due to the sensitive nature of these experiments, crudeness of the antenna fabrication techniques, and experimental setup, which give rise to experimental error as discussed previously, it is not possible to draw any concrete conclusions from these measurements. In order to improve upon the reliability and accuracy of any future experiments, improvements in the following areas are needed: fabrication techniques used in the construction of the planar and doubly curved patch antennas, fabrication of the mounting platform used to simulate a doubly curved surface, and the method by which the antenna is mounted on the surface in order to eliminate buckling.

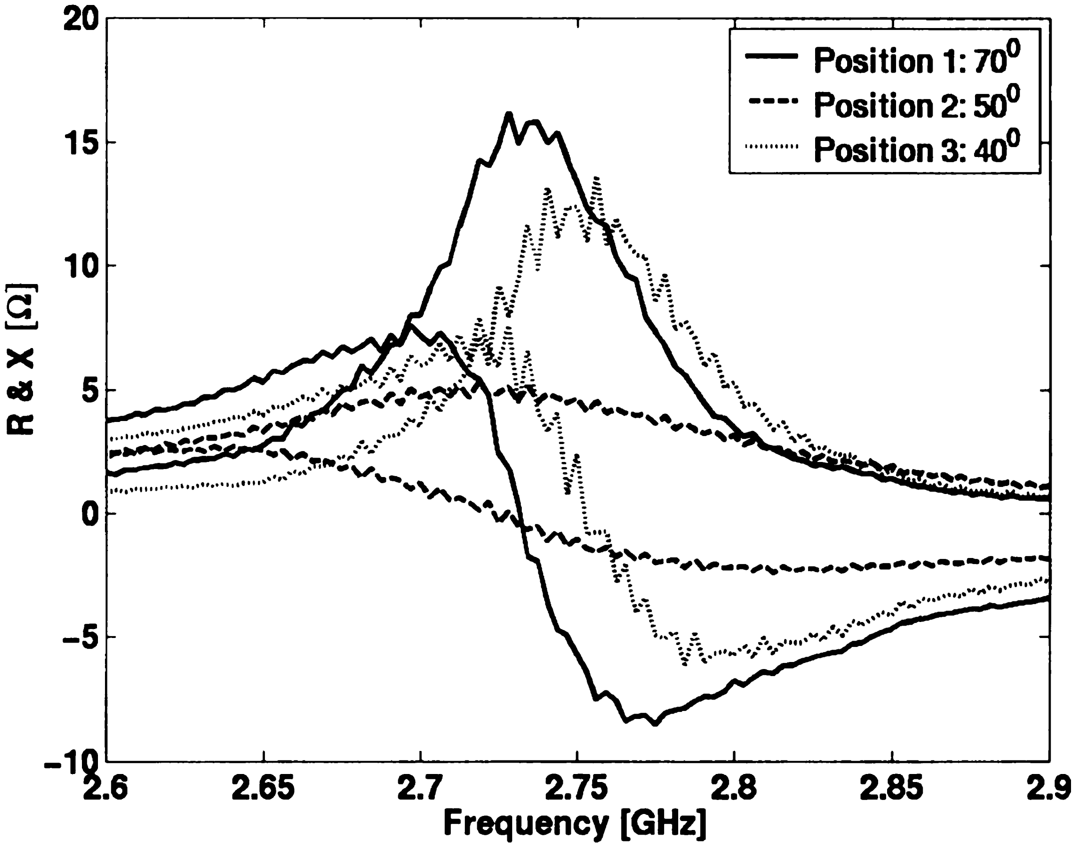

Figure 5.9 Measured input impedance as a function of the elevational position of a 3.0 x 3.0 cm patch antenna excited for axial polarization.

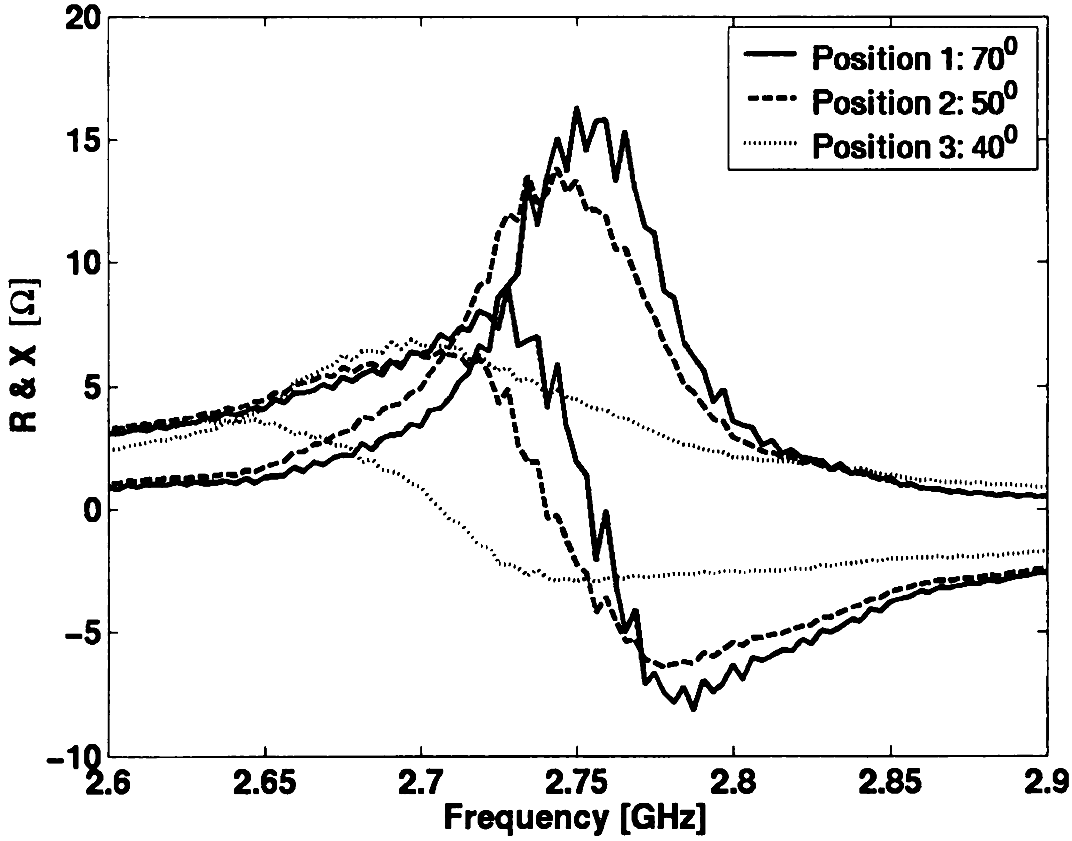

Figure 5.10 Measured input impedance as a function of the elevational position of a 3.0 x 3.0 cm patch antenna excited for azimuthal polarization.

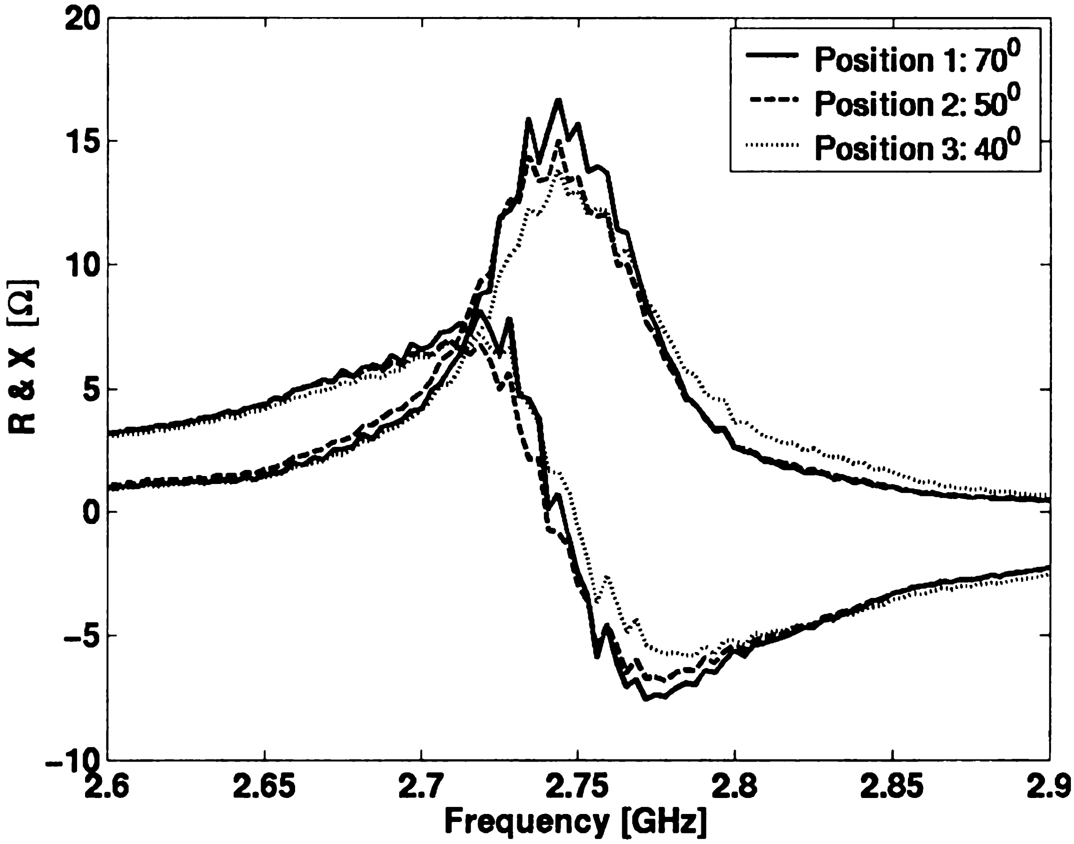

Figure 5.11 Measured input impedance of the 45^0 rotated 3.0 x 3.0 cm patch antenna as a function of elevational position.

CHAPTER 6

CONCLUSION

6.1 Summary

In this dissertation, a new approach to modeling the behavior of conformal antennas on doubly curved convex surfaces utilizing the finite element-boundary integral method has been presented. This method provides a practical alternative to previous methods such as the cavity model and the rigorous integral equation based approaches for analyzing these types of antennas. In this approach, a doubly curved, closed, convex surface is modeled by a canonical prolate spheroid. The advantage of using a prolate spheroid is that it is sufficiently general to represent the curvature of an arbitrary doubly curved surface through the careful selection the azimuthal and elevational radii of curvatures. The PEC surface boundary condition is enforced within a boundary integral whose formulation relies upon an asymptotic prolate spheroidal dyadic Green's function. This approach, which essentially is a hybridization of traditional FE-BI and UTD, is well suited for modeling conformal antennas on electrically large doubly curved surfaces that enforces the Neumann boundary condition. In Chapter 1, a historical overview of the problem of determining the radiation by sources on prolate spheroids was given. It was concluded that exact formulations based upon the eigenfunction expansion method in a prolate spheroidal coordinate system leads to extremely complex eigenfunctions expressed in terms of spheroidal wave functions. Due to their complexity, they are not practical for numerical implementation and are limited by the well-known convergence problems associated with electrically large bodies.

In Chapter 2, an overview of the uniform theory of diffraction was given. In this chapter, the solutions for the canonical problems associated with a magnetic dipole radiating on the surface of an PEC cylinder and on the surface of a PEC sphere were generalized to accommodate a magnetic dipole radiating in the presence of an arbitrary closed convex doubly curved PEC surface. The generalized solution was expressed in terms of surface Fock functions that provide a smooth transition from the shadow boundary to the deep shadow region. Since these functions are well tabulated, they are highly amenable to numerical computation.

In Chapter 3, the generalized dyadic Green's function was specialized to a prolate spheroidal geometry by means of differential geometry. The prolate spheroidal dyadic Green's function physically represents creeping waves that are excited by a magnetic current on the spheroid surface. Since creeping waves traverse the surface along geodesic paths, the mathematical property of torsion that is exhibited by a geodesic curve was discussed. It was shown that, unlike that canonical circular cylinder and sphere, an intrinsic property of the prolate spheroid is that a geodesic lying along a non-meridianal line is characterized by variable torsion. This important property precludes the existence of closed-form analytical expressions for such geodesics. Differential geometry was applied to develop an expression for the geodesic path that can be evaluated by numerical integration. The validation of the Green's function was based on the premise that the magnitude of the prolate spheroid Green's function should approach the magnitude of the circular cylinder Green's function within the quasi-cylindrical midsection of the spheroid. It was found that there was good agreement between the prolate spheroid and circular cylinder Green's function within this region. The magnitudes of the prolate spheroid

Green's function along arbitrary geodesics were presented in order to provide reference data for possible future work and to gain additional insight into the nature of coupling along the spheroid surface. The prolate spheroidal dyadic Green's function was incorporated into the boundary integral. The magnetic current in the aperture was expanded in terms of RWG vector basis functions over triangular regions. With the specification of appropriate volumetric basis functions defined over tetrahedral elements for the cavity region, the finite element-boundary integral equation was formulated.

In Chapter 4, the FE-BI method was used to model the resonant frequency and input impedance of a cavity-backed slot antenna and patch antenna conformal to a prolate spheroid as its surface curvature was varied. The curvature of the spheroid was controlled via the specification of the azimuthal and elevational radii of curvature. Due to the lack of published reference data, the numerical results were verified through comparisons with planar and cylindrical FE-BI results, which have been experimentally confirmed elsewhere. The resonant frequency of the cavity-backed slot antenna for various orientations was modeled. It was found that the resonant frequency of a horizontally oriented slot exhibits a stronger curvature dependence than the resonant frequency of a vertically oriented slot. A slot oriented at 45^0 with respect to the vertical axis exhibits a curvature dependence that lies in between that of the horizontal or vertical orientations. From an examination of the electric structure beneath a patch antenna, it was found that by varying the location of the probe feed, an electric field exhibiting either an azimuthal or axial polarization was excited. The azimuthally polarized electric field was found to exhibit a greater curvature dependence than the axially polarized electric field. A similar result was obtained for a 45^0 rotated patch that was moved along the prolate spheroid from a region of low to a region of high curvature near the tip. For this patch orientation, however, the excited resonant mode split into two resonant modes. The difference in the resonant frequency between the two modes was found to increase with increasing curvature. Finally the far field pattern of a patch radiating in the geometrical optics region of the spheroid was calculated. It was found that the E_φ component exhibits a strong curvature dependence. Specifically, the null of this component shifted and became shallower as the curvature increased. Moreover, the gain of this component was found to increase with the increasing curvature. Conversely, the E_θ component is practically invariant with respect to curvature, except when radiating on the 10 x 8 cm prolate spheroid. On this highly curved surface, the shape of the pattern grew slightly narrower as the curvature increased. The gain of this component, however, remained constant.

In Chapter 5, experimental results for the patch antenna radiating on a planar surface and on a doubly curved surface were given. The FE-BI simulation for a patch radiating on a prolate spheroid was specialized to the planar limit and compared with measured data results. The agreement between the simulated resonant frequency and measured resonant frequency was good. Next, the input impedance of a patch antenna mounted at various points on a bowl, was measured. The bowl provided a crude model of a prolate spheroid surface. Due to the crude nature of this experimental setup, no conclusions could be drawn from these experiments beyond general behavior consistent with a patch radiator.

6.2 Future Studies

Several areas of future study arise from this research. An improvement in the efficiency and speed at which geodesic paths on prolate spheroids are calculated is needed. Such an improvement would provide a significant increase in the ability to analyze complex apertures. Another avenue of possible research is the investigation of the effects of doubly curved surface curvature variation on the coupling between multiple apertures. In this work, a near-to-far field transformation for calculating the radiated field in the geometrical optics region was developed. As an extension of this work, a near-to-far field transformation for the transition and deep shadow region that is amenable to computation could be developed. This would provide a means to study the effects of doubly curved surface curvature variation on the radiation pattern in these regions. Another possible extension of this work is the development of a suitable surface dyadic Green's function to model cavity-backed apertures on coated doubly curved surfaces.

APPENDIX A

EVALUATION OF POTENTIAL SURFACE INTEGRALS OVER TRIANGULAR REGIONS

A.1 1-, 4-, and 7-Point Approximation Weights

A table listing the approximation weights that are used for numerical integration over triangular regions in this work is provided for the convenience of the reader. The values listed in this table are taken from [7]. The triangle integration points are depicted in Figure A.1.1.

Table A.1.1 Approximation weights for numerical integration over triangular regions. Note that $\alpha_1 = 0.0597158717$, $\beta_1 = 0.4701420641$, $\alpha_2 = 0.7974269853$, and $\beta_2 = 0.1012865073$.

Points	Triangular Coordinates $(\varsigma_1, \varsigma_2, \varsigma_3)$	Weights
a	$1/3, 1/3, 1/3$	1.0
a	$1/3, 1/3, 1/3$	$-27/48$
b	$0.6, 0.2, 0.2$	$25/48$
c	$0.2, 0.6, 0.2$	
d	$0.2, 0.2, 0.6$	
a	$1/3, 1/3, 1/3$	0.2250000000
b	$\alpha_1, \beta_1, \beta_1$	0.1323941527
c	$\beta_1, \alpha_1, \beta_1$	
d	$\beta_1, \beta_1, \alpha_1$	
e	$\alpha_2, \beta_2, \beta_2$	0.1259391805
f	$\beta_2, \alpha_2, \beta_2$	
g	$\beta_2, \beta_2, \alpha_2$	

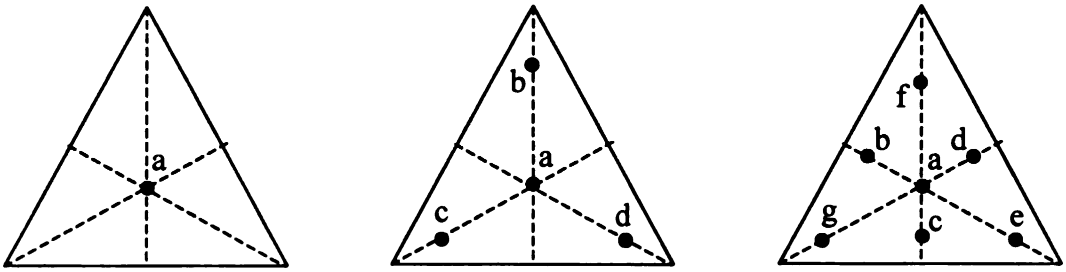

Figure A.1.1 The integration points on a triangular patch for 1-, 4-, and 7-point numerical integration.

A.2 Analytical Formulas

The expressions for integration over triangular regions encountered in the evaluation of boundary integral by the method of moments in this work include singular integrals that must be evaluated analytically. The technique for deriving analytical solutions to these types of integrals is discussed in detail in [39] and, therefore, will not be repeated here.

The form of the integral of a uniform source distribution over a triangular patch is given by

$$\int_T \frac{1}{R} dS' \tag{A.1}$$

where T is the triangular patch region. The analytical solution for integrals of the type (A.1) is given by [39]

$$\int_T \frac{1}{R} dS' = \sum_i \hat{\mathbf{P}}_i^0 \cdot \hat{\mathbf{u}}_i \left\{ P_i^0 \ln\left(\frac{R_i^+ + l_i^+}{R_i^- + l_i^-}\right) - |d| \left[\tan^{-1}\left(\frac{P_i^0 l_i^+}{\left[R_i^0\right]^2 + |d| R_i^+}\right) \right.\right.$$
$$\left.\left. - \tan^{-1}\left(\frac{P_i^0 l_i^-}{\left[R_i^0\right]^2 + |d| R_i^-}\right)\right]\right. \tag{A.2}$$

The form of the integral of a linearly varying source distribution over a triangular patch is given by

$$\int_T \frac{\boldsymbol{\rho}'-\boldsymbol{\rho}}{R} dS' \qquad (A.3)$$

The analytical solution for integrals of the type (A.3) is given by [39]

$$\int_T \frac{\boldsymbol{\rho}'-\boldsymbol{\rho}}{R} dS' = \frac{1}{2}\sum_i \mathbf{u}_i \left[\left(R_i^0\right)^2 \ln\left(\frac{R_i^+ + l_i^+}{R_i^- + l_i^-} \right) + l_i^+ R_i^+ - l_i^- R_i^- \right] \qquad (A.4)$$

The definitions of the various parameters used in (A.2) and (A.4) are listed here for convenience [39].

$$\hat{\mathbf{l}}_i = \frac{\mathbf{r}_i^+ - \mathbf{r}_i^-}{\left|\mathbf{r}_i^+ - \mathbf{r}_i^-\right|} \qquad (A.5)$$

$$\hat{\mathbf{u}}_i = \hat{\mathbf{l}}_i \times \hat{\mathbf{n}} \qquad (A.6)$$

$$R_i^\pm = \left|\mathbf{r} - \mathbf{r}_i^\pm\right| \qquad (A.7)$$

$$l_i^\pm = \left(\boldsymbol{\rho}_i^\pm - \boldsymbol{\rho}\right) \cdot \hat{\mathbf{l}}_i \qquad (A.8)$$

$$\boldsymbol{\rho}_i^\pm = \mathbf{r}_i^\pm - \left(\hat{\mathbf{n}} \cdot \mathbf{r}_i^\pm\right)\hat{\mathbf{n}} \qquad (A.9)$$

$$P_i^0 = \left|\left(\boldsymbol{\rho}_i^+ - \boldsymbol{\rho}\right) \cdot \hat{\mathbf{u}}_i\right| \qquad (A.10)$$

$$\hat{\mathbf{P}}_i^0 = \frac{\left(\boldsymbol{\rho}_i^+ - \boldsymbol{\rho}\right) - l_i^+ \hat{\mathbf{l}}_i}{P_i^0} \qquad (A.11)$$

$$R_i^0 = \sqrt{\left(P_i^0\right)^2 + d^2} \qquad (A.12)$$

$$d = \hat{\mathbf{n}} \cdot \left(\mathbf{r} - \mathbf{r}_i^\pm\right) \qquad (A.13)$$

Referencing Figure A.2.1, $\mathbf{r}'$ is the position vector from the origin to a source point on the triangular patch, $\mathbf{r}$ is a position vector from the origin to an observation point in space, $\boldsymbol{\rho}'$ and $\boldsymbol{\rho}$ are the projections of $\mathbf{r}'$ and $\mathbf{r}$ onto the plane of the patch, $\mathbf{r}_i^\pm$ denotes the position vectors from the origin to the endpoints $l_i^{\pm}$, $\boldsymbol{\rho}_i^{\pm}$ is the projection of the position vectors $\mathbf{r}_i^{\pm}$ onto the patch plane, and d is the height of the observation point above the patch surface. The parameter P_i^0 is the perpendicular distance of the projected observation point in the plane of the patch to the i^{th} edge of the patch. The unit vector $\hat{\mathbf{l}}_i$ is tangent to the i^{th} edge and points in the direction of increasing length. The unit vector $\hat{\mathbf{u}}_i$ is the outward normal vector to the i^{th} edge.

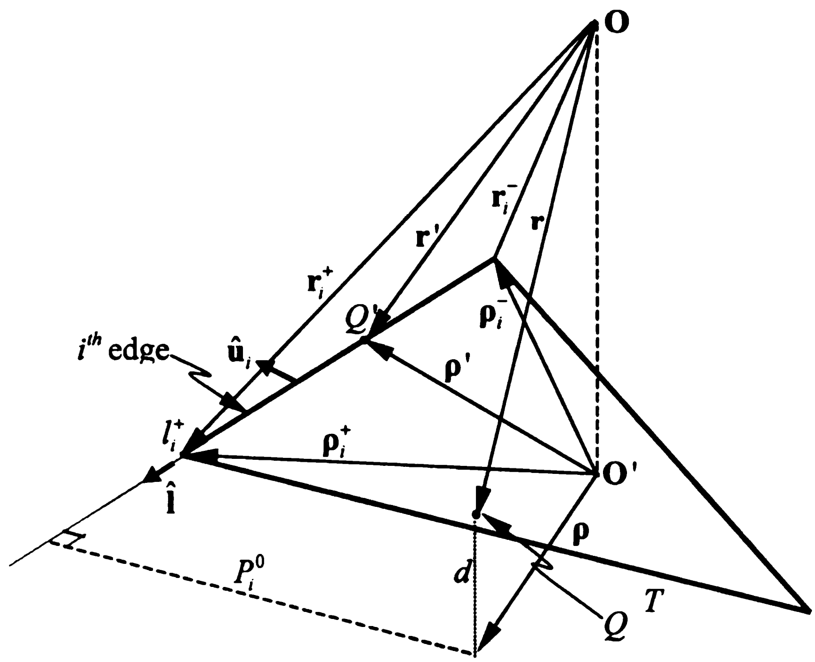

Figure A.2.1 The geometrical parameters associated with the evaluation of potential integrals over the triangular patch T.

APPENDIX B

PARAMETERIZATION OF THE PROLATE SPHEROID UNIT VECTORS IN TERMS OF SPHERICAL COORDINATES

To facilitate the numerical implementation of the prolate spheroidal unit vectors in this work, it is desirable to eliminate their dependence on the hyperbolic terms involving the prolate spheroidal parameters ξ and η and instead express the prolate spheroidal unit vectors in terms of the major and minor semiaxes a and b, respectively, via the usual spherical coordinates θ and φ. The parameters ξ and η are defined as follows [6], [4], [49]

$$\xi = \cosh\Omega \tag{B.1}$$

$$\eta = \cos\theta \tag{B.2}$$

where θ is the usual elevation angle in spherical coordinates and Ω is a constant that defines the surface of a prolate spheroid. The major a and minor b semiaxes are defined in the prolate spheroidal coordinate system by means of (B.1) and (B.2) as follows [31]

$$a = c\cosh\Omega \tag{B.3}$$

$$b = c\sinh\Omega \tag{B.4}$$

where $c = \sqrt{a^2 - b^2}$ and is equivalent to one-half of the interfocal distance.

The expression of the prolate spheroidal unit vectors ($\hat{\boldsymbol{\eta}}, \hat{\boldsymbol{\xi}}, \hat{\boldsymbol{\varphi}}$) in terms of the Cartesian unit vectors ($\hat{\mathbf{x}}, \hat{\mathbf{y}}, \hat{\mathbf{z}}$) is given by [5]

$$\hat{\boldsymbol{\xi}} = \sqrt{\frac{1-\eta^2}{\xi^2-\eta^2}}\xi\cos\varphi\,\hat{\mathbf{x}} + \sqrt{\frac{1-\eta^2}{\xi^2-\eta^2}}\xi\sin\varphi\,\hat{\mathbf{y}} + \sqrt{\frac{\xi^2-1}{\xi^2-\eta^2}}\eta\,\hat{\mathbf{z}} \tag{B.5}$$

Substituting (B.1) and (B.2) into (B.5)

$$\hat{\boldsymbol{\xi}} = \frac{\cosh\Omega}{\sqrt{\cosh^2\Omega-\cos^2\theta}}\sin\theta\cos\varphi\,\hat{\mathbf{x}}+\frac{\cosh\Omega}{\sqrt{\cosh^2\Omega-\cos^2\theta}}\sin\theta\sin\varphi\,\hat{\mathbf{y}}$$
$$+\sqrt{\frac{\cosh^2\Omega-1}{\cosh^2\Omega-\cos^2\theta}}\cos\theta\,\hat{\mathbf{z}} \tag{B.6}$$

Expressing $\cosh\Omega$ in terms of a and c via (B.3) and substituting into (B.6)

$$\hat{\boldsymbol{\xi}} = \frac{a/c}{\sqrt{(a/c)^2-\cos^2\theta}}\sin\theta\cos\varphi\,\hat{\mathbf{x}}+\frac{a/c}{\sqrt{(a/c)^2-\cos^2\theta}}\sin\theta\sin\varphi\,\hat{\mathbf{y}}$$
$$+\sqrt{\frac{(a/c)^2-1}{(a/c)^2-\cos^2\theta}}\cos\theta\,\hat{\mathbf{z}}$$
$$=\frac{a\sin\theta\cos\varphi}{\sqrt{a^2-c^2\cos^2\theta}}\hat{\mathbf{x}}+\frac{a\sin\theta\sin\varphi}{\sqrt{a^2-c^2\cos^2\theta}}\hat{\mathbf{y}}+\sqrt{\frac{a^2-c^2}{a^2-c^2\cos^2\theta}}\cos\theta\,\hat{\mathbf{z}}$$

$$=\frac{a\sin\theta\cos\varphi}{\sqrt{a^2-c^2\cos^2\theta}}\hat{\mathbf{x}}+\frac{a\sin\theta\sin\varphi}{\sqrt{a^2-c^2\cos^2\theta}}\hat{\mathbf{y}}+\sqrt{\frac{a^2-c^2}{a^2-c^2\cos^2\theta}}\cos\theta\,\hat{\mathbf{z}}$$

$$\Rightarrow\ \hat{\boldsymbol{\xi}} = \frac{1}{\sqrt{a^2\sin^2\theta+b^2\cos^2\theta}}\left(a\sin\theta\cos\varphi\hat{\mathbf{x}}+a\sin\theta\sin\varphi\hat{\mathbf{y}}+b\cos\theta\,\hat{\mathbf{z}}\right) \tag{B.7}$$

Following the same procedure for $\hat{\boldsymbol{\eta}}$, beginning with [6]

$$\hat{\boldsymbol{\eta}} = -\sqrt{\frac{\xi^2-1}{\xi^2-\eta^2}}\eta\cos\varphi\,\hat{\mathbf{x}}-\sqrt{\frac{\xi^2-1}{\xi^2-\eta^2}}\eta\sin\varphi\,\hat{\mathbf{y}}+\sqrt{\frac{1-\eta^2}{\xi^2-\eta^2}}\xi\,\hat{\mathbf{z}} \tag{B.8}$$

substitute (B.1) and (B.2) into (B.8) and simplifying

$$\hat{\boldsymbol{\eta}} = \sqrt{\frac{(a/c)^2-1}{(a/c)^2-\cos^2\theta}}\cos\theta\cos\varphi\,\hat{\mathbf{x}}-\sqrt{\frac{(a/c)^2-1}{(a/c)^2-\cos^2\theta}}\cos\theta\sin\varphi\,\hat{\mathbf{y}}$$
$$+\frac{a/c}{\sqrt{(a/c)^2-\cos^2\theta}}\sin\theta\,\hat{\mathbf{z}}$$
$$=-\sqrt{\frac{a^2-c^2}{a^2-c^2\cos\theta}}\cos\theta\cos\varphi\hat{\mathbf{x}}-\sqrt{\frac{a^2-c^2}{a^2-c^2\cos^2\theta}}\cos\theta\sin\varphi\hat{\mathbf{y}}$$

$$+\frac{a\sin\theta}{\sqrt{a^2-c^2\cos^2\theta}}\hat{\mathbf{z}}$$

$$\Rightarrow\ \hat{\boldsymbol{\eta}}=\frac{1}{\sqrt{a^2\sin^2\theta+b^2\cos^2\theta}}\left(-b\cos\theta\cos\varphi\,\hat{\mathbf{x}}-b\cos\theta\sin\varphi\,\hat{\mathbf{y}}+a\sin\theta\,\hat{\mathbf{z}}\right) \quad \text{(B.9)}$$

Finally, the azimuthally directed unit vector $\hat{\boldsymbol{\varphi}}$ is the same in prolate spheroidal and spherical coordinates and is given by

$$\hat{\boldsymbol{\varphi}}=-\sin\varphi\,\hat{\mathbf{x}}+\cos\varphi\,\hat{\mathbf{y}} \quad \text{(B.10)}$$

Conversely, the Cartesian unit vectors may be expressed in terms of prolate spheroidal unit vectors. Beginning with [5]

$$\hat{\mathbf{x}}=\sqrt{\frac{1-\eta^2}{\xi^2-\eta^2}}\xi\cos\varphi\,\hat{\boldsymbol{\xi}}-\sqrt{\frac{\xi^2-1}{\xi^2-\eta^2}}\eta\cos\varphi\,\hat{\boldsymbol{\eta}}-\sin\varphi\,\hat{\boldsymbol{\varphi}} \quad \text{(B.11)}$$

Following the same procedure as before, substitute (B.1) and (B.2) into (B.11) and simplify which results in

$$\hat{\mathbf{x}}=\sqrt{\frac{1-\cos^2\theta}{\cosh^2\Omega-\cos^2\theta}}\cosh\Omega\cos\varphi\,\hat{\boldsymbol{\xi}}-\sqrt{\frac{\cosh^2\Omega-1}{\cosh^2\Omega-\cos^2\theta}}\cos\theta\cos\varphi\hat{\boldsymbol{\eta}}-\sin\varphi\,\hat{\boldsymbol{\varphi}} \quad \text{(B.12)}$$

Expressing $\cosh\Omega$ in terms of a and c as before leads to

$$\hat{\mathbf{x}}=\frac{a\sin\theta\cos\varphi}{\sqrt{a^2-c^2\cos^2\theta}}\hat{\boldsymbol{\xi}}+\sqrt{\frac{a^2-c^2}{a^2-c^2\cos\theta}}\cos\theta\cos\varphi\,\hat{\boldsymbol{\eta}}-\sin\varphi\,\hat{\boldsymbol{\varphi}} \quad \text{(B.13)}$$

After further simplification by means of the Pythagorean relationship between a, b, and c the final expression for $\hat{\mathbf{x}}$ is obtained

$$\hat{\mathbf{x}}=\frac{1}{\sqrt{a^2\sin^2\theta+b^2\cos^2\theta}}\left(a\sin\theta\cos\varphi\,\hat{\boldsymbol{\xi}}-b\cos\theta\cos\varphi\,\hat{\boldsymbol{\eta}}-\sin\varphi\,\hat{\boldsymbol{\varphi}}\right) \quad \text{(B.14)}$$

In the same manner, $\hat{\mathbf{y}}$ initially is given by [6]

$$\hat{\mathbf{y}} = \sqrt{\frac{1-\eta^2}{\xi^2-\eta^2}}\xi \sin\varphi \hat{\boldsymbol{\xi}} - \sqrt{\frac{\xi^2-1}{\xi^2-\eta^2}}\eta \sin\varphi \hat{\boldsymbol{\eta}} + \cos\varphi \hat{\boldsymbol{\varphi}} \tag{B.15}$$

which, upon the substitution of (B.1) and (B.2), and simplification becomes

$$\hat{\mathbf{y}} = \frac{1}{\sqrt{a^2 \sin^2\theta + b^2 \cos^2\theta}}\left(a \sin\theta \sin\varphi \hat{\boldsymbol{\xi}} - b\cos\theta \sin\varphi \hat{\boldsymbol{\eta}} + \cos\varphi \hat{\boldsymbol{\varphi}}\right) \tag{B.16}$$

The unit vector $\hat{\mathbf{z}}$ is written initially as [6]

$$\hat{\mathbf{z}} = \sqrt{\frac{\xi^2-1}{\xi^2-\eta^2}}\eta \hat{\boldsymbol{\xi}} + \sqrt{\frac{1-\eta^2}{\xi^2-\eta^2}}\xi \hat{\boldsymbol{\eta}} \tag{B.17}$$

which, by the same procedure, becomes

$$\hat{\mathbf{z}} = \frac{1}{\sqrt{a^2 \sin^2\theta + b^2 \cos^2\theta}}\left(b \cos\theta \hat{\boldsymbol{\xi}} + a \sin\theta \hat{\boldsymbol{\eta}}\right) \tag{B.18}$$

Summarizing, the prolate spheroidal unit vectors parameterized in terms of the spherical coordinates θ and φ and expressed in terms of the Cartesion unit vectors are given by

$$\hat{\boldsymbol{\xi}} = \frac{1}{\sqrt{a^2 \sin^2\theta + b^2 \cos^2\theta}}\left(a \sin\theta \cos\varphi \hat{\mathbf{x}} + a \sin\theta \sin\varphi \hat{\mathbf{y}} + b\cos\theta \hat{\mathbf{z}}\right) \tag{B.19}$$

$$\hat{\boldsymbol{\eta}} = \frac{1}{\sqrt{a^2 \sin^2\theta + b^2 \cos^2\theta}}\left(-b \cos\theta \cos\varphi \hat{\mathbf{x}} - b\cos\theta \sin\varphi \hat{\mathbf{y}} + a\sin\theta \hat{\mathbf{z}}\right) \tag{B.20}$$

$$\hat{\boldsymbol{\varphi}} = -\sin\varphi \hat{\mathbf{x}} + \cos\varphi \hat{\mathbf{y}} \tag{B.21}$$

The Cartesian unit vectors, parameterized in terms of the spherical coordinates θ and φ and expressed in terms of the prolate spheroidal unit vectors, are given by

$$\hat{\mathbf{x}} = \frac{1}{\sqrt{a^2 \sin^2\theta + b^2 \cos^2\theta}}\left(a \sin\theta \cos\varphi \hat{\boldsymbol{\xi}} - b\cos\theta \cos\varphi \hat{\boldsymbol{\eta}} - \sin\varphi \hat{\boldsymbol{\varphi}}\right) \tag{B.22}$$

$$\hat{\mathbf{y}} = \frac{1}{\sqrt{a^2 \sin^2\theta + b^2 \cos^2\theta}}\left(a \sin\theta \sin\varphi \hat{\boldsymbol{\xi}} - b\cos\theta \sin\varphi \hat{\boldsymbol{\eta}} + \cos\varphi \hat{\boldsymbol{\varphi}}\right) \tag{B.23}$$

$$\hat{\mathbf{z}} = \frac{1}{\sqrt{a^2 \sin^2\theta + b^2 \cos^2\theta}} \left(b\cos\theta\,\hat{\boldsymbol{\xi}} + a\sin\theta\,\hat{\boldsymbol{\eta}} \right) \tag{B.24}$$

For the case of a sphere where $a = b$

$$\begin{aligned} \hat{\boldsymbol{\xi}} &= \frac{1}{\sqrt{a^2 \sin^2\theta + b^2 \cos^2\theta}} \left(a\sin\theta\cos\varphi\,\hat{\mathbf{x}} + a\sin\theta\sin\varphi\,\hat{\mathbf{y}} + b\cos\theta\,\hat{\mathbf{z}} \right) \\ &= \sin\theta\cos\varphi\,\hat{\mathbf{x}} + \sin\theta\sin\varphi\,\hat{\mathbf{y}} + \cos\theta\,\hat{\mathbf{z}} = \hat{\mathbf{R}} \end{aligned} \tag{B.25}$$

$$\begin{aligned} \hat{\boldsymbol{\eta}} &= \frac{1}{\sqrt{a^2 \sin^2\theta + b^2 \cos^2\theta}} \left(-b\cos\theta\cos\varphi\,\hat{\mathbf{x}} - b\cos\theta\sin\varphi\,\hat{\mathbf{y}} + a\sin\theta\,\hat{\mathbf{z}} \right) \\ &= -\cos\theta\cos\varphi\,\hat{\mathbf{x}} - \cos\theta\sin\varphi\,\hat{\mathbf{y}} + \sin\theta\,\hat{\mathbf{z}} = -\hat{\boldsymbol{\theta}} \end{aligned} \tag{B.26}$$

$$\hat{\boldsymbol{\varphi}} = \hat{\boldsymbol{\varphi}} \tag{B.27}$$

The Cartesian unit vectors expressed in terms of the prolate spheroidal unit vectors now become

$$\begin{aligned} \hat{\mathbf{x}} &= \frac{1}{\sqrt{a^2 \sin^2\theta + b^2 \cos^2\theta}} \left(a\sin\theta\cos\varphi\,\hat{\boldsymbol{\xi}} - b\cos\theta\cos\varphi\,\hat{\boldsymbol{\eta}} - \sin\varphi\,\hat{\boldsymbol{\varphi}} \right) \\ &= \sin\theta\cos\varphi\,\hat{\mathbf{R}} + \cos\theta\cos\varphi\,\hat{\boldsymbol{\theta}} - \sin\varphi\,\hat{\boldsymbol{\varphi}} \end{aligned} \tag{B.28}$$

$$\begin{aligned} \hat{\mathbf{y}} &= \frac{1}{\sqrt{a^2 \sin^2\theta + b^2 \cos^2\theta}} \left(a\sin\theta\sin\varphi\,\hat{\boldsymbol{\xi}} - b\cos\theta\sin\varphi\,\hat{\boldsymbol{\eta}} + \cos\varphi\,\hat{\boldsymbol{\varphi}} \right) \\ &= \sin\theta\sin\varphi\,\hat{\mathbf{R}} + \cos\theta\sin\varphi\,\hat{\boldsymbol{\theta}} + \cos\varphi\,\hat{\boldsymbol{\varphi}} \end{aligned} \tag{B.29}$$

$$\begin{aligned} \hat{\mathbf{z}} &= \frac{1}{\sqrt{a^2 \sin^2\theta + b^2 \cos^2\theta}} \left(b\cos\theta\,\hat{\boldsymbol{\xi}} + a\sin\theta\,\hat{\boldsymbol{\eta}} \right) \\ &= \cos\theta\,\hat{\mathbf{R}} - \sin\theta\,\hat{\boldsymbol{\theta}} \end{aligned} \tag{B.30}$$

which express the Cartesian unit vectors in terms of the spherical coordinate unit vectors.

APPENDIX C

DERIVATION OF THE EXACT EIGENFUNCTION SERIES FOR THE CIRCULAR CYLINDER DYADIC GREEN'S FUNCTION

The second-kind electric dyadic Green's function for the infinite perfectly conducting circular cylinder is derived most expediently from the free-space magnetic dyadic Green's function $\overline{\overline{\mathbf{G}}}_{m0}$. Beginning with the dyadic form of the vector wave equation, expressed in terms of the free-space electric dyadic Green's function, a relationship between the free-space electric dyadic $\overline{\overline{G}}_{e0}$ and the free-space magnetic dyadic Green's function $\overline{\overline{\mathbf{G}}}_{m0}$ may be derived [10]. Beginning with

$$\nabla \times \nabla \times \overline{\overline{\mathbf{G}}}_{e0}(\mathbf{R}|\mathbf{R}') - k^2 \overline{\overline{\mathbf{G}}}_{e0}(\mathbf{R}|\mathbf{R}') = \overline{\overline{\mathbf{I}}}\delta(\mathbf{R}-\mathbf{R}') \tag{C.1}$$

where $\mathbf{R}$ and $\mathbf{R}'$ are three-dimensional position vectors to the field and source points, respectively. Employing the relationship

$$\nabla \times \overline{\overline{\mathbf{G}}}_{e0}(\mathbf{R}|\mathbf{R}') = \overline{\overline{\mathbf{G}}}_{m0}(\mathbf{R}|\mathbf{R}') \tag{C.2}$$

results in

$$\nabla \times \overline{\overline{\mathbf{G}}}_{m0}(\mathbf{R}|\mathbf{R}') = \overline{\overline{\mathbf{I}}}\delta(\mathbf{R}-\mathbf{R}') + k^2 \overline{\overline{\mathbf{G}}}_{e0}(\mathbf{R}|\mathbf{R}') \tag{C.3}$$

Since $\overline{\overline{\mathbf{G}}}_{m0}$ is piecewise continuous with a discontinuity at $\rho = 0$, it may be decomposed into two components

$$\overline{\overline{\mathbf{G}}}_{m0} = \overline{\overline{\mathbf{G}}}_{m0}^{+} U(\rho - \rho') + \overline{\overline{\mathbf{G}}}_{m0}^{-} U(\rho' - \rho) \tag{C.4}$$

where the unit step functions are defined by

$$U(\rho - \rho') = \begin{cases} 1, & \rho > \rho' \\ 0, & \rho < \rho' \end{cases}$$

$$U(\rho'-\rho)=\begin{cases}1, & \rho<\rho' \\ 0, & \rho>\rho'\end{cases} \tag{C.5}$$

Taking the curl of (C.4) and invoking an appropriate dyadic identity from [10] yields

$$\begin{aligned}\nabla\times\overline{\overline{\mathbf{G}}}_{m0} &= \left(\nabla\times\overline{\overline{\mathbf{G}}}_{m0}^{+}\right)U(\rho-\rho')+\nabla U(\rho-\rho')\times\overline{\overline{\mathbf{G}}}_{m0}^{+} \\ &+\left(\nabla\times\overline{\overline{\mathbf{G}}}_{m0}^{-}\right)U(\rho'-\rho)+\nabla U(\rho'-\rho)\times\overline{\overline{\mathbf{G}}}_{m0}^{-}\end{aligned} \tag{C.6}$$

From the theory of distributions, the following relationships can be derived [10,49]

$$\begin{aligned}\nabla U(\rho-\rho') &= \hat{\boldsymbol{\rho}}\delta(\rho-\rho') \\ \nabla U(\rho'-\rho) &= -\hat{\boldsymbol{\rho}}\delta(\rho-\rho')\end{aligned} \tag{C.7}$$

Substituting (C.7) into (C.6) gives

$$\begin{aligned}\nabla\times\overline{\overline{\mathbf{G}}}_{m0} &= \left(\nabla\times\overline{\overline{\mathbf{G}}}_{mo}^{+}\right)U(\rho-\rho')+\left(\nabla\times\overline{\overline{\mathbf{G}}}_{m0}^{-}\right)U(\rho'-\rho) \\ &+\hat{\boldsymbol{\rho}}\delta(\rho-\rho')\times\left(\overline{\overline{\mathbf{G}}}_{m0}^{+}-\overline{\overline{\mathbf{G}}}_{m0}^{-}\right)\end{aligned} \tag{C.8}$$

The boundary condition on tangential magnetic fields across an interface may be expressed in dyadic form as

$$\hat{\mathbf{n}}\times\left(\overline{\overline{\mathbf{G}}}_{m0}^{+}-\overline{\overline{\mathbf{G}}}_{m0}^{-}\right)=\overline{\overline{\mathbf{I}}}_{s}\delta(\mathbf{r}-\mathbf{r}') \tag{C.9}$$

where $\overline{\overline{\mathbf{I}}}_s=\overline{\overline{\mathbf{I}}}-\hat{\mathbf{n}}\hat{\mathbf{n}}$ is the two-dimensional idem factor, $\overline{\overline{\mathbf{I}}}$ is the three-dimensional idem factor, $\mathbf{r}$, and $\mathbf{r}'$ are position vectors from the origin to the field point and source point on the surface, respectively, and $\hat{\mathbf{n}}$ is the outward unit normal vector to the interface. Evaluating (C.9) in cylindrical coordinates yields

$$\hat{\boldsymbol{\rho}}\times\left(\overline{\overline{\mathbf{G}}}_{m0}^{+}-\overline{\overline{G}}_{m0}^{-}\right)=\left(\overline{\overline{\mathbf{I}}}-\hat{\boldsymbol{\rho}}\hat{\boldsymbol{\rho}}\right)\delta(\varphi-\varphi')\delta(z-z') \tag{C.10}$$

and rewriting (C.8) in terms of (C.10) yields

$$\nabla\times\overline{\overline{\mathbf{G}}}_{m0}=\left(\nabla\times\overline{\overline{\mathbf{G}}}_{mo}^{+}\right)U(\rho-\rho')+\left(\nabla\times\overline{\overline{\mathbf{G}}}_{m0}^{-}\right)U(\rho'-\rho)$$
$$+\left(\overline{\overline{\mathbf{I}}}-\hat{\boldsymbol{\rho}}\hat{\boldsymbol{\rho}}\right)\delta(\varphi-\varphi')\delta(z-z')\delta(\rho-\rho') \tag{C.11}$$

Rewriting (C.3) in terms of (C.11) and solving for $\overline{\overline{G}}_{e0}$

$$\left(\nabla\times\overline{\overline{\mathbf{G}}}_{mo}^{+}\right)U(\rho-\rho')+\left(\nabla\times\overline{\overline{\mathbf{G}}}_{m0}^{-}\right)U(\rho'-\rho)+\left(\overline{\overline{\mathbf{I}}}-\hat{\boldsymbol{\rho}}\hat{\boldsymbol{\rho}}\right)\delta(\varphi-\varphi')\delta(z-z')\delta(\rho-\rho')$$
$$=\overline{\overline{\mathbf{I}}}\delta(\mathbf{R}-\mathbf{R}')+k^2\overline{\overline{\mathbf{G}}}_{e0}$$
$$\Rightarrow\left(\nabla\times\overline{\overline{\mathbf{G}}}_{mo}^{+}\right)U(\rho-\rho')+\left(\nabla\times\overline{\overline{\mathbf{G}}}_{m0}^{-}\right)U(\rho'-\rho)+\left(\overline{\overline{\mathbf{I}}}-\hat{\boldsymbol{\rho}}\hat{\boldsymbol{\rho}}\right)\delta(\varphi-\varphi')\delta(z-z')\delta(\rho-\rho')$$
$$=\overline{\overline{\mathbf{I}}}\delta(\varphi-\varphi')\delta(z-z')\delta(\rho-\rho')+k^2\overline{\overline{G}}_{e0}$$

$$\Rightarrow\ \overline{\overline{\mathbf{G}}}_{e0}(\mathbf{R}|\mathbf{R}')=\frac{-1}{k^2}\left[\left(\nabla\times\overline{\overline{G}}_{m0}^{+}\right)U(\rho-\rho')+\left(\nabla\times\overline{\overline{G}}_{m0}^{-}\right)U(\rho'-\rho)\right.$$
$$\left.-\hat{\boldsymbol{\rho}}\hat{\boldsymbol{\rho}}\delta(\mathbf{R}-\mathbf{R}')\right] \tag{C.12}$$

Thus, (C.12) expresses the free-space electric dyadic Green's function $\overline{\overline{\mathbf{G}}}_{e0}$ in terms of the free-space magnetic dyadic Green's function $\overline{\overline{\mathbf{G}}}_{m0}$ which satisfies the dyadic form of the wave equation

$$\nabla\times\nabla\times\overline{\overline{G}}_{m0}(\mathbf{R}|\mathbf{R}')-k^2\overline{\overline{G}}_{m0}(\mathbf{R}|\mathbf{R}')=\nabla\times\left[\overline{\overline{\mathbf{I}}}\delta(\mathbf{R}-\mathbf{R}')\right] \tag{C.13}$$

At this point, the method of Ohm-Rayleigh is employed whereby the source term in (C.13) is expanded in the orthogonal basis of solenoidal vector wave functions $\mathbf{M}$ and $\mathbf{N}$ and manipulated according to the procedure in [10] resulting in

$$\overline{\overline{G}}_{m0}^{\pm}(\mathbf{R}|\mathbf{R}')=\frac{-jk}{8\pi}\int_{-\infty}^{\infty}dk_z\sum_{n=-\infty}^{\infty}\frac{1}{k_\rho^2}\begin{cases}\mathbf{N}^{(2)}(k_z)\mathbf{M}'(-k_z)+\mathbf{M}^{(2)}(k_z)\mathbf{N}'(-k_z), & \rho>\rho'\\ \mathbf{N}(k_z)\mathbf{M}^{(2)}{}'(-k_z)+\mathbf{M}(k_z)\mathbf{N}^{(2)}{}'(-k_z), & \rho<\rho'\end{cases} \tag{C.14}$$

where the vector wave functions are given by

$$\mathbf{M}^{(2)}(k_z)=\left\{\frac{jn}{x}H_n^{(2)}(x)\hat{\boldsymbol{\rho}}-H_n^{(2)'}(x)\hat{\boldsymbol{\varphi}}\right\}k_\rho e^{jn\varphi}e^{jk_z z} \tag{C.15}$$

$$\mathbf{M}'(-k_z)=\left\{\frac{-jn}{x}J_n(x')\hat{\boldsymbol{\rho}}'-J_n'(x')\hat{\boldsymbol{\varphi}}'\right\}k_\rho e^{-jn\varphi'}e^{-jk_z z'} \tag{C.16}$$

$$\mathbf{N}^{(2)}(k_z)=\left\{jk_z H_n^{(2)'}(x)\hat{\boldsymbol{\rho}}-\frac{nk_z}{x}H_n^{(2)}(x)\hat{\boldsymbol{\varphi}}+H_n^{(2)}(x)k_\rho\hat{\mathbf{z}}\right\}\frac{k_\rho}{k}e^{jn\varphi}e^{jk_z z} \tag{C.17}$$

$$\mathbf{N}'(k_z)=\left\{-jk_z J_n'(x')\hat{\boldsymbol{\rho}}'-\frac{nk_z}{x'}J_n(x')\hat{\boldsymbol{\varphi}}'+J_n(x')k_\rho\hat{\mathbf{z}}'\right\}\frac{k_\rho}{k}e^{-jn\varphi'}e^{-jk_z z'} \tag{C.18}$$

where $x=k_\rho\rho$, $x'=k_\rho\rho'$, and $H_n^{(2)}(x)$ is the second-kind Hankel function representing outgoing cylindrical waves.

Taking the curl of each component (i.e. $\overline{\overline{\mathbf{G}}}_{m0}^{+}$ or $\overline{\overline{\mathbf{G}}}_{m0}^{-}$) and exploiting the symmetrical property of the vector eigenfunctions

$$\nabla\times\mathbf{M}=k\mathbf{N}$$

$$\nabla\times\mathbf{N}=k\mathbf{M} \tag{C.19}$$

the following expressions are obtained

$$\nabla\times\overline{\overline{\mathbf{G}}}_{m0}^{+}=\frac{-jk^2}{8\pi}\int_{-\infty}^{\infty}dk_z\sum_{n=-\infty}^{\infty}\frac{1}{k_\rho^2}\left[\mathbf{M}^{(2)}(k_z)\mathbf{M}'(-k_z)+\mathbf{N}^{(2)}(k_z)\mathbf{N}'(-k_z)\right],\quad \rho>\rho' \tag{C.20}$$

$$\nabla\times\overline{\overline{\mathbf{G}}}_{m0}^{-}=\frac{-jk^2}{8\pi}\int_{-\infty}^{\infty}dk_z\sum_{n=-\infty}^{\infty}\frac{1}{k_\rho^2}\left[\mathbf{M}(k_z)\mathbf{M}^{(2)}{}'(-k_z)+\mathbf{N}^{(2)}(k_z)\mathbf{N}^{(2)}{}'(-k_z)\right],\quad \rho<\rho' \tag{C.21}$$

Substituting (C.20) and (C.21) into (C.12) to obtain the free-space electric dyadic Green's function $\overline{\overline{G}}_{e0}$ in terms of the vector wave functions

$$\begin{aligned}\overline{\overline{G}}_{e0}(\mathbf{R}|\mathbf{R}')&=\frac{-1}{k^2}\hat{\boldsymbol{\rho}}\hat{\boldsymbol{\rho}}\delta(\mathbf{R}-\mathbf{R}')\\&+\frac{-j}{8\pi}\int_{-\infty}^{\infty}dk_z\sum_{n=-\infty}^{\infty}\frac{1}{k_\rho^2}\begin{cases}\mathbf{M}^{(2)}(k_z)\mathbf{M}'(-k_z)+\mathbf{N}^{(2)}(k_z)\mathbf{N}(-k_z), & \rho>\rho'\\ \mathbf{M}^{(2)}(k_z)\mathbf{M}^{(2)}{}'(-k_z)+\mathbf{N}(k_z)\mathbf{N}^{(2)}{}'(-k_z), & \rho<\rho'\end{cases}\end{aligned} \tag{C.22}$$

The second-kind electric dyadic Green's function may now be obtained by exploiting the principle of scattering superposition

$$\overline{\overline{\mathbf{G}}}_{e2}(\mathbf{R}|\mathbf{R}') = \overline{\overline{\mathbf{G}}}_{e0}(\mathbf{R}|\mathbf{R}') + \overline{\overline{\mathbf{G}}}_{2s}(\mathbf{R}|\mathbf{R}') \tag{C.23}$$

where $\overline{\overline{\mathbf{G}}}_{2s}$ is proposed such that when it is added to $\overline{\overline{\mathbf{G}}}_{e0}$, the composite function $\overline{\overline{\mathbf{G}}}_{e2}$ will satisfy the Neumann boundary condition $\hat{\boldsymbol{\rho}} \times \nabla \times \overline{\overline{\mathbf{G}}}_{e2} = 0$ on the cylinder surface $\rho = a$ and the Sommerfeld radiation condition at infinity. Hence, the following expression for $\overline{\overline{\mathbf{G}}}_{2s}$ is proposed

$$\overline{\overline{G}}_{2s}(\mathbf{R}|\mathbf{R}') = \frac{-j}{8\pi} \int_{-\infty}^{\infty} dk_z \sum_{n=-\infty}^{\infty} \frac{1}{k_\rho^2} \left[a_n \mathbf{M}^{(2)}(k_z) \mathbf{M}^{(2)}{}'(-k_z) + b_n \mathbf{N}^{(2)}(k_z) \mathbf{N}^{(2)}{}'(-k_z) \right] \tag{C.24}$$

After enforcing the Neumann boundary condition on the cylindrical surface

$$\hat{\boldsymbol{\rho}} \times \nabla \times \left[\mathbf{M} + a_n \mathbf{M}^{(2)} + \mathbf{N} + b_n \mathbf{N} \right]_{\rho=a} = 0 \tag{C.25}$$

and defining $\gamma = x' = k_\rho a$ the expansion coefficients are given by

$$a_n = \frac{-J_n}{H_n^{(2)}(\gamma)} \text{ and } b_n = \frac{-J_n{}'(\gamma)}{H_n^{(2)}{}'(\gamma)} \tag{C.26}$$

Substituting (C.26) into (C.24) and evaluating (C.23), the electric dyadic Green's function of the second kind for the perfectly conducting infinite circular cylinder is obtained

$$\begin{aligned} \overline{\overline{G}}_{e2} = \frac{1}{(2\pi)^2} \sum_{n=-\infty}^{\infty} e^{jn\bar{\phi}} \int_{-\infty}^{\infty} dk_z e^{-jk_z \bar{z}} \Bigg\{ \left[\frac{-jnH_n^{(2)}(x)}{\gamma x H_n^{(2)}(\gamma)} + \frac{jn}{\gamma^2} \left(\frac{k_z}{k_0} \right)^2 \frac{H_n^{(2)}{}'(x)}{H_n^{(2)}{}'(\gamma)} \right] \hat{\boldsymbol{\rho}} \hat{\boldsymbol{\varphi}}' \\ - j \left[\frac{k_z k_\rho H_n^{(2)}{}'(x)}{\gamma k_0^2 H_n^{(2)}{}'(\gamma)} \right] \hat{\boldsymbol{\rho}} \hat{\mathbf{z}}' + \left[\frac{H_n^{(2)}{}'(x)}{\gamma H_n^{(2)}(\gamma)} - \left(\frac{nk_z}{k_0 \gamma} \right)^2 \frac{H_n^{(2)}(x)}{x H_n^{(2)}{}'(\gamma)} \right] \hat{\boldsymbol{\varphi}} \hat{\boldsymbol{\varphi}}' + \left[\frac{nk_z k_\rho H_n^{(2)}(x)}{\gamma x k_0^2 H_n^{(2)}{}'(\gamma)} \right] \hat{\boldsymbol{\varphi}} \hat{\mathbf{z}}' \\ + \left[\frac{nk_z k_\rho H_n^{(2)}(x)}{\gamma^2 k_0^2 H_n^{(2)}{}'(\gamma)} \right] \hat{\mathbf{z}} \hat{\boldsymbol{\varphi}}' - \frac{1}{\gamma} \left[\left(\frac{k_\rho}{k_0} \right)^2 \frac{H_n^{(2)}(x)}{H_n^{(2)}{}'(\gamma)} \right] \hat{\mathbf{z}} \hat{\mathbf{z}}' \end{aligned} \tag{C.27}$$

where $\bar{\varphi} = \varphi - \varphi'$, $\bar{z} = z - z'$, and $x = k_\rho \rho$.

APPENDIX D

FOCK FUNCTIONS

In his investigations into the phenomenon of diffraction by convex bodies, Fock encountered certain recurring canonical integrals. These canonical integrals take the form of a contour integral whose integration path encloses the complex poles of Airy functions or their derivatives and are known as Fock functions [23]. Two varieties of Fock functions are encountered in this work: the on-surface and far-zone. Furthermore, these types of Fock functions occur in two forms: hard and soft. The hard Fock functions arise from canonical problems where the Neumann boundary condition has been enforced, while the soft Fock functions arise in cases where the Dirichlet boundary condition has been enforced.

The on-surface Fock functions are given by

$$u(\xi) = e^{j3\pi/4} \frac{\xi^{3/2}}{\sqrt{\pi}} \int_{-\infty e^{-j2\pi/3}}^{\infty} \frac{w_2'(\tau)}{w_2(\tau)} e^{-j\xi\tau} d\tau \tag{D.1}$$

$$v(\xi) = \frac{1}{2} e^{j\pi/4} \sqrt{\frac{\xi}{\pi}} \int_{-\infty e^{-j2\pi/3}}^{\infty} \frac{w_2(\tau)}{w_2'(\tau)} e^{-j\xi\tau} d\tau \tag{D.2}$$

where $u(\xi)$ is the soft type and $v(\xi)$ is the hard type. The Fock-type Airy function of the second kind, denoted by, $w_2(\tau)$, and its derivative, $w_2'(\tau)$, are defined as

$$w_2(\tau) = \frac{1}{\sqrt{\pi}} \int_{\Gamma_2} e^{\tau z - z^3/3} dz \tag{D.3}$$

$$w_2'(\tau) = \frac{1}{\sqrt{\pi}} \int_{\Gamma_2} z e^{\tau z - z^3/3} dz \tag{D.4}$$

where the integration contour Γ_2 in the complex τ plane is depicted in Figure D.1. The relationship between the Fock-type Airy function and Miller-type Airy function, $Ai(\cdot)$, is expressed as

$$w_2(\tau) = 2\sqrt{\pi}e^{-j\pi/6}Ai\left(-\tau e^{j\pi/3}\right) \tag{D.5}$$

The asymptotic expansions of (D.1) and (D.2) for small arguments $(\xi < 0.6)$ are given by [2]

$$u(\xi) \sim 1.0 - \frac{\sqrt{\pi}}{2}e^{-j\pi/4}\xi^{3/2} + j\frac{5}{12}\xi^3 + \frac{5}{64}\sqrt{\pi}e^{-j\pi/4}\xi^{9/2} + \ldots \tag{D.6}$$

$$v(\xi) \sim 1.0 - \frac{\sqrt{\pi}}{4}\xi^{3/2} + j\frac{7}{60}\xi^3 + \frac{7}{512}\sqrt{\pi}e^{-j\pi/4}\xi^{9/2} + \ldots \tag{D.7}$$

The asymptotic expansions of (D.1) and (D.2) for large arguments $(\xi > 0.6)$ take the form of rapidly converging pole residue series and are given by [2]

$$u(\xi) \sim 2e^{j\pi/4}\sqrt{\pi}\xi^{3/2}\sum_{n=1}^{10}(\tau_n)^{-1}e^{-j\xi\tau_n} \tag{D.8}$$

$$v(\xi) \sim e^{-j\pi/4}\sqrt{\pi\xi}\sum_{n=1}^{10}(\tau_n')^{-1}e^{-j\xi\tau_n'} \tag{D.9}$$

where the complex zeroes of $w_2(\tau)$ and $w_2'(\tau)$ are denoted by τ_n and τ_n', respectively. The values of τ_n and τ_n' are listed in Table D.1.

The far-zone Fock functions are given by

$$f^{(n)}(\xi) = \frac{j^n}{\sqrt{\pi}}\int_{\Gamma_1}\frac{\tau^n e^{j\xi\tau}}{w_1(\tau)}d\tau \tag{D.10}$$

$$g^{(n)}(\xi) = \frac{j^n}{\sqrt{\pi}}\int_{\Gamma_1}\frac{\tau^n e^{j\xi\tau}}{w_1'(\tau)}d\tau \tag{D.11}$$

where $f^{(n)}(\xi)$ is the soft type, $g^{(n)}(\xi)$ is the hard type, and $w_1(\tau)$ is the Fock-type Airy function of the first kind. Note that $w_1(\tau)$ is the complex conjugate of $w_2(\tau)$. The integration contour Γ_1 in the complex τ plane for the far-zone Fock functions is depicted in Figure D.2. The formulas given below are valid within the specified domains of ξ and are used for the numerical computation of these functions [2].

for $g^{(0)}(\xi)$:

$$\xi < -1.3 : g^{(0)}(\xi) = 2.0e^{-j\xi^3/3} \tag{D.12}$$

$$-1.3 \le \xi \le 0.5 : g^{(0)}(\xi) = 1.39937 + \sum_{m=1}^{6} \frac{c(m)}{m!}(\kappa\xi)^m \tag{D.13}$$

$$0.5 < \xi \le 4.0 : g^{(0)}(\xi) = \sum_{m=1}^{10} \frac{e^{[\kappa\alpha'(m)\xi]}}{\alpha'(m)Ai(m)} \tag{D.14}$$

$$\xi > 4.0 : g^{(0)}(\xi) = 1.8325e^{\left[-(0.8823-j0.5094)\xi - j\xi^3/3\right]} \tag{D.15}$$

for $g^{(1)}(\xi)$:

$$\xi < -2.8 :\ g^{(1)}(\xi) = -j2.0\left(\xi^2 + j\frac{0.25}{\xi} - \frac{0.25}{\xi^4}\right)e^{-j\xi^3/3} \tag{D.16}$$

$$-2.8 \le \xi \le 0.5 :\ g^{(1)}(\xi) = \sum_{m=1}^{6} \frac{c(m)\kappa^m}{m!}(\xi)^{m-1} \tag{D.17}$$

$$0.5 < \xi \le 4.0 :\ g^{(1)}(\xi) = \kappa\sum_{m=1}^{10} \frac{e^{[\kappa\alpha(m)\xi]}}{Ai(m)} \tag{D.18}$$

$$\xi > 4.0 :\ g^{(1)}(\xi) = -1.8325\left(0.8823 - j0.5094 + j\xi^2\right)e^{\left[-(0.8823-j0.5094)\xi - j\xi^3/3)\right]} \tag{D.19}$$

for $f^{(0)}(\xi)$:

$$\xi < -1.1: \; f^{(0)}(\xi) = j2\xi\left(1 - \frac{0.25}{\xi^3} + \frac{0.5}{\xi^6}\right)e^{-j\xi^3/3} \tag{D.20}$$

$$-1.1 \le \xi \le 0.5: \; f^{(0)}(\xi) = 0.77582 + e^{-j\pi/3}\sum_{m=1}^{6}\frac{c(m)}{m!}(\kappa\xi)^m \tag{D.21}$$

$$0.5 < \xi \le 4.0: f^{(0)}(\xi) = e^{-j\pi/3}\sum_{m=1}^{10}\frac{e^{[\kappa\alpha(m)\xi]}}{Ai'(m)} \tag{D.22}$$

$$\xi > 4.0: \; f^{(0)}(\xi) = 0.0 \tag{D.23}$$

In (D.12)-(D.23), $\kappa = e^{-j5\pi/6}$, the coefficients used in (D.12)-(D.19) are listed in Table D.2, and the coefficients used in (D.20)-(D.23) are listed in Table D.3.

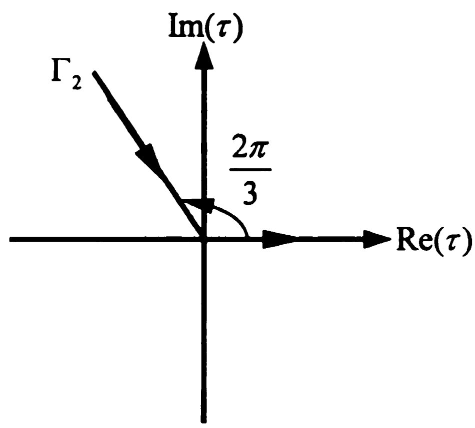

Figure D.1 Integration contour for $w_2(\tau)$.

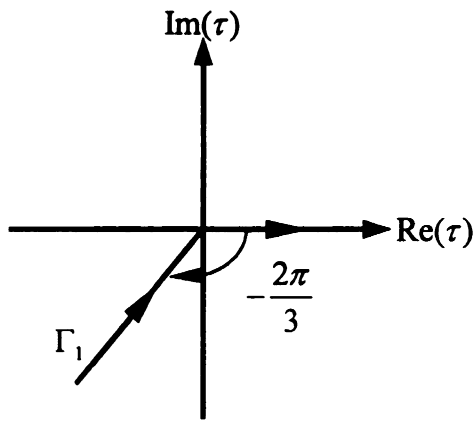

Figure D.2 Integration contour for the far-zone Fock functions.

Table D.1 Zeros of the Fock-type Airy function of the second kind $w_2(\tau)$ and of its derivative $w_2'(\tau)$. Note that $\tau_n = |\tau_n| e^{-j\pi/3}$ and $\tau_n' = |\tau_n'| e^{-j\pi/3}$.

n	$\lvert\tau_n\rvert$	$\lvert\tau_n'\rvert$
1	2.33811	1.011879
2	4.08795	3.24819
3	5.52056	4.82010
4	6.78661	6.16331
5	7.94413	7.37218
6	9.02265	8.48849
7	10.0402	9.53545
8	11.0085	10.5277
9	11.9300	11.4751
10	12.8288	12.3848

Table D.2 Constants for $g^{(0)}(\xi)$ and $g^{(1)}(\xi)$.

m	$c(m)$	$\alpha'(m)$	$Ai(m)$
1	0.7473831	1.01879297	0.5356566
2	-0.6862081	3.2481975	-0.41901548
3	-2.9495325	4.82009921	0.38040647
4	-3.4827075	6.16330736	-0.35790794
5	8.9378967	7.37217726	0.34230124
6	56.1946214	8.48848673	-0.33047623
7		9.53544905	0.32102229
8		10.52766040	-0.31318539
9		11.47505663	0.30651729
10		12.38478837	-0.30073083

Table D.3 Constants for $f^{(0)}(\xi)$.

m	$c(m)$	$\alpha(m)$	$Ai'(m)$
1	1.146730417	2.33810741	0.70121082
2	0.86284558	4.08794944	-0.80311137
3	-2.0192636	5.52055983	0.86520403
4	-9.977776	6.78670809	-0.91085074
5	-14.59904	7.94413359	0.94733571
6	49.0751	9.02265085	-0.97792281
7		10.04017434	1.00437012
8		11.00852430	-1.02773869
9		11.93601556	1.04872065
10		12.82877675	-1.06779386

APPENDIX E

BiCONJUGATE GRADIENT PSEUDOCODE

An iterative solver approach is employed to solve the FE-BI system of equations. Iterative solvers are more efficient than direct solvers at solving the large sparse matrices that arise from PDE based techniques in that direct solvers employ matrix fill-in, whereas iterative solvers do not. Consequently, iterative solvers preserve the sparseness of the system. The Biconjugate Gradient (BiCG) iterative solver employing Jacob's algorithm has proven to be readily applicable to the solution of sparse linear systems [46].

Initialize

$$\mathbf{r}_0 = \mathbf{b} - \mathbf{A}\mathbf{x}_0$$
$$\mathbf{p}_0 = \mathbf{r}_0$$

Do until (res. $\leq$ tol.)

$$\alpha_k = \frac{\langle \mathbf{r}_k^*, \mathbf{r}_k \rangle}{\langle \mathbf{p}_k^*, \mathbf{A}\mathbf{p}_k \rangle}$$
$$\mathbf{x}_{k+1} = \mathbf{x}_k + \alpha_k \mathbf{p}_k$$
$$\mathbf{r}_{k+1} = \mathbf{r}_k - \alpha_k \mathbf{A}\mathbf{p}_k$$
$$\beta_k = \frac{\langle \mathbf{r}_{k+1}^*, \mathbf{r}_{k+1} \rangle}{\langle \mathbf{r}_k^*, \mathbf{r}_k \rangle}$$
$$\mathbf{p}_{k+1} = \mathbf{r}_{k+1} + \beta_k \mathbf{p}_k$$

End Do

where $\mathbf{x}$ is the unknown solution vector for which an accurate estimate is to be determined, $\mathbf{p}$ is the search vector which points in the direction in the n-dimensional space that the algorithm must move in order to improve upon the solution estimate, and $\mathbf{r}$ is the residual vector. The subscript 0 denotes an initial guess which for $\mathbf{x}_0$ can be set equal to $\{0\}$, subscripts k and $k+1$ denote the previous and current estimates, respectively.

The complex scalar coefficient α_k, which dictates how far the algorithm moves along the search vector, is chosen to enforce the biorthogonality condition

$$\langle \mathbf{r}^*_{k+1}, \mathbf{r}_k \rangle = \langle \mathbf{r}_{k+1}, \mathbf{r}^*_k, \rangle = 0$$

While the complex scalar coefficient β_k is chosen to enforce the biconjugacy condition

$$\langle \mathbf{p}^*_{k+1}, \mathbf{A}\mathbf{p}_k \rangle = \langle \mathbf{p}_{k+1}, \mathbf{A}^{*T}\mathbf{p}^*_k \rangle = 0$$

The solution is said to converge when a prescribed tolerance condition

$$\frac{\langle \mathbf{r}_{k+1}, \mathbf{r}_{k+1} \rangle}{\langle b, b \rangle} \leq \varepsilon$$

is satisfied, where ε is a tolerance threshold value.

BIBLIOGRAPHY

BIBLIOGRAPHY

[1] J-M. Jin and J.L. Volakis, "A Finite Element-Boundary Integral Formulation for Scattering by Three-Dimensional Cavity-Backed Apertures," *IEEE Trans. Antennas and Propagat.*, vol. 39, no. 1, pp. 97-104, Jan. 1991.

[2] L.C. Kempel, J.L. Volakis and S. Bindiganavale, "Radiation and scattering from printed antennas on cylindrically conformal platforms," Radiation Laboratory, Dept. Elec. Eng. And Comp. Sci., The University of Michigan, Ann Arbor, Michigan, Rep. 030601-3-T, Jan. 1994, prepared under NASA Grant NAG-1-1478, NASA Langley Research Center, Hampton VA.

[3] L.C. Kempel, J.L. Volakis and R.J. Sliva, "Radiation by cavity-backed antennas on a circular cylinder," *IEE Proc.-Microw. Antennas Propagat.*, vol. 142, no. 3, pp. 233-239, June 1995.

[4] C. Flammer, *Spheroidal Wave Functions*, Stanford Univ. Press, Stanford, CA., 1957.

[5] M. Zhang and A.A. Sebak, "Radiation characteristics of a slot antenna on a conducting prolate spheroid," *Can. J. Phys.*, vol. 73, pp. 376-385, 1995.

[6] B.P. Sinha, *Electromagnetic Scattering from Conducting Prolate Spheroids in the Resonance Region*, Ph.D. Dissertation, University of Waterloo, Waterloo, Ontario, Canada, 1974.

[7] J.A. Stratton, *Electromagnetic Theory*, McGraw-Hill, New York, 1941.

[8] F.V. Schultz, *Scattering by a Prolate Spheroid*, Ph.D. Dissertation, University of Michigan, Ann Arbor, Michigan, 1950.

[9] R.D. Spence and C.P. Wells, "Vector Wave Functions," *Symposium on the Theory of Electromagnetic Waves* under the sponsorship of the Washington Square College of Arts and Science, the Institute for Mathematics and Mechanics of New York University, and the Geophysical Research Directorate of the Air Force Cambridge Research Laboratories, June, 1950.

[10] C.T. Tai, *Dyadic Green Functions in Electromagnetic Theory*, IEEE Press, New Jersey, 1994.

[11] E.C. Hatcher, Jr. and A. Leitner, "Radiation from a Point Dipole Located at the Tip of a Prolate Spheroid," *J. Appl. Phys.*, vol. 25, no. 10, pp. 1250-1253, Oct. 1954.

[12] C.D. Taylor, "On the Exact Theory of a Prolate Spheroidal Receiving and Scattering Antenna," *Radio Science*, vol. 2, no. 3, pp. 351-360, March 1967.

[13] A.J. Giarola, "Dyadic Green's functions in the prolate spheroidal coordinate system," *1995 IEEE APS Int. Symp. Dig.*, vol. 2, Newport Beach, CA, pp. 826-829, 1995.

[14] L-W. Li, M.S. Leong, P-S Kooi, and T-S Yeo, "Spheroidal Vector Wave Eigenfunction Expansion of Dyadic Green's Functions for a Dielectric Spheroid," *IEEE Trans. Antennas and Propagat.*, vol. 49, no. 4, pp. 645-659, April 2001.

[15] R.G. Kouyoumjian, "Asymptotic High-Frequency Methods," *Proc. IEEE,* vol. 53, pp. 864 – 876, August 1965.

[16] B.R. Levy and J.B. Keller, "Diffraction by a Smooth Object," *Comm. Pure Appl. Math.*, vol. 12, pp. 159-209, 1959.

[17] J.B. Keller, "Geometrical Theory of Diffraction," *J. Opt. Soc. of America*, vol. 52, no. 2, pp. 116-130, Feb. 1962.

[18] A. Ishimaru, *Electromagnetic Wave Propagation, Radiation, and Scattering*, Prentice-Hall, New Jersey, 1991.

[19] R.G. Kouyoumjian, *Numerical and Asymptotic Techniques in Electromagnetics*, vol. 3, Springer-Verlag, New York, 1975.

[20] P.H. Pathak and R.G. Kouyoumjian, "An Analysis of the Radiation from Apertures in Curved Surfaces by the Geometrical Theory of Diffraction," *Proc. IEEE*, vol. 62, no. 11, pp. 1438-1461, Nov. 1974.

[21] P.H. Pathak, W.D. Burnside and R.J. Marhefka, "A Uniform GTD Analysis of the Diffraction of Electromagnetic Waves by a Smooth Convex Surface," *IEEE Trans. Antennas and Propagat.*, vol. 28, pp. 631-642, Sept. 1980.

[22] P.H. Pathak and R.G. Kouyoumjian., "The Radiation from Apertures in Curved Surfaces," ElectroScience Lab., Dept. Elec. Eng., Ohio State Univ., Columbus, Ohio, Rep. NASA CR-2263, July 1973, prepared under Contract NGR 36-008-144 for National Aeronautics and Space Administration, Washingtion D.C.

[23] V.A. Fock, *Electromagnetic Diffraction and Propagation Problems*, Pergamon Press Inc., New York, 1965.

[24] J.J. Bowman, T.B.A. Senior, and P.L.E. Uslenghi, *Electromagnetic and Acoustic Scattering by Simple Shapes*, Hemisphere Publishing Corp., 1987.

[25] R.F. Goodrich, "Fock Theory—An Appraisal and Exposition," *IRE Trans. Antennas and Propagat.*, pp. S28-S36., December 1959.

[26] P.H. Pathak and N. Wang, "Ray Analysis of Mutual Coupling Between Antennas on a Convex Surface," *IEEE Trans. Antennas and Propagat.*, vol. 29, no. 6, pp. 911-922, Nov. 1981.

[27] J.R. Wait, *Electromagnetic Radiation From Cylindrical Structures*, Pergamon Press, New York, 1959.

[28] R. Mittra and S.S.-Naini, "Source radiation in the presence of smooth convex bodies," *Radio Science*, vol. 14, no. 2, pp. 217-237, March-April 1979.

[29] P.H. Pathak and N.N. Wang., "An Analysis of the Mutual Coupling Between Antennas on a Smooth Convex Surface," ElectroScience Lab., Dept. Elec. Eng., Ohio State Univ., Rep. 784583-7, Oct. 1978, prepared under Contract N62269-76-C-0554 for Naval Air Development Center, Warminster Pa.

[30] J.L. Volakis, A. Chatterjee and L.C. Kempel, *Finite Element Method for Electromagnetics*, IEEE Press, New York, 1998.

[31] M. Abramowitz and I.A. Stegun, *Handbook of Mathematical Functions*, National Bureau of Standards, Washington D.C., June 1964.

[32] J. Gong, J.L. Volakis, A. Woo, and H. Wang, "A hybrid finite element boundary integral method for analysis of cavity-backed antennas of arbitrary shape," *IEEE Trans. Antennas and Propagat.*, vol. 42, no. 9, pp. 1233-1242, September 1994.

[33] T. Ozdemir and J.L. Volakis, "Triangular prisms for edge-based vector finite element antenna analysis," *IEEE Trans. Antennas and Propagat.*, pp. 788-797, May 1997.

[34] C.A. Macon, L.C. Kempel, and S.W. Schneider, "Radiation and Scattering by Complex Conformal Antennas on a Circular Cylinder," to appear in the journal *Advances in Computational Mathematics*

[35] L.C. Kempel, "Implementation of Various Hybrid Finite Element-Boundary Integral Methods: Bricks, Prisms and Tets," *1999 ACES Meeting*, Monterey, California, pp. 242-249, 1999.

[36] S.M. Rao, D.R. Wilton, A.W. Glisson, "Electromagnetic Scattering by Surfaces of Arbitrary Shape," *IEEE Trans. Antennas and Propagat.*, vol. 30, no. 3, May 1982.

[37] J. VanBladel, *Electromagnetic Fields*, McGraw-Hill, New York, 1964

[38] P.R. Haddad, "Scattering By Non-Planar Surfaces," University of Michigan, 1991.

[39] S.M. Wilton, S.M. Rao, A.W. Glisson, D.H. Schaubert, O.M. Al-Bundak, and C.M. Butler, "Potential Integrals for Uniform and Linear Source Distributions on Polygonal and Polyhedral Domains," *IEEE Trans. Antennas and Propagat.*, vol. 32, no. 3, March 1984.

[40] M.M. Lipschutz, *Differential Geometry, Schaum's Outline Series*, McGraw-Hill, New York, 1969.

[41] J.B. Marion and S. T. Thornton, *Classical Dynamics of Particles and Systems*, 3rd ed., Harcourt Brace Jovanovich, Inc., 1988.

[42] P.F. Byrd and M.D. Friedman, *Handbook of Elliptic Integrals*, 2nd ed., Springer-Verlag, New York, 1971.

[43] W. Franz and K. Klante, "Diffraction by Surfaces of Variable Curvature," *IRE Trans. Antennas and Propagat.*, pp. S68-S70, Dec. 1959.

[44] D.R.Voltmer, *Diffraction by Doubly Curved Convex Surfaces*, Ph.D. Dissertation, Ohio State University, 1970.

[45] J-M Jin, *The Finite Element Method in Electromagnetics*, Wiley-Interscience, New York, 1993.

[46] C.F. Smith, A.F. Peterson, and R. Mittra, "The Biconjugate Gradient Method for Electromagnetic Scattering," *IEEE Trans. Antennas and Propagat.*, pp. 938-940, June 1990.

[47] L. Josefsson and P. Persson, "An Analysis of Mutual Coupling on Doubly Curved Convex Surfaces," *2001 IEEE AP-S Int. Symp. Dig.*, vol. 2, Boston, MA, 2001, pp. 342-345, 2001.

[48] L.C. Kempel and K. Trott, "Progress in modeling complex conformal antennas using the finite element-boundary integral method," *1998 URSI Radio Science Meeting*, Atlanta, GA, June 1998.

[49] A. Papoulis, *The Fourier Integral and its Applications*, McGraw-Hill, New York, 1962.